Analysis of junctional and F-actin dynamics during blood vessel morphogenesis

Inauguraldissertation

zur

Erlangung der Würde eines Doktors der Philosophie

vorgelegt der

Philosophisch-Naturwissenschaftlichen Fakultät

der Universität Basel

von

Cora Wiesner

aus Deutschland

Basel, 2020

Genehmigt von der Philosophisch-Naturwissenschaftlichen Fakultät
auf Antrag von

Prof. Dr. Markus Affolter

Prof. Dr. Holger Gerhardt

Basel, den 17. März 2020

Prof. Dr. Martin Spiess
Dekan

Table of contents

List of Abbreviations

AJ	adherens junction
Arp2/3	actin-related protein 2/3
ATP	adenosine triphosphate
BAC	bacterial artificial chromosome
bp	base pairs
BSA	bovine serum albumin
Ca^{2+}	calcium
Cdc42	cell division control protein 42
cmlc2	cardiac myosin light chain-2
DA	dorsal aorta
DLAV	dorsal longitudinal anastomotic vessel
DMSO	dimethyl sulfoxide
DNA	deoxyribonucleic acid
dpf	days post fertilization
E-cadherin	epithelial cadherin
E. coli	Escherichia coli
E3	„egg water“
EGFP	enhanced green fluorescent protein
Ena/VASP	enabled/vasodilator-stimulated phosphoprotein
Esam	endothelial Cell Adhesion Molecule
F-actin	filamentous actin
F1 generation	Filial-Generation
FAJ	focal adherens junctions
fli	friend leukemia insertion
FLIM	fluorescence-lifetime imaging microscopy
Fmole	femtomole
FRET	Förster Resonance Energy Transfer
FWD	forward
G-actin	globular actin

GDP	guanosine diphosphate
GEF	guanine nucleotide exchange factors
GTP	guanosine triphosphate
hpf	hours post fertilization
iRFP	near-infrared fluorescent protein
ISV	intersegmental vessel
JAIL	junction-associated intermittent lamellipodia
JAM	junction adhesion molecule
JBL	junction-based lamellipodia
kdrl	kinase insert domain receptor like
kV	kilovolt
LB	lysogeny broth
LMA	low melting agarose
LOV	light-oxygen voltage
MLCK	myosin light chain kinase
MLCP	myosin light chain phosphatase
NFP	nucleation promoting factor
NMII	non-muscular myosin II
ON	overnight
PA	photoactivatable
PBS	phosphate-buffered saline
PBST	phosphate buffer saline with Tween-20
PCAM	platelet cell adhesion molecule
PCR	polymerase chain reaction
PCV	postcardinal vein
PFA	paraformaldehyde
pH	potential hydrogen
PI3K	phosphoinositide 3-kinase
PTU	phenylthiourea
Rac	ras-related C3 botulinum toxin substrate
REV	reverse

Rho	ras homolog family member
RLC	regulatory light chain
RNA	ribonucleic acid
ROCK	Rho-associated protein kinase
ROI	region of interest
rpm	rounds per minute
RT	room temperature
SV40	simian-Virus-40
TAE	TRIS-Acetat-EDTA (buffer)
TE	Tris-EDTA (buffer)
Tg	transgene
TGF	transforming growth factor
TJ	tight junction
TMD	transmembrane domain
TS	tension sensor
UAS	upstream activating sequence
Ubs	University of Basel
UCHD	calponin homology domain of utrophin
VE-cadherin	vascular endothelial cadherin
VEGF	vascular endothelial growth factor
VEGFR	vascular endothelial growth factor receptor
WASP	viskott-Aldrich syndrome protein
WAVE	WASP-family verprolin-homologous protein
ZO1	Zona Occludens- 1

Abstract

Organ morphogenesis relies on dynamic cell behaviors, which are highly coordinated to ensure a functional cellular organ architecture. During vascular morphogenesis, the process of angiogenesis is driven by cell migration, cell shape changes and cell rearrangements. Here, a dynamic balance between inter-endothelial cell adhesion and plasticity allows angiogenic sprouting while maintaining the endothelial seal.

Previous analyses on blood vessel formation and anastomosis in zebrafish have shown that junctional remodeling is central to many aspects of morphogenetic endothelial cell-cell interactions. In particular, the adhesion molecule VE-cadherin (Cdh5) is essential for coordinated cell shape changes during multicellular tube formation, as loss of VE-cadherin was shown to inhibit cell rearrangements (Sauteur et al., 2014). This study also proposed an active, force generating function for VE-cadherin in this process. This hypothesis is supported by our study showing that cell elongation is mediated by junction-based lamellipodia (JBL), which are thought to provide a tractile force for junction elongation (Paatero et al., 2018).

In my thesis, my goal was to further analyze the molecular mechanisms which underly JBL function. In particular I focused on molecular players that influence F-actin dynamics or contractility (Arp2/3, Rac1 and ROCK) in order to identify critical players in the process of the cell elongation movement. Furthermore, I elucidated, how JBL might generate motile forces and how these forces are transmitted onto endothelial cell junctions (e.g. VE-cadherin)

In the course of my experiments I identified the actomyosin contractility as an important basis for junctional ring elongation. Inhibition of ROCK did interfere with the correct localization of junctional protein ZO1 as it is abrogated formation of double junctions- a hallmark during JBL oscillations and an indispensable step to since it leads to the formation of a new attachment site. Furthermore, I found that the establishment of differential VE-cadherin tension is also ROCK-dependent, which might provide the basis for junctional remodeling. Junctional rearrangements were not only impaired after inhibition of ROCK.

Also, interference with the F-actin dynamics significantly altered junctional ring elongation. Arp2/3 (and concomitant formation of branched F-actin networks) is necessary for maintaining junctional stability and responsible for the correct localization of F-actin during the process, whereas Rac1 mostly seem to play a role in the induction phase of the JBL. Last but not least I generated two new transgenic fish lines (fli:iRFP-UCHD and kdrl:mCherry-PA-Rac1), which will open up a whole lot of new possibilities for future experiments. Making use of the photoactivatable Rac1 will give manifold new insights into processes during vascular morphogenesis, which underly Rac1 activity (sprouting, anastomosis, etc.).

In summary JBL function and subsequent endothelial cell rearrangements rely on a tight interplay between generation and maintenance of a dynamic F-actin cytoskeleton and regulation of junctional proteins. The F-actin cytoskeleton furthermore provide a basis for local force generation, which is reflected in differential VE-cadherin tension and thus exert mechanical forces, which in turn are a major driver of the process of junctional ring elongation. Last but not least my experiments suggest, that JBL formation and local protrusion formation might be a general mechanism of endothelial cells to induce cell movements and cell shape changes (e.g. in the dorsa aorta).

I.

Introduction

1. Introduction

1.1. Biological tubes in multicellular organisms

Tubular systems exist in all multicellular organisms throughout the animal kingdom and represent the fundamental structural architecture of several organs including the intestine, the kidney, the lung and the cardiovascular system. Tubes serve different functions in an organism such as transport and absorption of gases, nutrients, waste and hormones within or between organs. Furthermore, they are crucial for providing a barrier and necessary for the compartmentalization of organ functions. Tube architecture is very much determined by organ function and tailored to serve organ-specific processes. The architectural features are multi-variant and come along with the organization of cells and processes that lead to the formation of tubes. Despite the great variety, there are basic structures that are commonly shared or processes of tube formation that can be used for classification of tubes. They have been already extensively reviewed for epithelial tubes (Andrew and Ewald, 2010; Baer et al., 2009; Lubarsky and Krasnow, 2003) and for blood and lymphatic vessels, which are made up by endothelial cells (Carmeliet, 2000; Ellertsdóttir et al., 2010). Here, briefly two aspects will be described in more detail for epithelial tubes: cellular architecture of biological tubes (see 1.1.1.) and lumen formation in tubular systems (1.1.2).

1.1.1. Cellular architecture of biological tubes

Tubes are always made up of polarized cells that surround a central luminal space. Cells are either endothelial (for the vasculature) or epithelial cells (for all other organs), with the apical site pointing towards the lumen and the basal side facing other tissues or the basement membrane. Depending on their cellular architecture, tubes can be classified into different types (reviewed among others in Baer et al., 2009; Lubarsky and Krasnow, 2003): multicellular, auto-cellular and intracellular (or seamless) tubes, whereas the latter two both are representative of a unicellular tube architecture (Figure 1). In multicellular tubes, several cells form the tube as observed in a cross section. This type of tube is most commonly found in mature tubular organs of vertebrates.

In unicellular tubes only one cell is wrapped around the lumen (one cell in a cross section visible) and forms an auto cellular junction (also referred to as a self-contact). Such simple tubes have been among others described in the *Caenorhabditis elegans* (*C. elegans*) intestine, the drosophila tracheal system and have also been reported to be present in the vertebrate vasculature. Sealing of tubes without the formation of adherens junctions can be observed in seamless tubes (also referred to as transcellular tube). Here, the lumen is confined within a single cell, which was described among others for tubes in the digestive tract of C. elegans or fusion and terminal tracheal cells in drosophila.

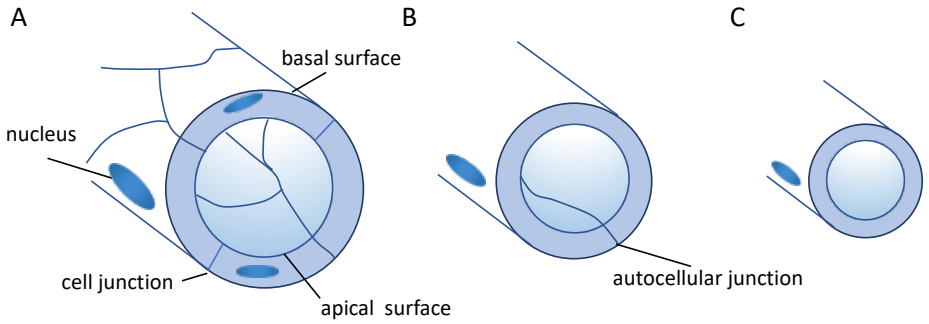

Figure 1: Architecture of epithelial tubes. Based on their cellular architecture, three distinct types of tubes can be distinguished: In a multicellular tube (A), several cells make up the cross section of a tube (here four are depicted with respective cell junctions), whereas in a unicellular tube, the luminal surface is formed by a single cell (B). A unicellular tube, that has an established lumen within a single cell is called seamless tube (C).

The architectural diversity of biological tubes implicates different physical and cellular constraints for each type and indicates that the morphogenetic processes that underlying their formation might be manifold. Indeed, five different principles of tube formation can be discerned and each process gives rise to a specific type of tube.

1.1.2. Lumen formation in tubes

Generally, tubes can form from an already polarized epithelium (wrapping or budding) or from an unpolarized epithelium (cord hollowing, cell hollowing or cavitation). During the process of wrapping a flat sheet of epithelial cells as a portion of the whole tissue rolls up until the edges meet and seal, forming a tubular structure. The final tube runs parallel to the plane of the epithelium. This process has been reported during neural tube formation in vertebrates (Colas and Schoenwolf, 2001).

During budding, branches are formed from already existing tubes, thereby enlarging an existing tubular network. Here, a group of cells migrate out and the epithelial sheet consecutively invaginates and forms a new branch. The new branch extends away from the epithelial plane and the lumen is a direct extension of the parental branch lumen. This process has been studied extensively in different systems (e.g. lung or kidney development, drosophila salivary gland or tracheal development), as it provides the most common used strategy to increase the complexity of tubular organs. The mechanism of cavitation has been reported in the context of the development of the mammalian salivary gland or the formation of the pro-amniotic cavity (Coucouvanis and Martin, 1995; Melnick and Jaskoll, 2000). Here, the cells in the center of a thick cylindrical mass of cells are eliminated, thereby generating a hollow tube.

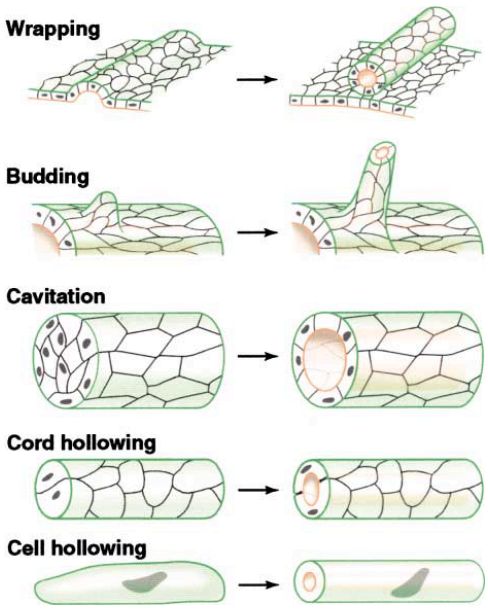

Figure 2: Morphological processes of tube formation. Distinct modes of tube formation give rise to different types of tubes. During wrapping, a part of the epithelial sheet invaginates. The edges roll up until they meet and seal the tube. In budding, a group of cells migrate out from an already existing tube, extending a new branch. Cavitation describes the process, in which cells in the center of a solid cylindrical cell mass are eliminated. In cord hollowing, a *de novo* lumen is formed by formation of an open space. Remodeling of the apical cells lead to a lumenized tube. In cell hollowing, the lumen is formed within the cytoplasm of a single cell, spanning its entire length. Image taken from Lubarsky and Krasnow, 2003 (with permission).

Another process of lumen formation whereby a space is created within a solid cylindrical cord of cells is chord hollowing. In this case, the lumen is subsequently formed by an open space, which is created between the remodeling cells that point towards the future lumen. In contrast, cell hollowing is very different from the processes describes so far. Instead of a group of cells, only a single cell is involved and the lumen is formed within single cells, thereby resulting in a seamless tube. For instance, this mechanism of tube formation has been described in terminal tracheal cells and has been hypothesized to occur in vascular capillaries (Wolff and Bär, 1972).
On overview of the described processes is provided in Figure 2. The descriptions were based on information published in excellent reviews (Andrew and Ewald, 2010; Baer et al., 2009; Lubarsky and Krasnow, 2003).

Although a lot of general knowledge of common principles has already been collected, major questions have to be answered individually in the context of the particular organ/ process one is interested in. What molecules mediate certain cell behaviors? Can we describe cellular and molecular mechanisms or principles that are crucial for all the different processes of tube formation? In order to answer these questions different model systems each having their strengths and limitations are available and have to be chosen carefully. For my thesis, I have employed embryonic zebrafish and chose to study endothelial tube morphogenesis during development. In the following, I will specifically (and somewhat complementary to section 1.1.2) describe the processes of lumen formation in the zebrafish vasculature in detail. Following up, I will highlight advantages of the zebrafish as a model organism (1.2.) as well as highlight and explain cellular behaviors that are important for vascular morphogenesis and tube formation.

1.1.2.1. Mechanisms of vascular lumen formation in the zebrafish

Proper function of the cardiovascular system relies on the lumenization of blood vessels. Several mechanisms have been suggested, including cord hollowing, budding, lumen ensheathment and cell hollowing, each of them being specific or predominant during certain processes such as sprout formation or anastomosis. Some of these processes have been already described in 1.1.2, but will be further elaborated on in the context of the zebrafish vascular network.

Cord hollowing

The best analyzed model for cord hollowing in zebrafish and mice is represented by the dorsal aorta, the first axial vessel to form (Jin et al., 2005). The endothelial cells are assembled in a vascular chord, which subsequently polarize and forme an apical membrane (by the deposition of sialomucins). This is followed by cell shape changes (from round to elongated) and cell rearrangements, which allow for the formation of a potent lumen within elongated endothelial cells (Strilić et al., 2010, 2009). Besides the dorsal aorta, a cord hollowing process has also been described in the dorsal longitudinal anastomotic vessel (DLAV) (Herwig et al., 2011) (compare Figure 3).

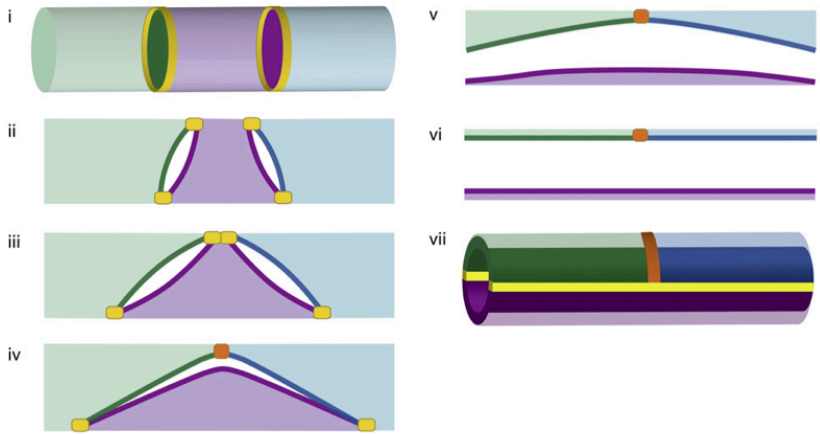

Figure 3: Cord hollowing mechanism forming a multicellular tube. Two junctional rings (encircling a local lumen between two apical membrane compartments) are brought together by cell rearrangements. A new junction is formed (orange) and the middle cell (purple) detaches at the new contact site. Eventually, the two luminal compartments merge into one. Figure taken from Herwig et al., 2011 (with permission).

During the process of anastomosis, lumen formation commences with the establishment of several luminal pockets (local lumens), which are contained within junctional rings. Here, at least three adjacent cells contribute to this process, generating two junctional rigs at their respective contact sites. These junctional rings (driven by cell rearrangements) converge towards each other, until a novel contact can be established between the two outer cells. This new junctional contact is subsequently enlarged, followed by the detachment of the medial cell.

Thereby, the local lumens coalesce, resulting in a fully lumenized vessel of multicellular architecture. It is important to mention, that this process happens independent of blood pressure. Another mechanism that was described in the context of the DLAV and was determined to be the more frequent (in around 63 % of investigated cases) is described in the section of cell hollowing.

Budding

Budding can be observed during angiogenic sprouting, when a sprout grows out from a vessel with continuous lumen. Simultaneously, the blood pressure drives the expansion of the lumen into the sprout or even into the tip cell (Baer et al., 2009; Lenard et al., 2013). This process occurs predominantly in larger caliber vessels and was suggested to occur in the zebrafish cranial vasculature, as determined by time lapse *in vivo* recording (Huisken and Stainier, 2009)

Lumen ensheathment

Lumen ensheathment is a rather newly discovered process and was described to be the underlying principle of lumen formation in the zebrafish common cardinal vein (CCV) (Helker et al., 2013). The CCV is initially an open-ended tube, collecting all the blood in order to transport it back towards the heart. With the initiation of heart beat and blood flow, endothelial cells start to migrate, subsequently engulfing the lumen as they fold around the blood stream.

Cell hollowing (vacuole fusion and membrane invagination)

As mentioned in 1.1.2, cell hollowing describes the process, in which a lumen is formed within one single cell, ultimately leading to a unicellular architecture. This mechanism was shown to be prevalent in the intersegmental vessels (ISVs) and the DLAV of zebrafish embryos. Different mechanisms were proposed to occur in terms of ontogenesis of the intracellular lumen. In what way they have a joint or independent appearance remains elusive. One of the processes is vacuole fusion, which was investigated in Kamei et al., 2006. The results they obtained from high-resolution time-lapse two-photon imaging supported a model, in which inter and intracellular fusion of endothelial vacuoles are the driving mechanism of vascular lumen formation; intracellular vacuoles first fuse within stalk cells and then with the plasma membrane to generate an interconnected lumen.

This view was challenged more recently in a study conducted by Gebala et al., 2016. They report a process they term inverse blebbing, in which spherical deformations of the apical membrane appear during lumen expansion. These inverse blebs appear in response to high hemodynamic forces (blood pressure), inducing deformations in endothelial cells that ultimately lead to a unidirectional expansion of the lumen. A rather similar mechanism of forming a consecutive intracellular lumen that is based on membrane deformations (membrane invaginations, respectively) and is highly dependent on blood pressure was observed in the DLAV during the anastomosis process (Herwig et al., 2011) (Figure 4). Here, apical membrane invaginating into tip cells of already lumenized angiogenic sprouts (which are thus connected to the circulation) fuse with their second apical membrane that was previously established at the contact site with the neighboring cell. Under the effect of blood pressure, the cell membrane will push through and into the next, non-lumenized endothelial cell. This directional membrane invagination process is therefore based on the invagination and extension of a transcellular lumen and ultimately gives rise to a unicellular (or seamless) tube. In comparison to the lumen formation process during anastomosis in the DLAV described earlier (compare Figure 3), the cells exhibit less migratory behavior and the formation of lumen does not depend of cell rearrangements, neither on blood flow.

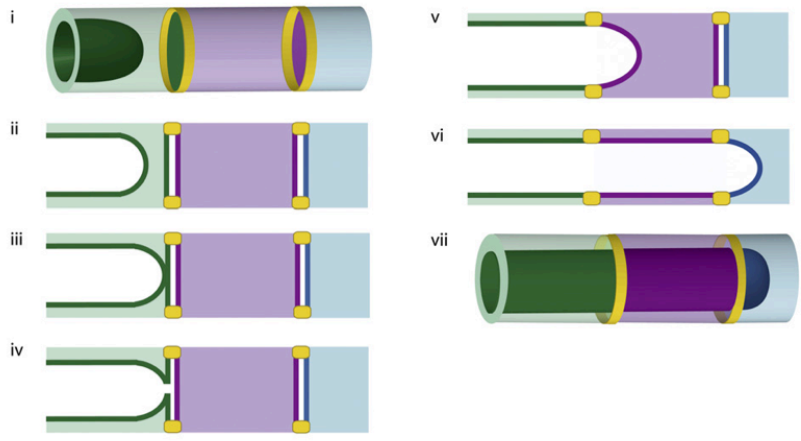

Figure 4: Formation of a unicellular, seamless tube by membrane invagination. The apical membrane of the green cell invaginates and fuses with its own apical membrane at the cell interface site. Driven by blood pressure, the lumen expands through the neighboring cell as the invagination continues (in the purple cell). Figure taken from Herwig et al., 2011 (with permission).

1.2. The zebrafish as model to study vascular morphogenesis

The zebrafish (*Danio rerio*) is a small tropical freshwater species, native to the region of India and Southeast Asia. The life span of an adult zebrafish is between two to three years, and they reach maturity at an approximate age of 3 months. One pair of zebrafish is capable to produce a large amount of offspring (around 200 eggs/week) (Hill et al., 2005). Embryos develop *ex-uterine* and show a rapid development. The first cell division is completed within 45 minutes after fertilization, and the following cell divisions occur within shorter periods of time. Zebrafish development is already well characterized (Kimmel et al., 1995). In recent years, the zebrafish has become a very powerful model organism in laboratory research due to several attributes. Besides the *ex utero* development, zebrafish embryos are transparent, which facilitates not only staging but also enables easy monitoring of different processes during development (Dooley and Zon, 2000; Lessman, 2011). One of these processes that can be easily investigated is the formation of complex vascular networks. Vascular development starts very early in the embryo and by 24 hours post fertilization (hpf), the first heart beats can be observed and blood circulation starts shortly thereafter (Kimmel et al., 1995). In terms of cardiovascular research, many different transgenic marker lines are available. This allows for live imaging of different processes of vascular development due to the exceptional optical clarity of the embryo. Furthermore, a considerable variety of genetic tools have been developed, which make functional analysis possible (e.g. CRISPR/Cas9, (Cong et al., 2013; Hwang et al., 2013)). Additionally, pharmacological studies (e.g. inhibitor treatments) can be performed easily and also enable large-scale drug screenings (Parng et al., 2002). Last but not least, zebrafish embryos are able to survive without a fully developed blood circulation until larval stages. Hence, cardiovascular defects that would lead to premature death in other model organism such as in mice, can be studied and characterized (Glickman and Yelon, 2002). In summary, all the mentioned aspects make the zebrafish an outstanding model to study vascular development. Even though there is a huge difference in the overall vascular anatomy between species, most molecular and cellular processes were described to be very similar between the zebrafish and other vertebrates (also mammals) (Howe et al., 2013).

Additionally, the branching program in the zebrafish vasculature is rather simple and is driven by only a few cells in comparison to other branched systems. As sprouting and anastomosis do not rely on a collective behavior of a larger group of cells, it makes it fairly easier to investigate and understand single-cell behaviors better (Kotini et al., 2019).

1.3. Blood vessel formation in the zebrafish: angiogenesis and vasculogenesis

During vascular tube formation, two distinct morphogenetic processes can be described: vasculogenesis and angiogenesis. Vasculogenesis describes the *de novo* formation of blood vessels via the assembly of angioblasts in a guided manner (Poole and Coffin, 1989). Angioblasts are mesoderm-derived precursors of endothelial cells (Kimmel et al., 1995). The first vessel with arterial cell fate that is built via vasculogenesis in the zebrafish is the dorsal aorta (DA) at around 13 hpf, followed by the posterior cardinal vein (PCV) via ventral sprouting at around 20 hpf (Isogai et al., 2001). Together, they establish a primitive vascular network in early steps of network formation. In order to meet the changing needs of the growing embryo and to adapt to environmental cues, the network grows in size and complexity. Further ramification of the vascular network, however, mostly results from a process called angiogenesis.

During sprouting angiogenesis, secondary (new) blood vessels are formed from preexisting vessels. Sprouting is very dynamic and needed for constant adaptation during physiological (e.g. growth, wound healing) but also pathological (tumor vascularization) conditions. The intersegmental vessels in the zebrafish embryo are the first ones to be formed by angiogenesis and emerge from the dorsal aorta at around 22 hpf onwards (Isogai et al., 2003). In the meantime, there are two different mechanisms described, termed sprouting angiogenesis and intussusception (Makanya et al., 2009). As initially described and extensively studied in Patan, 2000, three different major events happen sequentially: selection of a tip cell and initial sprout formation, followed by the extension and final interconnection of sprouts to form a fully functional network upon lumen formation. An overview of the fully established zebrafish vasculature is depicted in Figure 5.

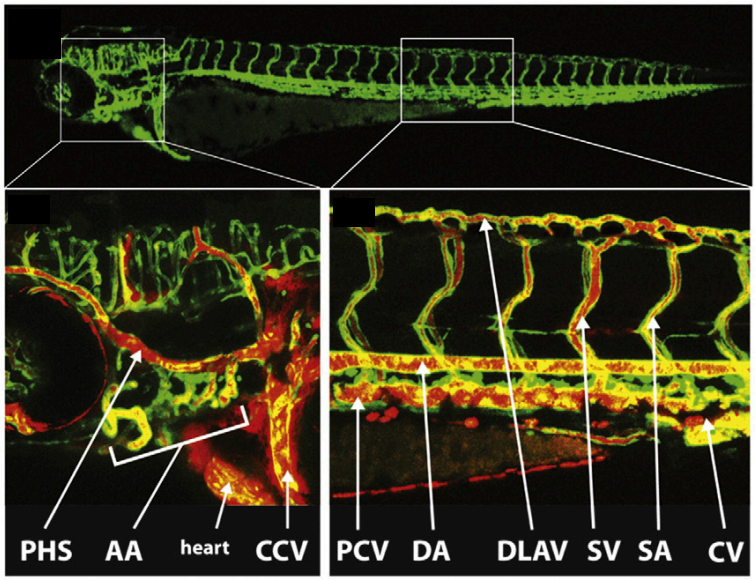

Figure 5: The vascular system in the zebrafish embryos. The zebrafish vasculature of a 72 hpf old embryo expressing Tg(kdrl:EGFP) in green and using microangiography (red quantum dots). PHS: primary head sinus, AA: aortic arches, CCV: common cardinal vein, PCV: posterior cardinal vein, DA: dorsal aorta, DLAV: dorsal longitudinal anastomotic vessel, SV: segmental vein, SA: segmental artery, CV: caudal vein. Adapted from Ellertsdóttir et al., 2010 (with permission).

Angiogenesis is accompanied by a lot of different cellular behaviors, that will be briefly described in the next paragraph. Hereby, I will exclusively focus on the cellular processes rather than on molecular pathways, that were considered to occur in the zebrafish vasculature.

1.3.1. Morphogenetic processes during angiogenesis

Vascular networks are formed by a variety of morphogenetic processes such as cell migration, anastomosis, membrane invagination, cell rearrangements or cell division. Some of the mentioned behaviours (like membrane invagination) were already mentioned or discussed in a previous paragraph, therefore I will elucidate only on some of them in greater detail.

1.3.1.1. Cell migration

Cell migration mainly occurs during vascular sprout formation, when ISVs arise from the dorsal aorta and grow dorsally. The sprout is guided by an endothelial tip cell at the front, which is connected to trailing stalk cells (Siekmann et al., 2008).

Tip cells are highly migratory leader cells, that scan the environment for information with long filopodial extensions. High migratory capacity is reflected in the activity of different pathways; tip cells have higher activity of VEGFR2/3 but comparably lower activity of Notch and TGF-ß (Habeck et al., 2002; Siekmann and Lawson, 2007; Wild et al., 2017). Pathfinding is determined by attractive (Vegf-a) and repulsive signals (e.g. Semaphorin 3a) from the environment (Zygmunt et al., 2011). Stalk cells are the more proliferative element of this cell group and therefore represent the building blocks of the growing sprout. Extension of the sprout is highly dependent on coordination of tip cell and stalk cell behavior, and relies not only on proper cell proliferation but most importantly on cell migration and on elongation of single stalk cells (Sauteur et al., 2014).

1.3.1.2. Cell elongation

Proliferation of tip and stalk cells (in addition to migration) supports the growth of the sprout (Costa et al., 2016; Siekmann and Lawson, 2007). However, it is not the only mechanism important for sprout extension. Sauteur et al., 2014 added a new facet to this morphogenetic process by showing that the elongation of stalk cells is associated with prominent cell shape changes and rearrangements of junctional contacts (Figure 6).

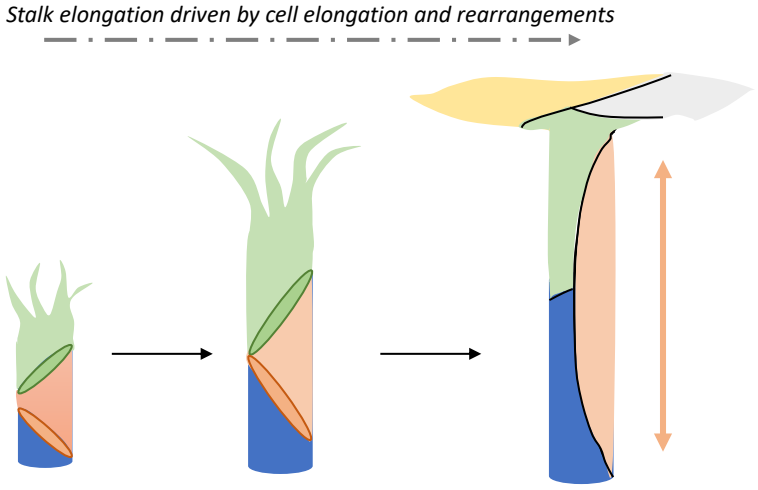

Figure 6: Stalk elongation during angiogenic sprouting. An angiogenic sprout is shown, consisting of three different cells at the beginning (blue, orange and green). Cell junctions are indicated as rings. In the sprouting phase, the junctional ring undergoes a round to elliptic shape transformation. Cell migration as well as cell elongation lead to an extension of the vascular sprout and a multicellular tube architecture (left image).

Junctional contacts undergo a transition from a round towards a more elliptic shape, which drives the process of cell elongation. In mutants lacking VE-cadherin function, the capacity of ring elongation is diminished. Cell elongation is strongly dependent not only on the presence of VE-cadherin, but also on its interaction with the actin cytoskeleton. It was hypothesized that contact extension between two cells and concomitant junctional ring elongation requires an active deforming force. This force is specifically transmitted by VE-cadherin and promotes the transformation of the junctional ring from a round to elliptic shape (Sauteur et al., 2014).

1.3.1.3. Cell behaviours during anastomosis and membrane invagination

When sprouts of the ISVs reach their dorsal-most point (around the position of the neural roof), tip cells extent both anterior and posterior ("T-shape") in a process called bifurcation (Carmeliet and Tessier-Lavigne, 2005). Neighboring sprouts of two ISVs eventually will get interconnected via a process called anastomosis (Adams and Alitalo, 2007; Blum et al., 2008; Herwig et al., 2011). This happens in a quite stereotypical manner, including a sequence of different steps which finally will lead to the formation of a new circulatory loop (more detailed description in Lenard et al., 2013). Two tips cells that move towards each other establish their first contact by filopodial extension. Once this contact is established, junctional proteins such as VE-cadherin and ZO1 are deposited at the contact site for further manifestation. The contact area increases and leads to the formation of a ring-shaped junction. During this step, an apical compartment is created at the contact site, marked by the localization of Podocalyxin within the ring-shaped junctions. From this point onwards, two different mechanisms are used to complete the anastomosis process in the DLAV, either leading to unicellular or multicellular tube architecture (independent or dependent on blood pressure, respectively). These processes were described earlier in the sections describing cord hollowing or transcellular lumen formation.

In the PLA of the zebrafish cranial vasculature, the processes following the establishment of an initial contact site and an apical membrane are very stereotypical and always proceed like described in the following:

Once the apical-basal polarity is established, the protrusive activity of filopodia decreases and cells continue to move along each other, thereby enlarging their mutual surface. While the apical compartment continues to grow, it subsequently fuses with a transcellular lumen initially formed in the tip cell, which invaginates rapidly due to blood pressure. This results in the formation of a unicellular tube with a transcellular lumen. Cell rearrangement processes (including cell splitting) finally lead to the conversion of the unicellular architecture into a more potent multicellular tube (Lenard et al., 2013). A simplified version of anastomosis is summarized in Figure 7. Steps of lumenization are excluded; but can be found in section 1.1.2.1.

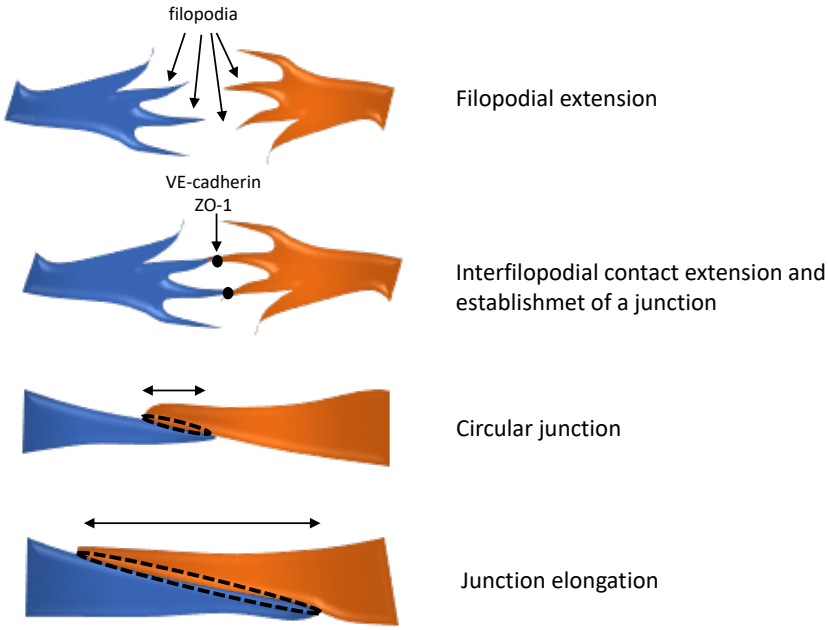

Figure 7: Steps of blood vessel fusion during anastomosis. Two tips cells (blue and orange) extent filopodia in the direction of migration. Upon filopodial contact between the two opposing sprouts, a new contact site is established and junctional material is deposited (marked by ZO1 and VE-cadherin). Subsequently, the cell junction elongates (ring shaped), thereby increasing the mutual cell surface contact. Eventually, cell rearrangements will convert the initial unicellular tube into a multicellular tube architecture (not shown). Intracellular lumens are not depicted for simplicity reasons of simplicity.

For the establishment of a continuous vessel during the process of anastomosis, proper junctional connections are inevitable. In VE-cadherin mutants, tip cells maintain a dynamic sprouting behavior, even after they have already encountered the opposing cell.

Since they fail in establishing a stable adherens point after the initial (single) contact, they compensate by formation multiple rather short contact points. Filopodia of VE-cadherin mutant embryos indeed do adhere and polarize, albeit less efficiently (Lenard et al., 2013). The formation of super numerous contacts was also reported to be true for the DLAV, implying a defect in endothelial cell recognition (Sauteur et al., 2014). However, mutants lacking both VE-cadherin and Esama (endothelial cell-selective adhesion molecule) show completely interrupted filopodia interaction, showing that these two molecules are important in endothelial cell recognition, in particular during the establishment of *de novo* junction formation in anastomosis (Sauteur et al., 2017).

1.3.1.4. Cell rearrangements

Cell rearrangements processes occur throughout development and are a major aspect of all steps of angiogenesis. Continuous rearrangements and remodeling behaviors are inevitable to respond to different contextual cues or needs of the developing organisms. For instance, during sprouting, rearrangement processes drive the elongation of the stalk cell, whereas during anastomosis they drive the architectural conversion from a unicellular tube to a multicellular tube. Generally, unicellular tube architecture is considered to be rather transient, whereas a multicellular structure is the favored and considered to be the more stable architecture of vessels. Even in a potent, mature vessels, cells remain dynamic and change their position within a sprout (Jakobsson et al., 2010). Cell rearrangement processes rely on cell-cell interactions and among others require the protein VE-cadherin.

In 2014, Sauteur et al. hypothesized for the first time, that VE-cadherin is required to transmit a deforming force on endothelial junctions and thereby promote cell elongation. Furthermore, they identified F-actin polymerization to be necessary in this process and stated that this might be one of the mechanisms underlying the process of force generation. A couple of years later, in 2018, the role of VE-cadherin was further described. A study conducted by Paatero et al., 2018 provided substantial support for the previous hypothesis; the authors identified and characterized so called junction-based lamellipodia (JBL). JBL function relies on both actin dynamics and polymerization as well as proper VE-cadherin interaction, and were described to be the driving process of cell elongation and

consecutive cell rearrangements. These finding confirmed to a great extent the hypothesis of Sauteur et al., 2014 and will be described in more detail below.

Junction based lamellipodia during cell rearrangements

JBL can be observed at cell-cell junctions during endothelial cell movements and might provide a means for the cells to move along each other and to rearrange. They were identified as VE-cadherin and ZO1-rich polarized thicknesses of the junctions during junctional ring elongation. Moreover, JBL are oscillating F-actin based lamellipodia-like protrusions that appear in the direction of endothelial cell movements or elongation. It was shown that JBL exhibit specific spatio-temporal localization of VE-cadherin, ZO1 and F-actin during a protrusion and retraction cycle (one JBL oscillation cycle is depicted in Figure 8). A protrusive leading front is established by polymerization of actin, which mainly colocalizes with a diffuse accumulation of VE-cadherin. Homophilic interaction of VE-cadherin molecules then might lead to the recruitment of ZO1, which localizes in a more distinct pattern. This is represented by two “lines” - a distal and a proximal junction (“double junctions”), a phenomenon that is temporally restricted. In a last step, they hypothesize, that he two junctions are eventually pulled towards each other, by a so far unknown mechanism.

The formation of JBL strongly relies on F-actin polymerization and dynamics, as well as mechanistic coupling of the actin cytoskeleton to the junctions. JBL formation is abolished in mutants lacking the F-actin binding domain of VE-cadherin. Furthermore, inhibiting F-actin polymerization or interfering with remodeling, both lead to an impaired cell rearrangement process or JBL formation. JBL formation was described as means employed by endothelial cells to move along each other. Dependence on a functional F-actin cytoskeleton and dynamics as well as coupling to the junctions led to the hypothesis that migratory movements are initiated by local force generation. This hypothesis, however, needs to be further investigated.

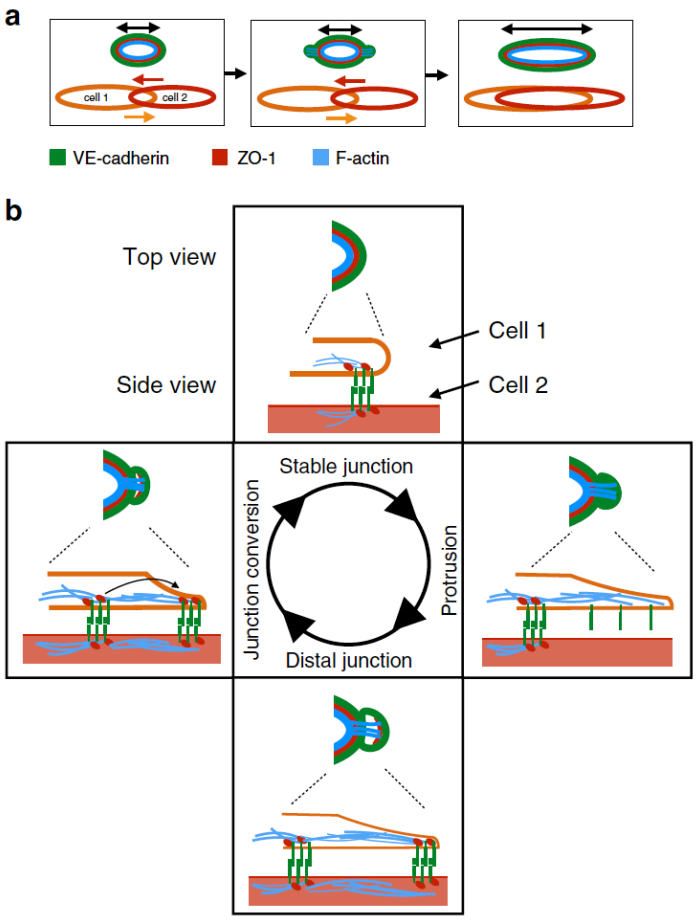

Figure 8: JBL drive junctional remodeling and cell rearrangements. Stepwise elongation of two endothelial cells as they move over each other (top view in a). A schematic scheme of events happening in a sequential manner is shown in b. Three different proteins are shown in different colors. During one oscillation cycle, an actin protrusion (blue) emanates from a stable junction. In these protrusions, VE-cadherin is diffusely localized. At later stages, a new junction is formed at the distal end, marked by the presence of ZO1. In a final step, dynamic F-actin remodeling results in pulling the two junctions towards each other. Image taken from (Paatero et al., 2018).

As described in this section for VE-cadherin and in previous chapters for other proteins, it became obvious that junctional proteins and cell adhesion play a major role during several processed of angiogenesis. Therefore, endothelial cell junctions will be described in more detail the following sections, with particular focus on VE-cadherin, as this was repeatedly reported to play a major role in different processes.

1.4. Endothelial cell junctions

Cell junctions are sites of contacts between two cells (cell-cell) or between cells and the extracellular matrix in a tissue of a multicellular organism (Alberts et al., 2002). All junctional proteins are anchored by a transmembrane domain and interact intracellularly with specific partners (e.g. with actin for stabilization purposes). Generally, cell junction proteins in the endothelium can be classified into two distinct groups, that intermingle along the cell- cell interface: Adherens Junctions (AJs) and Tight Junctions (TJs), both of which mediate adhesion. Major functions for TJs include providing a barrier within the membrane, they regulate the passage of solubles and ions and are important for maintenance of cell polarity (reviewed in Bazzoni and Dejana, 2004). Tight junctions are protein complexes containing Claudins, Occludins and JAMs (e.g. Esam), of which Claudin5b and Esama show endothelial specific expression. Another example is Zona Occludens 1 (ZO1), which is most commonly considered to be a component of TJs. However, it is associated with AJs in earlier steps of their assembly and organization, where it binds temporally to α-catenin (Itoh et al., 1997). At AJs, adhesion is mediated by cadherins, which interact in homophilic manner *in trans* and form lateral junctions *in cis* conformation (for a review e.g. Bazzoni and Dejana, 2004; Vestweber et al., 2009). Besides their adhesive properties, AJs are responsible for the correct organization of new vessels and regulate paracellular permeability. Additionally, they are required for actin cytoskeleton remodeling and for local signaling. Although the most prominent example is VE-cadherin, other AJs are found in the vasculature such as N-cadherin (Navarro et al., 1998) or PECAM-1 (platelet/ endothelial adhesion molecule 1). The latter, however, is concentrated at the intracellular cleft but its localization is not specifically confined to AJs or TJs (DeLisser et al., 1994). AJs are multiprotein complexes composed of cadherins (transmembrane) and catenins, that are attached to cytoplasmic actin filaments. The structure of AJs is further explained by taking VE-cadherin as an example.

1.4.1. VE-cadherin

1.4.1.1. Structure of VE-cadherin

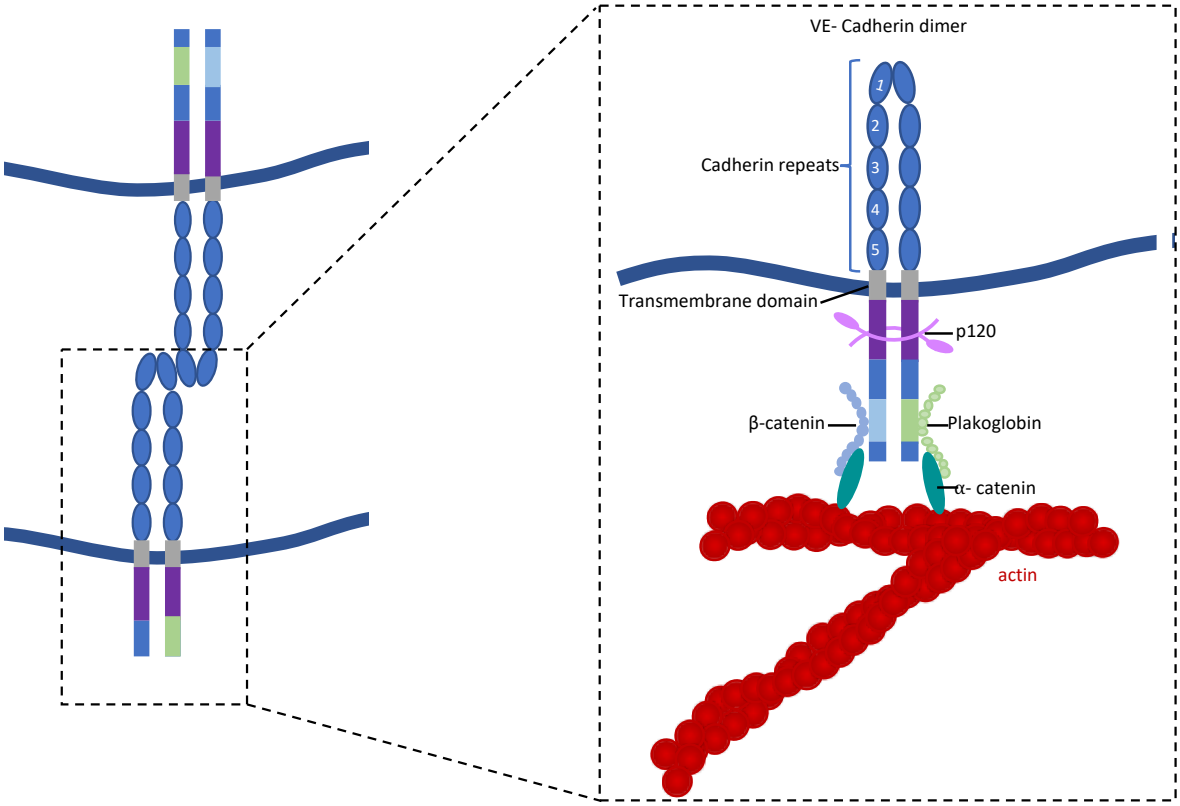

Figure 9: Schematic representation of VE-cadherin and its intracellular binding partners. A homophilic trans-interaction between two molecules is shown on the left. Intracellular binding partners are depicted on the right. VE-cadherin has five extracellular cadherin repeats and is anchored in the cell membrane via a transmembrane domain. Its minimal functional unit is a dimer. Proteins that are known to interact with VE-cadherin are p120, β-catenin and Plakoglobin. P120 interacts with the juxtamembrane domain and stabilizes the junctional complex, whereas the latter two associate with the distal binding site. Plakoglobin and β–catenin bind α–catenin and thereby provide a link to F-actin.

VE-cadherin is a single-pass transmembrane protein, composed of 5 extracellular cadherin repeats, and a highly conserved cytoplasmic tail (see Figure 9). Expression of VE-cadherin is restricted to the endothelium, where it mediates adhesion in a homophilic, calcium-dependent manner (Bazzoni and Dejana, 2004). It connects opposing cells by forming a zipper-like structure of extracellular domains, and cadherins are among the first proteins, that accumulate at new cell-cell interfaces (reviewed by Ebnet, 2008). Through its cytoplasmic tail, VE-cadherin is connected to AJ proteins p120, ß-catenin and plakoglobin.

β-catenin serves as a scaffold and is important for the recruitment and regulation of proteins associated with the cytoskeleton and α-catenin. The latter is important for interaction with several actin binding proteins like ZO1 or α-actinin (see Weis and Nelson, 2006). Plakoglobin exerts similar functions as described for the homologue ß-catenin. Hydrophobic and electrostatic properties of p120 are important for stabilization of VE-cadherin at the junction (Vincent et al., 2004). Furthermore, mutants lacking the ß-catenin binding site fail to establish links to the actin cytoskeleton and are unable to form proper cell adhesion contacts (Nagafuchi and Takeichi, 1988).

The biological impact of cell-cell contacts arises from their ability to functionally link adhesion to the actin cytoskeleton and to coordinate it with cell signaling (in addition to inhibiting cells from disconnecting from neighbors), which will be therefore integral part of the following paragraph. The following findings, however, were mainly obtained from cell culture experiments. *In vivo* observations were mostly based on mutant analysis in mouse or zebrafish embryos, which will be summarized upfront.

1.4.1.2. Role of VE-cadherin *in vivo*

Generally, VE-cadherin function is most studied with respect to leucocyte transmigration and vascular permeability and less is known about its precise role in the vascular system (reviewed in Dejana and Vestweber, 2013).

In the vasculature, loss of VE-cadherin in mice leads to premature death of the embryos at E10.5. However, mutant embryos remain undistinguishable from their littermates until E8, indicating that VE-cadherin is dispensable for angioblast differentiation. Shortly after, severe vascular phenotypes are observed, including detachment of cells or a failure in the lumenization or expansion of vessel diameter (Carmeliet et al., 1999; Gory-Fauré et al., 1999). Partially knocking down VE-cadherin in the zebrafish by a morpholino-antisense knockdown approach leads to a hypersprouting phenotype with several small but collapsing vessels present. Additionally, the tendency to develop brain hemorrhages is increased, mainly pointing towards a role in maintenance of vessel integrity (Montero-Balaguer et al., 2009). In zebrafish, homozygous mutants develop a severe cardiac phenotype (edema) and do not survive beyond 5 dpf as they are not able to establish a proper vascular network.

Cell elongation as well as cell rearrangements are impaired in endothelial cells (Paatero et al., 2018; Sauteur et al., 2014). Furthermore, initial contact formation during anastomosis is affected, implicating a potential role of VE-cadherin in contact-mediated adhesion (Lenard et al., 2013).

Most studies indeed point towards a rather passive role of VE-cadherin in line with maintenance of endothelial barrier formation (Dejana et al., 2009; Harris and Tepass, 2010; Lagendijk and Hogan, 2015). However, recently evidence supports a rather active role of VE-cadherin in morphogenetic processes that underlie blood vessel formation (Paatero et al., 2018; Perryn et al., 2008). Perryn et al., 2008 show that motion of endothelial cells in vascular sprouts is strongly dependent on VE-cadherin and necessary for sustaining vasculogenic sprouting during expansion of the whole tissue.

1.4.2. Cadherins and the junctional F-actin cytoskeleton

Cadherin-actin interaction is not only about how adhesion influences the cell cytoskeleton per se, but also how the contractile elements of neighboring cells (the actomyosin-cytoskeleton) are coupled. Furthermore, it is important to understand, how this cooperation finally translates into biological outcomes, both at cell and at tissue level. Interfering with F-actin (dis)assembly, actin regulatory proteins but also with myosin II negatively influence junctional integrity and stability. Based on these findings, the cooperation can be reflected by three processes (compare Liang et al., 2015): cadherins interaction with F-actin (see VE cadherin chapter), regulation of cytoskeletal dynamics and actin assembly and ability to recruit and activate myosin II.

1.4.3. Mechanism of F-actin assembly

Generally, F-actin filaments are formed by the polymerization of monomeric G-actin (“building blocks”). Actin filaments are very dynamic structures with constant turnover (assembly and disassembly) of G-actin at the pointed ends. Actin assembly and elongation preferentially takes place at the barbed ends of the filaments. Elongation at the barbed ends of actin filaments usually drive membrane protrusions (Tilney et al., 1981). Even when associated with junctions, dynamic properties are maintained and F-actin turns over with half-times of tens of seconds (Kovacs et al., 2011; Smutny et al., 2010).

F-actin filaments can assembly in form of actin bundles or as branched networks and are often associated with non-muscular myosin for generation of contractile forces.

Actin assembly can be classified into two different processes: The first is actin nucleation, which refers to the process of actin trimer formation out of monomers, and is considered to be the rate limiting step. Actin filament nucleation first occurs after cadherin contacts are established and is mainly regulated by the Arp2/3 complex (Chesarone and Goode, 2009; Pollard et al., 2000). The second process involved in actin assembly is the growth of trimeric actin into filaments by self-assembly accelerated by proteins like post-nucleation actin regulators Ena/VASP (Chesarone and Goode, 2009; Krause et al., 2003; Pasic et al., 2008; Winkelman et al., 2014). These proteins prevent premature capping of barbed ends (Bear and Gertler, 2009) and act as actin polymerases (Hansen and Mullins, 2010), thereby supporting the growth of the actin filaments.

1.4.3.1. Actin in the endothelium

In the endothelium, actin filaments are components of several structures, including cortical actin, stress fibers, forming networks at the cell edge and are integral part of the cytoskeleton (Schnittler et al., 2014). Actin protrusions forming at the cell edge of migrating cells include lamellipodia and filopodia (Rottner et al., 2017). Lamellipodia are protrusions forming at the leading edge of a migrating cell, and consist of densely branched actin networks and are often referred to as “membrane ruffles”. Lamellipodia formation is dependent on Arp2/3 activity, which gets activated downstream of Rac. Filopodia (reviewed in Mattila and Lappalainen, 2008) are finger-like cell surface protrusions (“microspikes”), that extent beyond the leading edge of lamellipodia. Generally, they play a role in several processes including cell migration and guidance towards chemoattractants. However they were reported to be dispensable for tip cell guidance in the endothelium (Phng et al., 2013). Filopodia formation is mainly regulated by Cdc42. Stress fibers have a smaller actin turnover compared to protrusions and can terminate in focal contacts or at inter-endothelial adherens junctions (compare Schnittler et al., 2014). Stress fibers are important for cellular contractility as they are not only composed of actin, but also contain non muscle myosin II (NMII) (e.g. in Rottner et al., 2017).

Concepts that were mentioned in this paragraph will be described in more detail in the following sections.

1.4.3.2. Regulation of actin assembly at junctions

Nucleation of actin itself happens at cadherin-based junctions and is mainly mediated by the Arp2/3 complex, favoring formation of branched actin networks (Pollard et al., 2000). Arp2/3 concentrates at junctions (Tang and Brieher, 2012; Verma et al., 2012) and was shown to coimmunoprecipitate with E-cadherin (Tang and Brieher, 2012; Verma et al., 2012). Arp2/3 itself has a poor intrinsic activity (Goley et al., 2006), and therefore needs other accessory proteins for stimulation, called nucleation promoting factors (NFPs). They include WASP and WAVE, which transduce signals from Cdc42 and Rac1 (Insall and Machesky, 2009). It was shown that Rac1 acts at E-cadherin adhesions and promotes actin assembly. Therefore, it is likely that Arp2/3 functions as mediator of Rac1 dependent actin assembly at junctions (Liang et al., 2015). Another NFP is cortactin, which was reported to contribute to actin assembly at the junction, promoted by its ability to recruit Arp2/3 and WAVE2 to the junction (Han et al., 2014) (see Figure 10).

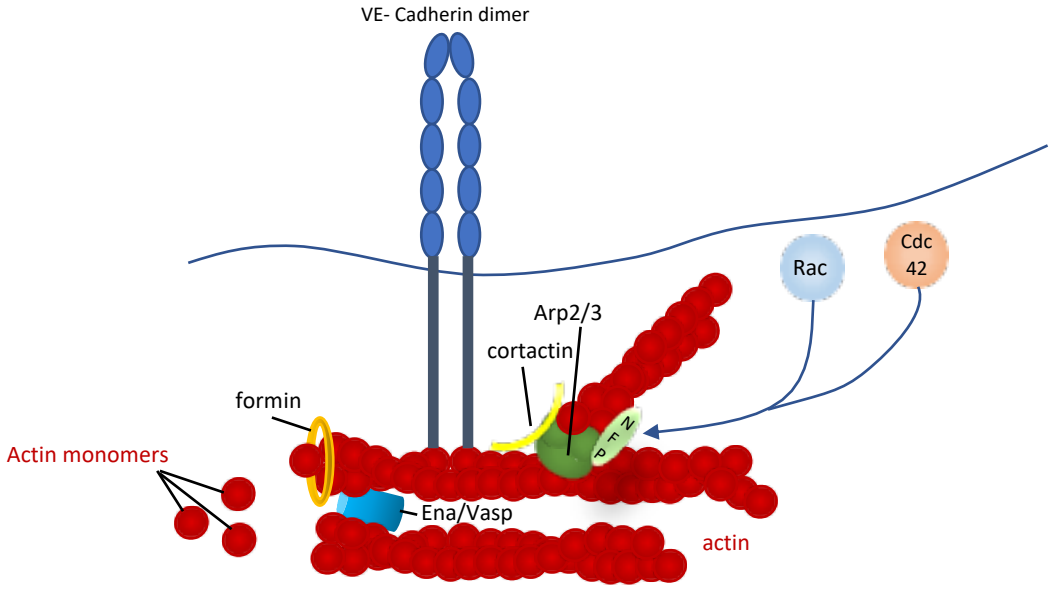

Figure 10: Regulation of actin assembly at the junction. Formin binds at the barbed ends of actin filaments, triggering the incorperation of single actin monomers. Ena/Vasp proteins promote the subsequent elongation of actin filaments. The Arp2/3 complex promotes the formation of branched actin networks. Arp2/3 transduces signals from Rac and Cdc42, through activation of WAVE and WASP, respectively (both NFPs). Cortactin stabilizes nucleation sites for actin branching. Intracellular binding partners of VE-cadherin are left out for simplicity. NFP=nucleation-promoting factors.

Another Arp2/3 dependent mechanism, that alters actin dynamics at VE-cadherin based junctions, is the formation of junction-associate intermittent lamellipodia (JAIL) (Abu Taha et al., 2014). In subconfluent cell culture experiments, where VE-cadherin shows a disrupted pattern and intracellular gaps, the formation of lamellipodia-like structures called JAIL can be observed. JAILs are spatio-temporally restricted actin-driven structures, dependent on Arp2/3 and WAVE2 (needed for actin polymerization). Locally appearing actin protrusions lead to an overlap of opposing endothelial membranes. This induces new VE-cadherin-meditated adhesion sites to form. The subsequently formed VE-cadherin clusters will eventually be incorporated into the cell-cell junctions upon JAIL retraction. Besides the importance of Arp2/3 as mediator for JAIL formation, Rac1 was identified to be of major importance. Inhibition of Rac1 blocked local formation lamellipodia (Breslin et al., 2015). This might be explained by the observation, that activated Rac1 binds to the WAVE complex, which in turn activates Arp2/3 (Eden et al., 2002). This mechanism was suggested to be important during dynamic junctional remodeling and maturation and crucial for the maintenance of the junctional barrier (Abu Taha et al., 2014).

In contrast to Arp2/3, which promotes the formation of branched filaments, members of the formin family typically act at the barbed ends of filaments and promote nucleation to create parallel actin filaments. Formins identified at the cell-cell junctions are mDia1 and Formin-1 (Chesarone and Goode, 2009). Formin-1 was identified as binding partner of α -catenin and can be found at radial F-actin bundles at nascent cell-cell contacts (Kobielak et al., 2004).

Depletion of Arp2/3 or cortactin in cell culture experiments decreased steady-state F actin content and influences dynamic cell behavior, reflected in a reduction of actin assembly at junctions (Han et al., 2014; Verma et al., 2012). Additionally, inhibition of Arp2/3 disrupts cadherin organization (Ivanov et al., 2005). Furthermore, in Verma et al., 2012 it was shown, that contractile tension as well as myosin II accumulation was reduced in Arp2/3 depleted cells (and therefore in cells, where local generation of branched F-actin networks was inhibited). Moreover, inhibition of myosin II decreased actin assembly at junctions, stressing tension-sensitivity of actin assembly (Leerberg et al., 2014).

1.4.4. Non-muscle myosin

Non-muscle myosins play a role in many fundamental processes including cell migration, cell adhesion or cell shape changes during tissue morphogenesis and development (extensively reviewed in Coluccio, 2008; Vicente-Manzanares et al., 2009). These processes are mainly influenced and regulated by its effects on actin bundling and contractility. Non-muscle myosin II (NMII) itself is tightly regulated among others through folding, filament assembly or actin binding. At the same time, it represents an important downstream endpoint where a lot of signaling pathways converge, which makes it central in the control of the already mentioned processes. In the following paragraphs, I will firstly introduce the structural properties of non-muscular myosin II and then focus on its effects on actin remodeling and cell adhesion.

1.4.4.1. Structure of non-muscle myosin

NMII is an actin-binding protein with contractile properties and represents the principle force generator in eukaryotic cells (referred to as actomyosin). NMII consists of two heavy chains, two light chains and two regulatory light chains (RLC), whereas the latter regulates myosin activity. NMII isoforms are determined by the heavy chain isoform (NMIIA, B and C in mammalian cells) (Vicente-Manzanares et al., 2009).

F-actin and ATP are bound in the head domain of the heavy chain, which is crucial for the motor activity. Contractility requires the assembly of several single filaments in bipolar manner, which in turn is regulated by phosphorylation of the RLC. Phosphorylation of RLC changes the conformation of NMII from a very compact molecule into an assembly-competent form. Minifilaments align in antiparallel manner (Heissler and Manstein, 2013), which allows F-actin to slide inward upon myosin activation (and thereby generating contractility). Phosphorylation happens on Ser19 (primarily) and effects can be further enhanced by T18 phosphorylation (Heissler and Manstein, 2013). Phosphorylation events are mainly promoted by myosin-light chain kinase (MLCK) or Rho- kinase (ROCK). The latter contributes to the generation of contractility mostly indirectly by inhibiting enzymatic activity of the myosin phosphatase, and thereby preventing RLC phosphorylation (Khasnis et al., 2014; Riddick et al., 2008).

Upon phosphorylation, contractility is not only achieved by assembly of NMII into minifilaments, furthermore it increases binding to F-actin and enhances myosin ATPase activity (Liang et al., 2015). The mechanisms of assembly at junctions and its molecular regulators are schematically shown in Figure 11.

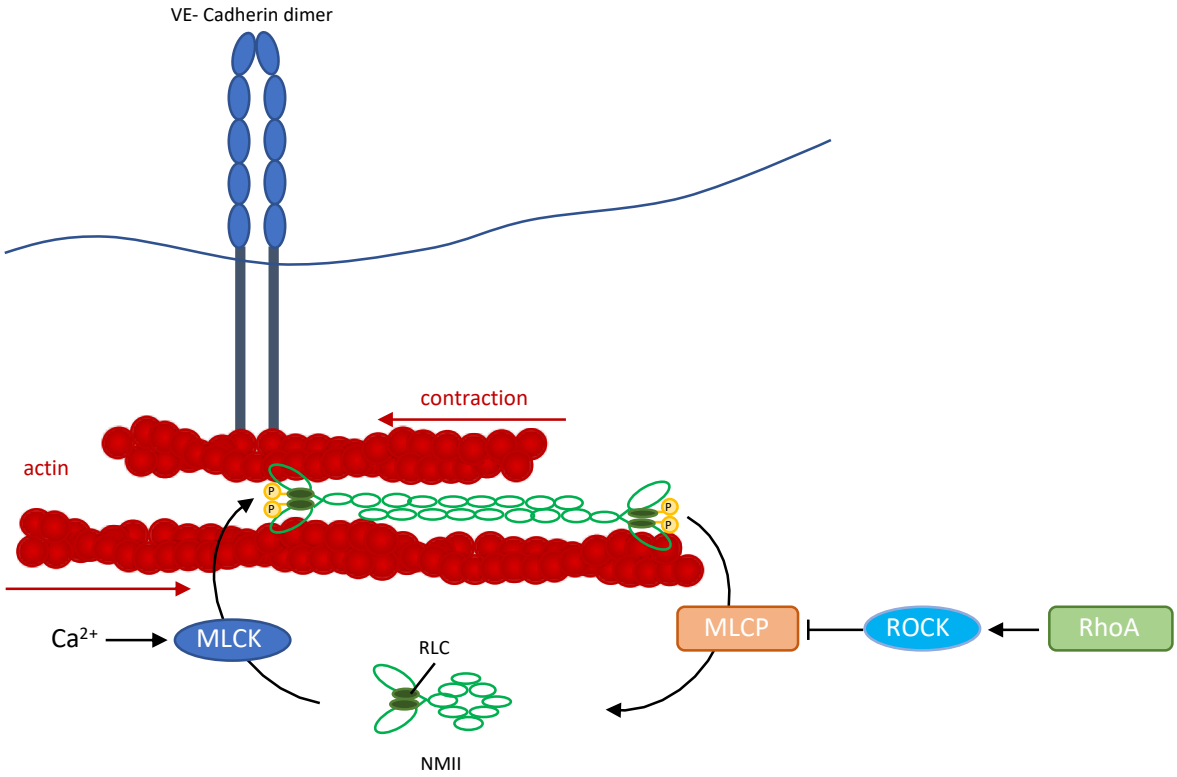

Figure 11: Non-muscular myosin at the junctions. NMII (non-muscular myosin-II) is present in an assembly incompetent head to tail conformation. Upon phosphorylation of the regulatory light chain (RLC) by MLCK (myosin light chain kinase) in calcium- dependent manner, NMII unfolds, which enables the assembly of antiparallel filaments which in turn can bind to actin. RLC phosphorylation is also favored by Rho associated Kinase (ROCK), which inhibits MLCP (myosin light chain phosphatase). Actin filaments upon NMII assembly can slide along each other, thereby generating contractility. ROCK is activated upstream by RhoA. Intracellular binding partners of VE-cadherin are left out for simplicity.

1.4.4.2. Non-muscle myosin at junctions

Homophilic interaction of E-cadherin at adherens junctions leads to recruitment of myosin II to the junctions and therefore might function as an instructive cue (Shewan et al., 2005). Furthermore, it induces activation of RLC, as activated NMII was found to be present at the junctions (Shewan et al., 2005; Watanabe et al., 2007).

In addition, both kinases (ROCK and MLCK) trigger the recruitment of NMIIA to the junctions, indicating that this recruitment might be linked to generation of contractility. Inhibition of ROCK disrupts recruitment of myosin II to cadherin junctions, implying that ROCK-dependent activation of myosin II functions in a cadherin-dependent way (Shewan et al., 2005).

Interestingly, NMIIA/B both fail to accumulate at the junctions, when the Arp2/3/WAVE2 mechanism was inhibited, pointing towards a fundamental role of F-actin assembly and dynamics in recruiting NMII to cell junctions (Verma et al., 2012).

Conversely, actin assembly itself is also tuned by contractility. In case of inhibited contractility, actin assembly is decreased, whereas increased when stimulated (Leerberg et al., 2014). This effect was explained to be dependent on the tension-sensitive recruitment of Vinculin (Ishiyama et al., 2013; Leerberg et al., 2014). Vinculin belongs to the family of Ena/Vasp proteins, and directly interacts with α-catenin that can promote actin assembly at adherens junctions. Recruitment of Vinculin decreases if myosin II is inhibited and, vice versa, inhibition of Vinculin (which diminished tension-sensitive actin assembly) decreases tension (Leerberg et al., 2014; Yonemura et al., 2010). It is therefore thought that interaction of cadherin and actin might be tuned in response to junctional forces (Priya and Yap, 2015).

1.4.4.3. VE-cadherin and mechanotransduction

In the vasculature, VE-cadherin is not only important for cell adhesion, but itself is under tension and plays a crucial role in mechanosensation (Conway et al., 2013). Many of the studies reporting such a role were based on cell-culture experiments; to what extent these findings can be extrapolated to angiogenesis *in vivo* needs to be carefully elucidated. However, the role of VE-cadherin and its mechanotransduction role became apparent by several studies investigating fluid shear stress sensing (Tzima et al., 2005) and the vascular response to it. VE-cadherin itself is under tension and together with PECAM-1 and VEGFR2 and 3 forms a mechanosensory complex (compare Figure 12). Direct binding of VE-cadherin to VEGFR2/3 via their transmembrane domains was demonstrated in Coon et al., 2015.

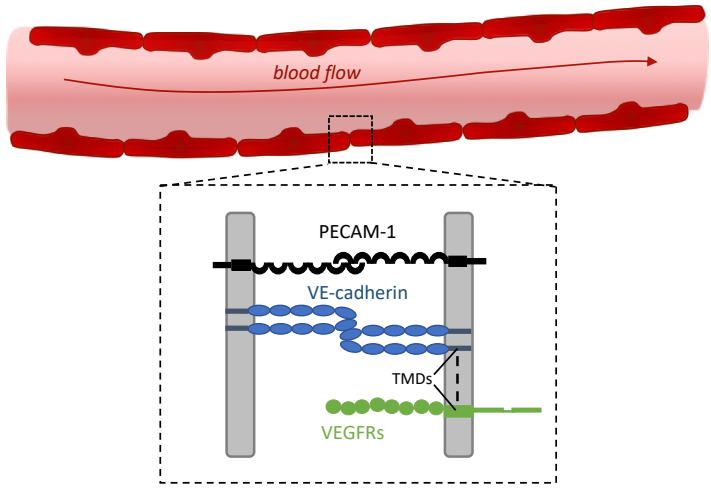

Figure 12: Mechanosensory unit in endothelial cells. Fluid shear stress (blood flow) activates the mechanosensory complex which consists of PECAM-1, VE-cadherin and VEGFR2/3. The latter two interact via their transmembrane domains. Changes are transmitted via PECAM-1 onto VEGFR2/3 probably through VE-cadherin, affecting endothelial function (not shown).

Conway et al., 2013 showed for the first time using FRET-based biosensors, that endothelial cells rapidly respond to shear stress by changing tension across junctional proteins. Furthermore, the authors suggested that cells actively respond to extracellular forces by modulation of tension across the junctional proteins, instead of passively transferring forces across the cytoskeleton. Increase in shear stress after onset of flow led to a decrease of VE-cadherin tension, whereas tension in PECAM-1 simultaneously increased (Conway et al., 2013; Conway and Schwartz, 2015). Endothelial signaling pathways that are flow-dependently activated include activation of Rho, PI3K and Src family kinase (Barry et al., 2015; Collins et al., 2012; Osawa et al., 2002; Tzima et al., 2005).

Another important experiment in cell culture investigating junctional remodeling, revealed that upon increase of cytoskeletal tension, VE-cadherin based junctions grew larger , but at the same time, no loss of tension was observed (Liu et al., 2010), potentially due to enhanced adhesive forces. Besides the mechanistic point of view, some molecular events that play a role in mechanotransduction responses at VE-cadherin based remodeling junctions have been unraveled. The transition from stable, mature junctions with linear and continuous VE-cadherin (parallel actin bundles), into a discontinuous VE-cadherin type of junction (perpendicular actin bundles =focal adherens junctions = FAJ) is mediated by actomyosin (Huveneers et al., 2012). Actomyosin contraction exerts a pulling force on FAJs and is required for their formation and for junctional remodeling in general.

The switch from stable to remodeling junction relies on the tightly controlled activity of GTPases such as Rac or Rho (Yamada and Nelson, 2007). In mature VE-cadherin based AJs, Rac has a fundamental role in strengthening these. Local activation of Rac1 leads to a release of VE-cadherin tension by supporting and stabilizing linear junctions (Daneshjou et al., 2015; Timmerman et al., 2015), whereas Rho activation rather promotes the formation of discontinuous AJs (Liu et al., 2010). This is due to their differential role in modulation of cytoskeletal dynamics, with Rho increasing actomyosin-mediated tugging forces on the junctions. Cytoskeletal dynamics and their differential regulation by Rho-GTPases will be described further in the following chapter.

1.4.5. Regulation of actin/adhesion dynamics by Rho-GTPases

Members of the Rho family of small GTPases profoundly influence cytoskeletal dynamics and reorganize actin that is associated with junctions, thereby influencing adhesion. Active Rho-GTPases are bound to GFP and bind effector proteins to trigger downstream events. Activation of Rho-GTPases is initiated by GEFs (guanine nucleotide exchange factors) acting as catalysators for GDP to GTP exchange (Rossman et al., 2005).

Indeed, Rho, Rac and Cdc42 were all found at cadherin junctions and they belong to the best characterized GTPases. Furthermore, it was demonstrated, that homophilic interaction of cadherins (assembly of adherens junctions) leads to the recruitment of several RhoGTPases such as Rac1, Cdc42, Arp2/3 to the junction (Bershadsky, 2004; Kovacs et al., 2002; Nakagawa et al., 2001; Noren et al., 2001).

RhoA mainly plays a role in contractility-induced changes of the actin cytoskeleton. Its effector ROCK can phosphorylate myosin light chain, and thereby stimulate contractility (e.g. van Hinsbergh and van Nieuw Amerongen, 2002).Since tugging on the junctions increases forces acting on cadherins, Rho primarily has destabilizing effects on endothelial barriers.

The proposed roles for Rac1 in the regulation of F-actin dynamics appear to be quite contradictory. However, these conflicting observations could be due to a context-dependent specificity of Rac1 function or to fine-tuned spatial and temporal activation.

One the one hand Rac1 was reported to play a role in loss of VE-cadherin cell-cell contacts (e.g. Knezevic et al., 2009; Monaghan-Benson and Burridge, 2009; van Wetering et al., 2003). One the other hand, it seems to play a role in junctional stabilization and maintenance of the endothelial barrier. In junctions that were disrupted by thrombin treatment, Rac1 was active in the recovery phase and contributed to the reassembly of the junctions (Beckers et al., 2010; Timmerman et al., 2015). Nascent adherens junctions were stabilized by formation of cortical actin bundles (Timmerman et al., 2015). More detailed, in the reassembly phase Rac1 activation lead to the formation of lamellipodia-like protrusions. Upon homophilic interaction of two VE-cadherin molecules, a GEF called Trio was recruited to the junctions. This GEF in turn recruited additional Rac1, finally transforming nascent into mature junctions based on rearrangement of the actin cytoskeleton (Timmerman et al., 2015). In mature junctions, Rac1 reduces the rate of dissociation of VE-cadherin (Daneshjou et al., 2015).

Apart from activation of Rac1, cadherin binding also activates Cdc42, which seems to be crucial for junctional stabilization. Cdc42 was activated in a VE-cadherin mutant, which was not able to establish homophilic interactions (Broman et al., 2006). Based on this finding, it was hypothesized, that discontinuous junctions might induce Cdc42 activation (Spindler et al., 2010). In line with this, Cdc42 inhibition lead to junctional fragmentation (Georgiou et al., 2008; Shen and Turner, 2008). Overexpression of constitutively active Rac1 or Cdc42 in epithelial cells lead to accumulation of actin at cell-cell junctions and additionally enhanced levels of E-cadherin (Noren et al., 2001). In summary, these findings indicate that activities of Rac1 and Cdc42 are needed for the assembly of adherens junctions.

1.5. Tools to investigate intramolecular tension and actin dynamics

Although junctional remodeling has been topic of many studies, they mainly rely on *in vitro* data. Newly developed tools will make it possible to further investigate junctional rearrangement *in vivo*. With the help of FRET-based biosensors such as the VE-cadherin tension sensor it is possible to visualize and quantify force-dependent processes.

Furthermore, engineered photoactivatable proteins enable specific (temporal and local) activation of certain proteins and thereby allow to decipher their contribution to a distinct biological process. Both mentioned tools will be briefly described in the next paragraph, as they will be integral part of this thesis.

1.5.1. VE-cadherin Tension sensor

The VE-cadherin tension sensor line was generated for optical visualization of intra-molecular tension across VE-cadherin in zebrafish and thoroughly validated (Lagendijk et al., 2017). The tension sensor (TS) module consists of two fluorescent proteins, Teal and Venus, which are linked by an elastic linker peptide (Grashoff et al., 2010). Förster Resonance Energy Transfer (FRET) can be used to quantify changes in energy transfer between the fluorescent proteins upon stretching or contraction of the linker. The TS module has been placed in the cytoplasmic tail of zebrafish VE-cadherin, between the p120 binding domain and the β-catenin binding domain, as described previously for mouse VE-cadherin (Conway et al., 2013). The zebrafish cDNA construct (*ve-cadherin-TS*) was recombined into a *ve-cadherin* BAC clone in order to express TS protein at endogenous protein levels. The tension sensor module as well as the final BAC-clone are shown in Figure 13. The stable transgenic line *TgBAC(ve-cad:vecadTS)*^{uq11bh} showed expression restricted to the vasculature and to endothelial cell-cell junctions, which allows investigations of cell junctional morphology and VE-cadherin dynamics at high resolution. Furthermore, *Tg(ve-cad:ve-cadTS)* was crossed into a *ve-cadherin* mutant background (*cdh5*^{ubs8}) (Sauteur et al., 2014), to test the functionality of the VE-cadherin TS fusion protein. Analysis did not reveal any phenotypic abnormalities in genotypic mutant embryos, which shows that VE-cadherin-TS can rescue the null mutant phenotypes. Tension changes across VE-cadherin (reflected by changes in energy transfer measured by FRET) were observed during arterial maturation as well as upon perturbation of actomyosin contractility. Maturation of the dorsal aorta, inhibition of ROCK (and thereby perturbing actomyosin contractility) and a decrease of calcium signaling all lead to reduced VE-cadherin tension. Interestingly, acute reduction of blood flow did not alter tension within the VE-cadherin molecule (Lagendijk et al., 2017).

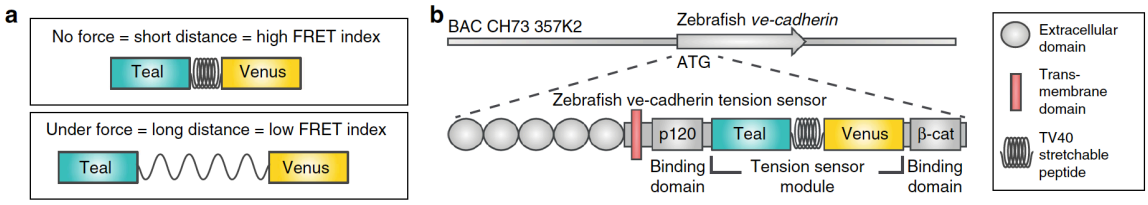

Figure 13: Schematic representation of the VE-cadherin tension sensor (TS) module. A stretchable linker peptide separates the donor fluorescent protein (Teal) from the acceptor (Venus) (in a). The tension sensor module was inserted between the p120 and the β -catenin binding domain of VE-cadherin and recombined into the VE-cadherin BAC clone (b). Image taken from Lagendijk et al., 2017.

1.5.2. Photoactivatable Rac1

Precise spatial and temporal activation of specific protein activity can be of major importance to study cellular behavior. In order to investigate Rac1-dependent actin dynamics Wu et al., 2009 developed a genetically encoded photoactivatable Rac1. Constitutive active Rac1 was fused to the photoreactive LOV (light-oxygen-voltage) domain, with a C-terminal helical extension (Jα). The LOV domain is naturally occurring in Phototropin in *Avena sativa* and the mechanism of protein light switch was described in Harper et al., 2004, 2003. In a closed conformation (darkstate), the LOV domain occludes the effector binding by sterical inhibition. Irradiation with 458 nm light induces a conformational change, leading to the unwinding of the Jα helix and revealing of effector binding sites, thereby leading to activation of Rac1.

Activation of Rac1 in mouse fibroblasts lead to actin polymerization and increased membrane ruffling, as well as to the recruitment of downstream effectors to the site of irradiation. Additionally, local activation of Rac1 resulted in the possibility to control and direct cell movement (Wu et al., 2009).

The latter was also shown *in vivo* in zebrafish neutrophils, where localized activation of Rac1 proved to be sufficient to induced directed migration (Yoo et al., 2010).

1.6. Aim of the thesis

The aim of this thesis is to further analyze the cell rearrangement process, in which two cells use junction-based lamellipodia to move along each other and elongate the mutual contact surface. Of particular interest are mechanisms, that endothelial cells might use to generate contractile forces that drive this process. Additionally, another major aspect of this thesis will be to analyze the regulation of F-actin dynamics. Questions that I will try to answer and focus on include: How is a tensile force generated during the process of junctional ring elongation? How is this force transmitted onto VE-cadherin based junctions? Which processes and molecules linked to actin dynamics contribute to JBL formation and ring elongation? Are JBLs a specific mechanism of anastomosis in the DLAV or might this be a general mechanism employed by other cell types?

II.

Materials & Methods

2. Materials and Methods

2.1. Materials

2.1.1. Chemicals

Unless otherwise stated, chemicals were obtained from AppliChem GmbH, Invitrogen GmbH, Merck KGaA, BD Biosciences, Fluka, Machinery Nagel, and Sigma Aldrich Chemie GmbH.

2.1.2. Buffers, media and solutions

Solutions	**Composition**
DNA loading buffer (10 x)	30 % (v/v) glycerol 20 % (w/v) Orange G in ddH_2O
Methylene blue solution	1 % methylene blue (Sigma Aldrich) ddH_2O
E3 (50 x)	250 mM NaCl 8.5 mM $CaCl_2$ 16.5 mM $MgSO_4$ adjusted to pH 7.0-7.4 (with Na_2CO_3)
egg water (methylene blue + E3)	1:2000 methylene blue solution (0.0005%) 1x E3
LB	1 % (w/v) tryptone 0.5 % (w/v) yeast extract 1 % (w/v) NaCl ddH_2O (autoclaved)
LB w/o salt	1% (w/v) tryptone 0.5% (w/v) yeast extract ddH_2O (autoclaved)

Mounting agarose	0.7 % low melting agarose in E3 1x PTU 1x tricaine
Blocking buffer	5 % normal goat serum 1 % BSA 0.1 % Triton X-100 0.01 % sodium azide in PBST
2 % PFA	12 % PFA (Electron Microscopy Sciences) diluted in PBST
PBS (10x)	1.37 M NaCl 27 mM KCl 100 mM Na_2HPO_4 18 mM KH_2PO_4 ddH2O (autoclaved)
PBST	1x PBS 0.1 % Tween-20
PTU (50x, 2 mM)	0.15 % (w/v) 1-Phenyl-2-thiourea (PTU) (Sigma-Aldrich) in E3
TAE (50x)	2 M tris base 5.71 % (v/v) glacial acetic acid 50 mM EDTA in ddH_2O (autoclaved)
Tricaine (25x)	0.4 % (w/v) Tricaine (Sigma-Aldrich) ddH_2O adjust to pH 7 with 1M Tris HCl stored at -20 °C

TE	10 mM Tris HCl 1 mM EDTA in ddH_2O adjust to pH 8.0

2.1.3. Antibodies

2.1.3.1. Primary antibodies

	Anti-Species	**Dilution**	**Provider**
Anti- ZO1	mouse	1:500	Thermo Fisher Scientific
Anti-Cdh5	guinea pig	1:500	Blum et al., 2008
Anti-GFP	chicken	1:200	Abcam

2.1.3.2. Secondary antibodies

	Anti-Species	**Dilution**	**Provider**
Alexa Flour 488	mouse	1:2000	Thermo Fisher Scientific
Alexa Flour 488	guinea pig		
Alexa Flour 568	guinea pig		
Alexa Flour 568	mouse		
Alexa Flour 633	guinea pig		
Alexa Flour 633	mouse		
Alexa Fluor 647	chicken		

2.1.4. Primer

Generally, primer stock solutions (100 µM) as well as working solutions (10 µM) were kept at -20°C and ordered from Microsynth.

Primer Name	**Sequence 5`-3`**
***att*B primers**	
PA-Rac1-FWD *att*B1	*GGGGACAAGTTTGTACAAAAAAGCAGGCT*TCACAGCCAACATGGCACA CCATCACCACCA

RA-Rac1-REV *att*B2	*GGGGACCACTTTGTACAAGAAAGCTGGGTC*GCCAGAAGTCAGATGCTC AAGG
UCHD-FWD-*att*B2R	*GGGGACAGCTTTCTTGTACAAAGTGGAT*TCCGGAACCATGGCCAAGTA
UCHD-REV-*att*B3	*GGGGACAACTTTGTATAATAAAGTTGG*AAAAAACCTCCCACACCTCCC
Sequencing primer	
PA-Rac1-REVmChe	TCTGGCAATCTTGGGTCAGT
mCherry_2_FWD	AGTTCATGTACGGCTCCAAG
*att*B1_for	ACAAGTTTGTACAAAAAAGCAGGC
*att*B2_rev	CCACTTTGTACAAGAAAGCTGGG
UCHD-FWD	GGACCTGCAGCAGACGAAC
UCHD-REV	CACTGTTCGTCTGCTGCAGG

2.1.5. Antibiotics

Antibiotic	**Stock concentration**	**Working concentration**
Ampicillin	100 mg/ml	100 µg/ml
Kanamycin	50 mg/ml	50 µg/ml

2.1.6. Bacterial strains

Strain	**Provider**
E.coli TOP10 electrocompetent cells	Invitrogen

2.1.7. Inhibitors

Name	**Working concentration**	**Provider**	**Inhibition**
CK-666	200 µM	Sigma Aldrich	Arp2/3
Y-27632	45-75 µM	Sigma Aldrich	ROCK
NSC23766	900 µM	Sigma Aldrich	Rac1

2.1.8. Plasmids

Name	Purpose	Reference
pTriEx-mCherry-PA-Rac1	Template plasmid for *att*b PCR	Klaus Hahn, Addgene plasmid # 22027
pCS2+eGFP-utrophin		William Bement, Burkel et al. 2007
Donor vectors		
pDONR™ 221	*att*P1-P2 sites	Invitrogen
pDONR™ 221 P2r-P3	*att*P2r-P3 sites	Invitrogen
5`entry clones, attL4-R1 sites		
p5E-fli1ep	Promoter	Nathan Lawson
p5E-kdrl	Promoter	Massimo Santoro
Middle entry clones, attL1-L2		
pME-IRFP670	fluorophore	Etienne Schmelzer
pME-mCherry-PA-Rac1	fluorophore-protein fusion	This study
3`entry clones, attR2-L3 sites		
p3E-polyA	SV40 late polyA signal	Kristen Kwan, Chien lab
P3E- UCHD-polyA	Protein-fluorophore fusion	This study
Destination vectors		
cb24 395 bb eye betacrys TagBFP	transgenesis reporter, betacrystalline TagBFP	Charles Betz
cb58 395 ck heart cmlc2 mKate	transgenesis reporter, cmcl2: mKate2	Charles Betz

2.1.9. Fish lines

Genotype	Allele Designation	Reference
Wildtype lines		
AB		ZIRC, Eugene, Oregon, USA
TU		ZIRC, Eugene, Oregon, USA

Transgenic lines		
Tg(kdrl:EGFP)	s843	Jin et al., 2005
UAS:EGFPhZO1, cmlc2:EGFP	Ubs5	Herwig et al., 2011
4xUAS:EGFP-UCHD	Ubs18	Sauteur et al., 2014
Kdrl:Myl9a-EGFP; cmlc2:EGFP		Lancino et al., 2018
Ve-cad:ve-cadTS; ubs8	Uq11bh	Lagendijk et al., 2017
ve-cad:ve-cadTS (tension sensor)	Uq11bh	Lagendijk et al., 2017
10x UAS:Teal	Uq13bh	Lagendijk et al., 2017
10x UAS:Venus	Uq8bh	Lagendijk et al., 2017
Fli:iRFP-UCHD, cmlc2:mKate		This study
Kdrl:mCherry-PA-Rac1, beta-crystalline: BFP		This study

2.1.10.Microscopes and binoculars

2.1.10.1. Binoculars

Microscope	**Manufacturer**	**Information**
Binocular Stemi SV 11	Zeiss	binocular
M205 FA stereo binocular	Leica	fluorescence binocular

2.1.10.2. Point scanning confocal microscopes

Microscope	**Manufacturer**	**Objectives**	**Magnification**	**NA**
SP5-II-Matrix	Leica	HCX IRAPO L	25x (water)	0.95
		HCX PLAN APO CS	40x (water)	1.1
SP8 (BSL2)	Leica	HC PL APO CS2	20x (IMM)	0.75
		HC PL APO CS	40x (water)	1.1
Zeiss 710 FCS	Zeiss		40x (oil)	1.3

2.2. Methods

2.2.1. Zebrafish protocols

2.2.1.1. Zebrafish maintenance

Zebrafish were maintained and bred under standardized conditions with constantly adapted and controlled pH-levels, conductivity and water temperature. Conditions are further described in "The Zebrafish book"(Westerfield, 2000). Embryos were kept at 28.5 °C and staged by hours post fertilization (hpf) according to Kimmel et al., 1995.

2.2.1.2. Embryo dechorionation

Embryos (> 24 hpf) were exclusively manually dechorionated using forceps (Dumont #5F).

2.2.1.3. Pigmentation inhibition

In order to facilitate and improve image acquisition of zebrafish embryos, pigmentation was inhibited by incubation in 1-phenyl 2-thiourea (1x PTU) in E3 starting around 24 hpf.

2.2.1.4. Microinjection/ transient expression

Prior to injection, injection plates (1 % agarose in E3 water) were prepared. Capillaries (outer diameter 1.0 mm, inner diameter 0.5 mm, 10 cm length, Sutter Instruments) were used to produce borosilicate glass needles with a needle puller (Sutter Instruments). Needles were loaded with the respective injection mixture (see Table 1) using Microlader tips (Eppendorf) and the tip was opened by breaking it with forceps. The needle was connected to the injector (Pneumatic PicoPump, World Precision Instruments) and pressure was adjusted to obtain a volume of approximately 5 nl. The embryos were aligned in the indentations of the injection ramps. All embryos were injected at one cell stage. After injection, the embryos were transferred into petri dishes containing E3 with methylene blue.

Plasmids were injected at concentrations ranging from 70-200 ng/ul.

Table 1: Type of injection mixes and respective concentrations.

Name	Type	
Kdrl:mCherry-PA-Rac1	Plasmid DNA	70-150 ng/µl
Fli:iRFP-UCHD	Plasmid DNA	150-200 ng/µl
Double injection	Plasmid DNA	Total of 150 ng/µl

2.2.1.5. Generation of transgenic fish lines

In order to generate transgenic fish lines, wild-type embryos were injected at one cell stage. To facilitate integration, plasmids (30 ng/µl) were injected together with tol2 RNA (35 ng/µl).

From 30 hpf onwards embryos were screened for the respective transgenesis marker and positive embryos were raised to adulthood. Eventually, fish were individually outcrossed to wild-type zebrafish. Repeatedly, embryos were screened for positive expression of the transgene and finally raised in order to generate a stable transgenic fish line.

2.2.1.6. Inhibitor treatment of zebrafish embryos

Zebrafish embryos were selected for the desired transgene and dechorionated. Inhibitor treatment was done in 24 well plates, incubating max. 12 embryos per well in 2 ml solution. Inhibitors were diluted in 1x E3 containing 1x PTU to obtain the required concentration (see 2.1.7). As a control 1 % DMSO was used. Embryos were incubated 2 h prior to imaging starting at 30 hpf for imaging of the DLAV and around 48 hpf for imaging of the DA. The inhibitor was present during the whole imaging period in the agarose as well as provided medium in the glass bottom dish.

For FRET imaging, incubation time for the DLAV as well as DA ranged between 4-5 hours.

2.2.2. Immunostaining

Zebrafish embryos of the desired developmental stage were fixed after dechorionation using 2 % PFA or Glyofixx (Thermo Fisher Scientific) and incubated at 4°C overnight (ON) in 1.5 ml Eppendorf tubes (max. 20 embryos per tube). The next day, embryos were washed four times for 5 minutes in 1x PBST at room temperature (RT) on a rocking platform. Following the washing step, the embryos were permeabilized using 0.5-1 % Triton-X100 in

PBST for 30 min at RT. After that, blocking solution (see 2.1.2) was added for a 2 h incubation at RT or overnight incubation at 4 °C. After blocking, the primary antibody solution was added. A list of used primary antibodies and respective concentration can be found in 2.1.3.1. The primary antibodies were either diluted in blocking solution or Pierce Immunostain Enhancer Solution (Thermo Fisher Scientific). Primary antibody incubation was done at 4 °C and ranged between 1-3 days. After that, the solution was removed and the embryos were washes at least 4 times for 30 min with PBST at 4 °C or overnight. This step was followed by the incubation of the secondary antibodies (see 2.1.3.2), which were diluted 1:2000 in blocking solution and incubated at 4 °C ON. Finally, embryos were washed at least 4 times for 30 min in PBST at 4 °C or ON.

2.2.3. Image acquisition

2.2.3.1. Mounting of zebrafish embryos

For live imaging, zebrafish embryos were positively selected for the desired transgene using a fluorescence binocular (2.1.10.1). Selected embryos were dechorionated and anesthetized in 1x E3 containing 1x tricaine. Embryos were mounted using 0.7 % low melting agarose (LMA) (Sigma Aldrich) supplemented with tricaine and PTU on a glass bottom dish (MatTek). During the mounting procedure, the agarose was kept at 55 °C. Embryos were aligned in lateral orientation (anterior to the left). After solidification of the agarose, E3 medium (+ PTU and tricaine) was added to the dish.

For imaging of fixed embryos, the process was performed as described above with minor differences. Addition of PTU or tricaine was not required. Furthermore, the head and yolk of the embryo was removed during the mounting process in order to guarantee flat alignment of the embryos.

2.2.3.2. Confocal imaging

Prior to live imaging the incubation chamber was set to 28.5 °C. Generally, laser intensities were set according to the strength of the fluorescent signal to obtain single saturated pixels. The z-step size was set automatically and roughly ranged from 0.1 to 1 µM. The point scanning speed ranged between 400-700 Hz with various zooms and bidirectional scanning. Frame size was adjusted according to the needs of the imaging session. For imaging of fixed

embryos, sequential scanning was used. Imaging settings for each experiment are summarized in below in Table 2.

Table 2: Confocal imaging settings according to performed experiment.

Experiment	Objective	Zoom	Scanning speed	Frame size	Time interval	Result figure
Ring elongation	40 x	3 x	400 Hz	512x512	10 min	Figure 21
Actin dynamics in the junctional ring	40 x	5.5	400 Hz	512x512	1 min	Figure 22
ZO1 localization	40 x	4	400 Hz	512x512 or 1024x512	1 min	Figure 25 /26
ZO1 localization in the DA	40 x		400 Hz	512 x 512		Figure 33
Actin dynamics in the DA	40 x	3	700 Hz	1024x512	1 min	Figure 34 / 35

2.2.3.3. FRET imaging

Sample preparation was done as described in 2.2.3.1. For each imaging session, three different transgenic fish lines (Tg(10xUAS:Teal), Tg(10xUAS-Venus), Tg(ve-cad:vecadTS)) were mounted. Teal and Venus lines were used as control to correct the FRET signal for donor bleed through (DBT) and acceptor bleed through (ABT). Controls were imaged at 48-72 hpf in the dorsal aorta. Imaging of the tension tensor line was performed at 32 hpf for the DLAV and 48-50 hpf for the DA. All FRET imaging was performed on Zeiss 710 FCS confocal microscopes, line-sequential scanning and GaAsP high sensitivity detectors. Imaging settings were optimized for the expression of Tg(ve-cad:ve-cadTS) and remained unchanged during one session. Generally, imaging was performed using the 40x oil objective and 4x Zoom. Furthermore, laser intensities below 60 % a maximum gain of 800 were used. Frame size was set to 1024*1024 pixels, Z-stack size 0.99 and laser speed to 5. Control embryos were imaged with the same settings.

2.2.3.4. FLIM imaging

FLIM imaging was mainly performed by Dr. Anne Lagendijk with the help of Dr. Sean Warren using an HC PL APO CS2 40 Å~ 1.1 NA water objective on an inverted DMI 6000 SP8 confocal microscope (Leica Microsystems). Protocol was done according to the description in Lagendijk et al., 2017.

2.2.3.5. Imaging of kdrl:PA-Rac1

Generally, for imaging of Kdrl:mCherry-PA-Rac1 the 561 nm laser was used. For activation, 458 nm laser was set to an intensity of 20 %. Imaging was performed in the absence of UV-light to avoid unwanted activation.

Determination of filopodia number and cell size

Figure 14: Cell imaged in the DLAV

For imaging, single cells in the DLAV > 48 hpf were chosen (see Figure 14, orange cell). The first 12 frames were acquired using only the 561 nm laser. Time intervals were minimized in order to avoid any dark states. Following, the 458 nm laser was turned on additionally in order to activate Rac1 and imaging continued with unchanged settings. After that, another 12 frames were taken without the activation laser (see Figure 15). Time frames ranged from 46.7 s to approximately 2 minutes.

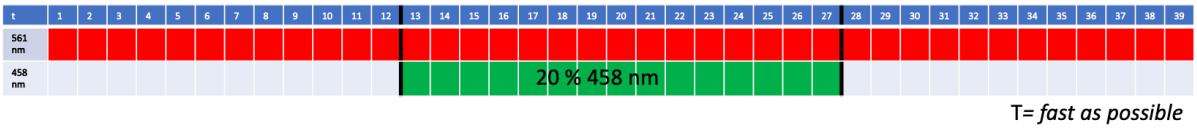

Figure 15: Scheme of time-lapse imaging performed. 12 time points were imaged pre and post activation. Imaging during activation with the 458 nm laser was done for 15 time points.

Transient coexpression of fli:iRFP-UCHD and Kdrl:mCherry-PA-Rac1

First, live still images of double positive cells in the DLAV were acquired, followed by time lapse imaging of fli:iRFP-UCHD only. Similar to the procedure above, UCHD was imaged before activation and during 458 nm activation (the whole frame was irradiated) of PA-Rac1.

2.2.4. Image Processing and Analysis

2.2.4.1. General image processing

Image analysis was done using Fiji (open source, ImageJ). Routinely, maximum projections were used. Where necessary, background was subtracted, brightness and contrast adjusted.

2.2.4.2. Quantification of junctional ring elongation speed

Junctional elongation was determined by analysing isolated junctional rings during anastomosis in the DLAV in embryos transgenically expressing EGFP-UCHD. Isolated junctional rings were imaged every 10 min. The diameter of the junctional ring in µm (along the vessel axis) was measured using Fiji at t (0) = 0 min and 40 to 70 minutes later (t (1) = 40 – 70 min) depending on the imaging quality. Elongation speed in µm/hour was calculated using following equation:

$$elongation\ speed\ in\ \frac{\mu m}{h} = \frac{diameter\ t(1)}{diameter\ t(0)} * \frac{60}{t(1) - t(0)}$$

2.2.4.3. Processing of FRET data

All processing was done in ImageJ (National Institutes of Health, USA). A custom-written Matlab (Mathworks) script 54 was used to measure nonlinear DBT and ABT from the images obtained from Tg(10xUAS:Teal) and Tg(10xUAS:Venus). Based on these values, images were thresholded and a MASK was generated (TEAL_MASK) and VENUS_MASK). Applying the MASK ensured, that embryos that fell outside the confidence boundaries were excluded from the analysis. By that only those RAW-FRET expressing pixels were processed, for which donor and acceptor intensities allowed precise calculation of DBT and ABT constants. The MASK was applied on median filtered Raw images. Venus and Teal channels were multiplied with the Venus_MASK and Teal_MASK generating Real intensity values (RIV) for Teal (Teal_RIV) and Venus (Venus_RIV). The RIVs were again multiplied with the values for ABT und DBT (Teal_RIV*DBT and Venus_RIV*ABT). Described values and masks were used to process the raw images. The process is schematically summarized in Figure 16.

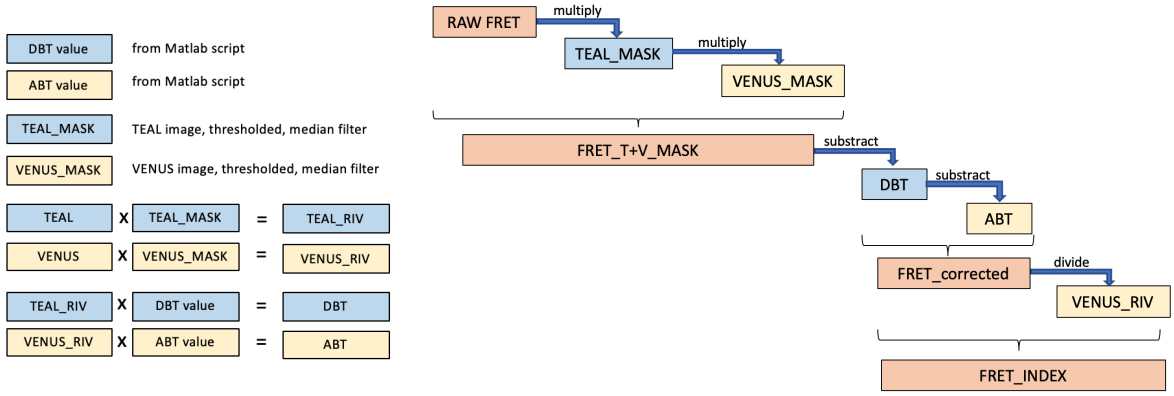

Figure 16: Scheme of processing of raw data to obtain FRET-Index images.

Therefore, the final FRET index represents a FRET, that is corrected for the bleed-through (BT) and divided by Acceptor (Venus) intensity in each pixel (Figure 17).

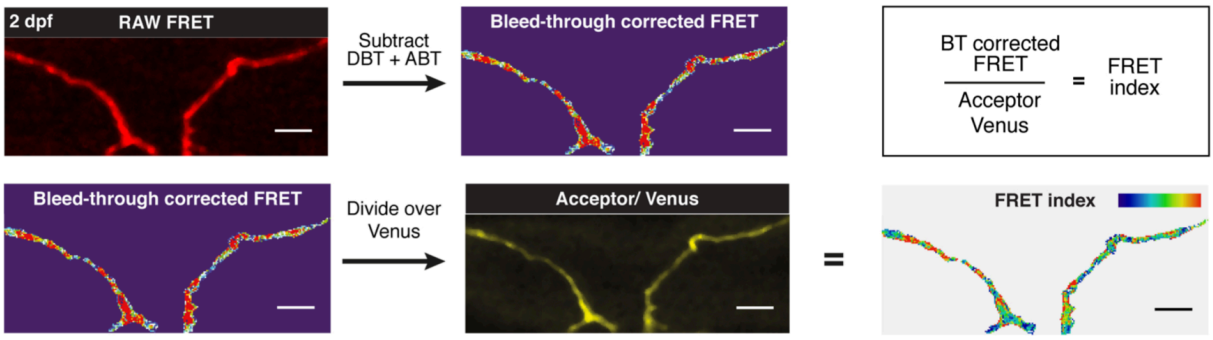

Figure 17. Explanation of RAW FRET processing. From the original RAW FRET image, values for DBT and ABT are subtracted per pixel, resulting in a corrected FRET image. This bleed-though corrected image is divided by the Venus intensity to normalise for protein amount. Final image represents ratio-metric FRET values. Scale bar 5 µM. Image taken from Lagendijk et al., 2017.

Images displaying the FRET index were used to measure FRET- Index in several regions of interest. Therefore, ROIs were manually drawn and mean intensity measurements were performed on single Z-Slices. Per structure (e.g. JBL, junction in the dorsal aorta etc.) FRET indexes from several slices were averaged.

2.2.4.4. Processing of FLIM data

Processing of RAW FLIM data was done uning FLIMfit software 5.0.1. (provided by Dr. Sean Warren) as described in Lagendijk et al., 2017.

2.2.4.5. Post- image analysis after activation of Rac1

Quantification of filopodia number and cell size

Quantification of filopodia number was done manually on each image acquired during time-lapse imaging. In order to compare filopodia number among different cells, individual values from each time point before, during and after activation were averaged. Number of filopodia are displayed in absolute values. For quantification of the cell area, the images were thresholded. The outline of the cell was marked by using the tracing tool and the cell area was measured for each time point. Similar to above, an average was determined for the time points before, during and after activation of Rac1. The cell size change is represented in % of the starting value (t=0).

2.2.4.6. Analysis of actin dynamics in the dorsal aorta using a kymograph-based method

Kymographs were generated in Fiji using sum Z-projections from time-lapse series (images acquired every minute for one hour, t=60 min). Sum Z-projections were corrected for drift using the StackReg (Rigid body option) plugin. Additionally, background was subtracted (rolling ball radius 50). A straight line was drawn perpendicular to the junction and the kymograph was generated using the reslice tool. For further analysis, a custom-written MatLab script was used, which identifies local signal maxima for each time point. The coordinates were used to generate a curve representing the junctional movement over time (1h). The workflow is summarized in Figure 18.

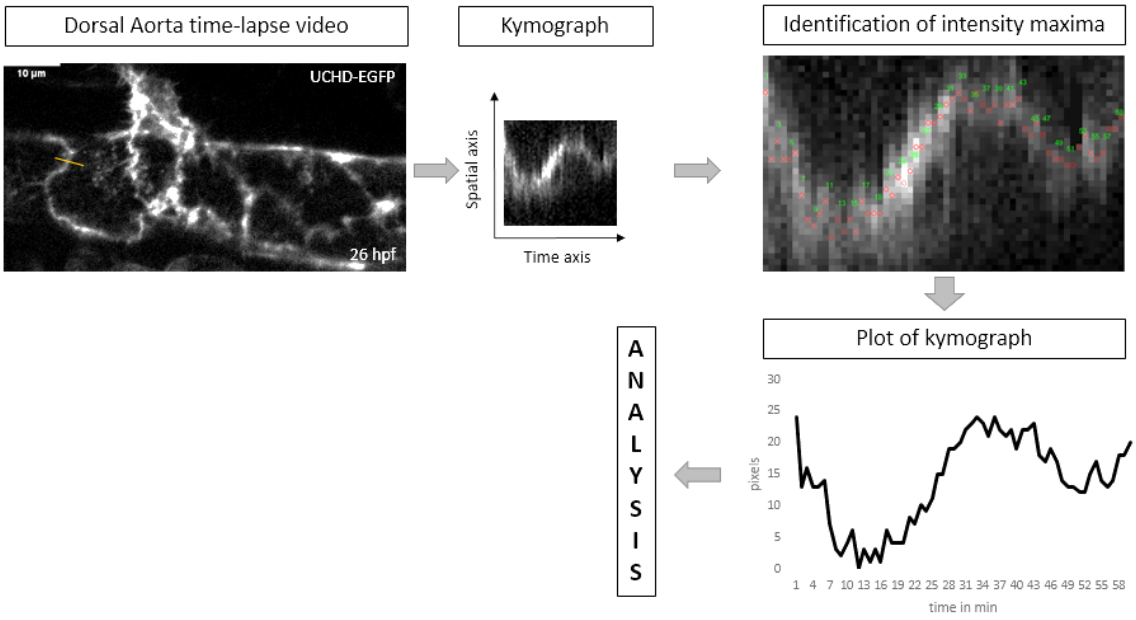

Figure 18: Post imaging quantification of actin dynamics in the dorsal aorta. The dorsal aorta was imaged each minute for 60 min. A line was drawn perpendicular to a junction and a kymograph was generated. With the help of a custom written Matlab script, a graphical representation of kymograph could be plotted. The Matlab algorithm identifies the intensity maximum per column (= per time point).

2.2.4.7. Statistical analyses

Statistical analyses were performed using GraphPad Prism version 8.3.0. Data was checked for normal distribution using the D'Agostino & Pearson test. For normal distributed data the two- sided paired t-test (to compare two means) or the One-way ANOVA multiple comparison- test, to compare more than two means) was used. If the data did not follow a normal distribution the non-parametric Kruskal-Wallis H-test (for comparison of multiple means) or the Mann-Whitney-U-test (two compare two means) were used. Furthermore, the Kolmogorov-Smirnov test was applied.

2.2.5. Molecular biology protocols

2.2.5.1. Transformation of electrocompetent cells

For bacterial transformation, the cells were takes out of the -80 °C freezer and thawed on ice for 20 minutes. In the meantime, 2 µl of plasmid was dialysed on a membrane (PVDF Membrane Filter, MilliporeSigma). After that, the dialysed sample was transferred to 50 µl of the electrocompetent cells and gently mixed by stirring with the pipet tip. The mixture was left for 15-30 min on ice and then transferred into a Gene Pulser 1mm Cuvette (Biorad). The cells were electroporated with 1.8 kV using a MicroPulser (BioRad). Transformed bacteria were immediately resuspended in 500 µl LB and incubated for 1-2 hours at 37 °C with 200 rpm. Bacteria were plated on LB plates with the appropriate antibiotics overnight at 37 °C.

2.2.5.2. Purification of PCR products

Routinely, PCR products were loaded onto a 1-2 % agarose gel. For that, the agarose was dissolved in 1x TAE buffer and heated up in the microwave until everything was dissolved. After cooling down, 0.3 % ethidium bromide was added. After polymerization, the gel was transferred to a chamber filled with 1x TAE buffer.

The samples were mixed with loading dye and loaded onto the gel. For later size determination a DNA ladder (100 bp or 1 kb ladder, Solis BioDyne), was loaded as well. The nucleic acids were visualized using UV-light and the desired PCR fragments were cut using a scalpel and transferred into an Eppendorf tube. PCR products were purified by gel extraction using NucleoSpinTissue (Machinery Nagel) according to the manufactures protocol. For elution of the product, water was used.

2.2.5.3. Plasmid purification

Single colonies were picked, inoculated in LB (5 ml for Mini Prep, 100 ml for a Midi Prep) containing the appropriate antibiotics and left ON at 37 °C with 200 rpm on a shaker. The next day, the plasmids were purified either using the NucleoSpin Plasmid purification kit (Mini Preps, Machinery Nagel) or the Xtra Midi Plus Plasmid Purification kit (Midi Prep, Machinery Nagel). The plasmids were eluted in water and stored in aliquots at -20 °C.

2.2.5.4. Sequencing

PCR products and plasmids were sequenced using the Economy Bar Service of Microsynth, Switzerland. The reactions were assembled according Table 3. The total volume per reaction was 15 µl. In case of a premixed sample (DNA template and primers), 2 µl of 10 µM primer solution was used.

Table 3: Sequencing reactions. Description of effective amounts of DNA per sequencing reaction.

DNA template	Concentration	Effective amount
Plasmid	40-100 ng/µl	480-1200 µg
PCR product	18 ng per 100 bases in 12 µl	

2.2.5.5. Molecular cloning

All constructs were cloned using the Multisite Gateway® Three Fragment Vector Construction Kit (Invitrogen). It is based on the Gateway® Technology and uses site-specific cloning, which allows simultaneous assembly of multiple DNA fragments in specific orientation and order. The generated expression clone typically contains the promoter, gene of interest and termination or polyadenylation sequence.

The three mentioned components are provided in an entry clone generated by BP-cloning out of an PCR product containing specific sites for recombination. The expression clone is generated by recombination of the entry clones in a LR reaction. Experimental procedures for each step are described in the following paragraph, a schematic overview is provided in Figure 19.

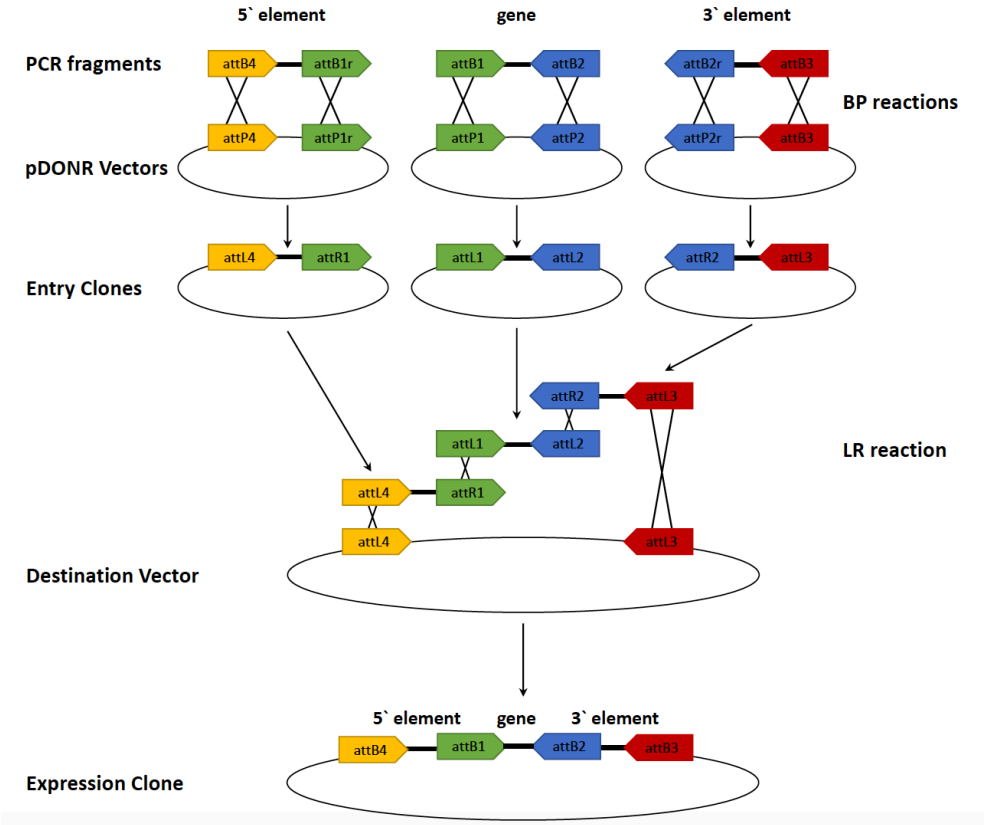

Figure 19: Scheme of Multisite Gateway Cloning Procedure. *Attb* flanked-PCR products will be generated by PCR, followed by a BP reaction to generate entry clones. Three entry clones will be combined in an LR reaction to finally give rise to the expression clone.

<u>*Att*B primer design</u>

The primer design was done according to the MultiSite® Gateway Three-Fragment Vector construction Kit Manual from Invitrogen. For amplification of the mCherry-PA-Rac1 *att*B1 and *att*B2 sites were added to the primers, to generate a fragment suitable for a middle entry clone. Furthermore, a Kozak sequence (CAGCCAAC) was added prior to the start codon (ATG).

For amplification of the UCHD-polyA, *att*B2R and *att*B3 sites were added in order to generate a 3`entry clone. Respective *att*B sequences are listed in Figure 20. Primer sequences are summarized 2.1.4.

Figure 20: attB Primer sequences.

*att*B1 5`-GGGG ACA AGT TTG TAC AAA AAA GCA GGC TNN—(template specific sequence)-3`
*att*B1

*att*B2r 5`-GGGG ACA GCT TTC TTG TAC AAA GTG GNN—(template specific sequence)-3`
*att*B2r

*att*B2 5`-GGGG AC CAC TTT GTA CAA GAA AGC TGG GTN—(template specific sequence)-3`
*att*B2

*att*B3 5`-GGGG AC AAC TTT GTA TAA TAA AGT TGN—(template specific sequence)-3`
*att*B3

Generation of *att*B- PCR products

The PCR was performed using following components (Table 4) and thermocycling conditions listed in table 5. The reaction was set up with a volume of 50 µl. Plasmids containing the gene of interest were used as template DNA for amplification (see 2.1.8).

Table 4: PCR components listed including final concentrations.

Component	**Final concentration**	**Provider**
5x Phusion HF buffer	1X	New England Biolabs
10 mM dNTPs	200 µM	Promega
10 µM forward primer	0.5 µM	
10 µM reverse primer	0.5 µM	
Template DNA	< 250 ng	
Phusion DNA polymerase	1.0 unit/ 50 µl PCR	New England Biolabs
Nuclease-free water	To 50 µl	Ambion

Table 5: Thermocycling conditions chosen for amplification of *attB* PCR products.

Step	Temperature	Time
Initial denaturation	98 °C	3 min
40 cycles	98°C	10 seconds
	72°C	30 seconds
	72°C	3 min
Final extension	72°C	10 minutes
Hold	4-10 °C	∞

The PCR was loaded onto an 1 % agarose gel and the product was purified as described in 2.2.5.2.

BP recombination reaction- generation of entry clones

Following the PCR, the BP recombination reaction was assembled as in described in Table 6. Two different donor vectors were used (pDONR™ 221, pDONR™ 221 P2rP3) according to the flanked PCR product. The amounts for the PCR product needed were calculated using following equation:

Equation 1

$$ng = (x\ fmoles)(N)(\frac{660\ fg}{fmoles})(\frac{1\ ng}{10^6\ fg})$$

N is the length of the DNA in base pairs and x the desired amount of fmoles.

Table 6: Components of a single BP reaction.

Component	Amount
*att*B PCR product (20-50 fmoles)	1-7 µl
pDONR™ vector 221(150 ng/µl)	1 µl
1x TE buffer, pH 8.0	to 8 µl
BP Clonase® II enzyme mix	2 µl

The reaction was assembled on ice and incubated for 2 h at 25 °C. The reaction was terminated by adding 1 µl of 2 µg/µl Proteinase K and incubation at 37 °C for 10 min. Upon dialyses, bacteria were transformed and plated on Kanamycin resistant plates.

Kanamycin resistant clones were screened with Mini Preps and sequenced with the M13 primers. Correct clones were reinoculated and purified with a Midi Prep, followed again by sequencing.

LR recombination reaction- generation of expression clones

In the LR recombination reaction multiply entry clones are mixed with the destination vector, in order to generate an expression clone. The 5`entry clone (p5E) contains the promoter, the middle entry clone (pMe) provides the fluorophore (e.g. iRFP670) or a protein-fluorophore fusion (e.g. mCherry- PARac1). The 3`entry clones (p3E) generally contain the protein of interest (e.g. UCHD) or a SV40 late polyA signal. The destination vector (pDest) contain transgenesis marker, that facilitate the screening for founder fish in the F1 generation, as well as tol2 sites for Tol2 transposase mediated integration into the genome.

For the reaction following components were assembled on ice in calculated amounts (see Table 7):

Table 7: LR reaction components. Concentrations were calculated using Equation 1.

Component	**Concentration**	**sample**
*att*L4 and *att*R1 entry clone	10 fmoles	1-7 µl
*att*L4 and *att*R1 entry clone		
*att*L4 and *att*R1 entry clone		
pDEST	20 fmoles	0.4 µl
TE Buffer, pH 8.0		to 8 µl

The LR Clonase® Plus enzyme mix was briefly mixed and 2 µl were added to the reaction. Incubation was done ON at 25 °C. The next day, the reaction was stopped by adding 1 µl Proteinase K to the solution. Transformation was done as previously described and bacteria were plated on ampicillin resistant plates. Sequencing was performed using primers listed in 2.1.4.

III.

Results

3. Results

F-actin polymerization as well as actomyosin-based contractility is required for junction elongation

JBL function strongly relies on F-actin dynamics and polymerization, as was shown in Paatero et al., 2018. Inhibition of the small GTPase Rac1 by NSC23766 did not affect JBL formation per se, but instead led to a prolonged duration and a decreased periodicity (slower oscillations). Altered JBL behavior did affect cell rearrangements and led to a decrease in junctional elongation speed.

At the cellular level, active Rac1 is indispensable for lamellipodia formation during cell migration, and this activity has been shown to be mediated through Arp2/3 (Insall and Machesky, 2009; Liang et al., 2015). Arp2/3 is an F-actin nucleation factor, that leads to the formation of a branched F-actin network and is important for protrusion formation. In order to examine the effects on cell rearrangements upon Arp2/3 inhibition, embryos expressing EGFP-UCHD were treated with CK666 (Arp2/3 inhibitor) and cell elongation speed was measured starting two hours after treatment (compare to Material and Methods 2.2.4.2) (Figure 21 B).

Elongation speed was significantly decreased (mean 3.4 µm/h) compared to 8.0 µm per hour in DMSO treated controls (Figure 21 A). Interestingly, Rac1 inhibition led to a similar elongation speed (approximately 3 µm/h) (Paatero et al., 2018). However, control endothelial cells showed a different pattern of F-actin distribution compared to Arp2/3 inhibited embryos; in the latter embryos endothelial cells often showed very long and prominent F-actin cables reminiscent of stress fibers (Figure 21 H), which points towards the inability of cells to generate branched F-actin networks. Instead it might well be, that Arp2/3 inhibition shifts F-actin assembly mechanisms towards long, unbranched linear F-actin filaments.

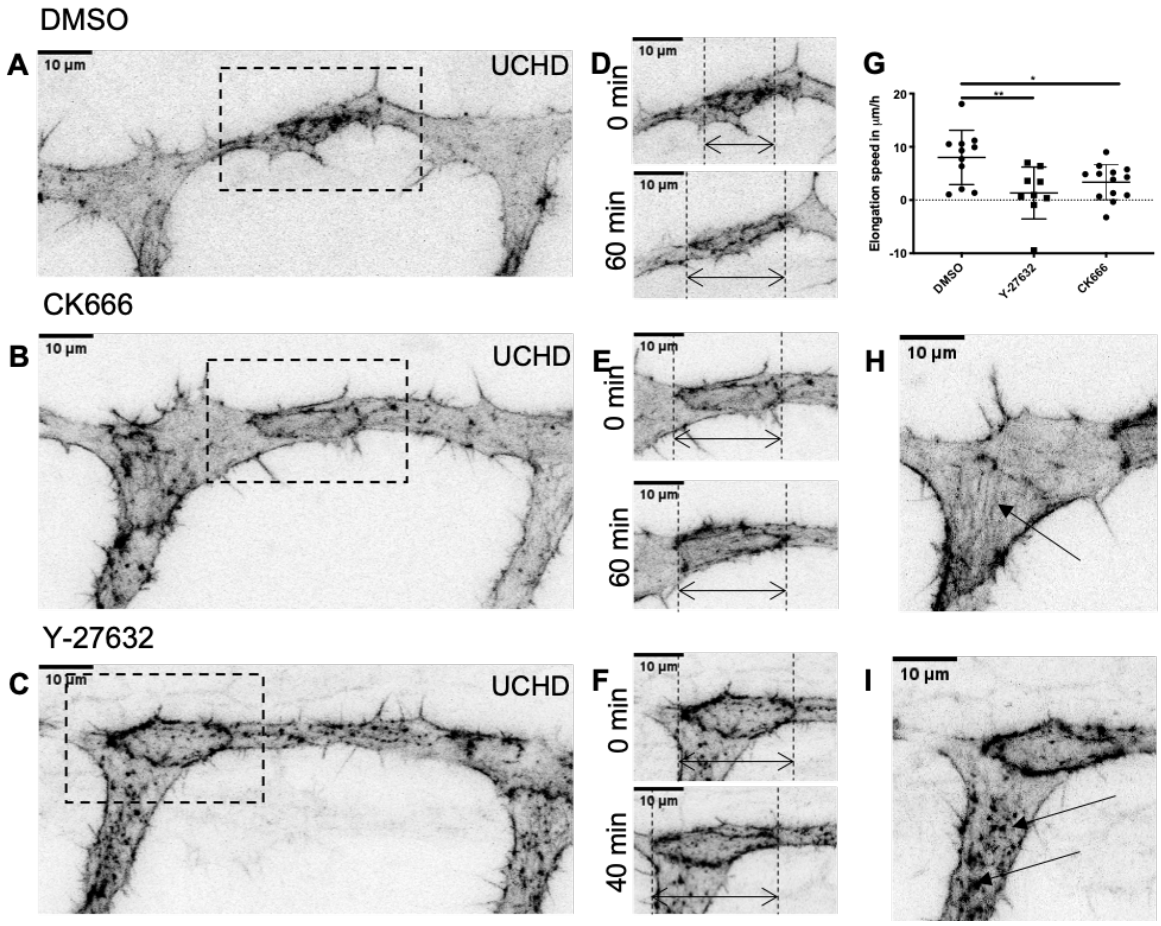

Figure 21: Junction elongation speed is reduced upon inhibition of Arp2/3 or ROCK. Representative still images from movies of embryos expressing EGFP-UCHD (Tg(fli:Gal4ff^{ubs3},UAS:EGFP-UCHD^{ubs18}) around 32 hpf in inversed contrast. **A-C.** Still overview images of 1 % DMSO treated control embryos (**A**) or treated with 200 µM CK666 (**B**) or 45 µM Y-27632 (**C**) 2 h prior to imaging. **D-F.** Magnification of junctional rings (region of the inset from **A-C**) at imaging start (0 min) as well as 40-60 min later. **G.** Quantification of junctional ring elongation speed. Junctional elongation speed is significantly reduced in embryos treated with a ROCK or Arp2/3 inhibitor. DMSO n=11 junctional rings, Y-27632 n=9 and n=13 in CK666 treated embryos (n>5 fish for all conditions). One data point represents the junctional elongation speed of one ring calculated in µm per hour. Mean ± SD displayed. Non-parametric Kruskal-Wallis test was used. ***p*=0.0057, **p*=0.0389. **H.** Magnification of embryo treated with CK666. Arrow points towards filamentous EGFP-UCHD. Arp2/3 inhibited embryos often show actin arranged in cables. **I.** Magnification of Y-27632 treated embryo. Arrows point towards EGFP-UCHD accumulation, that can frequently be observed. Scale bars 10 µm.

Analyzing the F-actin dynamics with higher temporal resolution showed, that Arp2/3 inhibition caused junctional instability in approximately 50 % of the time-lapse series acquired (supplemental figure 1 A).

EGFP-UCHD intensity was very strong and prominent, with specific F-actin localization along the junctional ring in treated embryos. Within shortest time, F-actin accumulation (EGFP-UCHD intensity signal) decreased. Although the cells maintained contact with their neighbors, the mutual contact surface lost F-actin support. This phenomenon is in line with results obtained from *in vitro* studies, where blocking of Arp2/3 lead to a reduced F-actin assembly at cadherin-based junctions (Han et al., 2014; Verma et al., 2004).

Additionally, I observed, that F-actin localization in the JBL region was altered in junctional rings that remained intact (Figure 22). In DMSO treated controls, F-actin localization is often presented in two distinct populations at the site of JBL (Figure 22). In a total of 8 movies this particular F-actin pattern was observed in 6 movies (75 %), usually at 1 or 2 time points (during an imaging period of 15 min). CK666- treated embryos displayed a drastically reduced appearance of F-actin in two distinct populations (I only observed this in 2 out of 10 videos (20 %)). Furthermore, in 30 % of the analyzed junctional rings, F-actin did form diffuse accumulations at the lateral sites of the ring (instead of two populations). An example of a prominent, diffuse F-actin accumulation is shown in Figure 22 C'. In Paatero et al., 2018 the establishment of two distinct lines of F-actin coincided with a distinct and transient localization of ZO1 in these double junctions. It been shown that ZO1 is recruited to the emerging endothelial junctions as they stabilize (reviewed in Bazzoni and Dejana, 2004; Itoh et al., 1997). I therefore wanted to study whether and how mis-regulation of F-actin polymerization and dynamics impact on the formation of de novo junctions during JBL cycles, which will be discussed at later stages of this thesis.

Besides the importance of F-actin filament assembly and network formation, I was wondering whether and how actomyosin contractility may contribute to junction elongation. Especially from the point of view that junctions, due to their underlying actomyosin ring, are considered contractile structures and thus normally resist elongation, it was postulated that its elongation relies on an active process which is driven by a deforming force residing outside the EC junction (Sauteur et al., 2014). Furthermore, it is known that F-actin dynamics play a fundamental role in recruitment of NMII (and therefore generation of contractility) (Verma et al., 2012). Based on that, the contractile properties

of the actomyosin cytoskeleton were altered in a follow-up experiment by specifically inhibiting ROCK (Y-27632).

ROCK triggers the phosphorylation of the myosin regulatory light chain, and therefore enables the assembly of myosin and F-actin filaments, thereby allowing for contractility. Similar to the previously described experiment, inhibition of ROCK reduced elongation speed even more drastically (mean elongation speed at 1.33 µm/h, Figure 21 C, F and I). In addition, I observed specific phenotypic changes that were associated with ROCK inhibition (Figure 21 I). Endothelial cells often showed prominent accumulation of F-actin (visualized as dots) throughout the cell. It seems that inhibition of ROCK not only abolished contractile properties but also ultimately influenced the assembly or distribution of F-actin. This is consistent with the finding that inhibition of myosin II decreases F-actin assembly (Leerberg et al., 2014). While imaging F-actin behavior during junctional ring elongation with higher time resolution (every minute), I observed in approximately 60 % of the movies that the ring was not maintained (supplemental Figure 1 B). It seems that rather than extending the mutual surface of the two opposing cells, cells lose contact, thereby minimizing overlapping structures; instead of continuing moving over each other, they tend to move in opposite directions.

This finding cannot in simple terms be explained by the mis-localization of F-actin during the process. As described previously, F-actin localizes in two distinct populations during a JBL oscillation phase (Figure 22 A). I made similar observations in embryos, in which ROCK was inhibited with almost with the same frequency (in 7 out of 10 movies, 70 %). Figure 22 B and B' show an overview image of the junctional ring at two different time points. Magnifications of the two distinct F-actin pools are shown in A' and B' and a schematic drawing of the latter is shown in A" and B". One pool is associate more with the junctional ring, whereas the more distal F-actin population precedes in an arc-like fashion in the direction of the movement.

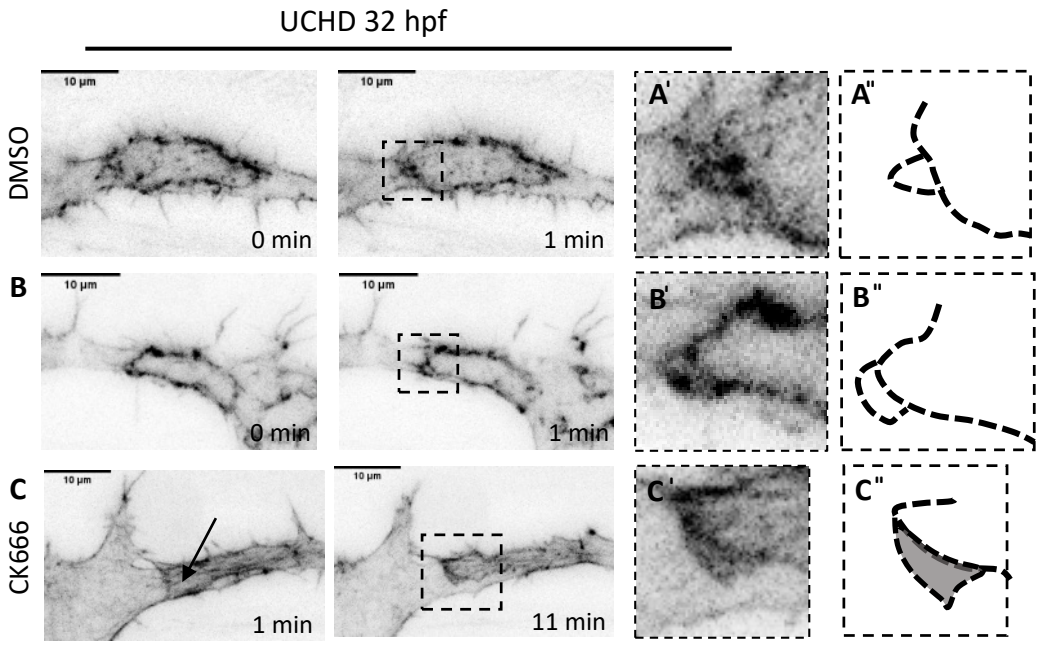

Figure 22: Distinct localization of actin during ring elongation and JBL formation in control and embryos treated with a ROCK or Arp2/3 inhibitor. Still images from movies of embryos expressing EGFP-UCHD (Tg(fli:Gal4ff^{ubs3},UAS:EGFP-UCHD^{ubs18}) in **A – C** in inversed contrast of the DMSO control (1 %) (**A**), Y-27632 treated (45 µM) embryos (**B**) or CK666 treated embryos (**C**). Images show the junctional ring in the DLAV around 32 hpf. Two different time points shown in **A – C**. **A' – C'** show magnification of insert in **A - C**. **A" – C"** are schematic representations of images in **A'**, **B'** and **C'**. Control embryos as well as Y-27632 treated embryos show two distinct actin populations at the lateral sites of a junctional ring, whereas treatment with CK666 often leads to a diffuse accumulation of actin rather than localization in two lines. Scale bar 10 µm.

To see, whether this somewhat abnormal F-actin behavior is reflected at the junctional level by visible defects, or leads to overall vascular defects, an antibody staining was performed. Embryos treated with inhibitors for Rac1, Arp2/3 and ROCK were analyzed with regard to expression of ZO1 (supplemental Figures 2 and 3). Short term treatments did not appear to affect junctional integrity. ZO1 localization was continuous and not interrupted, and junctional rings did form. Although changes in F-actin dynamics strongly affected the cell rearrangement behavior, junctional integrity seemed to be largely unaffected.

In summary, these experiments showed that JBL function and the resulting junctional rearrangements do not only rely on F-actin dynamics (e.g. nucleation, branching or remodeling) but are also strongly dependent on contractile forces generated within the established F-actin network.

The F-actin network might provide a scaffold for NMII for its recruitment and the generation of local forces at JBL, which in turn drive ring elongation. Therefore, I wanted to find out, whether anisotropy in F-actin localization and junctional behavior is reflected by differential localization of myosin regulator light chain (MLC) in the JBL vs the junctional ring as a whole.

Myosin light chain colocalized with junctional proteins and F-actin and is enriched at JBL

As described in the previous paragraph, inhibition of ROCK led to a reduced elongation speed of the junctional ring during the cell rearrangement process. However, inhibition with Y-27632 abolishes ROCK all over the junctional ring, including the medial and the JBL part. Therefore, we cannot distinguish whether the defect in junction elongation is due to an overall diminished contractile force (all over the junction) or, in particular, to a lack of a deforming force (thus, lack of contractility in the JBL). Since we postulate, that JBL provide a deforming force, there should be a "disbalance" between the contractile force (entire junctional ring) and the deforming force (JBL). If this was true, this could be reflected in an anisotropy of the distribution or activity of components of the actomyosin cytoskeleton.

In order to test this hypothesis, I examined embryos expressing MLC (Myl9-EGFP) in the endothelium from a transgene and compared its localization with that of VE-cadherin and ZO1 during anastomosis (Figure 23 A-F). Generally, I observed, that MLC was enriched at areas of cell-cell adhesion, consistent with the notion that MLC is recruited to junctions upon cell adhesion, where it promotes junctional contractility (23 A). It has indeed been reported, that homophilic interaction of E-cadherin leads to the recruitment of Myosin II (Shewan et al., 2005). In endothelial cells, I observed that MLC prominently and specifically accumulates in the JBL region of the junctional ring (23 B-F). Here, two distinct patterns were observed. Mostly, MLC clearly colocalized with ZO1 and VE-cadherin in the JBL (23 E/F). However, occasionally, MLC intensity was highest in areas more distal to VE-cadherin/ZO1 and manifested as a "preceding" front (23 B-C).

Heat map images of both VE-cadherin and ZO1 (23 D) showed a diffuse and broad (but rather weak) accumulation of junctional proteins at the site of high MLC intensity.

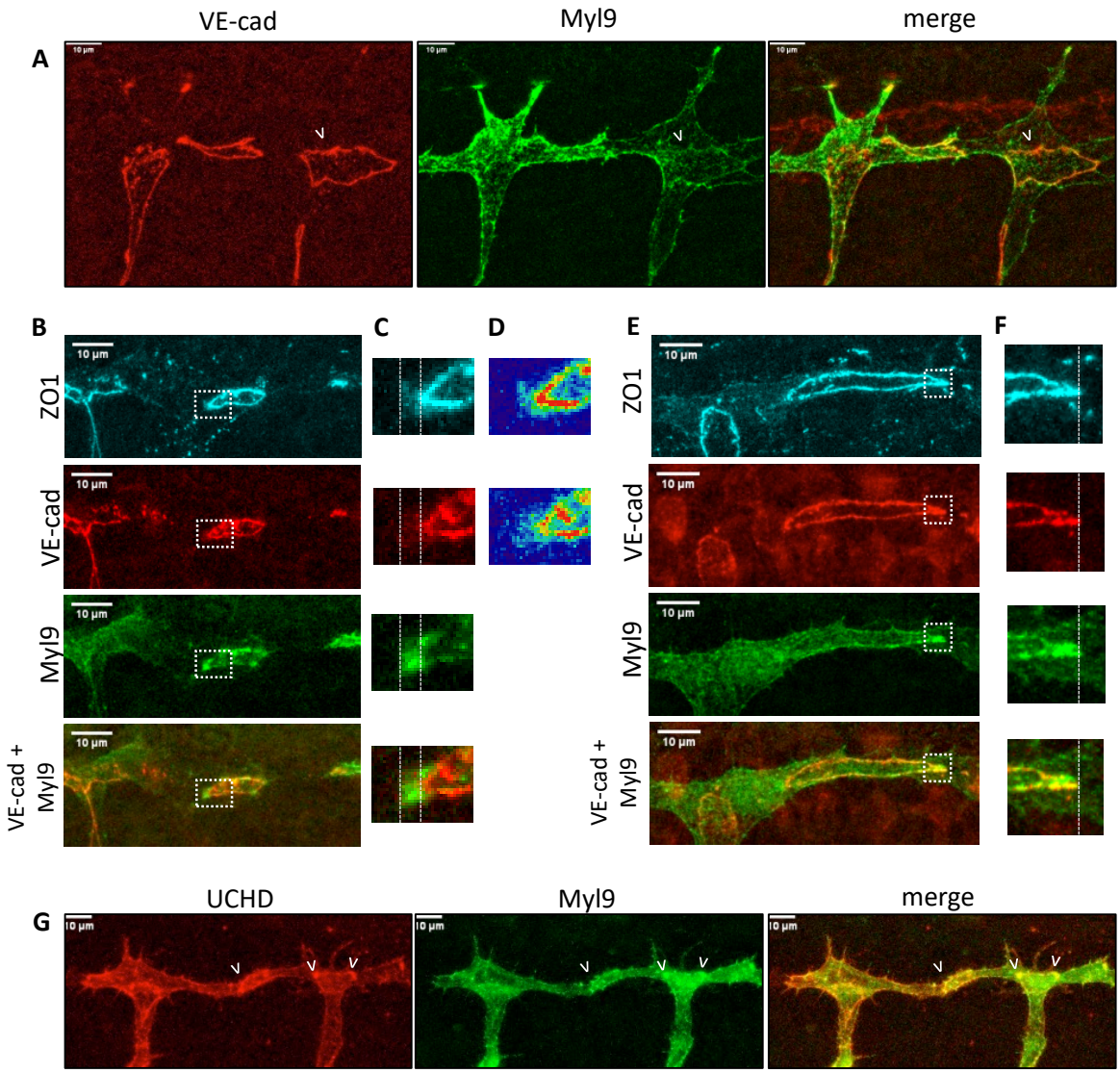

Figure 23: Colocalization of Myl9, junctional proteins and actin in junctional rings. A-E. Maximum projections of the DLAV of Tg(Kdrl:Mly9a) (green) embryos fixed in Gylofixx or 2 % PFA at 32 hpf and co-stained with VE-cadherin (red) and ZO1 (blue). **A.** Colocalization of Myl9 and VE-cadherin at the cell- cell junctions. Arrow points towards area with prominent colocalization. **B.** Myl9 precedes the distal portion of VE-cadherin and ZO1 in the JBL region of junctional rings and colocalizes in VE-cadherin /ZO1- low regions, a hallmark of JBL. **C** shows magnifications of inserts in B. Lines define border of Cdh5/ZO1 vs. Myl9 expression. **D**. Heat map- color coded staining of ZO1 and VE-cadherin. Note the very prominent distal portion of junctional proteins but additionally a spread weak accumulation in the JBL region **E.** Myl9 expression is strongly enriched in the JBL region. **F.** shows magnifications of inserts in **E**. **G.** Live still image of Tg(Kdrl:Myl9a) (green) and Tg(fli:Galff4^{ubs3}, UAS:mRuby2-UCHD^{ubs20}) (red). Arrows highlight colocalization of actin an Myl9 at cell-ell junctions in general as well as in JBL of a junctional ring. Scale bars 10 µm.

This behavior of junctional proteins is a characteristic during a particular time in the JBL cycle and is observed during and shortly after initial F-actin protrusions. Life still images of embryos expressing UCHD and Myl9 confirmed that MLC is indeed enriched in F-actin rich (JBL) regions (Figure 23 G).

The observed localization/enrichment patterns of MLC clearly show that specific localization changes dependent on the JBL cycle. Since JBL are highly dynamic and transient structures, it is not surprising that MLC expression patterns vary.

However, most importantly, anisotropy of MLC localization (specific accumulation at the sites of JBL) could be an indication that the deforming force indeed might be stronger than the contractile force within the ring.

It remains to be elucidated, how MLC, F-actin and junctional proteins are dynamically interlinked. To this point it seems like F-actin accumulations (protrusions) and recruitment of junctional proteins (diffuse ZO1 and VE-cadherin) could act jointly as the instructive cue to recruit MLC to the JBL. MLC therefore could be responsible for generating a contractile force within the F-actin cytoskeleton.

The F-actin cytoskeleton itself is directly linked to adhesion molecules like VE-cadherin. Therefore, I was wondering in a next step, whether potential actomyosin-induced tugging forces might be reflected in intramolecular tension changes in VE-cadherin.

VE-cadherin tension in JBL during junctional ring elongation

We hypothesized that the local adhesion patches generated by VE-cadherin in JBL during junctional elongation exhibit different local and temporal VE-cadherin tension and that this process is a major contributor to the elongating force. Therefore, the VE-cadherin tension sensor line was used to visualize and measure intra-molecular tension across VE-cadherin. In general, the goal was to use this tool to correlate JBL activity with the distribution of VE-cadherin tension during cell rearrangements along the junctional ring as well as during formation of the novel junction at the front of the JBL itself.

The first measurements using the FRET imaging technology *in vivo* were performed according to Lagendijk et al., 2017 to confirm that the imaging technique (plus post acquisition analysis) also work in my hands and gives reliable results.

Therefore, I determined ratio-metric FRET values in the dorsal aorta (where the tension sensor was validated in Lagendijk et al., 2017) in embryos around 50 hpf (Figure 24 A and B). Inhibition of ROCK led to a significant increase of ratio-metric FRET and therefore decrease in tension (Figure 24 B). That finding was in line with published results and confirmed that differences in energy transfer reflect tension changes through VE-cadherin (Lagendijk et al., 2017).

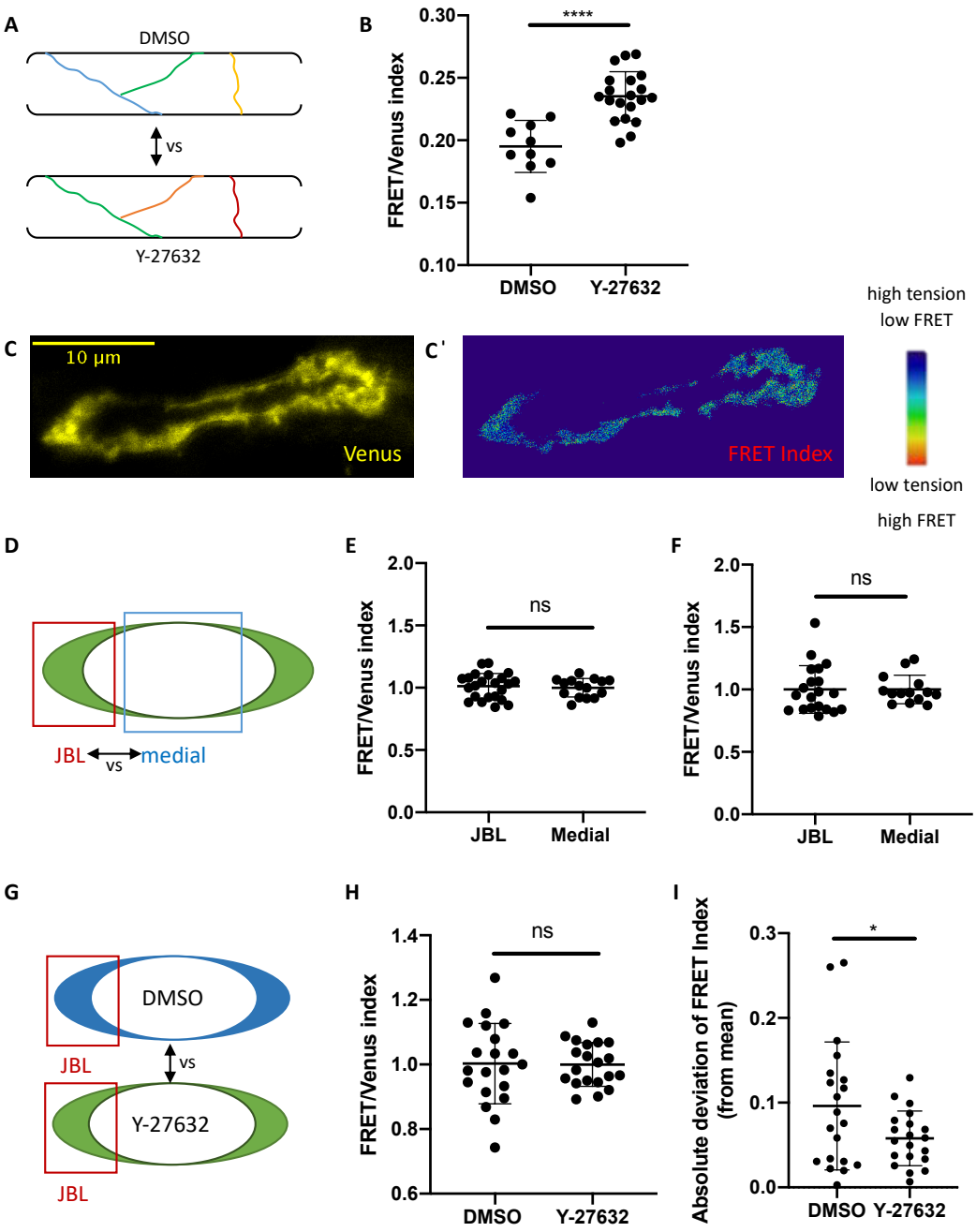

Figure 24: VE-cadherin tension in junctional rings and in JBL. A. Scheme of quantification done in **B.** Ratio metric FRET values were determined in linear junctions in the dorsal aorta > 50 hpf in 1 % DMSO vs. Y-27632-treated embryos. Ratio-metric FRET values in DMSO (n=10 junctions) and in Y-27632 treated embryos (n=20) in more than 5 embryos each. Treatment of embryos with Y-27632 led to a decrease in tension in the dorsal aorta at 50 hpf. ****p<0.0001 from unpaired two-sided t-test. **C.** Maximum projection of a junctional ring in the DLAV at around 32 hpf showing the expression of venus. Scale bar 10 µm. **C'.** Example of a heatmap image of ratio-metric FRET values in the junctional ring displayed in **C**. Blue indicates low FRET index (high tension) whereas red indicates high FRET (low tension). **D.** Scheme of quantifications done in **E** and **F**. Isolated junctional ring is shown. Basis of comparison are JBL vs. medial part of a junctional ring. **E.** Quantification of the ratio-metric FRET values of JBL vs. the medial junctional part in wild-type (**E,** n=23 JBL and n=15 medial part in 10 embryos) and Ve-cadherin$^{ubs8-/-}$ background (**F,** n=20 JBL and n=14 medial part in 13 embryos). Embryos show no significant mean difference in energy transfer (and therefore VE-cadherin tension) between the JBL region and the medial part of a junctional ring. Data of two independent experiments are shown together. Each datapoint represent one ROI. Unpaired two-sided t-test used in **E** and unpaired two-sided Mann-Whitney test in **F**. **G**. Schematic representation of the measurements quantified in **H**. Here, the VE-cadherin tension in JBL was determined of 1 % DMSO treated embryos vs. Y-27632 treated embryos by measuring ratio-metric FRET (n=20 for DMSO (13 embryos) and n=20 for Y-27632 (11 embryos). There was no significant mean difference between the two groups. Kolmogorov -Smirnhov test was used. **I**. Quantification of the absolute deviation (from the mean value) was calculated and is displayed in **H**. There is a significant decrease between the DMSO control and ROCK-inhibited JBL, pointing towards a loss of dynamic tension changes in VE-cadherin molecules. Unpaired t-test was used *p= 0.0444. **B, E, F, H, I** mean ± SD is displayed.

Based on the dynamic nature of JBL, the first experiment after the establishment of the method was to investigate temporal changes of VE-cadherin tension during the JBL oscillation cycle. Ratio-metric FRET values were determined every minute for several consecutive time points. Unfortunately, temporal changes of VE-cadherin tension could not be measured due to technical limitations and rapid bleaching of the fluorophores (see supplemental Figure 4 A/B). As time resolution of VE-cadherin tension could not be reliably performed, we decided to use still images of JBL. The goal of these experiments was to analyze the scattering/dispersion of FRET-values both in wild-type conditions (JBL and medial part) and upon inhibition of ROCK.

Figure 24 C and C' show examples of a junctional ring (maximum projection of the venus channel in C) and a representative heat map of the FRET-Index in C'. Colors range from blue (high tension, low FRET) to red (low tension, high FRET). Measurements were performed both on embryos expressing Tg(ve-cad:ve-cad-TS) in a WT background (24 E) as well as in a VE-cadherin mutant background (cdh5$^{ubs8-/-}$) (24 F). In both cases, there was no difference in mean values of JBL and the medial part of a junctional ring. Although this was an unexpected result, we observed a slight difference in the distribution of data points between JBL and the medial junction part, possibly reflecting the dynamic and non-uniform behavior of JBL. To further investigate this, I decided to focus on JBL and compare VE-cadherin tension between control embryos and embryos treated with a ROCK inhibitor. Based on the observed localization of MLC (see Figure 23) in the JBL, I hypothesized that upon inhibition of ROCK JBL dynamics might be abolished and scattering of data points might also decrease. Determination of ratio-metric FRET values again showed no difference between mean values in JBL from DMSO vs. Y-27632 treated embryos (Figure 24 H). However, I could observe a smaller scattering of individual datapoint around the mean value. Indeed, quantification of the absolute deviation from the mean proved to be statistically significant (24 I). The results for no mean difference between JBL and medial part as well as in DMSO vs. ROCK inhibited conditions were also confirmed using donor fluorescence lifetime imaging FLIM (Supplemental Figure 4 C & D).

In summary, these experiments proved and confirmed the dynamic nature of JBLs which is also reflected in differential VE-cadherin tension. Of special importance is the finding that interference with the actomyosin contractility reduces dispersal of VE-cadherin tension values. This shows that ROCK inhibition reduces the possibility of VE-cadherin molecules to exhibit differential tension throughout JBL formation.

The sum of these experiments hints towards a model proposing that JBL generate a contractile force via mechanical coupling to the actomyosin network. Furthermore, they could do so by transmitting differential tension onto VE-cadherin molecules themselves.

Distinct localization of ZO1 as a hallmark during JBL formation and ring elongation

Since the junctional protein VE-cadherin was demonstrated to play a major role in JBL formation (and link proteins to the F-actin cytoskeleton, see Paatero et al., 2018) and for force transmission processes (this study), I was wondering how other junctional proteins might be affected. During a certain phase during the JBL oscillation cycle (late phase), ZO1 in particular shows a distinct distribution pattern. It is often localized in two lines representing a distal and proximal junction, hereinafter referred to as “double junctions”. Double junction formation represents a distinct step during a JBL cycle, in which a new distal junction is formed while the “old” one is still maintained. The formation of a new junction is initiated by deposition of VE-cadherin and subsequent and transient recruitment of ZO1. ZO1 is recruited to new adhesion sites and can be considered as a good indicator for formation of new junctions (Itoh et al., 1997). The new junction provides a new anchor point more distally and is proposed to be important in driving the movement of endothelial cells. I was interested how interference with the F-actin dynamics impacts on the formation of a new distal junction, and whether a new attachment site can be formed.

Junctional adaptor proteins (like ZO1) provide the link between junctional molecules and the F-actin cytoskeleton. Therefore, it is very likely, that localization /recruitment of ZO1 is dependent on the F-actin cytoskeleton and that the double junction formation is impaired at different levels (e.g. formation/maintenance).

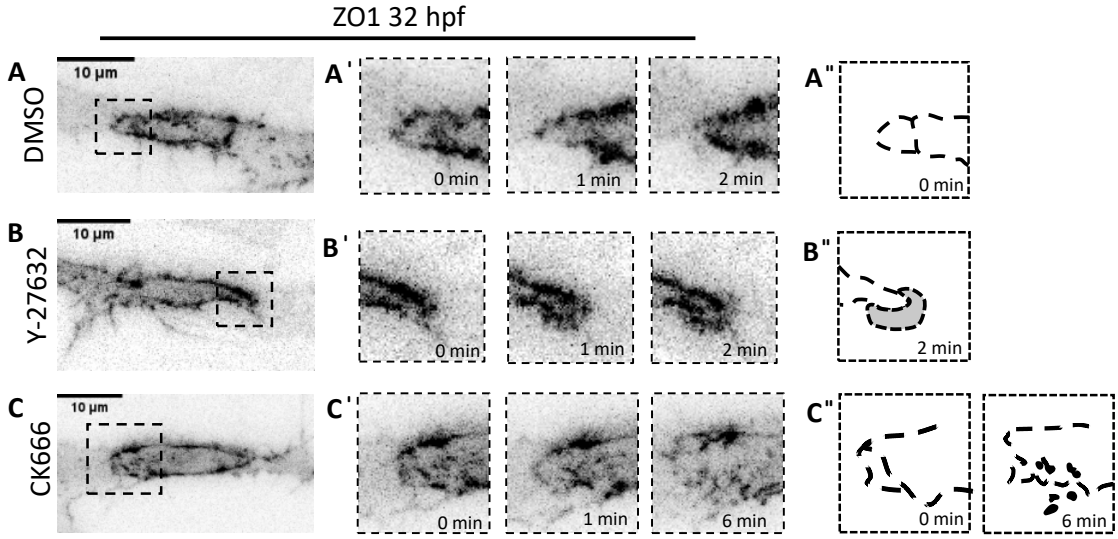

Figure 25: Distinct localization of ZO1 during ring elongation and JBL formation in control and embryos treated with a ROCK or Arp2/3 inhibitor.

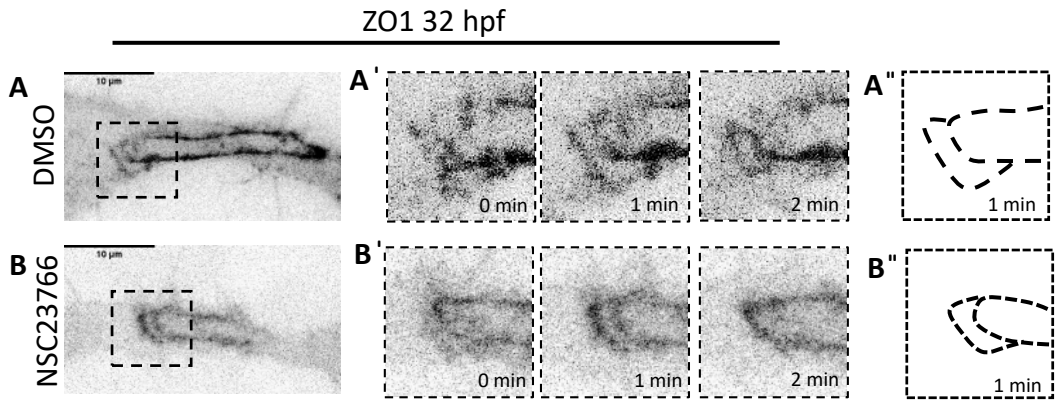

Figure 26: Distinct localization of ZO1 during ring elongation and JBL formation in control and embryos treated with a Rac1 inhibitor.

Figure 25/26 : Representative still images from movies of embryos expressing ZO1 Tg(fli:Gal4ff^{ubs3};UAS:EGFP-hZO1^{ubs5}) in inversed contrast of the DMSO control (1 %) (**A**), and embryos treated with Y-27632 inhibitor (**Figure 25 B-B"**) , CK666 (**Figure 25 C-C"**) and NSC23766 (**Figure 26 B-B"**). Images show the junctional ring in the DLAV around 32 hpf. **A' – C'** show magnification of insert in **A - C**. Three different time points shown. **A" – C**" are schematic representations of images in **A '- C '**. In control embryos ZO1 is often localized in two lines, a distal and proximal junction ("double junction" in **A**). Interfering with actomyosin tension (Y-27632 in **Figure 25 B**) often leads to diffuse proximal accumulation of ZO1 instead of a defined linear junction. Inhibition of Rac1 or Arp2/3 does not abrogate double junction formation (**Figure 26 B** and **25 C** respectively) Additionally, treatment with CK666 often leads to dissolution of the junctional ring (**Figure 25 C'** at 6 min). Scale bars 10 µm.

To this end, embryos transgenically expressing EGFP-ZO1 were treated with a Rac1, Arp2/3 or ROCK inhibitor and imaged ever minute, focusing on the appearance on double junction formation (Figure 25 and Figure 26). As mentioned earlier, ZO1 in DMSO controls often shows a very distinct localization in two lines, a more distal junction and a proximal one. The latter was shown to be the "old" junction, whereas the distal one is considered to be the newly formed junction at the site of the JBL. Double junctions in the DMSO treated embryos almost appear with a prevalence of almost 100 % (observed in 12 out of 13 movies) (compare Figure 25A and 26A).

Inhibiting Rac1 did not alter localization of junctional proteins, and double junctions were observed at similar frequency as in DMSO controls (9 double junctions observed in 12 movies). A representative example is shown in Figure 26 B.

When using the Arp2/3 inhibitor CK666, distal and proximal junctions still formed (Figure 25 C, 0 min), although only half as often as compared to DMSO controls (in 55 % of the movies). Interestingly, the junctions appeared to be less stable. In 7 (out of 11) movies the junctional ring showed signs of instability or diffuse ZO1 accumulation, up to dissolution of the junctions (C' at 6 min). At this stage, it is noteworthy to remember, that Arp2/3 inhibition led to an altered F-actin localization (compare Figure 22 C). The localization of F-actin in two distinct outlines might provide a scaffold for junctional proteins to adhere to (or vice versa). Sine correct F-actin localization is diminished, this might be reflected in the localization of junctional proteins and their disability to maintain integrity.

In embryos treated with Y-27632, double junctions appear less frequently (in 6 out of 12 movies). Additionally, I observed that ZO1 manifests as a diffuse but yet prominent accumulation which precedes the proximal junction (Figure 25 B). This diffuse accumulation of ZO1 was observed in 50 % of the movies. In these cases, elongating cells were unable to form double junctions and were impaired in “correctly” localizing ZO1 at the JBL. Interestingly, that F-actin localization remained unaffected (as described in Figure 22). Therefore, the recruitment of ZO1 and the coherent formation of double junctions, is therefore not exclusively dependent on F-actin localization, but rather influenced by ROCK functioning as a mediator between ZO1 and the F-actin cytoskeleton.

Additionally, Arp2/3 inhibition influenced junctional stability, showing that junctional integrity and maintenance rely on proper nucleation of the F-actin network, specifically downstream of Rac1 (since Rac1 inhibition did neither alter double junction formation nor junctional integrity). However, the most obvious phenotype did arise upon ROCK inhibition. Loss of double junction formation (resulting in loose accumulation of ZO1) points to the possibility that the actomyosin cytoskeleton signals back to the junctions and influences their localization.

In summary, I found that the formation and stabilization of a new distal junctions, which is reflected in the intermediate state of double junction formation is altered after interfering with F-actin dynamics at different levels. Whereas Rac1 inhibition does not impact the formation nor stabilization a new junction, ROCK interfered with recruitment of ZO1 to a newly formed adheres-based junction. Arp2/3, on the other hand, led to normal unimpaired formation of the new junction; however, Arp2/3 seemed to be required for its maintenance and stabilization.

It is very interesting that in all of these studied cases the cell rearrangement process was impaired (compare Figure 21). Thus, the elongation does not only dependent on the formation of a new distal junction but relies on several other components that interplay along the junctional ring.

Junctional ring elongation mediated by JBL seems to be a very complex process and requires a proper and tightly regulated interplay of F-actin dynamics and contractility but also proper localization and recruitment of junctional proteins. I hypothesize that double junction formation is indispensable for junction elongation, and these junctions need to be embedded in a functional and dynamic F-actin network.

Generation and transgenic expression of Kdrl:mCherry-PA-Rac1

Based on previous findings from Paatero et al., 2018 and on my own studies, Rac1 function does not seem to be strictly required for JBL function. Formation of JBL is largely unimpaired upon Rac1 inhibition, although the oscillatory behavior is slightly affected (increased oscillation time). Additionally, also the formation of a new distal junction seemed to be largely unaffected upon inhibition.

Although the requirement for Rac1 was relatively relaxed, we wanted to investigate whether Rac1 activation could drive JBL formation during cell rearrangements in the process of anastomosis.

Therefore, I decided to generate a plasmid containing a photoactivatable version of Rac1 (PA-Rac1) under an endothelial specific promoter. This construct has previously been already successfully expressed *in vivo* in zebrafish neutrophils, and it was subsequently shown that localized activation of Rac1 can indeed induce protrusion formation and induced directed cell migration (Yoo et al., 2010).

For transient expression in the zebrafish vasculature, I designed a plasmid construct containing the endothelial specific promotor *kdrl* as well as sequences encoding PA-Rac1 fused to mCherry. Using the gateway multisite cloning approach, also a Kozak sequence and a poly-A tail were included. Furthermore, a transgenesis marker was added for future screening purposes. A scheme of the final plasmid is presented in simplified version in Figure 27 A.

Injection of plasmid DNA into zebrafish embryos showed specific expression in the vasculature (Figure 27 C) and expression of the transgenesis marker in the eye (27 B).

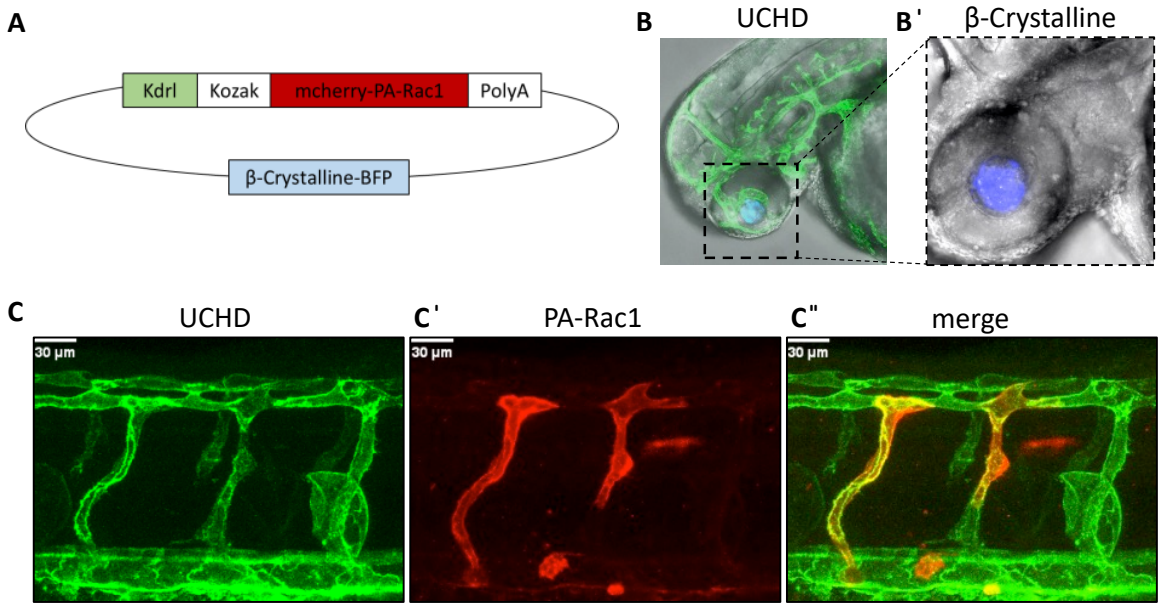

Figure 27: Design and generation of a Kdrl:mCherry-PA-Rac1 construct and its transient expression. A. Scheme of the designed expression vector, containing the endothelial specific *kdrl* promotor, the protein of interest (PA-Pac1) fused to a fluorophore (mCherry) in a beta crystalline backbone (transgenesis marker), resulting in the expression of BFP in the eyes. **B.** Expression of ß-crystalline-BFP in the eye of a 48 hpf old embryo expressing (Tg(fli:Gal4ff^{ubs3},UAS:EGFP-UCHD^{ubs18}). **B'** magnification of the insert in **B**. **C**. Transient endothelial expression of kdrl:mCherry-PA-Rac1 (**C'** in red) in an embryo expressing Tg(fli:Gal4ff^{ubs3},UAS:EGFP-UCHD^{ubs18} embryo at 48 hpf. Merge shown in **C**". Live still images. Scale bar 30 µm.

To date, there is no *in vivo* data available regarding endothelial- specific expression of Rac1 or its activation via PA-Rac1. Therefore, the functionality was tested at first, combined with the establishment of an appropriate experimental setup and imaging method.

Activation of Rac1 leads to a decrease in filapodial number as well as in cell size

mCherry-PA-Rac1 was transiently expressed and initial experiments were performed at around 50 hpf in the DLAV. Time lapse imaging was done for 12 timepoints in an inactivated state, then Rac1 was activated with 20 % intensity of the 458 nm laser for 15 time points (while imaging continued), followed again by post- activation image acquisition. Activation of Rac1 was not locally restricted but performed on the whole frame/image.

Temporal activation of Rac1 led to the observation of two different phenomena, which were all confirmed in at least three independent experiments.

Firstly, during the time of Rac1 activation, the number of dynamic filipodia was reduced (even to zero), but recovered after the 458 nm laser was turned off again. In Figure 28 A, three exemplary images are shown for each imaging period. Quantifications are presented in C and D. Furthermore, it looked like cell membrane ruffles did increase (Figure 28 B). Secondly, the cell size temporarily decreased during the time of Rac1 activation (28 E-G).

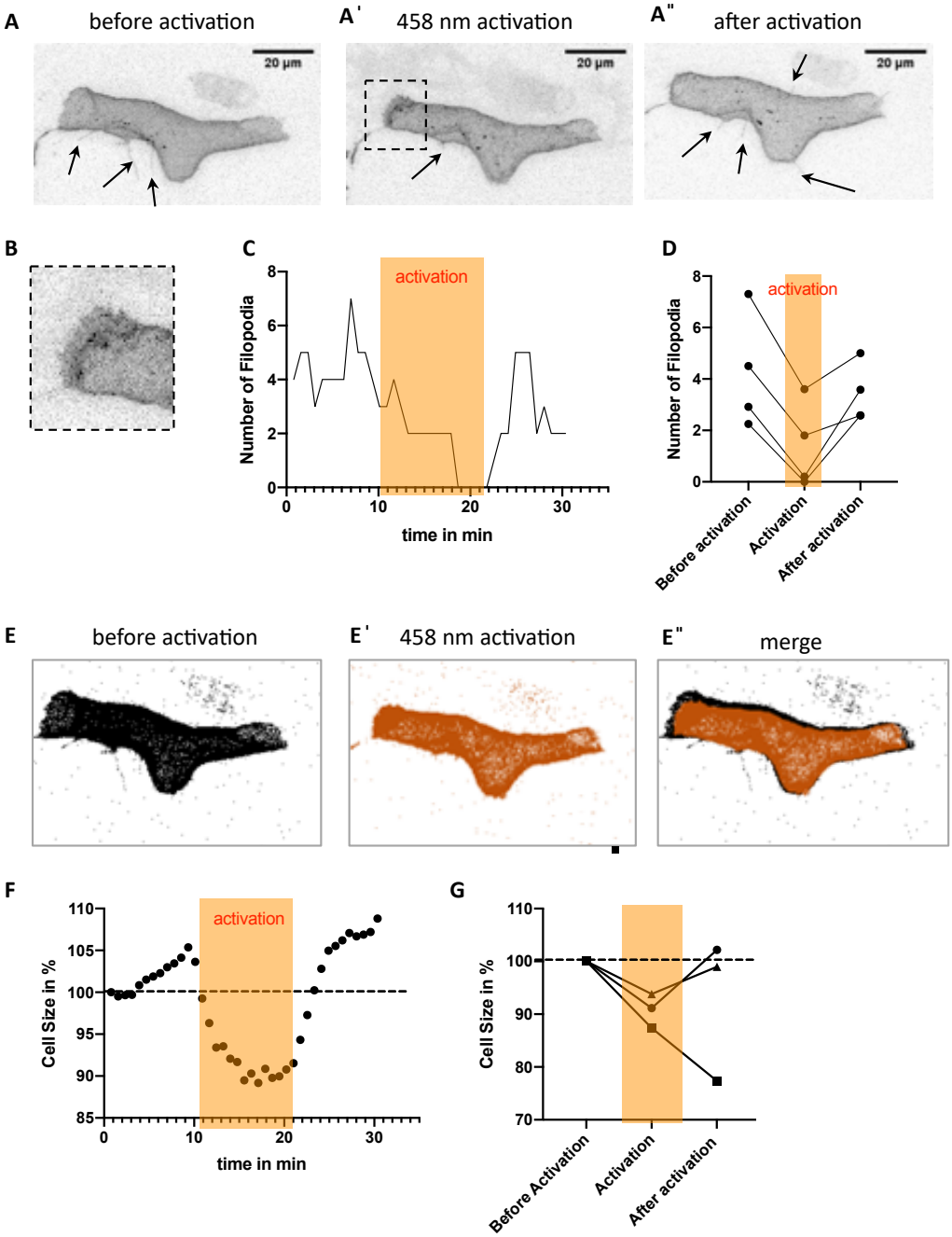

Figure 28: Change of cell size and filopodia number in endothelial cells after temporal photoactivation of PA-Rac1. **A-A"** Endothelial cell at 48 hpf in the DLAV transiently expressing mCherry-PA-Rac1. Images were taken out of a movie and shown in inversed contrast. Representative images were chosen before activation (**A**) of Rac1, during activation with 20 % 458 nm (**A')** and after activation (**A**"). Arrows point toward filopodia. Scale bars 20 µm. Magnification of insert in **A"** shown in **B**. Membrane ruffling seems to increase after Rac1 activation at the cell-cell border **C**. shows a quantification of the absolute number of filopodia of the cell displayed in **A**, during the imaging period (12 time points before activation, 15 with activation of PA-Rac1 and 12 post activation). Time of activation is highlighted in orange. Activation of Rac1 led to a reduction of filopodia number, which again increased in the post-activation period. **D.** Quantification of number of filopodia in four different cells in the DLAV (n=4 fish). Numbers before, during and after activation are displayed as average during the respective time period. **D-D'** Show the same cell as in **A-A"** but with emphasize on the cell shape and area. In **D** the cell area is colored in black (before activation), **D'** during activation (orange) and the merge is displayed in **D**"**. E.** Quantification of the cell size during the imaging period. For each time point the cell area is displayed. Cell size at t=0 is considered to be 100 %. Cell size decreased upon Rac1 activation, but went back to the original cell size (or bigger) post-activation. **F.** Quantification of the cell area of three independent cells in the DLAV (n=3 fish). For each time period (before, during and after activation) the average cell size is displayed in % of the cell size determined at t=0.

Filopodia reduction and cell size decrease represented an unexpected finding. However, since this cell behavior only occurred during the time of Rac1 activation and returned to the baseline state (before activation) afterwards, it appeared to be a specific response to Rac activation. Nevertheless, how this might be induced by the activation of Rac1 remains to be elucidated. Rac1 is mainly known to be an important factor for lamellipodia formation and accumulation of F-actin in larger protrusions at the cell edge, but not for the formation of filopodia.

How Rac1 directly regulates cell size, is to the best of my knowledge, not known. However, two possible scenarios might account for the change in cell size. Firstly, Rac1 overactivation could alter the cortical actomyosin network and leading to increased tension. Secondly, it could act on the cell junctions. Overactivation of Rac1 could lead to increased tension at cell-cell interfaces, leading to the shrinkage of the cell.

To further explain this phenomenon, it would be really interesting to analyze ubiquitous activation of Rac1 in an isolated cell (without affecting cell junctions).

Another explanation would be, that ubiquitous activation of Rac1 alters or abolishes polarity of the cell. This aspect proves the importance of locally restricted activation of Rac1, in order to not change the entire polarization of the cell.

Based on these findings, I decided that activation of Rac1 needs to be not only temporarily but also locally restricted. Furthermore, I considered it as a necessity to concomitantly visualize F-actin in these experiments.

Generation of a new iRFP- UCHD fishline

In all available transgenic fish lines, F-actin is either fused to the fluorophore EGFP or to mRuby, neither of which is compatible with the coexpression with PA-Rac1. Imaging EGFP with the 488 nm laser already leads to unwanted activation of PA-Rac1 (data not shown), whereas mRuby is imaged using the same wavelength as mCherry (561 nm).

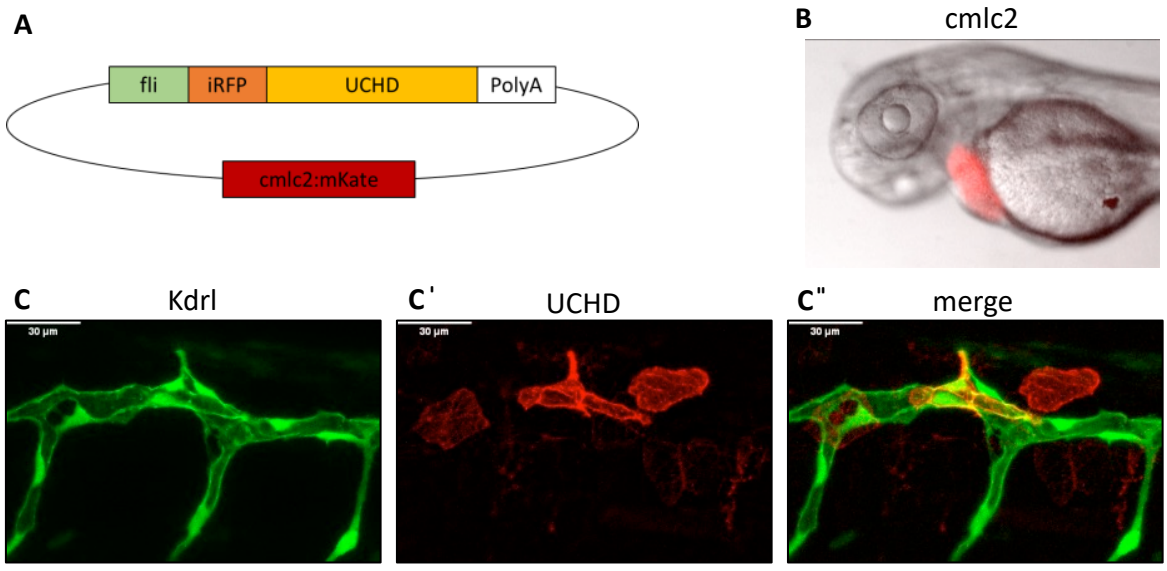

Figure 29: Design of the fli:iRFP-UCHD; cmlc2-mKate2 vector and its transient expression. **A.** Scheme of the designed expression vector, containing a vascular endothelial specific promoter *fli*, the fluorophore (iRFP) as well as the protein (UCHD) labelling actin in a cmlc2:mKate2 backbone vector, resulting in mKate2 expression in the heart. **B.** Expression of the transgenesis marker (cmlc2:kate2) in the heart (red) of a 2 dpf embryo. **C-C".** Transient and vascular expression of fli:iRFP-UCHD (**C'**) in a Tg(Kdrl:EGFP^{s843}) expressing embryo (**C**). Merge is shown in **C"**. Live still images. Scale bars 30 µm.

To overcome this problem, I generated another transgenic fish line with an iRFP-UCHD-reporter, which can be visualized using the 633 nm laser and thus does not interfere with activation of the PA-Rac1 transgene. The design of the plasmid is displayed in Figure 29 A. A transient expression pattern in the zebrafish vasculature after injection is shown in C. Both constructs (kdrl:mCherry-PA-Rac1 and fli:iRFP-UCHD) were injected and successfully co-expressed, which is shown in Figure 30 A.

Activation of PA-Rac1 leads to recruitment of F-actin to cell-cell junctions

In order to examine the effects of Rac1 activation on F-actin linked behaviors, activation of PA-Rac1 was performed ubiquitously in an endothelial cell of the DLAV in embryos around 50 hpf. In these experiments, time lapse imaging was only performed in the UCHD channel pre-activation (Figure 30 B) and during activation of PA-Rac1 (Figure 30 B').

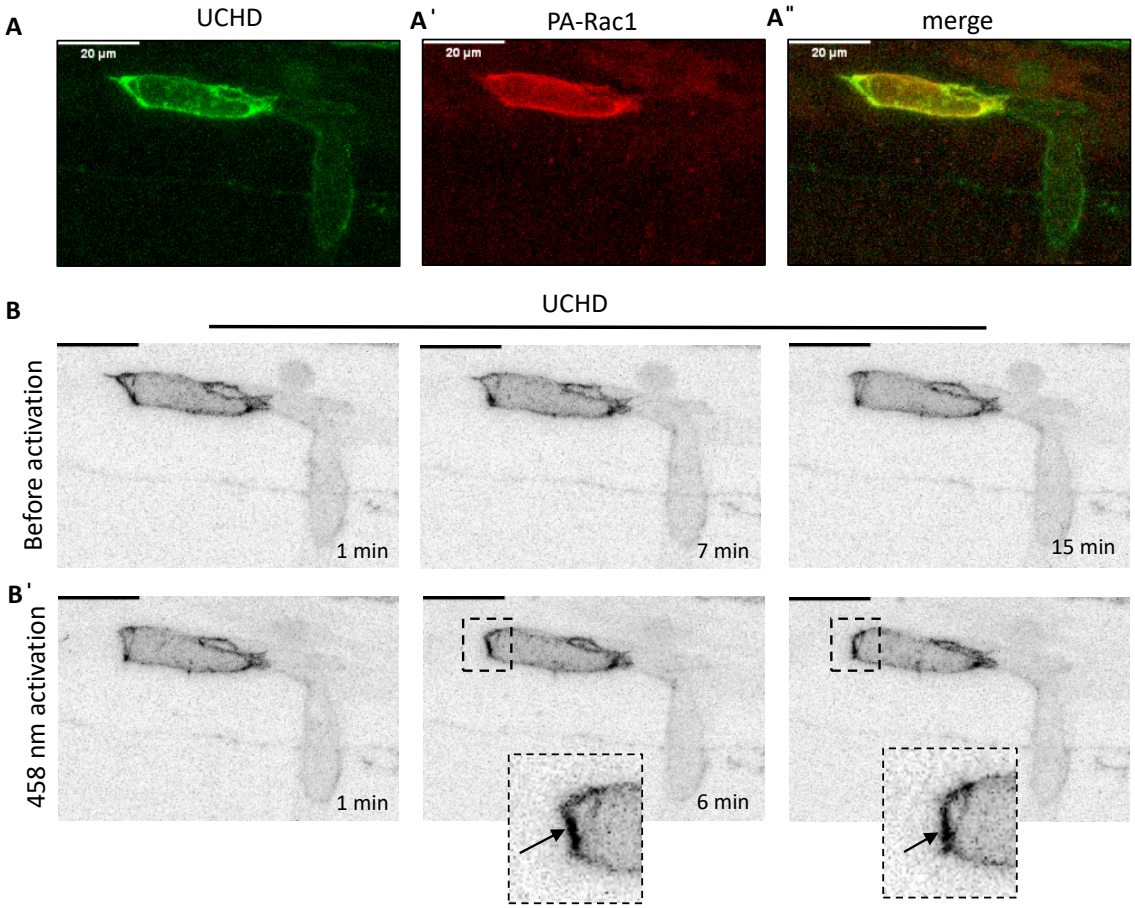

Figure 30: UCHD localization upon temporal activation of PA-Rac1 in embryos expressing kdrl:mCherry-PA-Rac1 and fli:iRFP-UCHD transiently at around 50 hpf. **A-A"** Still images from a movie of a cell in the DLAV showing transient expression of iRFP-UCHD (**A**) and kdrl:mCherry-PA-Rac1 **(A')** after co-injection of the two constructs. Colocalization is shown in **A"**. **B** and **B'** show still images of the same cell as shown in **A**. Only iRFP-UCHD was imaged. Three different time points are shown for the un-activated state (**B**, before activation) as well as for the activated state (**B'**; PA-Rac1 activation with 20 % 458 nm in the whole image). Images shown in inversed contrast. Activation of Rac1 leads to actin accumulation at the cell borders. In **B'** also magnifications of the inserts at 6 min as well as 15 mins are shown. Arrows point towards actin accumulation at the cell junction. Scale bars 20 µm.

After activation of PA-Rac1 an immediate increase of UCHD-signal at the region of the cell-cell junction was observed (see Figure 30 B' at 6 min and 15 min). This F-actin accumulation was not present before activation and furthermore, did remain at this specific localization during the activation period.

Having zebrafish transgenically expressing both proteins (iRFP-UCHD and mCherry-PA-Rac1) at hand, I decided to repeat the previous experiments. Using a stable line, instead of relying on transient expression, offers several advantages. First of all, the yield of double positive cells is much higher, and secondly, it enables analyses, that go beyond single cells. The latter allows to include the surrounding cells in the analysis, rather than focusing on a single cell without looking at effects of or in direct neighbors. Last but not least, working with stable lines provides a certain flexibility concerning duration or timepoint of the analyses.

The expression pattern of G0 founder fish is presented in Figure 31. In A and A', iRFP-UCHD is shown during two timepoints of embryonic development (2 dpf in A and 5 dpf in A'). An embryo coexpressing both constructs (incross of the two G0 founder fish) is shown in Figure 3 in the trunk (B) and head (C) region. Generally, I observed, that expression of PA-Rac1 is mosaic in the trunk and much stronger (and not mosaic) in the brain vasculature. iRFP-UCHD expression, on the other hand, is rather uniform throughout the vasculature.

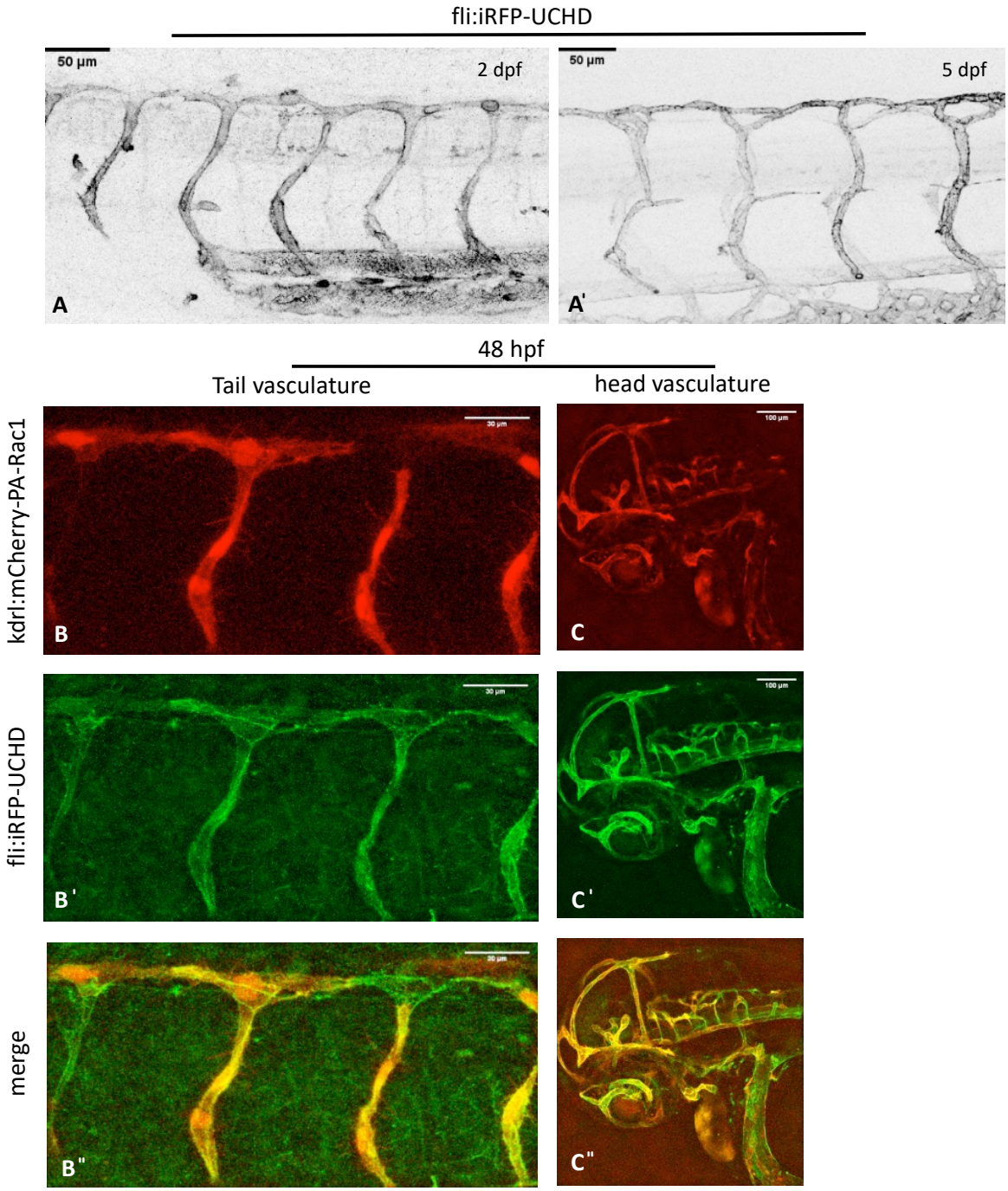

Figure 31: Endothelial specific expression of fli:iRFP-UCHD and Kdrl:mCherry-PA-Rac1 in transgenic fish lines. **A** and **A'**. Live still images of the vasculature of an embryo expressing Tg(fli:iRFP-UCHD) at 2 dpf (**A**) and 5 dpf (**A"**). Images shown in inversed contrast. Scale bar 50 µm. **B-C**. Still live images of a Tg(fli:iRFP-UCHD; kdrl:mCherry-PA-Rac1) expressing embryo at 48 hpf in the tail (**B-B"**) and head (**C- C"**) region. Individual channels are shown in red Tg(Kdrl:mCherry-PA-Rac1) (**B** and **C**) and green (fli:iRFP-UCHD) (**B'** and **C'**). Merges are shown in (**B"** and **C"**). Scale bars 30 µm.

Imaging was performed as previously described. A still image of the vasculature at 50 hpf is shown in Figure 32 A-A''. Still images from embryos expressing iRFP-UCHD from movies are shown in inversed contrast in B and B''.

Activation of Rac1 led to a prominent accumulation of UCHD at cell-cell junctions (arrow and magnification in B'), which confirmed the observation of my initial experiments. Specific, Rac1-induced F-actin accumulation at the junctions point towards an increase of junctional F-actin. This finding supports the previous hypothesis, that changes in cell shape might be linked to enhanced junctional contractility, as overactivation of Rac1 led to enhanced junctional F-actin.

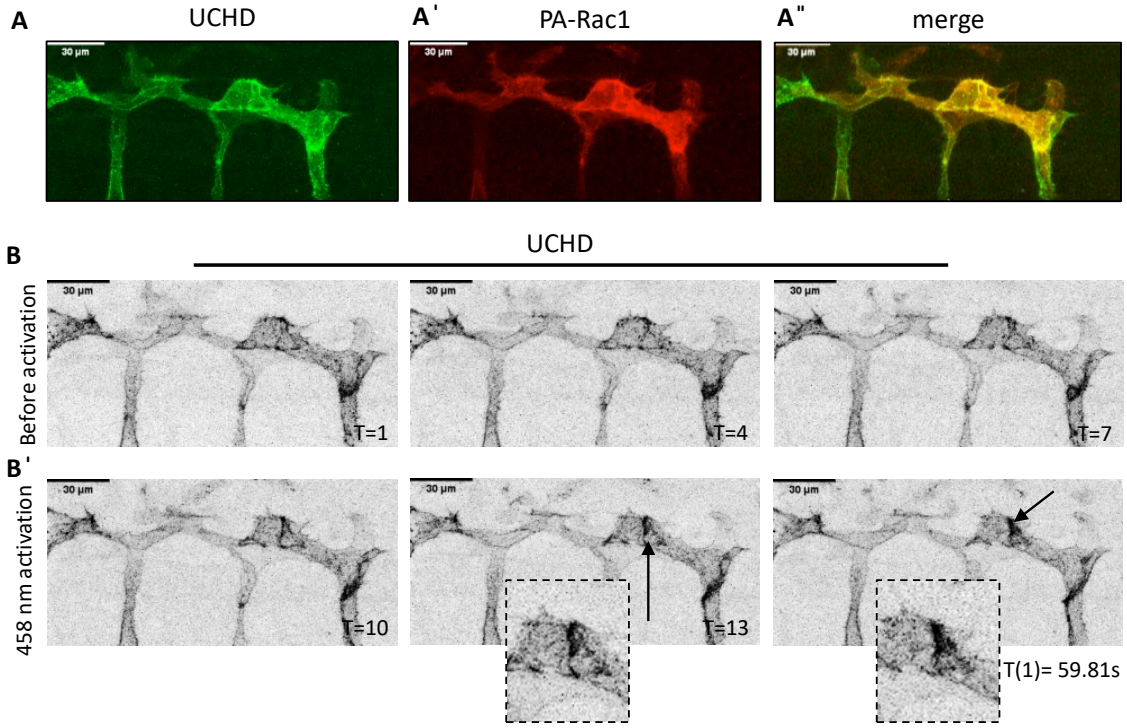

Figure 32: Temporal activation of PA-Rac1 led to the recruitment of actin to the junctions. For this experiment two individual founder fish were crossed. **A-A"** live still images of the vasculature expressing both iRFP-UCHD (**A**) and mCherry-PA-Rac1 (**A"**) at around 50 hpf. Merge is shown in **A"**. **B** and **B'** show still images from movies of the region as shown in **A**. Time-lapse imaging was only performed in the iRFP-UCHD channel. Three different time points are shown for the un-activated state (**B**, before activation) as well as for the activated state (**B'**); PA-Rac1 activation with 20 % 458 nm in the whole image). Inversed contrast. Temporal activation of Rac1 led to accumulation of actin at the cell-cell junction, confirming previous results (Figure 30). Arrow in **B'** (at T=13) points towards actin accumulation at the cell junction. Magnifications are shown as well. Scale bars 20 µm. One time point is equal 59.81 s.

It should be kept in mind that these experiments were performed at rather late stages during vascular development (50 hpf), when compared to the majority of the other experiments presented in this thesis (32 hpf). At 50 hpf, the DLAV is already fully established and carries blood flow, whereas at 32 hpf, during anastomosis, prominent cell rearrangements take place. Whether Rac1 activation has a different effect on cell behavior at earlier time points will be very interesting to test. In general, analyzing the effects of Rac1 at earlier stages during vascular development will give important insights into differential effects of Rac1 activation during cell rearrangement processes. Whereas at 50 hpf recruitment of F-actin might serve to stabilize the mature junctions, activation of Rac1 might lead to a different phenotype at earlier stages. Presumably, Rac1 might rather act at the leading edge in migratory cells and its activation might result in enhanced protrusive activity (and F-actin assembly).

Analysis of JBL dynamics in the dorsal aorta

JBL were identified and characterized in the DLAV during cell rearrangement processes. Whether this behavior is restricted to the process of anastomosis or might possibly be a general mechanism that cells use for cell shape changes/rearrangements or migration, has not been analyzed in much detail. However, analyzing F-actin intensity fluctuations at 50 hpf in the DA showed that local forward movements correlated with higher intensity of UCHD. This indicates that F-actin protrusions also are present in the DA and mechanistically contribute to behaviors linked to cell migration (Paatero et al., 2018). Analysis in this study identified double junction formation as an important hallmark of JBL formation. Specific protein localization in conjunction with a functional and contractile F-actin network provide the basis for cell rearrangements. Therefore, I wanted to analyze whether the observed cell protrusions during later development of the vasculature are similar or equivalent to the JBL observed during anastomosis. Therefore, I first checked for the presence of double junctions, since they appear to be a salient feature of JBL.

Double junction formation in the dorsal aorta

I imaged embryos transgenically expressing EGFP-ZO1 starting around 50 hpf in the DA and mainly focused on the formation of double junctions along cell-cell interfaces.

Indeed, I did observe this specific transient structure (compare Figure 33). They seemed to last much longer and were observed consecutively during 10-13 min (A ') (3 independent examples observed). The overall frequency was not quantified. This observation supports the hypothesis, that JBL are of more general nature, and employed in different tissue context throughout the vasculature.

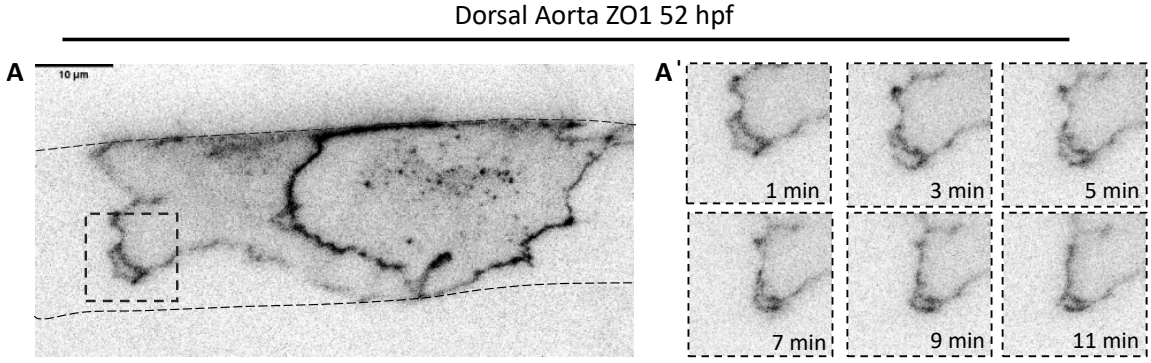

Figure 33: ZO1 double junctions in the dorsal aorta at 52 hpf. A. Still images from a movie of a cell in the dorsal aorta expressing Tg(fli:Gal4ff^{ubs3};UAS:EGFP-hZO1^{ubs5}) at around 52 hpf shown in inversed contrast. Dashed lines mark the outline of the DA. Magnifications of the inset in **A** are shown in **A'** at 6 different time points. Double junctions can be also observed at cell-cell junctions in the dorsal aorta. ZO1 accumulates in two distinct outlines. Scale bar 10 µm.

Since cells in the dorsal aorta are embedded in a very different cellular context, I was wondering what cell behaviors might be influenced by JBL in the DA. For this purpose, I imaged the dorsal aorta (EGFP-UCHD) during three different time points (26 hpf, 50 hpf, and 74 hpf) in embryonic development and vascular maturation. Hereby I focused on changes in the cell architecture and on F-actin dynamics at the cell junctions (Figure 34).

Cell shape changes and F-actin dynamics during maturation of the dorsal aorta

At 26 hpf (Figure 34 A) the cells in the DA show very dynamic behavior. Even during a 60 min imaging period, dynamic junctional behavior accompanied by very prominent cell shaped changes can be observed. Along the junctions themselves, F-actin intensity is fluctuating massively, indicative for a very high F-actin turnover and local protrusion formation.

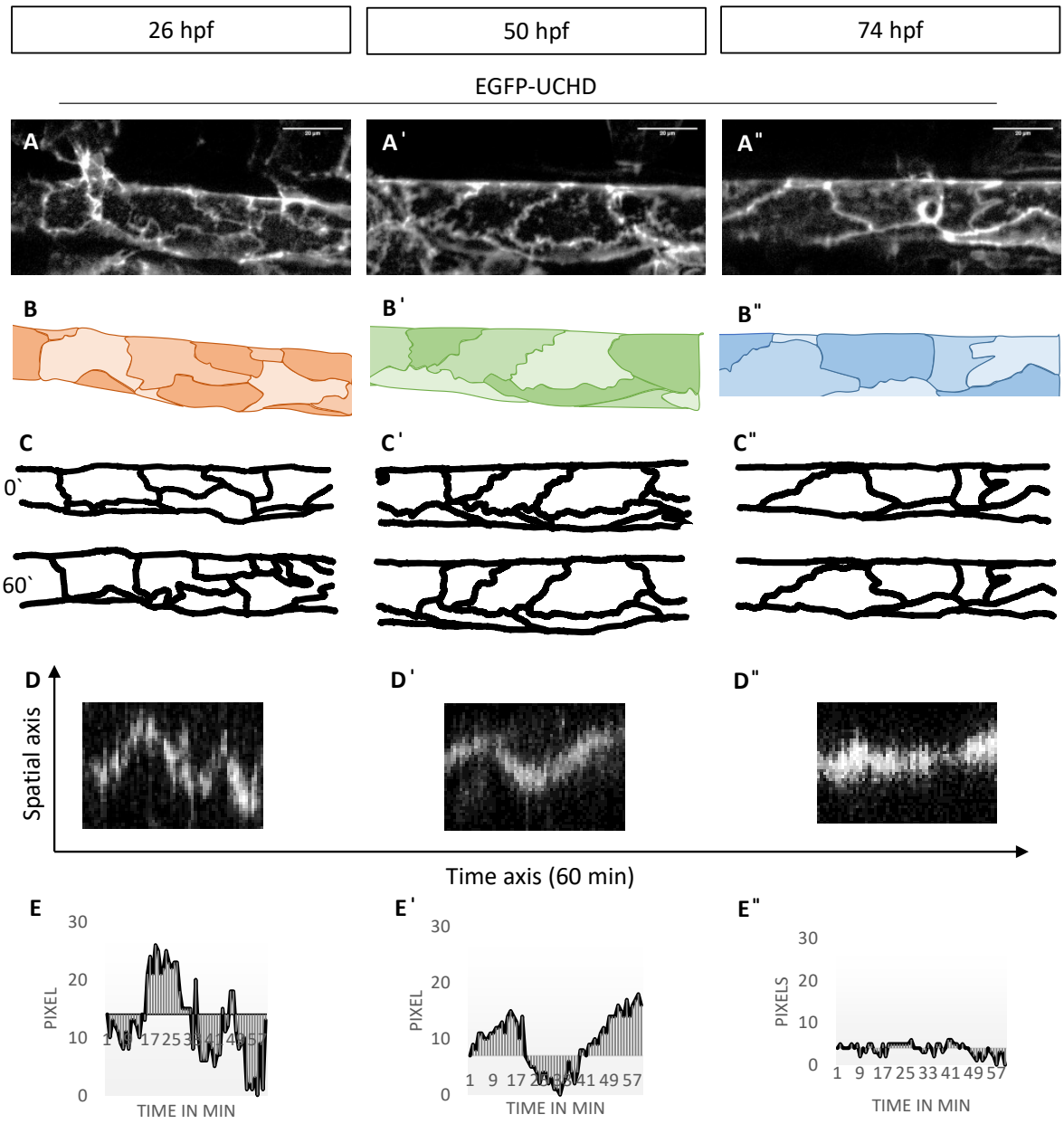

Figure 34: Cell shape changes and actin dynamics in the dorsal aorta during vascular maturation. **A-A"**. Still images from movies of embryos expressing Tg(fli:Gal4ff^{ubs3},UAS:EGFP-UCHD^{ubs18}) in the dorsal aorta at 26 hpf (**A**), 50 hpf (**A'**) and 74 hpf (**A**") shown in grey scale. Scale bar 20 µm. **B-B".** Schematic representation of cell shaped based on the image displayed in **A-A"**. Note the change of cell shape during time of development. **C-C".** Shell shape changes during an imaging period of 60 minutes. Schemes are drawn based on movies at imaging start 0 minutes and 60 minutes later. At 26 hpf, cell shape changes can be observed within shortest time, whereas among more mature cells the architecture is mostly maintained. **D-D**" Kymographs across the junction during an imaging period of 60 minutes (X-axis). Representative examples picked. **E-E**" Plots of the kymographs in **D-D"** based on a custom written Matlab algorithm.

Cell shape changes occur in very short time and can be observed remarkably already 60 min after imaging start (Figure 34 C). 24 hours later, at 50 hpf (34 A'), endothelial cell shape in the DA became much more stable, as reflected by less junctional movement. Although F-actin was still recruited to the junctions (local intensity changes) and protrusions were still formed, these activities did not translate into prominent cell architectural changes. The cell contacts remained almost stable and F-actin dynamics was only be observed very locally. During 60 minutes, cell shape changes are minimal (34 C'). At 74 hpf (34 A''), the cells seemed to become almost entirely quiescent. The junctional F-actin turnover was almost abolished (no intensity peaks). Furthermore, there was no protrusive activity. This is reflected in the very stable and rigid architecture/network. Changes in junctional dynamics over time, were also well reflected in kymographs. Kymographs draw a graphical representation of a certain point of the junction over time (here 60 min, C''). The actual kymograph is presented in D-D'', whereas a graphical representation is plotted in E-E''. The kymograph at 26 hpf shows a clear movement of junction (E), which gets reduced over time. By 74 hpf (D''), the kymograph is almost a flat line, meaning that the followed point at the junction did not change its position.

In summary, these observations pointed towards a potential role of JBL/local F-actin protrusions during the maturation process and concomitant morphological changes. They might be of importance for corrects alignment of endothelial cells, potentially in response to shear stress. Further studies will be needed to support this hypothesis.

<u>Junctional integrity and dynamics are altered upon interfering with F-actin branching, protrusion formation and actomyosin contractility.</u>

Because I was able to confirm the presence of JBL in the DA and furthermore observed F-actin based JBL dynamics in the young DLAV (32 hpf), I was wondering whether interference with regulators of F-actin also impact on junctional F-actin dynamics in the dorsal aorta (a fully lumenized vessel). Similar to the experiments performed in the DLAV, ROCK, Arp2/3 and Rac1 were inhibited and F-actin dynamics was analyzed (Figure 35).

F-actin based junctions in ROCK inhibited embryos (Figure 35 A) appeared as linear and continuous structures. F-actin dynamics (reflected in intensity changes) seemed to be reduced compared to the wildtype vasculature, indicating a reduced F-actin dynamic. However, this was not quantified and observations were purely made visually by video analysis of the time-lapse series. Interestingly, I did observe locally formation of F-actin accumulations and protrusions (see 35 A'). Although inhibition of ROCK did not seem to affect junction stability per se, F-actin turnover seemed to be decreased, pointing towards a defect in recruitment of new F-actin, which in turn initiates JBL formation at the junctions. Inhibition of Arp2/3 led to a more pronounced phenotype (B and B'). The junctions were interrupted and F-actin localization at the junctions was less defined ("fuzzy" appearance and gap formation). This suggests that inhibition of Arp2/3 reduces F-actin assembly at junctions and is in line with findings obtained during anastomosis. Furthermore, it points toward the necessity of branched F-actin networks to stabilize junctions and to maintain endothelial barrier integrity. Moreover, the cells appear to be stacked one behind the other, potentially pointing towards impaired cell rearrangements. Disruption of junctions was also observed when inhibiting Rac1 (Figure 25 C and C'), an upstream activator of Arp2/3; however, the effect was not as dramatic as when Arp2/3 was inhibited. Additionally, junctions also appeared less "defined". Interestingly, I observed the formation of very prominent F-actin protrusions that resemble filopodia (C'). Generally, it seemed that junctions are more dynamic leading to subtle but yet visible cell shape changes. The latter observation is rather unexpected, and enhanced dynamics might be explained by increased filopodia formation. That in turn might be translated into increased junctional movement which lead to cell shape changes. Junctional movement and cell shape changes over 60 minutes are schematically represented in A"-C". In general, the cellular architecture upon ROCK and Arp2/3 inhibition appeared to be quite constant and unchanged over time, whereas in Rac1 inhibited embryos a small change of cell shape was detectable.

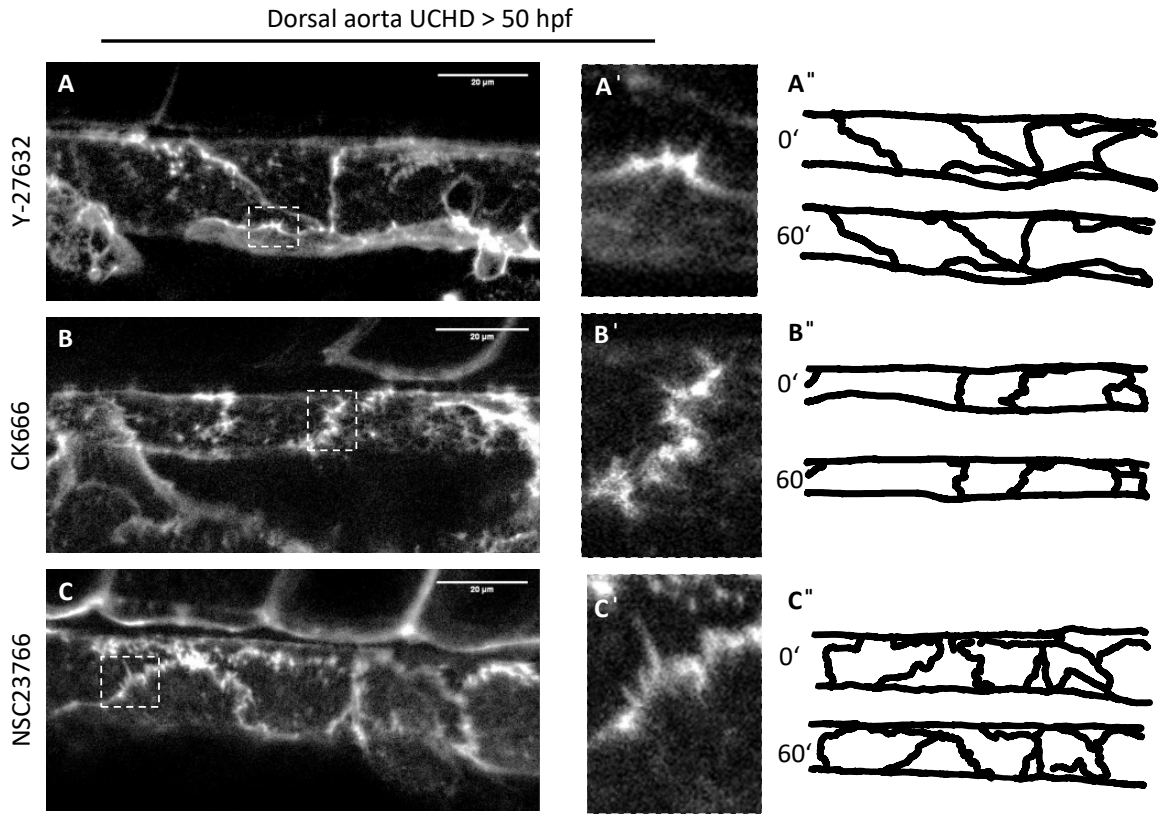

Figure 35: Actin dynamics in the dorsal aorta upon interfering with the F-actin network. A-C. Still images from movies of embryos expressing Tg(fli:Gal4ff^{ubs3},UAS:EGFP-UCHD^{ubs18}) in the dorsal aorta treated with Y-27632 (**A**), CK666 (**B**) or NSC23766 (**C**) shown in grey scale. Scale bar 20 µm. **A'-C'** Magnifications of inserts in **A-C**. Prominent UCHD accumulation and long actin protrusions can be observed (**A'** and **C'**), resembling filopodia. Furthermore, junctions appear to be discontinuous (**B'** and **C'**) and disrupted after Arp2/3 or Rac1 inhibition. Junctional integrity was maintained in embryos where ROCK was inhibited (**A)**. Endothelial cell shape after Inhibition of ROCK (**A"**) and Arp2/3 (**B"**) did not change in a 60 min imaging interval, whereas Rac1 inhibition (**C"**) lead to increased morphogenetic changes. Observations were made based on movies.

In summary, the experiments provide evidence to support the hypothesize that JBL are required for morphogenetic cell shape changes during vascular development. JBL function and junctional integrity rely on and can only be maintained when the F-actin network is fully functional. Further experiments need to done in order to get a full picture e.g. analyzing the dynamics of F-actin and junctional components in parallel.

IV.

Discussion

4. Discussion

Organ morphogenesis relies on dynamic cell behaviors, which are tightly coordinated to ensure a functional cellular organ architecture. The vasculature represents one of the most ramified organs in vertebrates and captivates due to its enormous plasticity, which is crucial for the organism to respond to different contextual cues e.g. responses to inflammation or would healing. Organ plasticity on cellular level requires a repertoire of dynamic cell behaviors, which include cell migration, proliferation, cell shape changes and cell rearrangements during formation of new blood vessels. Here, a dynamic balance between inter-endothelial cell adhesion and plasticity allows angiogenic sprouting while maintaining the endothelial seal. In order to get an insight into the physical and molecular dynamics underlying cell rearrangements and dynamic cell shape changes, I have analyzed so-called junction based lamellipodia (JBL), that were recently identified (Paatero et al., 2018). JBL were found to be employed by endothelial cells for movement and rearrangement behavior and appear to function via a VE-cadherin/F-actin driven ratchet mechanism. During the work of my thesis, I focused in particular on the cytoskeletal F-actin dynamics, its regulation and consequences of changes in F-actin dynamics on JBL formation and function.

As discussed below, my work has led me to a better understanding of F-actin dynamics, which can be used to refine the existing working model of JBL oscillations.

Proposed oscillatory mechanism of JBL

One cycle of JBL during the elongation of endothelial cell junctions can be schematically subdivided into four steps. In a first step, an F-actin protrusion emanates distally from a stable junction, representing sites of F-actin polymerization. Inhibition of F-actin polymerization by latrunculin (but not Rac1) drastically reduced the appearance of JBL, supporting a key role for actin polymerization. However, inhibition of Rac1 did interfere with the oscillation time (longer oscillation cycle). Furthermore, protrusion formation and correct localization of F-actin at the sites of JBL relies on Arp2/3 and its activity as F-actin nucleation factor and generator of branched F-actin networks.

F-actin based membrane protrusions lead to the recruitment of the junctional protein VE-cadherin in diffuse manner (step 2). Next (step 3), the adaptor protein ZO1 is recruited to the sites of newly established VE-cadherin junctions, thereby stabilizing them. At this point, a very distinct localization of ZO1 in two lines can be observed. We call this transient structure “double junctions”. Double junction formation was impaired upon ROCK inhibition, indicative for the necessity of actomyosin contractility for correct localization of junctional proteins. Additionally, maintaining the double junctions, but not the initial formation required the presence Arp2/3. In a last step (step 4), it is hypothesized that the two junctions are eventually pulled towards each other, generating the motile force which is necessary for junction elongation. This force that is needed for the junction conversion seemed to be mediated by actomyosin contractility and this could be supported by the finding, that the myosin regulatory light chain specifically localizes at the sites of the JBL. Changes in actomyosin contractility were also reflected in differential VE-cadherin tension. The latter was shown to be dependent on ROCK as well.

Actin driven membrane protrusions: JBL vs. JAIL

Recently, oscillatory protrusions have been described also *in vitro* in HUVECs. Abu Taha et al., 2014 identified highly dynamic and spatiotemporally confined actin-driven structures, that they call junction-associated intermittent lamellipodia (JAIL). JAIL also lead to the formation of new VE-cadherin sites and during their oscillation cycle distinct steps can be identified. JAIL (*in vitro*) and JBL (*in vivo*) both were postulated to contribute to cell migration; however, besides their structural and behavioral similarities, it is necessary to look at them closely to compare them.

A prerequisite for JAIL to form is a local decrease of VE-cadherin density/concentration, whereas the actin-driven membrane protrusions in JBL emanate from a stable junction at the pole oriented in the direction of cell movement. In both scenarios, the establishment of protrusion is Arp2/3-dependent and VE-cadherin protein is diffusely localized in this area. However, during JAIL formation, VE -cadherin forms cluster at the respective end of the protrusion, which leads to the formation of a new junction. The basis of the lamellipodia is not supported by a junction. During the JBL oscillatory cycle, a new junction is established as well (marked by the presence of VE-cadherin and ZO1).

However, the new junction is formed, while the "old" one is still maintained- leading to the characteristic intermediate state of double junction formation. These two junctions are hypothesized to be pulled towards each other, whereas during JAIL formation, the junction rather "dissolves". Conceptually, maintenance of junctional integrity during JBL formation might be an important factor to ensure proper vascular sealing and to prevent hemorrhages. Therefore, although the appearance of actin-driven membrane protrusions as described *in vitro* and *in vivo* might share similar properties, they potentially play different biological roles, which is reflected in their different structural appearance. The two mentioned concepts are contrasted in Figure 36.

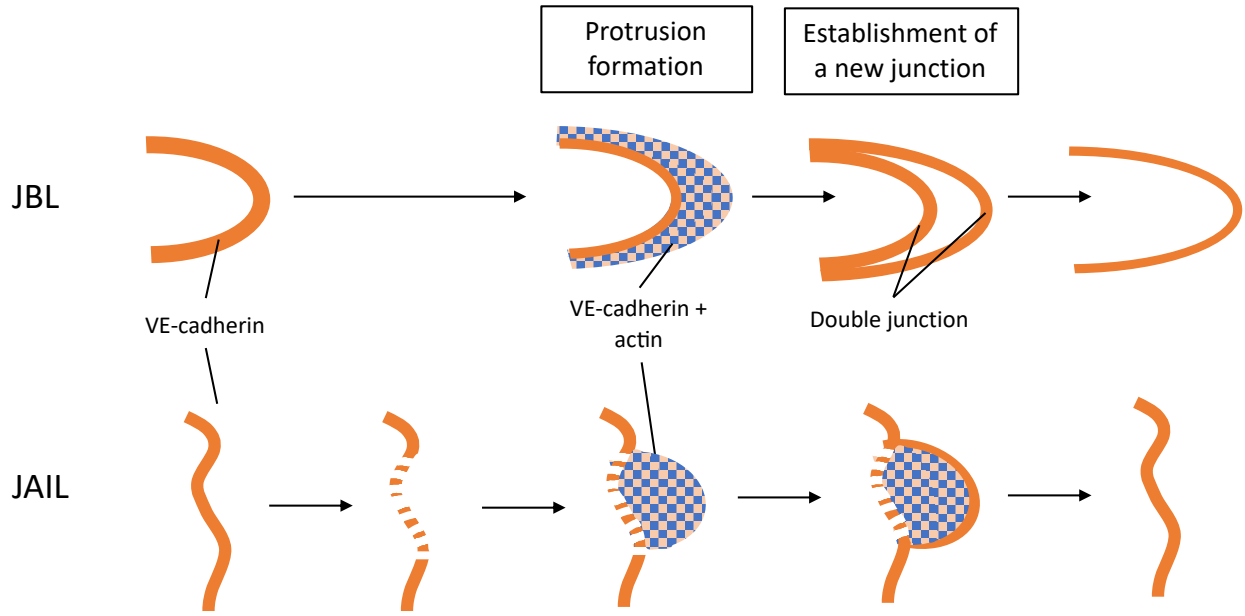

Figure 36: Formation of JAIL vs JBL. During one JBL oscillation cycle (top row), an F-actin-based protrusion emanates from a stable junction. Subsequently a new distal junction is formed, leading to double junction formation as an intermediate step. In a last step, the two junctions are eventually pulled towards each other. Bottom row: JAIL (junction-associated intermittent lamellipodia) have originally been described in HUVECs, where they form under subconfluent conditions (Abu Taha et al., 2014). JAIL formation is preceded by the local decrease of VE-cadherin density at the junctions and following the protrusions are formed. New VE-cadherin clusters form at the front of lamellipodia, giving rise to a stable junction. VE-cadherin is indicated in orange. Protrusions contain F-actin (blue) and VE-cadherin.

Last but not least, JAIL formation was discovered in subconfluent HUVECs cultures, where they are required to maintain the integrity of a monolayer. The model system in which I investigated JBL formation and regulation is very different. Anastomosis in the zebrafish DLAV is a two-cell mechanism, and therefore allows analyses at single (or two) cell level, rather than statements based on a multicellular system. Findings obtained in multicellular systems regarding junctional remodeling and cell shape changes conceptually might underlie very different morphogenetic and physical principles, which will be discussed in the following section.

Junctional ring elongation and cell rearrangements require a deforming force

Previous work has identified JBL as a central means of endothelial cells to drive cell movements as well as cell rearrangements during the process of anastomosis. Cell rearrangements and movements are reflected in extensive junctional remodeling, ultimately changing the vessel architecture from a unicellular to a multicellular tube (Lenard et al., 2013; Paatero et al., 2018).

Generally, how local cell shape changes and regulation of cell-cell contacts are drivers for tissue-level deformations such as elongation has been addressed in several studies throughout the last decades (reviewed among others in Heisenberg and Bellaïche, 2013; Lecuit et al., 2011). It is known that intercellular adhesion enables extensive remodeling and that these rely on the generation of traction forces by the actomyosin cytoskeleton transmitted onto the cell cortex. Morphogenetic processes such as convergence extension movements in drosophila tissue elongation or tissue invaginations due to apical constriction illustrate how the polarized regulation of force generation and transmission leads to changes in tissue shape. In this specific cellular context, cells are mechanically coupled and e.g. local contractility generated in a single cell coordinates and influences behavior of the neighboring cell, up to tissue level effects (Martin et al., 2010). This ultimately raised the questions of what drives cell elongation and rearrangements during anastomosis in the DLAV (as investigated in this study). It is important to mention that this process relies on the interaction of two single neighboring cells.

The analyzed junction is of isolated nature and not influenced by several surrounding cells, as this is the case for multicellular systems (compare Figure 37). In consequence, no outside forces from surrounding cells are expected.

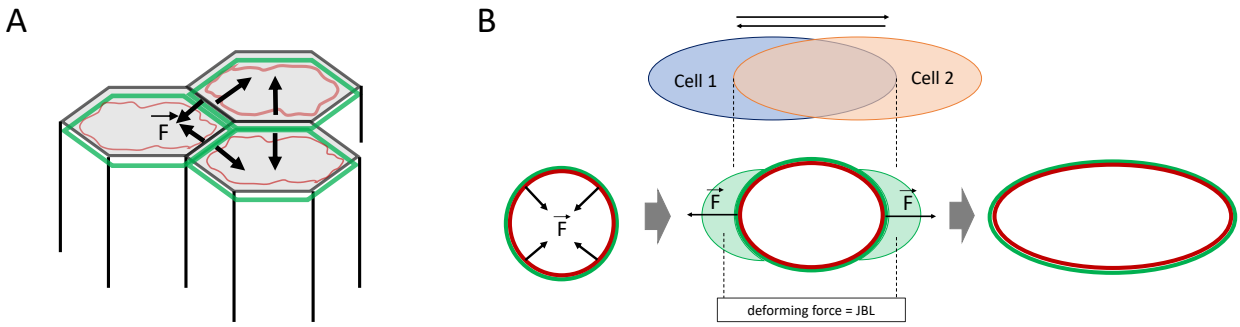

Figure 37: JBL as driving force for junctional elongation of an isolated ring-shaped junction. A. In a multicellular system, a single cell is surrounded by several neighbors, with which they establish junctions. A potential force tugging on the cell junctions has effects on the whole tissue, as they are all coupled to each other (indicated as arrows). **B.** During anastomosis in the DLAV, only two cells contribute to the process of ring elongation. The junction is isolated. Since no outside force can be generated, it is postulated that JBL provide the force needed for the round to elliptic shape conversion. Green= adherens junctions. Red= actomyosin ring.

If no force can be generated within a complex multicellular environment by secondary junctions in the surrounding, what exactly drives this junctional elongation? Based on these reflections we therefore postulated that in such a two-cell configuration with an isolated junction, a deforming force is required driving the round to elliptic shape conversion of the junction. This force in our case originates from the JBL and these are considered to be the active motor.

<u>JBL as local motile force generator during junctional ring elongation</u>

Postulating a local force originating from JBL has led me to investigate the role of actomyosin contractility in this cell rearrangement process. At that time, there was no data on non-muscular myosin II in the context of JBL. Therefore, I analyzed the localization of myosin regulatory light chain (MLC) in the junctional ring. Indeed, analysis of MLC in conjunction with the junctional markers ZO1 and VE-cadherin showed that MLC is specifically associated with EC junctions.

Not only did MLC localize to cell-cell junctions, I also found that it specifically localized to the JBL themselves. The exact localization of MLC seemed to be dependent on the timepoint during an oscillation cycle. I could distinguish several patterns, ranging from an enrichment in VE-cadherin/ZO1 low areas (where one expects F-actin protrusions) to a perfect colocalization with the distal junction (high ZO1 and VE-cadherin staining). Mosaicism in the expression of the transgenic line (kdrl:Myl9-EGFP) allowed me to further distinguish between the protein localization in the "donor" (migrating) and "receiving cell". In a Myl9 positive cell, MLC specifically accumulated at the migration front in the donor cell, whereas no enhance signal could be observed at the respective "back". This is illustrated in Figure 38. These findings supported the hypothesis that 1) actomyosin contractility could be involved in local force generation and 2) that this local contractility could be specifically restricted to the leading edge of the migratory cell. The latter might serve to drive the process of junction conversion, where the proximal and the distal junction are pulled towards each other.

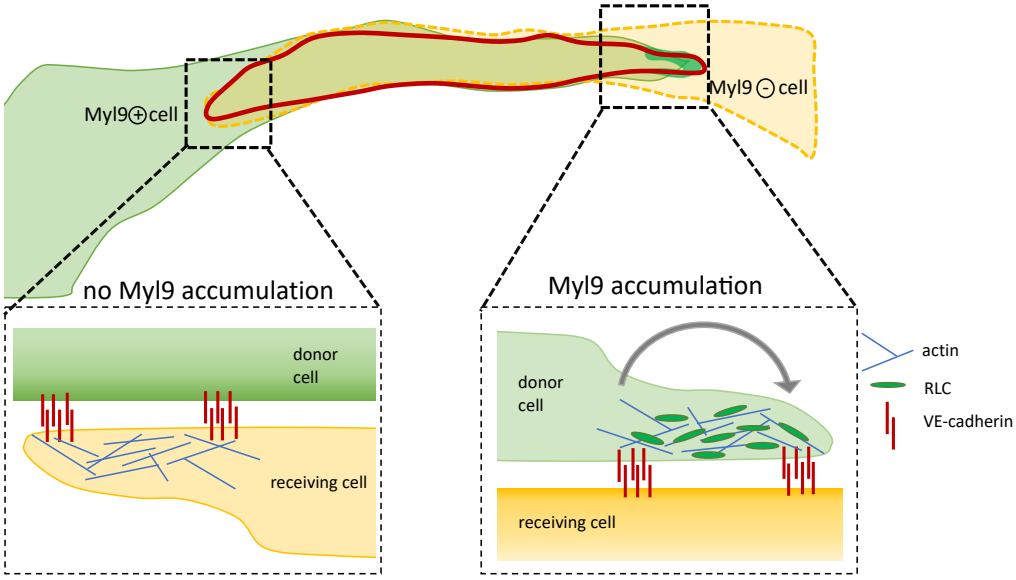

Figure 38: Mosaic expression of Myl9-EGFP on two tip cells during anastomosis (DLAV formation). Localization of myosin regulatory light chain (MLC) in the JBL. The cell in green is Myl9-EGFP positive, whereas the cell in yellow is negative. The two cells form a ring-shaped junction, in which Myl9 is accumulated at the site of the right JBL, but not at the left respectively. This indicates, that Myl9 accumulates or is recruited specifically in the "donor cell" at the site of the lamellipodia. It is postulated that Myl9 serves to pull the double junctions together, resulting in a forward movement of the cells.

The importance of the actomyosin network was further supported by evidence coming from experiments done with a ROCK inhibitor (Y-27632). Inhibiting ROCK in the experiment conducted during my study has shown that junctional rearrangements are impaired upon actomyosin contractility, manifesting in reduced junctional elongation speed. Since several evidences pointed to an importance of a of local force generation in order for JBL to function properly, I was wondering how or whether these forces are transmitted onto endothelial junctions. It was shown that polarization of forces require the presence of cadherin-based junctions (Mertz et al., 2013; Tambe et al., 2011), and that VE-cadherin tension is dependent on actomyosin contractility (observed among others in Borghi et al., 2012; Conway et al., 2013). This led me to investigate tension across VE-cadherin molecules during the process of anastomosis using the VE-cadherin tension-sensor line.

VE-cadherin tension in JBL

Using the VE-cadherin tension sensor line, I aimed for answering several questions that should have helped to understand the mechanical changes occurring during EC rearrangements: How is VE-cadherin tension in the junctional ring distributed? Does tension change over time during junction elongation? Do changes in VE-cadherin tension correlate with JBL oscillations?

I postulated that tension within the junctional ring is not evenly distributed, and that there is a difference in tension between the JBL and the medial cell part (1). Secondly, I hypothesized that VE-cadherin tension changes over time coherent with the JBL oscillatory behavior (2) and that thirdly there might be spatial differences of VE-cadherin tension within a single JBL (3).

I was assuming that VE-cadherin tension in the medial part of the junctions is evenly distributed and very homogenous. Instead, there might be local and temporal tension changes in the JBL, specifically where a local force is generated. However, analyzing tension within VE-cadherin molecules via determination of FRET-values did not show significant mean differences in JBL versus other junctional parts. Nevertheless, I noticed that values for JBL showed a greater spread, possibly representing the dynamic nature of JBL, and that the obtained values possibly strongly depend on the state of oscillation.

Based on this, and to prove or disprove my second and third hypothesis, I aimed for determining FRET values at consecutive time points to observe temporal changes of VE-cadherin tension. Furthermore, and ideally, FRET measurements would have provided the basis to obtain a topographical map of VE-cadherin tension in a JBL. Unfortunately, both of the mentioned approaches were not feasible due to technical limitations that will be discussed in the course of this discussion. Nevertheless, I will discuss expectations or potential outcomes in relation to a single JBL cycle (Figure 40).

Differential spatial and temporal VE-cadherin tension during a JBL cycle

The fact that VE-cadherin tension could reflect different intra and intercellular processes makes it intrinsically difficult to predict temporal and spatial changes and fluctuations in VE-cadherin molecules. Differences in ratio-metric FRET values could result from 1) differences in the adhesive strength between two VE-cadherin molecules upon homophilic interaction, where the actomyosin cytoskeleton can pull from two sites, or 2) reflect differences in actomyosin contractility from one cell (rather than from both cells). This would mean that e.g. tension could build up as result of an increase in 1) adhesive strength or a 2) high actomyosin contractility, pulling on the junctions (see Figure 39). These two scenarios cannot be distinguished by determining intermolecular FRET values.

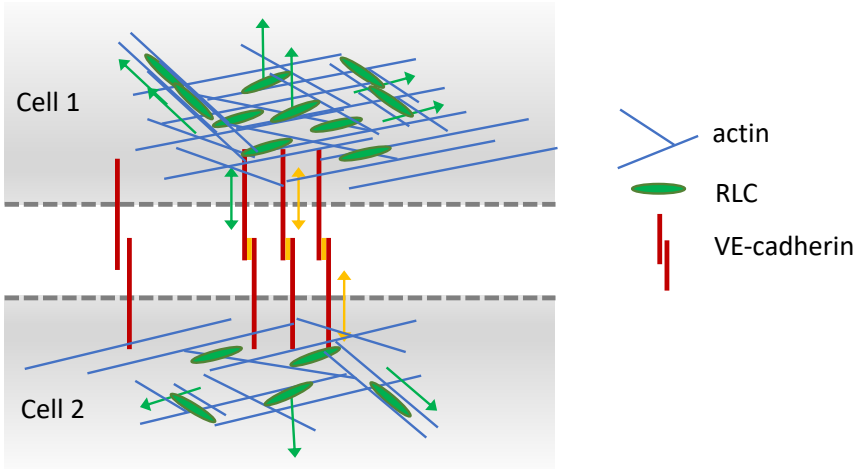

Figure 39: Determination of intramolecular FRET values as proxy for VE-cadherin tension.
Tension in the VE-cadherin molecular can arise from the actomyosin cytoskeleton pulling from one site of the cell (green arrow), or due to homophilic interaction and formation of adhesive bond (indicated in yellow).

How VE-cadherin tension in the JBL changes temporally and spatially remains very speculative. There are of course several possible scenarios how VE-cadherin tension might change, and I will propose only one possibility (Figure 40). I base my hypothetical model on the findings that VE-cadherin tension decreases during the maturation process of junctions in endothelial cells (Lagendijk et al., 2017) and that tension is released at mature adherens junctions in confluent endothelial cells (Daneshjou et al., 2015). Therefore, I indicated VE-cadherin tension as "medium" in the junction, where the JBL emanates from. Tension changes in the model have to be considered relative to this.

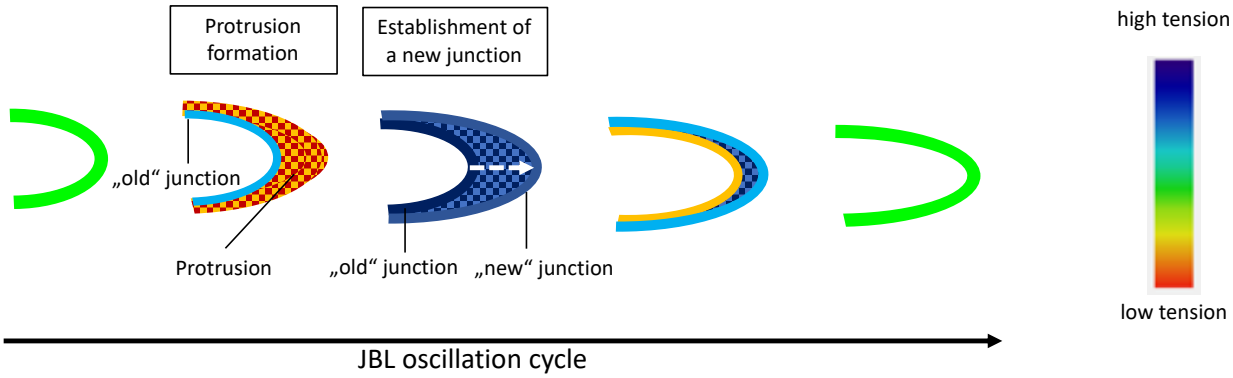

Figure 40: Hypothetical spatial and temporal distribution of VE-cadherin tension during one JBL cycle. From a stable junction (medium tension in green), a F-actin based membrane protrusion arises, also containing VE-cadherin (low tension). The forming protrusion pulls on the junction it emanates from, thereby temporally increasing its tension (blue). Subsequently, a new junction (high tension) is formed at the front of the protrusion and matures over time (shift from blue to green). At the same time, the old junction starts to decrease tension, indicative for a reduction of adhesive strength while the two junctions are pulled towards each other. The latter is achieved by actomyosin-generated contractility in the JBL, which is represented as tension change from rather low (red-yellow) to high (blue) in the protrusion itself.

Initially, a new protrusion is formed at the site of a stable VE-cadherin based junction (medium tension). The protrusion also contains diffuse VE-cadherin deposits, thought to be of rather low tension, as no homophilic interactions might be established yet. However, the emerging protrusion might pull on the junction, leading to a temporally limited increase in tension (blue). Subsequently, a new distal junction is formed. Since the VE-cadherin contact sites are still nascent adhesions, VE-cadherin tension might be relatively high.

As the cycle progresses, the distal junction matures, which is reflected in a decrease of tension over time (blue to green), whereas the old junction decreases tension as it "disappears". Dependent on the actomyosin cytoskeleton, the two junctions are eventually pulled towards each other, which would be reflected in very high VE-cadherin tension in the protrusion zone (blue area), as the actomyosin possible pulls on the junctions while generating contractility. Finally, once the two junctions are being merged, tension reaches again a high level similar to the first step, before the new cycle of protrusion formation starts.

That a certain force is generated during the formation of membrane protrusions was shown in Cai et al., 2014. The authors investigated collective cell migration behavior of so-called border cells in drosophila ovaries. Firstly, they propose that the formation of a F-actin based protrusion pushing the membrane outward gives rise to a membrane tension that ultimately generates tension within VE-cadherin molecules.
Similarly, Ji et al., 2008 spatially and temporally link filament assembly to forces across adhesions in epithelial cells. In context of specific localization of high vs low VE-cadherin tension areas, Cai et al., 2014 observed differences in tension in the front versus the back of the border cell clusters, independently from the number of E-cadherin molecules (homogenous distribution). Tension was higher at the front suggesting that cells actively disassemble (from each other, or disassemble forces) at the back. They argue that differences in FRET values possibly reflect differences in the strength of adhesive bonds or actomyosin contractility between front and back. Interestingly, high tension in the front correlated with high Rac activitiy.

Influence of actomyosin contractility on VE-cadherin tension

In order to investigate whether VE-cadherin tension might be dependent on actomyosin contractility (as proposed in Cai et al., 2014), I used an inhibitor for ROCK and analyzed VE-cadherin tension in the JBL. FRET values in the JBL showed a high spread around the mean value, which significantly decreased upon inhibition of ROCK. This finding points towards an important role of the cellular force-generating machinery in the establishment of differential tension among VE-cadherin.

ROCK inhibition blocks actomyosin contractility, thereby abolishing a potential tugging force in VE-cadherin molecules, leading to VE-cadherin tension returning to a baseline level (as indicated by FRET values, represented by the mean).

These findings and evidence of spatial differences in VE-cadherin tension highlight the importance to investigate spatial patters in JBL in the future. It will be of great importance to map VE-cadherin tension on a JBL during different timepoints of the oscillation cycle, to fully elucidate the mechanism by which they generate and transmit forces. However, to the present days, experimental approaches are limited by technical restrictions, that need to be carefully considered.

Technical limitations using FRET imaging

From a technical point of view, several aspects have to be considered when using FRET-based biosensors and the ratio-metric method for FRET determination. This method is intensity-based, since for FRET index calculation, the ratio of the donor and acceptor is determined. Intensity related issued were the main limitations in my experimental setup. Intensity of the fluorophores can vary due to several aspects such as laser fluctuations, microscopy settings, penetration depth of the tissue and, most importantly for *in vivo* experiments, the biological heterogeneity of expression levels among zebrafish embryos (Eder et al., 2017). Microscope settings (e.g. laser intensities) are adjusted in each imaging setting based on control embryos expressing only the acceptor or donor, respectively. These settings remained constant throughout the entire imaging session and were identical for each sample. Variation in expression levels of the transgene often resulted in over-/underexposure, leading to a dropout of several images after post acquisition *in silico* processing. As a result, comparably low sample size decreased the significance of the obtained results; higher sample size would have been required to get a broader picture of JBL (especially since they are of such highly dynamic nature). Too low intensity levels of the fluorophores were never encountered in the dorsal aorta, increasing both quantity and quality of the obtained data from this vessel. For acquisition of still images, this problem could be overcome manifold. As JBL are proposed to be a general mechanism at work in endothelial cells, switching to another vascular bed as model system might indeed be very useful.

On that account, similar analyses could be performed in the dorsal aorta or in the cranial vasculature (PLA), where the process of anastomosis has been extensively described (Lenard et al., 2013).

Another way would be facing the technical site. FLIM (Fluorescence life time measurements) is a quantitative imaging technique that is reported to be less sensitive to artifacts compared to FRET (Cost et al., 2015; Wallrabe and Periasamy, 2005). It is based on the determination of the life time of individual fluorophores rather than relying on their emission spectra. Additionally, it is more robust compared to intensity-based methods as it does not depend on factors such as bleaching or excitation intensity, sample thickness etc. (picoquant.com).

In summary, during JBL formation and cellular rearrangements, I observed that VE-cadherin molecules indeed exhibit actomyosin-dependent tension. In order to fully explore and describe the mechanism that underlie force transmission, time-lapse analysis and temporal distribution of VE-cadherin tension will be inevitable. These experiments in fact will be dependent on the improvement of technical equipment (faster imaging technique) or biological improvements of FRET-sensors *in vivo*.

Besides the importance of VE-cadherin for JBL function and junctional ring elongation, I investigated the junctional behavior based on other proteins functioning in cell adhesion, namely ZO1.

Transient appearance of ZO1- based double junctions during the JBL oscillatory cycle

One very prominent hallmark during the JBL oscillation cycle is the appearance of so-called double junctions. They were discovered as an intermediate step, in which both a proximal ("old") and distal ("new") junction are visible at the same time, just before they eventually merge with each other. I postulate that this very specific junctional localization reflects a very important step, in which the cell can reach out in the direction of movement, establish a *de novo* junction while maintaining the old one in order to guarantee junctional integrity and maintenance of the vascular seal. The formation of a new distal junctions is an important step, as it provides a new attachment site, which we hypothesize is indispensable for junctional ring elongation.

To study how these double junctions form and how they are regulated, was part of my thesis, which I will now further discuss in the context of three proteins ROCK, Arp2/3 and Rac1.

ROCK is important for the formation of the distal junction

Upon inhibition of ROCK, I observed significant reduction in junctional ring elongation speed, which shows that ROCK is needed for the rearrangement process. Furthermore, ROCK not only influences VE-cadherin tension (as explained before), it also alters localization of the protein ZO1 and therefore has an impact on double junction formation. Correct localization of ZO1 in two distinct lines was impaired and resulted in a rather loose accumulation of junctional material (a schematic drawing is shown in Figure 41). In most cases, it was not possible to establish correct double junctions and therefore a new distal junction, which provides the basis for successful ring elongation.

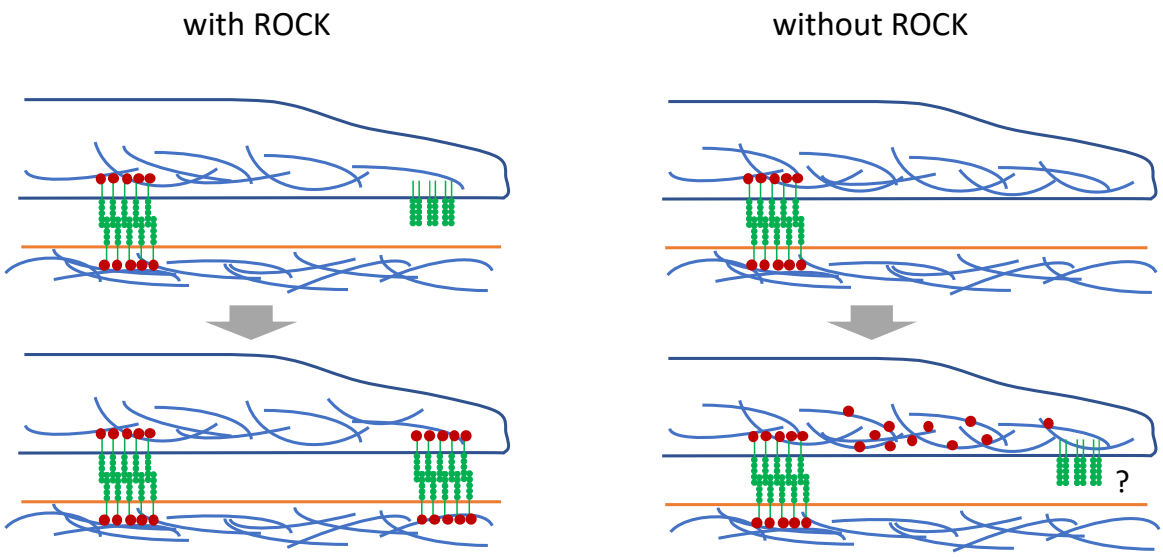

Figure 41: ROCK is indispensable for the formation of a distal junction. During a JBL cycle VE-cadherin gets deposited at the sites, where a new junction is formed at the front of the protrusion (left). Subsequently ZO1 is recruited to the VE-cadherin junction, stabilizing it. This leads to the characteristic intermediate step of double junction formation. Inhibition of ROCK interferes with recruitment of ZO1 to the new VE-cadherin attachment sites. This is represented as rather diffuse ZO1 localization distally from the "old" junction. Whether ROCK inhibition interferes with VE-cadherin localization is not clear. VE-cadherin in green, ZO1 in red. F-actin is represented in blue. Two cells (top in blue and lower one in orange) are shown.

This finding is in accordance with the literature, where a link between ZO1 localization and ROCK is provided. In Walsh et al., 2001 polarized intestinal epithelia were investigated and it was shown that ROCK colocalizes with ZO1 at the junctions and that inhibition is associated with the failure of tight junction molecule assembly. Furthermore, the authors concluded that targeting of TJ molecules to the membrane is altered due to the disorganization of apical F-actin, which ultimately results from ROCK inhibition.

Similarly, Tornavaca et al., 2015 showed that loss of ZO1 induces reorganization of the actomyosin cytoskeleton towards stress fiber formation and that junctional myosin II is reduced. Providing this connection, it is very likely that inhibiting ROCK also vice versa influences ZO1 localization (as reported in my case). Interestingly they provide a direct link between ZO1 and VE-cadherin tension. Depletion of ZO1 leads to increased FRET (decreased tension) using the VE-cadherin tension sensor, thereby identifying ZO1 as an essential regulator for maintenance of tensile forces on adherens junctions.

During the course of experiments, I could show that double junction formation is not only dependent on ROCK, and therefore on actomyosin contractility, but additionally requires a functional F-actin network. This will be elaborated in the following section.

Role of Arp2/3 in protrusion formation and maintenance of junctional integrity

Arp2/3 is a well know F-actin nucleation factor leading to the formation of branched F-actin networks, and is indispensable for protrusion/lamellipodia formation (Pollard, 2016; Pollard et al., 2000).

Consistent with this, JAIL formation in HUVECs was blocked upon inhibition of Arp2/3 and also Rac, where the GTP bound form binds to and activates Arp2/3 (Abu Taha et al., 2014). Furthermore, Arp2/3 is characteristically also recruited to sites of newly formed cadherin contacts, where contact zones were being extended (Verma et al., 2004).

When blocking Arp2/3 during the process of JBL formation and junctional ring elongation, I did not only observe defects in the F-actin dynamics but also on junctional protein level. I observed that JBL formation focusing on F-actin localization is impaired, stressing the importance for the formation of a branched F-actin network. Furthermore, I would like to mention that I observed the appearance of quite prominent, long, linear F-actin cables in the endothelial cell resembling stress fibers.

Inhibition of Arp2/3 and therefore reducing branched F-actin fibers might thus favor the formation of stress fibers, which possibly manifests throughout the cell. Besides, I could show that Arp2/3 interferes with junctional integrity using a transgenic EGFP-ZO1 line. As already mentioned, double junction formation during the JBL oscillation cycle is a very important intermediate step. Here, although a distal and proximal junction does form (albeit less frequent), the "new" junction often cannot be maintained and seems to "dissolve" over time (a scheme is presented in Figure 42).

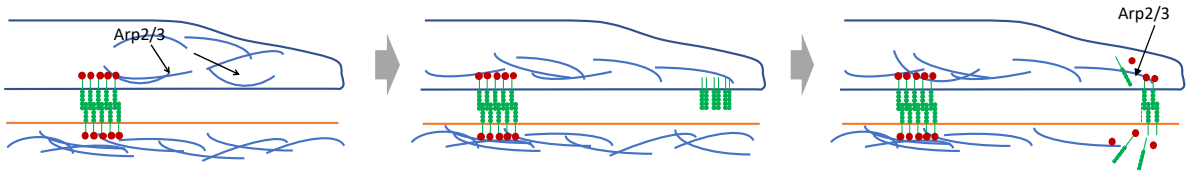

Figure 42: Arp2/3 is required for protrusion formation as well as stabilization of new junction (shown here). Arp2/3 is indispensable for formation of branched F-actin networks, which are crucial for lamellipodia formation. At later stages, a new VE-cadherin adhesion site is formed and ZO1 recruited. At this point, Arp2/3 is not necessary for the formation of the new junction itself, rather than maintenance. Inhibition of Arp2/3 led to destabilization of the distal junction (third image), which might be due to lack of F-actin support. Roles of Arp2/3 are only indicated in the upper cell. VE-cadherin in green, ZO1 in red. F-actin is represented in blue. Two cells (top in blue and lower one in orange) are shown.

These findings point towards a role of Arp2/3 in the stabilization of the newly formed junction; not being able to maintain and stabilize the newly formed junction at the distal end of the JBL ultimately has an impact on the forward movement of the cell.

Effects on adherens junction assembly upon Arp2/3 inhibition was also reported in Ivanov et al., 2005 and Verma et al., 2004. Arp2/3-mediated F-actin assembly is important for efficient cadherin contact formation, and blocking Arp2/3 reduced the ability of cells to extent cadherin adhesive contacts (Verma et al., 2004). Similarly, Ivanov et al., 2005 showed that assembly of cadherin junctions was prevented by blocking N-WASP (which activates Arp2/3). Based on these findings, it would be very interesting in the future to investigate the effects of Arp2/3 inhibition also on the level of VE-cadherin, and not only on ZO1.

In general, the formation of a branched F-actin network is not only indispensable for the initial protrusion formation, but also crucial in transmitting a stabilization effect at the junctional level. Additionally, it was proposed that F-actin assembly at the junctions is required for NMII recruitment (Verma et al., 2012). Therefore, I hypothesize that Arp2/3 inhibition indirectly also influences contractile properties and recruitment of NM to the junctions in the context of JBL.

The formation of a branched F- actin network might be needed for myosin II to adhere to and thereby provide the structural basis for generation of local contractility. In order to test this, the localization of MLC could be investigated using antibody staining, similarly to the experiment presented in Figure 23. In such a scenario, MLC would not be localized at site of JBL upon Arp2/3 inhibition. This is of particular interest as it would confirm the necessity of F-actin as basis for local force generation and highlight the importance of the actomyosin cytoskeleton in the process of junction elongation. Furthermore, it is indispensable to investigate the dynamics between F-actin and Myl9 accumulation using live imaging approaches. Following the localization of these two proteins and their differential expression in correlation to each other will provide more details about the underlying molecular mechanism.

As already mentioned, Rac1 as an upstream activator of Arp2/3 also inhibited JAIL formation, which made it interesting to investigate the role of Rac1 further in the context of JBL.

The role of Rac1 in JBL function

Classically, Rac1 is known to induce lamellipodia (Hall, 1998; Ridley, 2001) and it is well known to have a polarized activity highest at the leading edge in migrating cells, where it leads to enhanced protrusive activity and the formation of membrane ruffles (lamellipodia formation) (Ridley et al., 1992). This made Rac1 a good candidate to study during JBL formation.

Previous experiments done in Paatero et al., 2018 have shown that inhibition of Rac1 does not influence the formation of JBL per se, but increased the oscillation time. This indicates that Rac1 plays a role in maintaining the dynamic properties rather than the initial step of formation.

And since junctional rearrangement was yet significantly reduced, these findings at the same time point out that dynamic F-actin behavior is a crucial step for proper JBL function (compare to Figure 43).

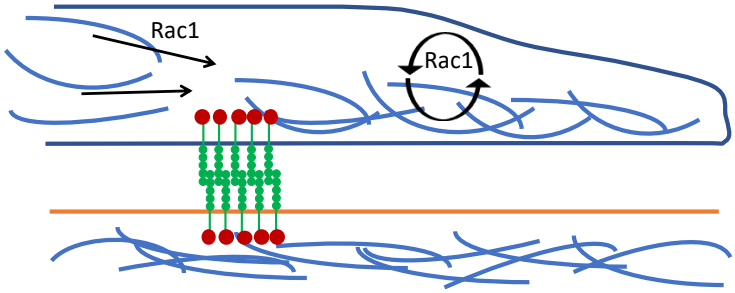

Figure 43: Rac1 during JBL formation. Rac1 is known to be a crucial player for the induction of lamellipodia. In JBL they mostly play a role in maintaining the F-actin dynamics within the JBL. Inhibition of Rac1 does not influence the formation of the JBL but interferes with the oscillation. Roles of Rac1 are only indicated in the upper cell. VE-cadherin in green, ZO1 in red. F-actin is represented in blue. Two cells (top in blue and lower one in orange) are shown.

Additionally, I could show in this study (also published) that inhibition of Rac1 does not influence structural properties; formation of ZO1-based double junctions is mostly unimpaired.

Generally, the observed defects upon Rac1 inhibition were rather mild, especially compared to Arp2/3 inhibition. It is possible that I didn't achieve full inhibition *in vivo*, even at high doses. Alternatively, the role of Rac1 might have a different role in JBL as compared to JAIL (where Rac1 did inhibit JAIL formation).

Alternative modes of actions for Rac1 could well be at the junctional level, although the role of Rac1 in mature cell-cell adhesions in ECs is not well understood and the collected evidences seem to be conflicting. One the one hand, Rac1 is reported to be required for stabilization and maintenance of the endothelial barrier in response to shear stress of barrier-enhancing mediators (e.g. sphingosine-1-posphate) (Liu et al., 2013; Mehta et al., 2005). On the other hand, Rac1 activation also leads to a loss of cell-cell contacts upon stimulation of endothelial cells with VEGF, for example (Gavard and Gutkind, 2006). These findings underline the importance of understanding the local and temporal activation of Rac1 as distinct spatio-temporal activation can have different effects.

In addition, Timmerman et al., 2015 show that Rac1 activation (downstream of thrombin) promotes the reassembly of cell-cell junctions during the phase of recovery, which is induced by the formation of lamellipodia protrusions. The stabilizing effect on VE-cadherin junctions occurs via Rac1-induced actin rearrangements at nascent junctions by promoting the formation of cortical F-actin bundles (Timmerman et al., 2015).

Generally, it is well documented that an increase in Rac1 activity is linked to junction assembly and maturation (Lampugnani et al., 2002; Noren et al., 2001). Additionally, activation of Rac1 leads to accumulation of F-actin and enhanced VE-cadherin levels, possible by reducing the dissociation in mature junctions.

Liu et al., 2010 propose a mechanism, in which Rac is responsible for the ability of adheres junctions to assemble in response to Rho-mediated tugging forces of actomyosin contractility.

In line with this, Daneshjou et al., 2015 show in their studies done in confluent endothelial monolayers that Rac1 induces stabilization of adheres junctions by decreasing the rate of VE-cadherin dissociation, but independently from protrusion formation. Interestingly, this response was coupled to a decrease in tension across VE-cadherin molecules. Stabilization of trans-dimers is achieved by counteracting RhoA- mediated tugging force, thereby modulating actomyosin force at the adherens junctions.

Based on this evidence, it might be very interesting to further investigate the role of Rac1 in the context of VE-cadherin in JBL formation and junction maturation.

Potentially, the role of Rac1 in stabilization of junctions can be linked to the observation that Rac1 inhibition leads to an increased oscillation cycle of JBL and increased lag phase (Paatero et al., 2018). Maturation of nascent adhesions coincides with periodic pauses of the forward moving leading edge (Parsons et al., 2010), and prolongation of the cycle might be therefore interpreted as impaired ability for adheres junction to mature.

One way to further elucidate the role of Rac1 in protrusion formation would be to specifically activate Rac1 rather than to inhibit it ubiquitously. This can be achieved by an engineered photoconvertible Rac1.

Altering F-actin dynamic using endothelial specific Photoactivatable Rac1 *in vivo*

As mentioned before, Rac1 is responsible for lamellipodia formation and its activity is highest at the leading edge of migratory cells (Ridley et al., 1992).

Specific (light-induced) activation of Rac1 at the leading edge is sufficient to direct migration with precise control (spatial and temporal) *in vivo* (Yoo et al., 2010). Based on evidence obtained from the literature, combined with the hypothesis that JBL have similar properties to classical lamellipodia and rely on actin-based protrusion formation, I generated a photoactivatable Rac1 reporter, which can be specifically expressed in endothelial cells of zebrafish embryos.

Temporally, albeit not spatially, restricted activation led to a reduction in the number of filopodia and a decrease of the cell area. Since these phenotypes were reversible (darkstate of the activation laser), they might indeed be specifically linked to enhanced Rac1 activity. However, these observations were very surprising, as Rac1 is (to the best of my knowledge) not directly linked to filopodia formation neither to cell shape determination. However, both lamellipodia and filopodia formation are dependent on Arp2/3 activation and on actin polymerization. Additionally, Arp2/3 transduces signals from Rac1 (lamellipodia) or Cdc42 (filopodia) either through WAVE or WASP proteins in order to polymerize actin (e.g. in Insall and Machesky et al., 2009). Assuming that these pathways are in equilibrium, over-activation of Rac1 might shift this potential balance favoring lamellipodia formation at the cost of filopodia. Another possible explanation would be that ubiquitous (not locally restricted) activation of Rac1 alters/abolished the polarity of cells, losing their ability to send out filopodia in a particular direction.

Explanations for changes in cell size are very speculative. In Yoo et al., 2010, Rac1 activity is linked (over a positive feedback loop in the PI3K pathway) to the generation of stable F-actin filaments at the rear of a migrating cell bearing a contractile actomyosin cytoskeleton. Potentially, over-activation of Rac1 could somewhat influence contractility in the cell cortex, leading to this “cell contraction”.

Generally, both of the observations show that future experiments need to be adapted in several ways, to guarantee reliability and meaningful biological results. Firstly, activation of Rac1 needs to be locally restricted (e.g. leading edge of a migrating cell) in order to not change the polarity of the entire cell.

Secondly, endothelial cells expressing a control construct will be crucial in order to confirm the specificity of the obtained results. A control construct harboring Rac1 with a mutation on the LOV domain (and thereby preventing unfolding and releasing the effector binding domain) will be of importance (compare Wu et al., 2009). Last but not least, effects of Rac1 activation need to be investigated in the context of the F-actin cytoskeleton.

My preliminary results have already proven an effect on the F-actin cytoskeleton, making this approach quite promising. Here, activation of Rac1 led to an enhanced EGFP-UCHD signal at cell-cell interfaces, indicating that F-actin is recruited to the junctions upon activation. This indeed is consistent with the literature, where overexpression of Rac1 lead to the accumulation of F-actin at cell-cell junctions (Noren et al., 2001). Furthermore, recruitment of F-actin to the junctions might be indicative for their stabilization. Enhanced stabilization and potentially decreased remodeling capacity (and flexibility?) might also be the mechanism underlying cell shrinkage in my experiments. This could be further investigated by abundant activation of Rac1 in a single cell context, where no cell-cell junctions are present and the observed behaviors are fully autonomous.

Based on these findings, and combined with my preliminary data, I suggest the following experiment to be done in the future: I hypothesize that JBL formation or initial protrusion formation respectively, are highly dependent on Rac1 activity and that JBL dynamics and formation can be altered by specific (local and temporal) activation of Rac1.

Questions that I would like to answer include: Does local activation of Rac1 at the lateral sites of the junctional ring influence formation or oscillation of JBL? Does activation of Rac1 lead to an increase in junctional elongation speed? And moreover, could specific spatial activation of Rac1 at the medial part of the junctional ring induce ectopic F-actin based membrane protrusions?

Therefore, Rac1 could be specifically activated during junctional ring elongation at the sites of the junctional ring, where JBL usually form (compare to Figure 44). Activation is supposed to be spatially and temporally restricted and the effects should be observed on the level of F-actin (in embryos expressing iRFP-UCHD). It will be interesting to see whether Rac1 is sufficient to alter F-actin dynamics, which could be reflected in a change of oscillatory behavior (shorter cycle, faster oscillation) or induction of JBL.

Potentially, activation of Rac1 in the medial parts of the junctional ring could induce artificial JBL at ectopic sites.

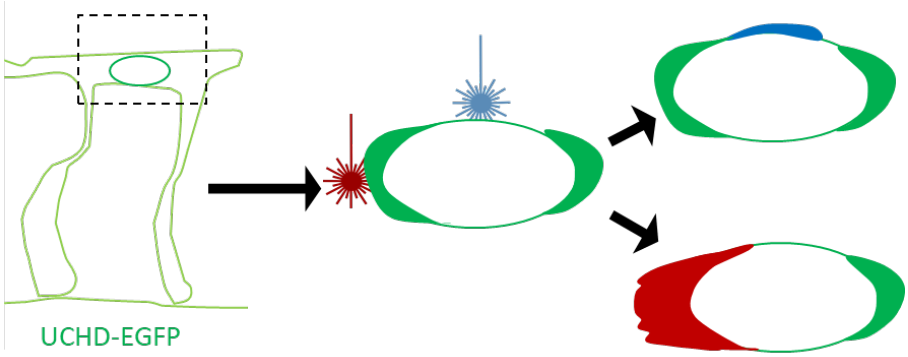

Figure 44: Overactivation of Rac1 during JBL formation. Spatially restricted specific overactivation of Rac1 will help to understand, whether Rac1 is sufficient enough to induce lamellipodia/JBL formation. To this end, Rac1 could be specifically activated at sites where JBL normally form (red) to see whether initial formation or dynamic behavior could be influenced (based on F-actin). Additionally, activation of Rac1 at the medial parts of the junctional ring will answer the question, whether Rac1 activation is able to induce ectopic JBL (blue)

Additionally, it is very fortunate that the stable transgenic kdrl:mCherry-PA-Rac1 fish line seems to be mosaic in its expression pattern. This will allow for experiments, where only one of two cells during anastomosis harbor PA-Rac1 expression.

Besides its effect on lamellipodia formation, Rac1 has also been linked to maturation of junctions as described in a previous paragraph. Active Rac1 is localized at sites of nascent adhesions and is implicated to induce stabilization (by actively remodeling the F-actin cytoskeleton (Timmerman et al., 2015) and regulating the strength of adherens junctions (Liu et al., 2010). Furthermore, in Seebach et al., 2007 it was reported that Rac1 is responsible for VE-cadherin clustering (in response to flow though) and that Rac1 activation reduces dissociation rate of VE cadherin from the junctions (Daneshjou et al., 2015). Keeping that into consideration, potential effects on JBL function might not exclusively originate from F-actin dynamics, but also be induced by changes in junctional properties. That this might be the case is supported by the evidence in my study that activation of Rac1 led to enhanced accumulation of recruitment of F-actin of the junctions.

Therefore, it might be very interesting to specifically analyze effects of Rac1 activation on VE-cadherin localization or clustering, as well as VE-cadherin tension. In case the contribution of Rac1 in JBL is rather observed at the junctional level, activation of Rac1 could lead to increased VE-cadherin stability due to altered VE-cadherin dissociation rate (as described in the literature). This, in turn, might, instead of inducing JBL, lead to an adverse situation, in which the dynamic behavior of JBL is abolished and reaches a more "stiff" and steady state, due to loss of adherens junction remodeling. However, this remains very speculative and needs to be investigated in the future.

JBL as general mechanism of endothelial cells underlying migration and cell shape changes

Junction based lamellipodia were also identified in larger caliber vessels such as the dorsal aorta (Paatero et al., 2018). Here, F-actin based membrane (or cell) protrusions could be observed in regular intervals, coinciding with oscillation in F-actin intensity. I could further support this observation by successfully proving the formation of double junctions in DA, a hallmark of JBL that was identified during anastomosis. Double junctions appeared to be present for a longer period of time (around 13 min) compared to the DLAV, where they are often just observed for 1-2 minutes. This might be indicative of a lower dynamic of cell junctions in the DA, or a lower need for rapid cell shape changes or movements. Double junctions were observed in 2 dpf embryos, where junctions appear still irregular and immature. Over time, they develop a more linear phenotype and align progressively in the direction of blood flow (Lagendijk et al., 2017). It would be interesting to examine, to what extent appearance of double junctions is linked to the state of junctional maturation and to blood flow. Cell shape changes in the DA are suggested to be induced by blood flow (Sugden et al., 2017) and potentially might also influence local protrusion formation. Further experiments could focus on the appearance of JBL and length of double formation in the DA during maturation and onset of blood flow. This will help to elucidate to what extent JBL are employed by endothelial cells to induce cell shape changes (dependent or independent of blood flow).

Summary and Outlook

For my thesis work, I have mainly focused on the characterization of JBL during the process of anastomosis, which relies on the coordinated interaction between two tip cells. However, I could also demonstrate that membrane protrusions in larger caliber vessels such as the dorsal aorta, representing a more complex cellular environment, show morphological and dynamic characteristics of JBL. Given their occurrence in different contexts, JBL may represent a general mechanism of cell rearrangements during vascular development and possibly also in other tissues. During anastomosis, JBL are thought to provide the motile force, which promotes EC intercalation and concomitant cell elongation, ultimately leading to a change in vascular architecture from a unicellular to a multicellular configuration. Cells in the early dorsal aorta also undergo extensive rearrangements and cell shape changes during blood vessel maturation. Therefore, endothelial cells could employ JBL as a general mechanism to induce or drive these morphogenetic processes throughout vascular development, for example in response to shear stress or injury. Here, JBL could underly dynamic endothelial cell behaviors, while maintaining the vascular seal. It remains to be elucidated, whether JBL are unique to blood endothelial cells or whether they might occur, for example, in lymphatic ECs during lymphatic vessel formation. Interestingly, VE-cadherin levels in the zebrafish lymphatic vasculature appear to be very low (H.G. Belting, personal communication), raising the possibility that lymphatics may not use a VE-cadherin based mechanism for cell rearrangements.

Finally, it will be important to better understand the physical mechanism underlying JBL-driven cell rearrangements. Several questions remain to be answered. For example: Do the newly formed distal junctions provide sufficient anchor for cell elongation? Does the extracellular matrix play a role? A detailed analysis at the molecular level will require a bona fide *in vitro* model for JBL function. The previously described junction-associated intermittent lamellipodia (JAIL), which occur under certain conditions in HUVECs, share similarities with JBL, but also display critical differences. Nevertheless, they may provide a useful entry point to study the role of cell protrusions in some aspects of blood vessel morphogenesis.

Acknowledgements

First of all, I would like to thank Prof. Dr. Markus Affolter for giving me the opportunity to pursue this fascinating project in his lab. Working in his lab throughout the last four years has unconditionally been great; there has never been a single day, when I didn't enjoy going to work. I really admire him for his unlimited passion and fascination for science, which he directly confers to his environment.

Lots of thanks goes to Dr. Heinz-Georg Belting, who has been a great supervisor and desk neighbor. Thanks for all the sincere and valuable advice, both scientifically and non-scientifically and for giving me so much freedom to explore and to realize my own project ideas. I always appreciated the fruitful discussions and support by brilliant ideas. Furthermore, I am more than thankful for the initial idea to start a collaboration with Prof. Dr. Benjamin Hogan's Lab in Brisbane, Australia and for the follow-up time and energy he invested in writing a grant with me and finally sending me to Australia.
Being given the chance to go abroad during my PhD was more than an exceptional experience for me that I will never forget.

At this point, I would like to express my gratitude to Prof. Dr. Benjamin Hogan for hosting and supervising me during my three months in Australia. I was more than deeply impressed by his brilliant mind. Thanks to Dr. Anne Lagendijk for the supervision at this time and to all the lab members of the IMB in Brisbane. These are among others Lin, Smrita and Tevin, for creating such a pleasant and fun work environment. I never expected that I will leave Australia with new friends at the other end of the world.

Next I would like to thank Prof. Dr. Holger Gerhardt and Prof. Dr. Gerhard Christofori for being in my PhD committee and for encouraging discussions.

In general, I also would like to say thank you for the financial support during the first three years of my PhD by the Fellowship of Excellence of the University of Basel, as well as

support for my abroad stay in Australia (short term fellowship, which was awarded by EMBO).

Special thanks goes to Dr. Martin Müller and Helen Mawer, who contributed enormously to maintenance and organization of the lab. Organization and maintenance of our fish facility and caretaking wouldn't be possible without Kumuthini Kulendra and Mattias Thimm- so thanks a lot!

Also, I would like to say thank for to all the people working behind the scenes. Without them, our labwork wouldn't be so convenient and easy as with your support. People I would like to mention at this point are our kitchen ladies Bernadette Bruno, Gina Evora and Karin Mauro as well as our floor manager Vaclav Mandak.
Additionally, a huge thanks goes to our imaging core facility, including Dr. Alexia Loynton-Ferrand, Dr. Kai Schleicher and Dr. Wolf Heusermann for their high-quality services and support.

Certainly, I shall not forget all the members of my lab. Thanks to all the former and current lab members for creating such a great, funny, relaxed and inspiring atmosphere. I truly hope, that the resulting friendship outlast my time in the lab.

Finally, I would like to express my particular thanks to my family and friends. Thanks to my parents and sister for all the professional and emotional support during the last years and for their continuous effort in trying to understand my research topic. Especially, it is great to be surrounded by people, who are able to see problems from a different perspective outside your own box.

My friends, what would I be without you. I am sure, there are no appropriate words which could express how thankful I am to have you in my life. Thanks for all the days, evenings and nights we spent with each other. Thanks for each single laughter (and it's been a lot!), every conversation or discussion, each dream and problem we share and of course for every solution. You are my source of energy, my comfort zone – I will never forget the time I spent with you and certainly this is nothing I would ever like to miss in my future.

A.

Appendix

A Appendix

A.1. Supplemental Figures

Supplemental Figure 1

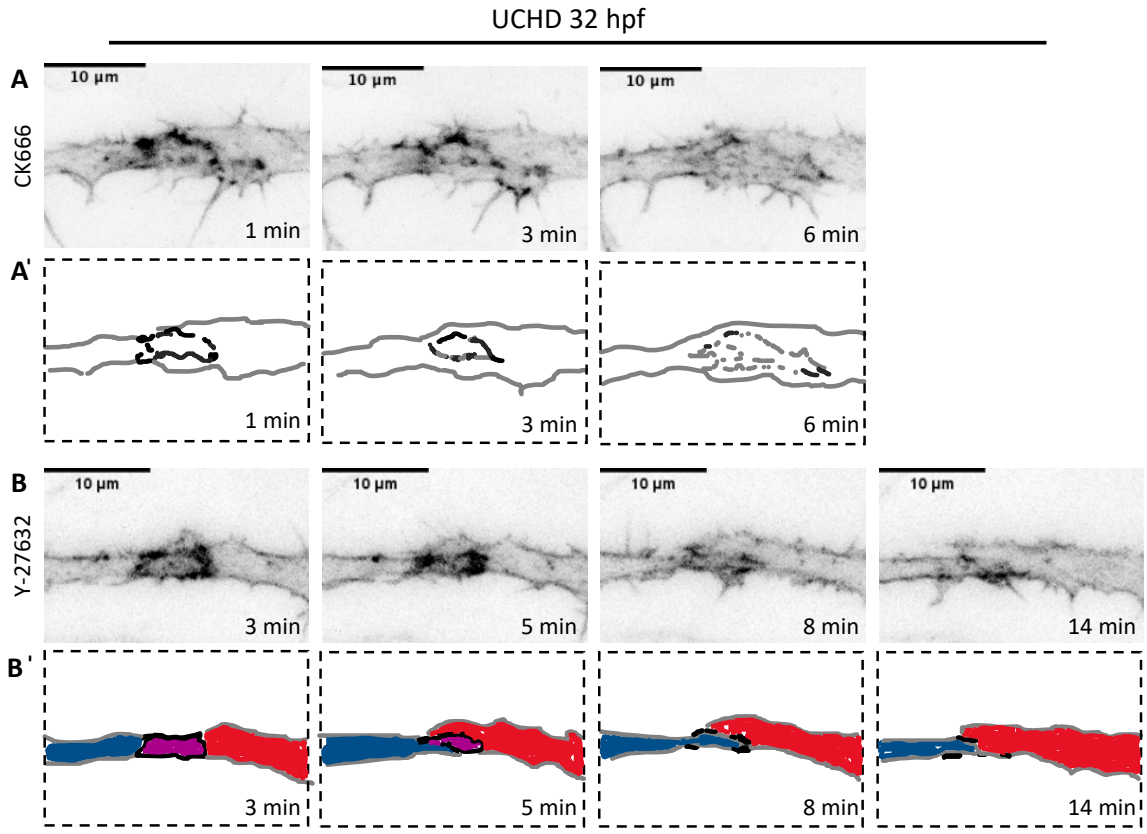

Supplemental Figure 1: Destabilization of actin at the junctional ring or ring dissolution upon treatment with a ROCK or Arp2/3 inhibitor. Live still images from movies of embryos expressing EGFP-UCHD (Tg(fli:Gal4ff^{ubs3},UAS:EGFP-UCHD^{ubs18}) in A – B in inversed contrast of CK666-treated embryos (**A**) or Y-27632-treated embryos (**B**). **A'** and **B'** are schematic drawings of A and B respectively. Images show the junctional ring in the DLAV around 32 hpf. Different time points shown. A-A' Inhibition of Arp2/3 led to destabilization of actin at the junctional ring. As a decrease of EGFP-UCHD signal over time could be observed. B-B' Instead of elongation of the junctional ring, the cells decrease their mutual contact face (indicated as purple in B'), rather moving away from each other. Scale bars 10 µm.

Supplemental Figure 2 & 3

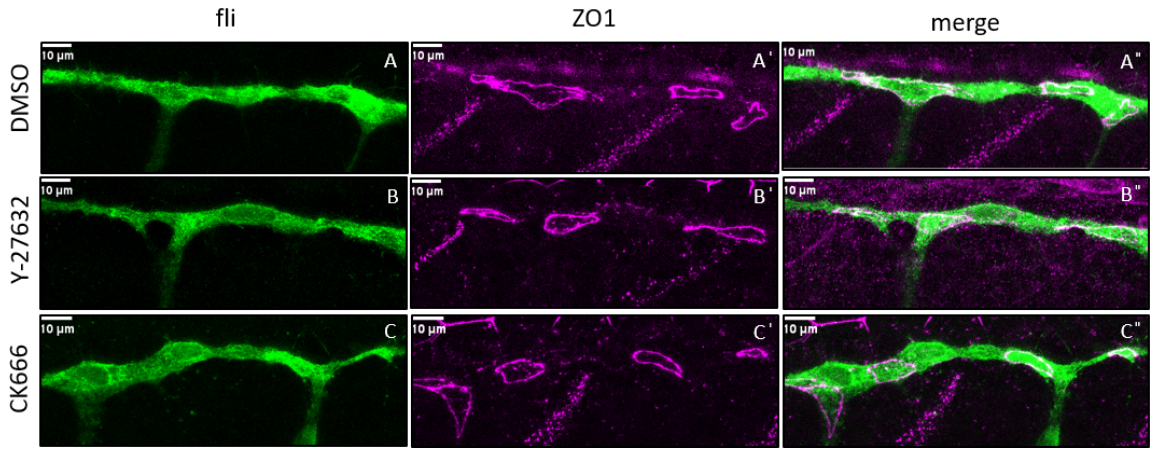

Supplemental Figure 2: Inhibition of neither ROCK nor Arp2/3 does not change localization of junctional proteins or integrity.

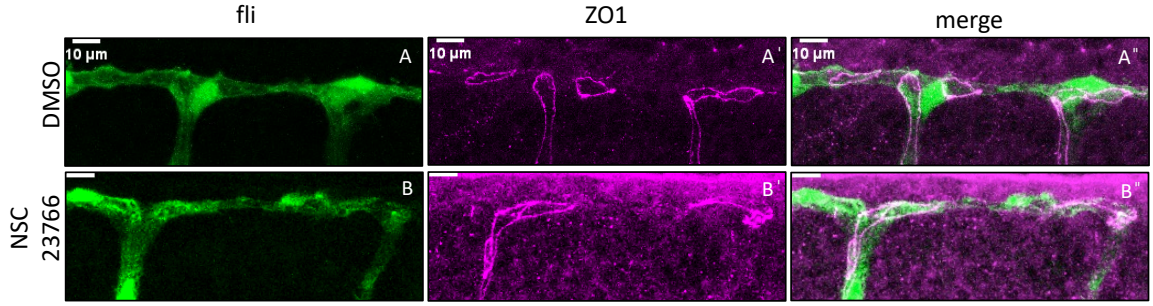

Supplemental Figure 3: Inhibition of Rac1 does not change localization of junctional proteins or integrity.

Supplemental Figures 2 and 3: Maximum projections of the DLAV of Tg(fli1a:EGFP)y1 (green) in control embryos (Supplemental **Figure 2 and 3 A**), Y-27632 (**2B**), CK666 (**2C**) and NSC23766 (**3A and B**) treated embryos. Embryos were stained for ZO1 (**A'-C'** and **A-B** in magenta) at around 32 hpf. **A"-D"** and **A"- B"** display merges. Junctions from inhibitor treated embryos do not show obvious defects, instead are continuous and comparable to control embryos. Scale bars 10 µm.

Supplemental Figure 4

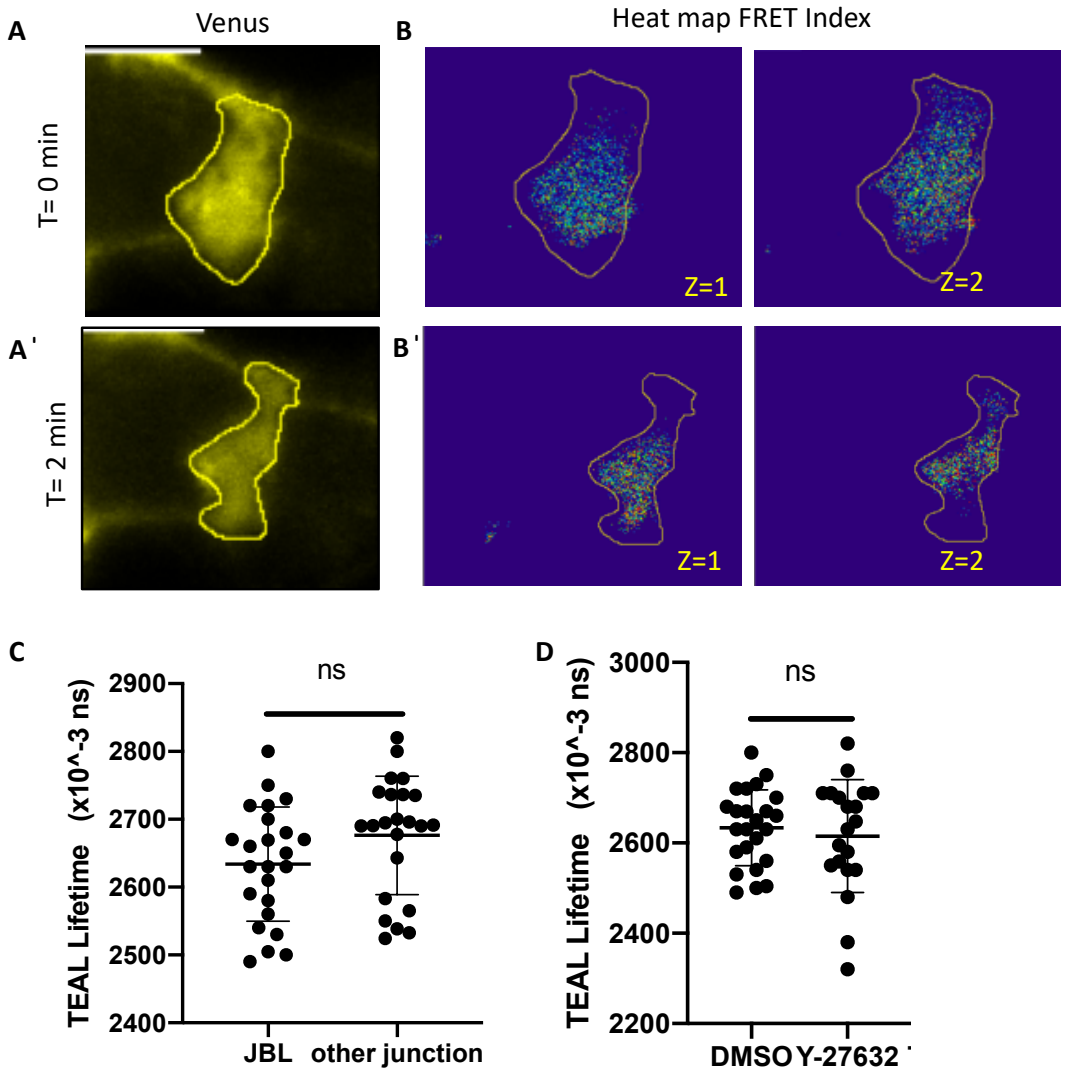

Supplemental Figure 4: Temporal and spatial differences in VE-cadherin tension in the JBL. **A and B.** Temporal changes of VE-cadherin tension during a JBL oscillation cycle. **A and A'.** Maximum projections of JBL at 32 hpf in the DLAV of Tg(ve-cad:ve-cad-Venus). **B and B'**. Heat map images of ratio-metric FRET values of JBL displayed in **A and A'. B and B'**. One JBL imaged twice within a timespan of 2 minutes. ROI marks the JBL. Temporal resolution of change in VE-cadherin tension was technically not possible due to bleaching of the fluorophores. Scale bars 5 µM. **C.** Teal life time values (obtained from FLIM) for JBL compared to other junctions in the DLAV. Here, as comparison to the JBLs, measurements were not exclusively done on the medial part but on every other junction in the DLAV (n=24 JBL and n=23 other junctions in > 5 embryos). There was no significant difference in mean lifetime values between the two groups. Unpaired two-sided t-test was used. **D.** Teal life time values (nano-sec) of JBLs in DMSO vs. Y-27632 treated embryos (n=24 for DMSO and n=20 for Y-27632 (> 5 embryos). No significant changes of mean values VE-cadherin tension could be measured upon inhibition of ROCK in the JBLs. Kolmogorov -Smirnhov test was used.

A.2. Contribution to publications

A.2.1. Hübner et al., 2018, Nature communications

Wnt/β-catenin signaling regulates VE-cadherin-mediated anastomosis of brain capillaries by counteracting S1pr1 signaling

Summary

Hübner et al., investigate the contribution of Wnt signaling to brain angiogenesis and blood barrier (BBB) formation and identify Wnt signaling as a coordinator of timing and as important factor for anastomosis regulation. They show, that Wnt is dispensable during sprout elongation however plays a crucial role in anastomosis events and lumen formation. Furthermore, they provide a link between processes of capillary angiogenesis and BBB formation.

Aim of the collaboration and my contribution:

Aim of the collaboration was to analyze events during anastomosis in the zebrafish hindbrain vasculature after Wnt-inhibition *in vivo* in zebrafish embryos. Therefore, I either supervised and guided *in vivo* experiments but mostly performed the experiments independently. I was included in experiments for the initial manuscript as well as during the revision procedure. Experiments that I have done included the analysis of the hindbrain vasculature in:

- in IWR-1 vs. DMSO treated embryos in embryos carrying *Tg*(*ve-cad:ve-cadTS)*, *cdh5* $^{ubs8-/-}$
- in cdh5$^{ubs8-/-}$ or cdh5$^{ubs8+/-}$ embryos plus subsequent genotyping
- in cdh5$^{ubs8-/-}$ embryos (DMSO vs. NSC23766)
- in Esama mutants (DMSO vs. VPC treated)

Post-acquisition analysis was done by the authors themselves. Obtained results were included in the supplemental figures of the manuscript. Furthermore, we provided them antibodies against Esama and VE-cadherin and assisted in performing whole-mount antibody stainings. last but not least, I reviewed the manuscript and suggested corrections.

nature COMMUNICATIONS

ARTICLE

DOI: 10.1038/s41467-018-07302-x OPEN

Wnt/β-catenin signaling regulates VE-cadherin-mediated anastomosis of brain capillaries by counteracting S1pr1 signaling

Kathleen Hübner[1,2], Pauline Cabochette[3], Rodrigo Diéguez-Hurtado[2,4], Cora Wiesner[5], Yuki Wakayama[1], Kathrin S. Grassme[1], Marvin Hubert[1], Stefan Guenther[6], Heinz-Georg Belting[5], Markus Affolter[5], Ralf H. Adams[2,4], Benoit Vanhollebeke[3,7] & Wiebke Herzog[1,2,4]

Canonical Wnt signaling is crucial for vascularization of the central nervous system and blood-brain barrier (BBB) formation. BBB formation and modulation are not only important for development, but also relevant for vascular and neurodegenerative diseases. However, there is little understanding of how Wnt signaling contributes to brain angiogenesis and BBB formation. Here we show, using high resolution in vivo imaging and temporal and spatial manipulation of Wnt signaling, different requirements for Wnt signaling during brain angiogenesis and BBB formation. In the absence of Wnt signaling, premature Sphingosine-1-phosphate receptor (S1pr) signaling reduces VE-cadherin and Esama at cell-cell junctions. We suggest that Wnt signaling suppresses S1pr signaling during angiogenesis to enable the dynamic junction formation during anastomosis, whereas later S1pr signaling regulates BBB maturation and VE-cadherin stabilization. Our data provides a link between brain angiogenesis and BBB formation and identifies Wnt signaling as coordinator of the timing and as regulator of anastomosis.

[1] University of Muenster, Schlossplatz 2, 48149 Muenster, Germany. [2] Cells-in-Motion Cluster of Excellence (EXC 1003 – CiM), University of Muenster, Waldeyerstrasse 15, 48149 Muenster, Germany. [3] Université libre de Bruxelles, Rue Prof. Jeener et Brachet 12, 6041 Gosselies, Belgium. [4] Max Planck Institute for Molecular Biomedicine, Roentgenstrasse 20, 48149 Muenster, Germany. [5] Biozentrum der Universität Basel, Klingelbergstrasse 70, 4056 Basel, Switzerland. [6] Max Planck Institute for Heart and Lung Research, ECCPS Bioinformatics and Deep Sequencing Platform, Ludwigstrasse 43, 61231 Bad Nauheim, Germany. [7] Walloon Excellence in Life Sciences and Biotechnology (WELBIO), Avenue Pasteur 6, 1300 Wavre, Belgium. Correspondence and requests for materials should be addressed to W.H. (email: wiebke.herzog@uni-muenster.de)

The central nervous system (CNS) depends on nutrient and oxygen delivery from blood vessels during the development and homeostasis, but also requires protection from blood-born toxins and pathogens. Endothelial cells (ECs) of CNS blood vessels acquire characteristic properties in order to fulfill the tasks of this blood-brain barrier (BBB), such as expression of a specific subset of junction molecules and nutrient transporters, down-regulation of vesicular transport and establishment of cell–cell interactions within the neurovascular unit[1]. During a defined time window of embryonic development, molecular cues from neuronal and perineuronal tissues orchestrate CNS angiogenesis and barriergenesis[2–4]. The process of brain angiogenesis is well conserved in vertebrates: After acquiring a pre-sprouting signature (hereafter called pre-tip cell), these specified cells migrate out from the resident vessel, with tip cells guiding sprout formation, and invade into the neuronal tissue, where they form cell–cell contacts and anastomose with other sprouts or extra-cerebral vessels in order to establish circulatory loops[1,3,5]. In zebrafish (*Danio rerio*), hindbrain capillaries (intra-cerebral central arteries, CtAs) invade the brain parenchyma at around 32 h post fertilization (hpf) from the primordial hindbrain channel (PHBC), extend dorsally and connect ventrally to the basilar artery (BA) or laterally to other CtAs (Fig. 1a)[4–7]. At 48 hpf, most CtAs carry blood flow and by 72 hpf most of the respective BBB properties are established[8,9].

Studies in mice and zebrafish demonstrate β-catenin-dependent Wnt signaling through Wnt7a–Wnt7b to be essential for brain vascularization[10–12]. Additionally, Wnt signaling has been shown to be involved in the establishment of BBB characteristics, such as upregulation of tight junction components (e.g., Claudin 1 and 3) or nutrient transporters (e.g., Glut1) and decrease of transcellular transport processes (e.g., Plvap)[10,13–15]. Recently, the Gpr124-Reck complex has been identified as an EC autonomous regulator of Wnt signaling essential for brain vascularization and BBB formation[12,15–20]. Single-cell analysis of brain vascular development through live imaging approaches in zebrafish further revealed that the control of pre-tip cell function by the Gpr124-Reck complex operates within the parental vessels (PHBCs) at pre-invasive stages. This early function of Wnt signaling has so far largely precluded the analysis of Wnt signaling functions at later stages of CNS vascular development, including the invasion process itself and subsequent patterning events.

Vascular endothelial (VE)-cadherin is the major endothelial-specific member of the cadherin protein family and is involved in EC migration, cell–cell contact formation, anastomosis, and barrier formation[5,21,22]. Together with the EC-selective adhesion molecule a (Esama), VE-cadherin is essential for EC–EC recognition and contact formation during intersegmental vessel anastomosis[23,24]. Experiments using mice and tissue culture revealed that VE-cadherin is subject to extensive post-transcriptional regulation, including intracellular complex formation and trafficking, membrane localization as well as association in cell–cell junctions. This dynamic regulation of VE-cadherin in adherens junctions is not only crucial for vascular patterning, but also for the function of mature blood vessels, e.g., for maintenance of EC integrity or during leukocyte extravasation[25,26], and can be regulated by Sphingosine-1-phosphate (S1p) signaling[27,28].

ECs express S1p receptor (S1pr) 1, 2, and 3[29] and in zebrafish, two paralogues exist for S1pr3 (S1pr3a and S1pr3b). S1pr1 signaling promotes BBB integrity in mice[30]. Additionally, postnatal EC-specific knockout of S1pr1 induces loss of VE-cadherin and vascular endothelial growth factor receptor 2 (VEGFR2) from the cell junctions[31]. To date, the contribution of neither S1pr nor VE-cadherin signaling has been addressed during brain capillary angiogenesis, leaving a missing link between brain EC angiogenesis and BBB formation.

In this study, we clarify the distinct requirements for Wnt signaling during brain angiogenesis. Whereas Wnt signaling is essential before sprouting to regulate yet to be defined early function of the future tip cells (pre-tip cells) within the parental vessel[12], it is surprisingly dispensable during sprout elongation and migration, although it remains continuously active in the invading sprout. We show that Wnt signaling is regulating brain capillary anastomosis and lumen formation. Interestingly, Wnt signaling is crucial for VE-cadherin and Esama localization at cell–cell junctions in a transcription-independent manner. During active brain capillary angiogenesis, Wnt signaling counteracts S1pr signaling, which enables VE-cadherin-dependent anastomosis and lumen formation. In contrast, when angiogenesis is completed at later stages, S1pr signaling regulates BBB formation. Our data therefore reveal an important functional link between the intertwined processes of brain capillary angiogenesis and BBB formation.

Results

Wnt signaling is required for hindbrain capillary patterning. Studies in mice have shown that Wnt signaling is essential for hindbrain capillary angiogenesis[10,11,14]. Studies using zebrafish revealed that this control by Wnt signaling reflects an essential function in defining the pre-tip cell during early, pre-invasive angiogenic events within the parental vessels (Fig. 1a[12]). As a result, no hindbrain capillaries (central arteries, CtA) are formed in the absence of Wnt signaling. In order to bypass this early requirement, we blocked Wnt signaling pharmacologically using IWR-1[32] and generated transgenic lines, which allow for temporally and spatially controlled expression of a dominant-negative Tcf transcription factor.

Treatment with Wnt signaling inhibitor IWR-1 after the pre-tip cell specification phase (29–72 hpf) resulted in severe vascular defects and hemorrhages in the brain, but not in the trunk vasculature (Supplementary Fig. 1a), indicating that there are further requirements for Wnt signaling during brain angiogenesis. We therefore analyzed during which stages of brain capillary angiogenesis active Wnt signaling can be observed using confocal live imaging and two different transgenic Wnt signaling reporter lines, which express short-lived fluorophores controlled by Wnt-responsive promoters: *Tg(axin2BAC:Venus-Pest)^{mu288}* and *Tg(14TCF:loxP-STOP-loxP-dGFP)^{mu202}*[33]. Both reporter lines showed robust fluorophore expression within the migrating CtA sprouts at 34 hpf (Supplementary Fig. 1b,c), which we confirmed to be EC specific (Supplementary Fig. 1d). We next performed time-lapse analysis using *cre* mRNA-injected *Tg(14TCF:loxP-STOP-loxP-dGFP)^{mu202}* embryos starting from 29 hpf (Fig. 1b, Supplementary movies 1, 2). We detected high Wnt reporter activity in the determined CtA pre-tip cells, which are forming within the PHBC. Despite a putative half-life of about 2 h, the destabilized GFP (dGFP) expression remained high in the emerging CtA sprouts during the following 5.5 h of development, indicating continuous Wnt signaling activity during CtA sprout migration and cell–cell contact formation (open arrow, Fig. 1b). With the onset of lumen formation about 2 h after cell–cell-contact formation, the dGFP signal decreased to a baseline level, which was maintained in the perfused CtAs, pointing to a post-determination role of Wnt signaling.

After pre-tip cell formation, CtA angiogenesis proceeds by sprouting and sprout invasion into the brain parenchyma. We asked whether endothelial Wnt signaling regulates these processes.

We therefore generated a transgenic zebrafish line expressing a dominant-negative Tcf transcription factor fused to mCherry (mCherry-dnTcf) under the control of a heat shock inducible

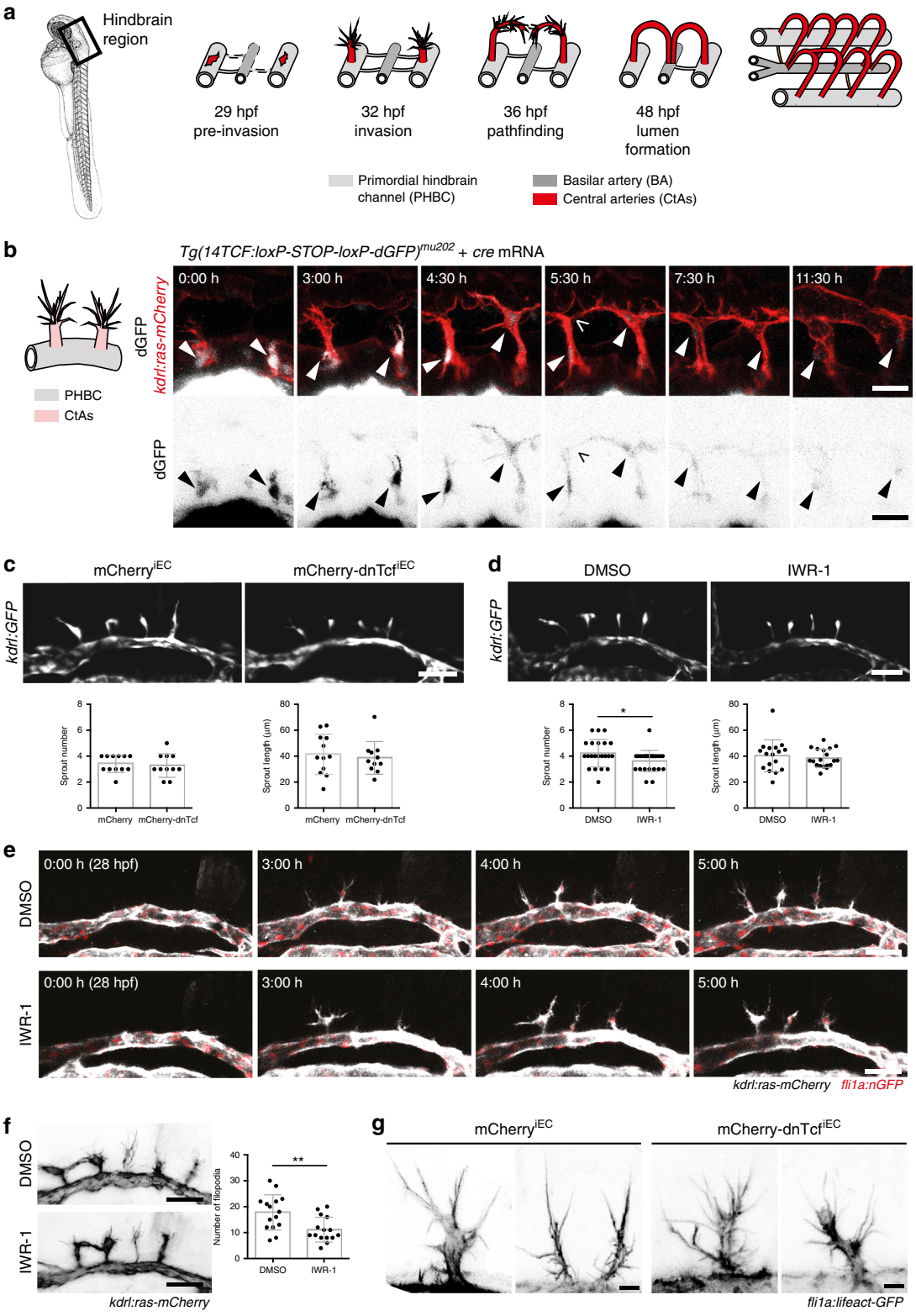

promoter (hsp70l). To restrict Wnt inhibition to ECs, we placed a loxP-flanked (floxed) STOP-cassette upstream of the mCherry-dnTcf coding sequence (Supplementary Fig. 2a, c). This STOP cassette was removed only in ECs by mating to fish with endothelial-specific Cre recombinase expression (*Tg(kdrl:cre)*^{s898}). Validation of Wnt inhibition by heat shock controlled mCherry-dnTcf expression is documented in Supplementary Fig. 2.

To address whether Wnt signaling regulates sprout elongation or EC migration, we blocked Wnt signaling by EC-specific mCherry-dnTcf expression or IWR-1 treatment starting from 26 hpf and analyzed CtA sprouts at 32 hpf (Fig. 1c, d). Surprisingly, we did not observe differences in CtA sprout number or sprout length after Wnt signaling inhibition (Fig. 1c, d). Furthermore, sprout formation, behavior, and filopodia appearance were not affected by IWR-1 treatment (Fig. 1e, f, Supplementary movies 3,

Fig. 1 Wnt signaling is not required for migration of brain capillary sprout ECs. **a** Illustration of hindbrain angiogenesis in zebrafish embryos. Black box indicates localization of the hindbrain. Brain capillary (central artery, CtA) pre-tip cells can be detected within two bilateral primordial hindbrain channels (PHBCs, light gray) and sprout dorsally from PHBCs around 32 hpf. Between 32 and 36 hpf, CtA sprouts extend long filopodia and migrate in an arch toward the basilar artery (BA, dark gray). At 48 hpf CtAs have fused with either the BA or neighboring CtAs and carry blood flow. **b** Time-lapse analysis of a *cre* mRNA-injected *Tg(14TCF:loxP-STOP-loxP-dGFP)*^{mu202} embryo starting from around 29 hpf showed continuously active Wnt signaling in CtAs (arrowheads) before and during sprouting, during invasion, cell–cell contact (open arrowhead) and lumen formation. The bottom panel represents single channel images in inverted color for better visualization. **c**, **d** Inhibition of Wnt signaling by EC-specific dnTcf expression after heat shock at 26 hpf (mCherry-dnTcf^{iEC}, **c**) or pharmacologically by IWR-1 treatment (**d**) resulted in normal CtA sprouting at 32 hpf. CtA sprout number or length of the sprouts was not affected by mCherry-dnTcf^{iEC} expression in *Tg(kdrl:GFP)*^{s843} embryos (**c**: mCherry-dnTcf^{iEC}: $n = 11$; mCherry^{iEC}: $n = 12$) or IWR-1 treatment (**d**: DMSO: number $n = 22$, length $n = 17$; IWR-1: number $n = 24$, length $n = 18$). **e** Still images from time-lapse movies starting at around 28 hpf displayed normal CtA sprout formation in *Tg(kdrl:ras-mCherry)*^{s896}*; (fli1a:nGFP)*^{y7} double transgenic embryos treated with IWR-1. **f**, **g** CtA sprout morphology was not affected by IWR-1 treatment (**f**) or dnTcf expression (**g**) in *Tg(fli1a:lifeact-GFP)*^{mu240} embryos. IWR-1 treatment slightly reduced the formation of long filopodia (>10 µm) compared to DMSO control (**f**: IWR-1: $n = 15$; DMSO: $n = 15$). Images are displayed in inverted color for better visualization. Confocal images show dorsal (**b**) or lateral views (**c**–**g**), anterior to the left. Values represent mean ± SD. $^{*}p < 0.05$, $^{**}p < 0.01$, $^{***}p < 0.001$, Student's *t*-test; *n*, number of analyzed embryos; BA, basilar artery; CtAs, central arteries; ECs, endothelial cells; hpf, hours post fertilization; PHBC, primordial hindbrain channel; Scale bars: 30 µm (**b**), 50 µm (**c**–**f**), 6 µm (**g**)

4). Only the formation of long filopodia (>10 µm) was marginally decreased after IWR-1 treatment (Fig. 1f). Similarly, heat shock-induced EC-specific overexpression of mCherry-dnTcf (mCherry-dnTcf^{iEC}) did not result in differences in filopodia morphology, but instead in high filopodia motility, which resulted in slightly blurry images due to fast filopodia movement (Fig. 1g).

We conclude that after being required early within the parental vessel, Wnt signaling is continuously active during CtA angiogenesis, but dispensable for efficient sprout elongation and invasion of CtA tip cells into the brain parenchyma.

Wnt regulates brain capillary anastomosis and lumenization. To address the role of the active Wnt signaling in the developing CtAs, we inhibited Wnt signaling by inducing mCherry-dnTcf expression in ECs at 26 hpf or by applying IWR at 29 hpf and analyzed CtA pattern and lumen formation at 48 hpf (Fig. 2a, b). We observed a reduced CtA number, reduced connections to the BA and ectopic connections between CtAs. CtA patterning appeared more disorganized, and CtAs had non-lumenized protrusions. To address whether the reduced number of CtAs (Fig. 2a, b) correlated to a reduced number of EC within CtAs, we blocked Wnt signaling as before, and quantified the number of cell nuclei in *Tg(fli1a:nGFP)*^{y7} embryos. Both, treatment with IWR-1 or heat shock-induced EC-specific mCherry-dnTcf expression, reduced the EC number within CtAs (Supplementary Fig. 3a, b). However, blocking cell proliferation via the administration of aphidicolin and hydroxyurea (AHU) did not result in any patterning defects in CtAs, and the combined inhibition of Wnt signaling and proliferation did not aggravate the phenotype of Wnt deficiency (Supplementary Fig. 3c). We therefore conclude that Wnt signaling is required for CtA patterning, but does not act via cell proliferation.

To understand the processes underlying the CtA patterning defects observed after Wnt signaling inhibition (Fig. 2a, b), we performed angiography following IWR-1 treatment (Fig. 2c). In control embryos, more than 80% of the CtAs were perfused at 48 hpf, whereas after IWR-1 treatment only about 25% of the CtAs carried the fluorescent tracer. We next performed time-lapse analysis following IWR-1 treatment or EC-specific mCherry-dnTcf expression using *Tg(fli1a:lifeact-GFP)*^{mu240} embryos to illustrate the actin cytoskeleton of ECs (Fig. 2d–f). We focused on laterally connecting CtAs for better visualization and quantified the time from cell–cell contact until completion of lumen formation until 48 hpf (Fig. 2d). In control embryos, the average time from cell–cell contact to lumen formation is less than 2 h (Fig. 2d, e). After inhibition of Wnt signaling by IWR-1, we noted a drastic delay in lumen formation or even completely impaired lumenization within the observation window (Fig. 2e; Supplementary movie 5-8). Additionally, tip cells in CtA sprouts of IWR-1-treated embryos failed to establish stable cell–cell contacts, but instead continuously produced filopodia, leading to the formation of multiple cell–cell contact sites (asterisk in Fig. 2e, f). This phenotype was fully reproduced by EC-specific mCherry-dnTcf expression (Fig. 2f; Supplementary movies 9, 10). However, the time difference was not as prolonged in the latter as in IWR-1-treated embryos, presumably due to the turnover time of mCherry-dnTcf, as mCherry is no longer detectable at the endpoint of analysis.

In summary, our analysis reveals that Wnt signaling is required for anastomosis of brain capillaries.

Block of Wnt signaling reduces VE-cadherin at cell junctions. To elucidate how Wnt signaling regulates CtA anastomosis, we investigated the abundance of the EC-specific adhesion molecules VE-cadherin and Esama at cell–cell junctions of the CtAs[23,24]. VE-cadherin, a member of the cadherin protein family expressed in ECs, has been shown to be crucial for EC contact formation during blood vessel anastomosis[5,22]. Esam belongs to the protein family of Junction adhesion molecules (Jam) and two paralogues exist in zebrafish, *esama* and *esamb*, of which *esama* is mainly expressed in the vasculature[24]. To address, whether Wnt signaling inhibition affects protein localization of VE-cadherin or Esama, we performed immunostaining for VE-cadherin, Esama and ZO-1 in 42 hpf-old embryos (Fig. 3a–d). In control embryos (DMSO), VE-cadherin and Esama were expressed continuously along cell–cell junctions of ECs within CtAs and in anastomosis rings, which form at positions where two CtAs fuse (arrows in Fig. 3b). After IWR-1 treatment (Fig. 3b) or EC-specific mCherry-dnTcf expression (Fig. 3c, d), we found that the protein abundance of VE-cadherin, Esama, and ZO-1 at cell–cell junctions was dramatically reduced. Furthermore, we frequently observed clustered protein aggregates (stars in Fig. 3b) and the formation of many small adhesion spots (arrows in Fig. 3b) in Wnt-inhibited embryos, which is in line with our previous observations of multiple filopodia contacts (Fig. 2e, f). Hence, reduction and aberrant localization of VE-cadherin and Esama at the cell junctions could cause the anastomosis defects. To validate these findings in another model, we isolated primary brain endothelial cells (BECs) from microvascular fragments[34] of either P3 or adult mice. We were able to block Wnt signaling using 10 µM IWR-1 for P3 and 20 µM for adult brain ECs (Fig. 3e, Supplementary Fig. 2e). To analyze the effect on VE-cadherin distribution we measured the length of the potential cell–cell contact area in form of opposing or touching membrane length and the actual

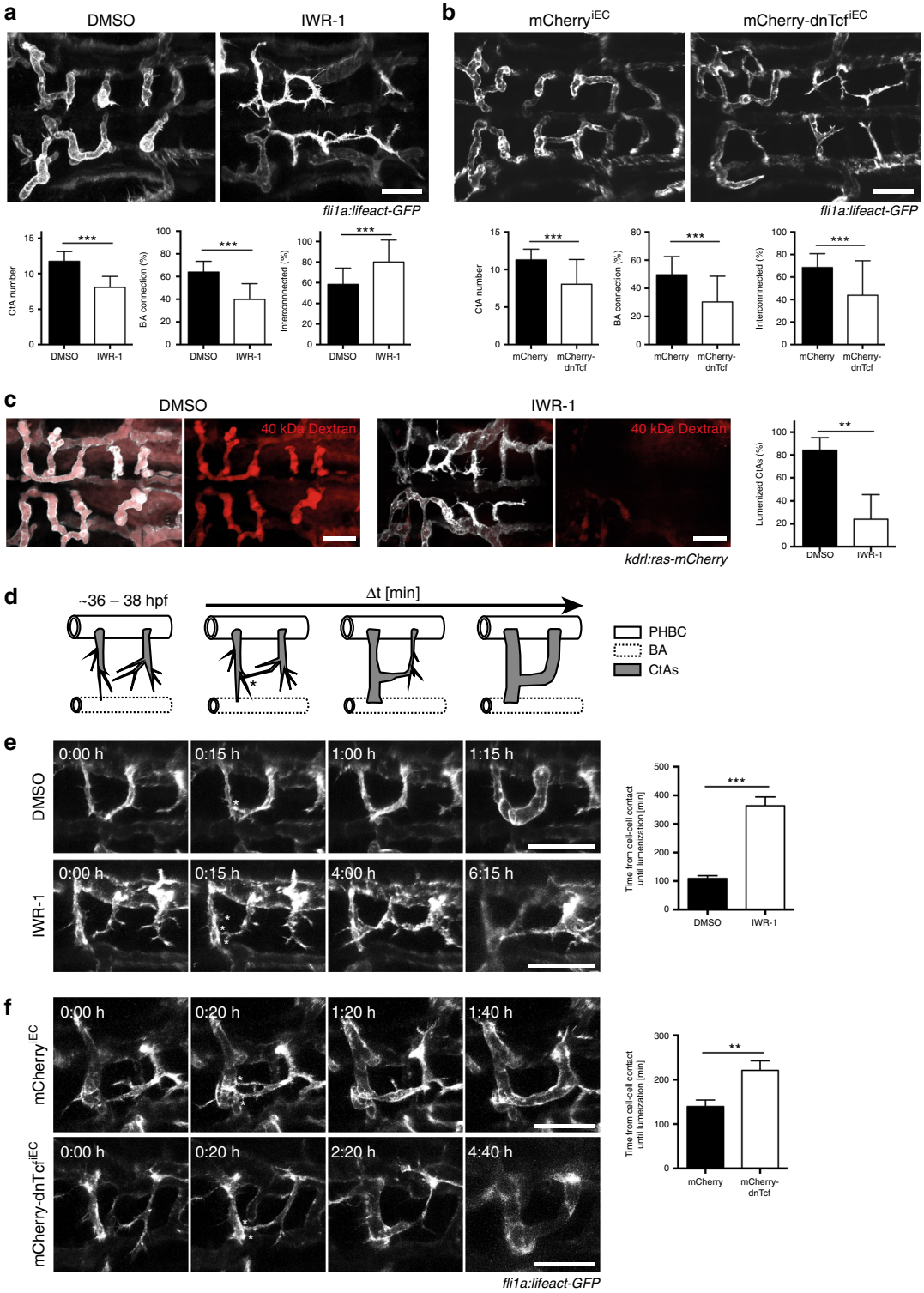

coverage of that area by VE-cadherin. We observed a marked reduction in the length of VE-cadherin junctions and the coverage of cell–cell contact sides by VE-cadherin in ECs isolated from P3 mice. Interestingly, Wnt signaling inhibition did not affect junctional VE-cadherin in adult brain ECs. We conclude that brain capillary ECs from P3 mice are capable of responding to Wnt signaling, presumably because these brain ECs are in a more angiogenic state, whereas ECs from adult mice gain mature BBB properties and are no longer sensitive to Wnt signaling inhibition.

We next analyzed how a complete loss of VE-cadherin affects CtA lumen formation using homozygous *ve-cadherin*^{ubs835} mutant embryos. In *ve-cadherin*^{ubs8}-deficient mutants, CtAs form and invade similarly to wild-type siblings (Supplementary movies 11, 12), but fail to establish stable cell–cell contacts, continuously produce filopodia toward the ECs in neighboring CtAs or BA and fail to form continuous lumens (Supplementary Fig. 4a, b, Supplementary movies 11, 12), a behavior, which mimics our observations after Wnt signaling inhibition (Fig. 2e, f). Interestingly, intracellular signaling via VE-cadherin and its

Fig. 2 Wnt signaling is crucial for brain capillary patterning and anastomosis. **a**, **b** Inhibition of Wnt signaling by IWR-1 treatment (**a**) or dnTcf expression (**b**) impaired CtA patterning. **a** IWR-1 treatment from 29 to 48 hpf reduced CtA number ($n = 39$) and the proportion of CtAs connecting to the BA ($n = 39$), but increased the proportion of interconnecting CtAs ($n = 33$), compared to DMSO treated embryos (CtA number: $n = 35$; BA connection: $n = 35$; interconnected: $n = 29$). **b** Expression of mCherry-dnTcf^{iEC} through heat shock at 26 hpf reduced the number of CtAs ($n = 40$) and decreased the proportion of CtAs connecting to the BA ($n = 32$) or interconnecting ($n = 32$), compared to mCherry^{iEC} control at 48 hpf (CtA number: $n = 39$; BA connection: $n = 33$; interconnected: $n = 33$). **c** Analysis of lumen formation by fluorescent tracer injection into the blood stream at 48 hpf. Treatment with IWR-1 decreased the proportion of lumenized CtAs ($n = 16$) compared to DMSO control ($n = 18$). **d** Schematic representation of CtA anastomosis (dorsal view, ~36 hpf). CtA sprouts (gray) migrate, extend filopodia and form cell–cell contacts to neighboring CtA sprouts (asterisk) or the BA. Cell–cell contact formation triggers anastomosis, cell rearrangements and lumen formation through the connected sprouts in a distinct time window (Δt). **e**, **f** Inhibition of Wnt signaling drastically extended the time window from cell–cell contact formation until lumen formation. Still images from time-lapse movies embryos treated with DMSO (**e**: $n = 58$, $N = 9$) or IWR-1 (**e**: $n = 33$, $N = 9$) or expressing mCherry^{iEC} (**f**: $n = 36$, $N = 6$) or mCherry-dnTcf^{iEC} (**f**: $n = 39$, $N = 8$) after heat shock treatment at 26 hpf. Note that for events, where lumen formation was not completed until the end of the time-lapse recording (~48 hpf), the last measured time point was used for quantification. Confocal images show dorsal views (anterior to the left) of *Tg(fli1a:lifeact-GFP)^{mu240}* (**a**, **b**, **e**, **f**) or *Tg(kdrl:ras-mCherry)^{s896}* (**c**) embryos. Values represent mean ± SD (**a**–**c**) or ± SEM (**e**, **f**). $^{*}p < 0.05$, $^{**}p < 0.01$, $^{***}p < 0.001$, Student's *t*-test; *n* number of analyzed embryos (**a**–**c**) or *n* number of CtA fusion events analyzed; *N*, number of embryos analyzed (**e**, **f**). BA, basilar artery; CtAs, central arteries; ECs, endothelial cells; Scale bars: 50 μm

association with intracellular adaptor proteins seems to be required, as overexpression of VE-cadherin lacking the intracellular domain could not rescue the lumen formation defects (Supplementary Fig. 4d). Additionally, rescuing the *ve-cadherin^{ubs8}* mutant by expression of endogenous levels of the VE-cadherin tension sensor (VE-cad-TS)[36,37] did not completely restore wild-type VE-cadherin function, (Supplementary Fig. 4a), indicating that the presence of the fluorophores within the intracellular domain of VE-cadherin reduces its signaling somewhat. We also analyzed lumen formation of CtAs in *esama^{ubs1924}* mutant embryos. Homozygous *esama^{ubs19}* mutants displayed fewer lumenized CtAs compared to heterozygous controls (Supplementary Fig. 4c). We conclude that VE-cadherin is required for CtA anastomosis and that Esama contributes to efficient CtA lumen formation, which is in agreement with previous reports[23,24]. Therefore, we reason that the lumen formation defects caused by Wnt signaling inhibition were the result from decreased VE-cadherin and Esama protein levels at the cell–cell contact sites in CtAs.

Wnt does not regulate transcription of *ve-cadherin* and *esama*. We hypothesized that the reduced protein levels of VE-cadherin and Esama could result from reduced transcription in embryos lacking Wnt signaling. In order to analyze *ve-cadherin* and *esama* mRNA expression levels, we performed whole mount fluorescent in situ hybridization (FISH) after Wnt signaling inhibition by IWR-1 or EC-specific mCherry-dnTcf expression (Fig. 4a, b, Supplementary Fig. 4e). We quantified the fluorescence intensity within CtAs at 32 or 42 hpf and normalized the fluorescence intensity to the respective CtA volume (generated from *Tg(kdrl:GFP)^{s843}* signal). Surprisingly, we did not find severe changes of the overall *ve-cadherin* or *esama* mRNA abundance in CtA ECs at 32 or 42 hpf (Fig. 4a, b, Supplementary Fig. 4e).

At 32 hpf, *ve-cadherin* mRNA was slightly decreased following IWR-1 treatment and slightly increased following mCherry-dnTcf^{iEC} expression. At 42 hpf, at which we detected reduced VE-cadherin protein levels at the cell–cell junctions (Fig. 4b), *ve-cadherin* mRNA was increased using either of the Wnt signaling inhibition approaches. This indicates, that *ve-cadherin* mRNA levels in CtAs were not decreased (as expected from a putative Wnt target gene), but rather slightly increased over time, presumably due to a compensatory mechanism. The mRNA level of *esama* in CtA ECs was slightly decreased after Wnt signaling inhibition by IWR-1 or mCherry-dnTcf expression both at 32 and 42 hpf (Fig. S4e).

Additionally, to gain insights into transcriptional changes in CtAs mediated by Wnt signaling inhibition, we isolated Kaede-photoconverted CtA ECs from 1.5 days-old *Tg(fli1a:Gal4)^{ubs3}; (UAS:Kaede)^{rk8}* embryos, which were treated with IWR-1 or DMSO (Fig. 4c, d) and performed gene expression profiling by RNA sequencing. We confirmed that *ve-cadherin* and *esama* expression levels were not regulated by Wnt signaling in sharp contrast to classical Wnt target genes (e.g., *axin2* and *lef1*, Fig. 4d). We also analyzed the effect of Wnt inhibition on *VE-cadherin* mRNA levels by qPCR in BECs isolated from P3 and adult animals. In line with our zebrafish data, we observed no transcriptional regulation of mouse *VE-cadherin* by Wnt signaling (Fig. 4e).

We therefore conclude that post-transcriptional mechanisms account for the changes in protein abundance at brain capillary cell–cell junctions following Wnt signaling inhibition.

Wnt signaling counteracts S1pr1 signaling in angiogenesis. To address how VE-cadherin localization at cell–cell junctions can be regulated during brain angiogenesis, we focused on Sphingosine-1-phosphate (S1p) signaling, as it is known to regulate EC integrity and behavior by modulating junction protein localization and cell contractility[27,28]. In particular, S1p-induced signaling mainly via S1p receptor 1 (S1pr1) has been shown in vivo and in vitro to increase recruitment of Cadherin protein family members, including VE-cadherin and N-cadherin, to the plasma membrane[31,38,39]. Additionally, S1p receptor 3 (S1pr3) was found to function cooperatively with S1pr1 in promoting adherens junction formation in ECs[38], whereas S1p receptor 2 (S1pr2) signaling disrupted EC junctions, thereby increasing vascular permeability[40]. We confirmed that similar to what is seen in mice[30], blocking of S1prs using the pharmacological antagonist VPC23019 (VPC) during barriergenesis (48–72 hpf) resulted in extravasation of red blood cells into the surrounding brain tissue, indicating breakdown of the BBB (Supplementary Fig. 5a).

Our RNA sequencing data showed expression of *s1pr1* and *s1pr5a* as well as very low level expression of *s1pr2* and *s1pr3b* in zebrafish brain capillary ECs (Supplementary Fig. 5b). In order to functionally dissect the contribution of these different S1pr's we validated various pharmacological antagonists by their potency to rescue phenotypes of S1pr overexpression (Supplementary Fig. 5c–g). In the zebrafish, VPC seems to antagonize the tested S1pr's (S1pr1, S1pr2, S1pr3a, and S1pr5a), whereas TY52156 (TY) acts specifically on S1pr1. In our hands the S1pr2 antagonist JTE013 (JTE) did not rescue S1pr2 overexpression (Supplementary Fig. 5c–g).

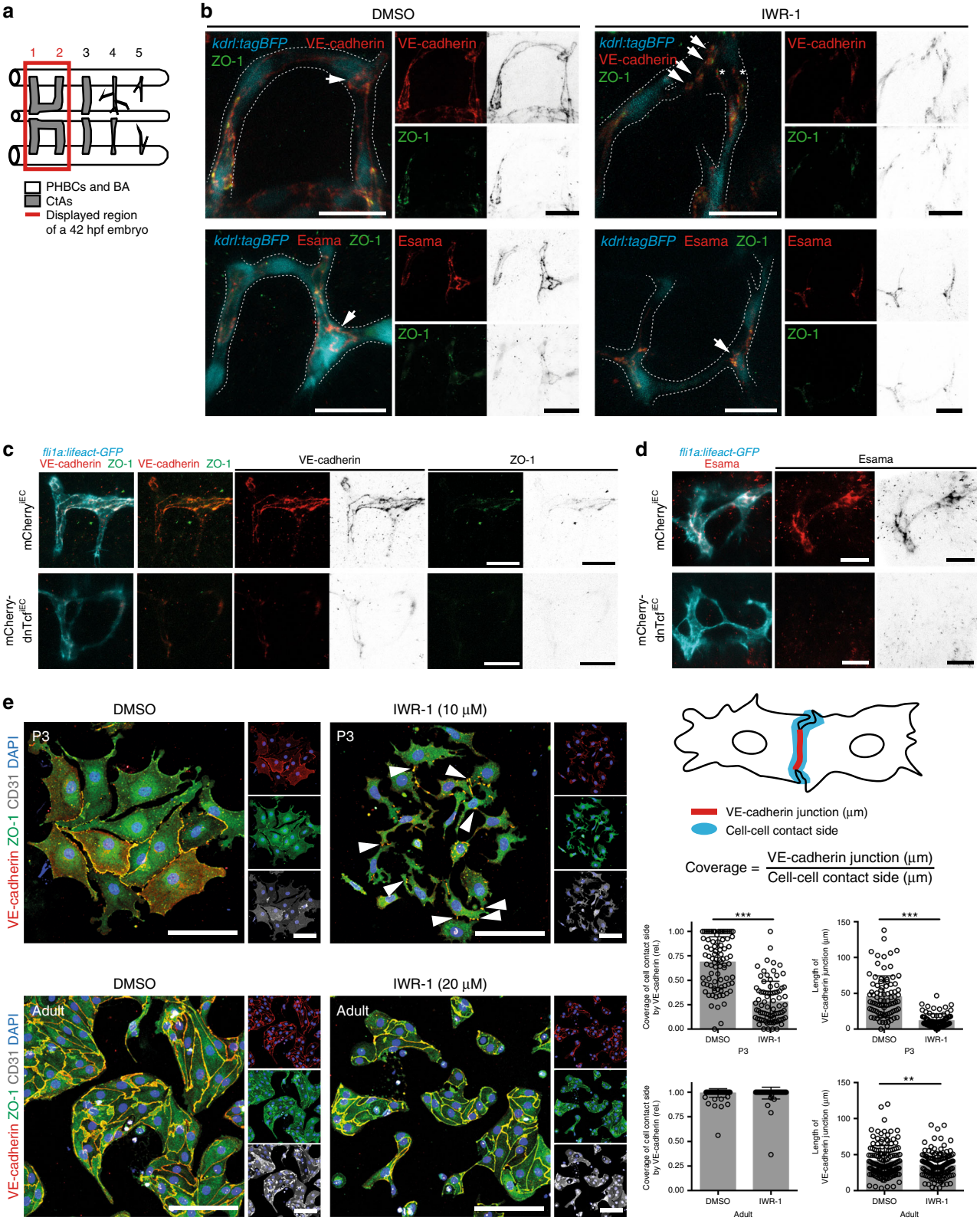

To test the effects of S1pr inhibition on lumen formation and VE-cadherin localization, we next applied the antagonists of S1pr signaling during CtA angiogenesis at 29 hpf and assessed patterning and lumen formation at 48 hpf. In contrast to barriergenesis, treatment during brain angiogenesis with either VPC or TY did not affect CtA development and lumen formation in zebrafish (Fig. 5a). It is therefore likely that in wild-type embryos S1pr signaling is required only after the onset of blood circulation in CtAs, presumably through delivery of high amounts of its ligand S1p by the blood[41]. To our surprise, co-treatment of embryos with the Wnt signaling inhibitor IWR-1 and either VPC or TY increased the proportion of lumenized CtAs compared to single IWR-1 treatment and rescued CtA patterning and lumen formation (Fig. 5a). S1pr inhibition by VPC was also able to

Fig. 3 Junctional localization of VE-cadherin and Esama is affected by Wnt signaling inhibition. **a** Schematic of the zebrafish hindbrain vasculature at 42 hpf. Red box indicates region of analysis. In the following images (**b**–**d**) half of the boxed region is displayed. **b**–**d** Inhibition of Wnt signaling by IWR-1 from 29 hpf (**b**) or by dnTcf expression (**c**, **d**) strongly reduced expression of VE-cadherin or Esama and ZO-1 at the cell–cell junctions. Immunostaining for VE-cadherin (**b**, **c**; red) or Esama (**b**, **d**; red) and ZO-1 (**b**, **c**; green). Single channel images were displayed in inverted colors for better visualization. **b** In control embryos (DMSO), VE-cadherin and Esama were detected in cell–cell junctions along the CtAs and in anastomosis rings (arrow). Inhibition of Wnt signaling resulted in reduced staining of VE-cadherin and Esama at the cell junctions, formation of multiple small anastomosis rings (arrows) and ectopic VE-cadherin-positive cell protrusions (asterisks). **c**, **d** In control embryos (mCherry^{iEC}), VE-cadherin and Esama are strongly expressed in cell–cell junctions. Expression of mCherry-dnTcf^{iEC} dramatically reduced VE-cadherin and ZO-1 (**c**) or Esama (**d**) at the cell–cell junctions. **e** Primary mouse BECs enriched from microvascular fragments from P3 mice exhibited impaired VE-cadherin junction formation following Wnt signaling inhibition by IWR-1 (DMSO: $n = 86$; IWR: $n = 80$; $N = 4$). In contrast, BECs isolated from adult mice had coverage of cell–cell contact sides by VE-cadherin similar to control (DMSO: $n = 143$; IWR-1: $n = 130$; $N = 4$). Immunostaining for VE-cadherin (red), ZO-1 (green), CD31 (white), and DAPI (blue) of cultured primary mouse BECs after treatment with IWR-1 (P3: 10 μM; adult: 20 μM) or DMSO, respectively. Values represent mean ± SD. *$p < 0.05$, **$p < 0.01$, ***$p < 0.001$, Student's *t*-test; *n*, number of analyzed junctions; *N*, number of biological replicates. BECs, brain ECs, CtAs, central arteries; ECs, endothelial cells; Scale bars: 20 μm (**b**–**d**); 100 μm (**e**)

rescue EC-specific loss of Wnt signaling in embryos over-expressing mCherry-dnTcf^{iEC} (Fig. 5b).

We further analyzed, whether not only lumen formation, but also VE-cadherin and Esama levels at cell–cell junctions were rescued by inhibiting S1pr signaling in Wnt-depleted embryos. We observed that the reduced VE-cadherin and Esama localization at cell–cell contact sides and in anastomosis rings after IWR-1 treatment was restored by co-treatment with the S1pr1 antagonist TY and similar to control embryos when analyzed either by immunostaining for VE-cadherin and Esama or by live imaging of the Venus-fluorophore distribution of the VE-cadherin-TS (Supplementary Fig. 6). Hence, blocking of S1pr1 in parallel to IWR-1 treatment was sufficient to rescue VE-cadherin and Esama protein levels at cell–cell junctions. In line with these results, inhibition of S1pr signaling by VPC restored VE-cadherin-positive junctions in IWR-1 treated P3 BECs (Fig. 5c).

As an alternative approach to pharmacological S1pr1 inhibition in zebrafish, we used transient CRISPR-Cas9-mediated *s1pr1* knockdown in combination with IWR-1 treatment. This manipulation restored lumen formation of CtAs (Fig. 5d) similar to VPC or TY treatment (Fig. 5a). Furthermore, Wnt signaling inhibition was unable to affect VE-cadherin localization in *S1pr1^{iEC}* knockout BECs isolated from P3 mice (Fig. 5e).

Therefore, loss of S1pr1 signaling rescued Wnt depletion phenotypes, such as impaired lumen formation and VE-cadherin localization. Taken together, the studies reveal that Wnt signaling regulates brain capillary angiogenesis by counteracting S1pr1 signaling in zebrafish and mouse ECs, presumably to prevent premature barrier formation, which would impair brain angiogenesis (Fig. 5f).

Wnt signaling prevents S1pr1-mediated Rac1 activation. So far we have shown that Wnt signaling regulates brain capillary angiogenesis in an EC-specific manner by post-transcriptionally influencing VE-cadherin localization. Furthermore, the mislocalization of VE-cadherin caused by Wnt signaling inhibition was dependent on S1pr1 signaling (Fig. 5, Supplementary Fig. 6). In order to understand the regulatory interaction of these two signaling pathways, we addressed at which level Wnt signaling interferes with S1pr1 signaling activation. We therefore stimulated S1pr1 signaling using a combination of two agonists (CYM5541 and CYM5542; validation for agonist activity, see Supplementary Fig. 5h). Overstimulation of S1pr1 signaling activity did not induce lumen formation defects (Fig. 6a) and therefore did not overcome the intrinsic counteraction by Wnt signaling. However, block of S1pr signaling in *ve-cadherin* or *esama*-deficient embryos did not result in a rescue of lumen formation defects (Supplementary Fig. 7a). Therefore, Wnt signaling antagonizes S1pr1 signaling downstream of receptor activation, but upstream of VE-cadherin and Esama function.

One potential mechanism that could account for the downregulation of VE-cadherin could be the regulation of VE-cadherin degradation or internalization. We therefore inhibited proteasomal degradation by MG132, dynamin-dependent internalization by Dynasore and lysosomal degradation by Chloroquine; however, none of these treatments rescued Wnt-deficiency (Supplementary Fig. 7b, c). Interestingly, we also observed a mislocalization of VE-cadherin to seemingly intracellular vesicular structures in Wnt signaling-deficient BECs (Fig. 6b), indicating changes in cellular architecture rather than VE-cadherin degradation following Wnt signaling inhibition.

S1p-induced signaling in cultured ECs has been linked to activation of the Rho/Rac-pathway for stabilization of the cytoskeleton and recruitment of junction proteins to the cell membrane[38,42,43]. Similar to S1pr signaling, Rac1 activation as well as Rho inactivation is known to promote EC barrier function in mature blood vessels[44]; however, their contribution to brain capillary angiogenesis has not been addressed yet. We therefore applied the pharmacological Rac1 inhibitor (NSC23766, NSC) or Rho inhibitor (CT03) alone or together with IWR-1 as described. Single treatment with either Rac1 or Rho inhibitors, did not affect CtA development or lumen formation. Indeed, co-treatment of IWR-1 and Rac1 inhibitor, but not of IWR-1 and Rho inhibitor, robustly restored the lumen formation defects caused by IWR-1 (Fig. 6c, Supplementary Fig. 8a).

We hypothesized that if Rac1 was mediating premature S1pr1 signaling activation, overexpression of constitutive-active Rac1 (CA-Rac1) should phenocopy Wnt signaling inhibition. Therefore, we mated *Tg(fli1a:Gal4)^{ubs3}* fish with *Tg(UAS:CA-Rac1)^{mu211}* and analyzed brain capillary lumen formation in 48 hpf-old embryos (Fig. 6d). Vascular-specific overexpression of CA-Rac1 caused strong lumen formation defects and was accompanied by multiple filopodia contact sides comparable to IWR-1-treated (Fig. 2a) or *ve-cadherin*-deficient (Supplementary Fig. 4a) embryos. Additionally, vascular-specific Gal4-UAS-mediated overexpression of dominant negative Rac1 (DN-Rac1, from *Tg(UAS:DN-Rac1)^{mu212}*) could partially rescued lumen formation in IWR-1-treated embryos (Fig. 6e).

Hence, Rac1 activation downstream of S1pr1 signaling is required and sufficient to mediate lumen formation defects caused by Wnt signaling inhibition.

In summary, we identified a temporal-specific function of Wnt signaling for brain capillary angiogenesis by post-transcriptionally and EC-specifically regulating junction protein localization upstream or at the level of Rac1 activity, but downstream of S1pr1 signaling. We suggest that EC-specific Wnt signaling

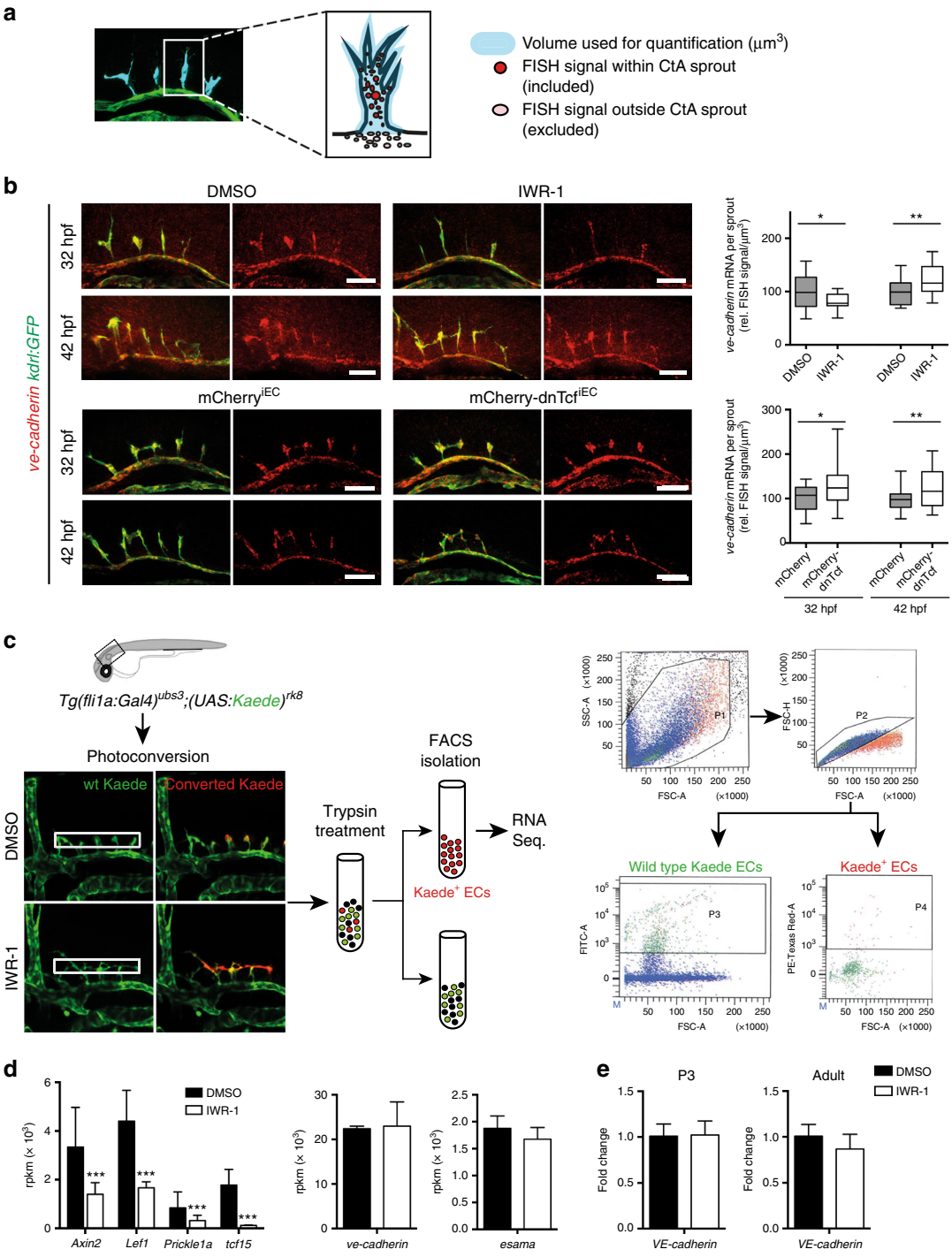

Fig. 4 Wnt signaling does not regulate *ve-cadherin* mRNA expression. **a** Whole mount fluorescent in situ hybridization (FISH, red) in combination with anti-GFP immunostaining (green) of *Tg(kdrl:GFP)*^{s843} embryos. For quantification the FISH signal within CtA sprouts was normalized to the respective GFP volume (blue) of each sprout. **b** Inhibition of Wnt signaling either by incubation with IWR-1 or expression of mCherry-dnTcf^{iEC} did not severely affect *ve-cadherin* mRNA expression at 32 or 42 hpf. Treatment with IWR-1 resulted in slightly decreased *ve-cadherin* mRNA levels in CtA sprouts at 32 hpf, but in increased *ve-cadherin* mRNA levels at 42 hpf (32 hpf: DMSO: $n = 16$, $N = 6$, and IWR-1: $n = 15$, $N = 6$; 42 hpf: DMSO: $n = 28$, $N = 7$, and IWR-1: $n = 19$, $N = 7$). After mCherry-dnTcf^{iEC} expression in ECs *ve-cadherin* mRNA expression was slightly increased (32 hpf: mCherry^{iEC}: $n = 20$, $N = 6$; mCherry-dnTcf^{iEC}: $n = 18$, $N = 7$; 42 hpf: mCherry^{iEC}: $n = 40$, $N = 7$; mCherry-dnTcf^{iEC}: $n = 16$, $N = 7$). Quantifications were represented by Box-and-Whisker plots with median (center line), 25th and 75th percentiles (bounds of box) and Min-to-Max (whiskers), $*p < 0.05$, $**p < 0.01$, $***p < 0.001$, Student's *t*-test; *n,* number of CtA volumes analyzed; *N,* number of embryos analyzed. Scale bars: 50 µm. **c**, **d** Expression levels of *ve-cadherin* or *esama* were not altered by inhibition of Wnt signaling, whereas classical Wnt-target genes (e.g., *axin2*, *lef1*) were downregulated. For RNA sequencing, CtA ECs of *Tg(fli1a:Gal4);(UAS:Kaede)* embryos, which were treated with IWR-1 or DMSO, were photoconverted using the confocal microscope laser and isolated by FACS (photoconverted Kaede ECs = Kaede^{+} cells = P4) ($n = 3$). **e** Expression levels of *VE-cadherin* are not affected by IWR-1 treatment. RT-qPCR analysis of Values in **d**, **e** represent mean ± SD, $*p < 0.05$, $**p < 0.01$, $***p < 0.001$, *n,* number of biological replicates. BECs, brain ECs, CtAs, central arteries; ECs, endothelial cells; FISH, fluorescent in situ hybridization

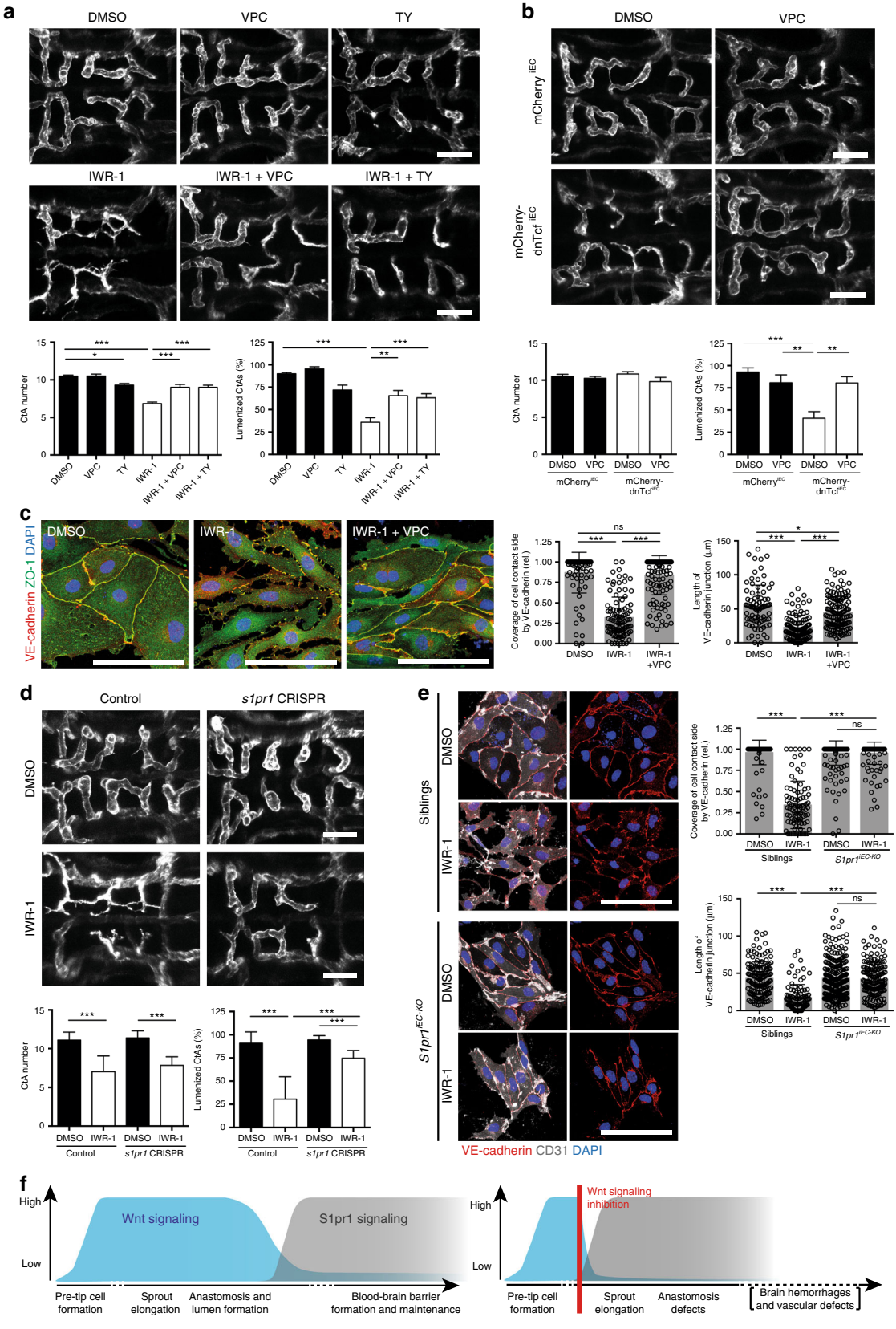

counteracts S1pr1 signaling during CtA angiogenesis, presumably to prevent premature barrier formation processes, which would impair brain angiogenesis (Fig. 6f,g).

Interestingly this mechanism seems to be specific to the role of Wnt signaling in regulating anastomosis and lumen formation, but not to the essential function of Wnt signaling during the earlier pre-tip cell phase[12,15]. Treatment of embryos lacking Wnt signaling following IWR-1 treatment or of *gpr124* mutants with S1pr antagonists did not restore CtA sprout formation (Supplementary Fig. 8b, c).

Fig. 5 Wnt signaling counteracts S1pr1 signaling during brain capillary angiogenesis. **a** Treatment with Sphingosine-1-phoshate receptor (S1pr) antagonists from 29 to 48 hpf did not affect CtA angiogenesis. Combining inhibition of Wnt signaling with antagonizing S1pr signaling led to a rescue of CtA angiogenesis and lumen formation. Embryos were single or co-treated with IWR-1 and S1pr antagonists VPC23019 (VPC), and TY52156 (TY) (DMSO: $n = 23$; VPC: $n = 8$; TY: $n = 10$; IWR-1: $n = 33$; IWR-1 + VPC: $n = 10$; IWR-1 + TY: $n = 15$). **b** Antagonizing S1pr signaling following EC-specific dnTcf expression rescues CtA lumen formation defects. Embryos expressing mCherry^{iEC} or mCherry-dnTcf^{iEC} were treated with VPC following heat shock at 26 hpf. (mCherry^{iEC}: DMSO: $n = 4$, VPC: $n = 4$; mCherry-dnTcf^{iEC}: DMSO: $n = 6$, VPC: $n = 5$). **c** Co-treatment with VPC restored the VE-cadherin junction formation defects of IWR-1-treated primary mouse BECs (from P3 animals; DMSO: $n = 84$; IWR-1: $n = 100$; IWR-1 + VPC: $n = 134$; $N = 3$). **d** Transient CRISPR-Cas9-mediated knockout of *s1pr1* resulted partial rescue of the lumen formation defects in Wnt-depleted embryos. Embryos were injected with gRNA targeting *s1pr1* and *cas9* mRNA (*s1pr1* CRISPR) or *cas9* mRNA (control) and treated with IWR-1 from 29 to 48 hpf (control: DMSO: $n = 11$, IWR-1: $n = 12$; s1pr1 CRISPR: DMSO: $n = 8$, IWR-1: $n = 12$). **e** EC-specific knockout of S1pr1 (*S1pr1*$^{iEC\text{-}KO}$) caused insensitivity to IWR-1 in mouse primary BECs. BECs isolated from *S1pr1*$^{iEC\text{-}KO}$ animals at P3 showed no difference in VE-cadherin junction formation after DMSO or IWR-1 treatment in contrast to control siblings (siblings: DMSO: $n = 152$; IWR: $n = 92$; $N = 4$; *S1pr1*$^{iEC\text{-}KO}$: DMSO: $n = 240$; IWR: $n = 156$; $N = 5$). **f** Illustration of Wnt and S1pr1 signaling during brain vascularization in wild type and Wnt-depleted embryos. Confocal images of zebrafish embryos (**a**, **b**, **d**) show dorsal views (anterior to the left) and GFP expression by *Tg(fli1a:lifeact-GFP)*^{mu240}. Images of mouse BECs (**c**, **e**) display immunostaining for VE-cadherin (red), ZO-1 (green), and DAPI (blue). Values represent mean ± SEM (**a**, **b**) or mean ± SD (**c**–**e**). $^{*}p < 0.05$, $^{**}p < 0.01$, $^{***}p < 0.001$, One-way ANOVA; *n*, number of analyzed embryos (**a**, **b**, **d**); *n*, number of analyzed junctions, *N*, number of biological replicates (**c**, **e**); BECs, brain ECs, CtAs, central arteries; ECs, endothelial cells; ns, not significant; S1pr, sphingosine-1-phosphate receptor; Scale bars: **a**, **b**, **d** = 50 µm; **c**, **e** = 100 µm

In conclusion, we describe a temporal control of different steps of brain angiogenesis and BBB formation, which are differentially regulated by Wnt signaling. We also discover an interplay between Wnt and S1pr signaling during brain angiogenesis.

Discussion

We addressed the role of β-catenin-dependent Wnt signaling during early brain capillary angiogenesis in vivo. We found that (1) Wnt signaling is highly active in brain capillary sprouts, but after pre-tip cell formation it is dispensable for brain capillary invasion into the brain parenchyma. Instead, (2) Wnt signaling is required for brain capillary anastomosis. During this process, (3) Wnt signaling influences the post-transcriptional regulation and cell–cell junction localization of the EC-specific adhesion molecules, VE-cadherin, and Esama, by counteracting S1pr1 signaling (Fig. 6f, g).

We and others have shown that Wnt signaling is active in brain capillaries during brain angiogenesis (Fig. 1,[11,12,14]). Recent reports demonstrate that Gpr124-Reck-mediated Wnt signaling is essential for brain vascularization, as homozygous *grp124* or *reck* mutants are completely devoid of brain capillaries[12,15–17]. We hypothesized that Wnt signaling might be involved in the formation of pre-tip cells within the parental vessel, which most likely occurs at earlier developmental stages[12]. In line with this, a role of Wnt signaling for EC specification has already been suggested to drive cell fate from the Fli1a-positive precursor cell population into ECs at the expense of primitive erythrocytes[33]. At later developmental stages, Wnt signaling is required for subspecification of EC populations within the vasculature, which has been shown for hemogenic EC formation[45,46] and lymphatic cell fate specification[47].

Here we demonstrate that Wnt signaling is continuously activated in CtAs during all stages of angiogenesis. Surprisingly, Wnt signaling is not involved in the process of CtA sprout invasion and filopodia formation (Fig. 1).

However, our data demonstrate that Wnt signaling is essential for brain capillary anastomosis (Fig. 2). During the anastomosis process in intersegmental vessels, VE-cadherin is required for cell–cell contact formation and together with Esama has been shown to be essential for efficient blood vessel fusion[23,24]. We detected reduced protein levels of VE-cadherin, Esama, and ZO-1 at the cell–cell junctions following Wnt signaling inhibition (Fig. 3), which presumably impair anastomosis and lumen formation. In line with these findings, knockouts of VE-cadherin (by *ve-cadherin*$^{ubs8/ubs8}$) or Esama (by *esama*$^{ubs19/ubs19}$) phenocopied CtA lumen formation defects (Supplementary Fig. 4). Surprisingly, neither *ve-cadherin* nor *esama* are transcriptional targets of Wnt signaling (Fig. 4). Similar to Hupe and colleagues, we detected mildly increased amounts *ve-cadherin* mRNA when Wnt signaling inhibition persists for longer time intervals (>12 h), indicating a compensatory response to the reduced protein levels of VE-cadherin at cell–cell junctions[48]. We therefore conclude that VE-cadherin and Esama downregulation occurs via a post-transcriptional mechanism, which interferes with their membrane localization. Using a series of inhibitors, we excluded internalization as well as proteasomal and lysosomal degradation as potential mechanisms (Supplementary Fig. 7). Previously, Wnt signaling has been shown to be required for the junction localization of Claudin 1 and 3 in murine brain ECs during BBB formation, but no direct transcriptional regulation has been detected[13,14]. As there have been no mechanisms proposed of how Wnt signaling could regulate these junctional molecules, we speculate that they might also be downregulated post-transcriptionally as a consequence of imbalanced S1pr signaling.

The concept that S1pr signaling regulates EC integrity by modulating translocation of junction proteins and actomyosin contractility is widely accepted[27,28]. So far, S1pr signaling has not been linked to brain capillary angiogenesis and our data also indicate that the endogenous S1pr signaling is neither required for CtA tip cell specification (Supplementary Fig. 5) nor for other aspects of CtA angiogenesis (Fig. 5). However, as recently shown in mice[30], we demonstrate that S1pr signaling indeed regulates BBB formation and integrity in zebrafish (Supplementary Fig. 5). Moreover, our data points to a novel regulatory mechanism of Wnt signaling during brain capillary angiogenesis, which is to counteract S1pr-induced BBB formation in order to ensure efficient anastomosis (Fig. 5). We propose that Wnt signaling suppresses S1pr1-mediated signaling in CtAs during early stages of brain vascularization. After lumen formation, Wnt signaling activity within brain capillaries decreases to a low baseline level (Fig. 1[14]). In lumenized vessels, activation of S1pr signaling would occur and be most likely enhanced by increased supply of the ligand S1p through the blood circulation[41], which would enable functional S1pr signaling for BBB formation and maintenance (Supplementary Fig. 5).

It seems likely that the S1pr1-mediated pathway signals via $G_{\alpha i}$ and activates Rac1 (Fig. 6[27,49]). We hypothesize that overactivation of Rac1 after Wnt signaling inhibition interferes with efficient cellular junction formation during brain capillary angiogenesis. To date, Rac1 activation is well described to promote EC barrier formation in mature blood vessel[44], indicating

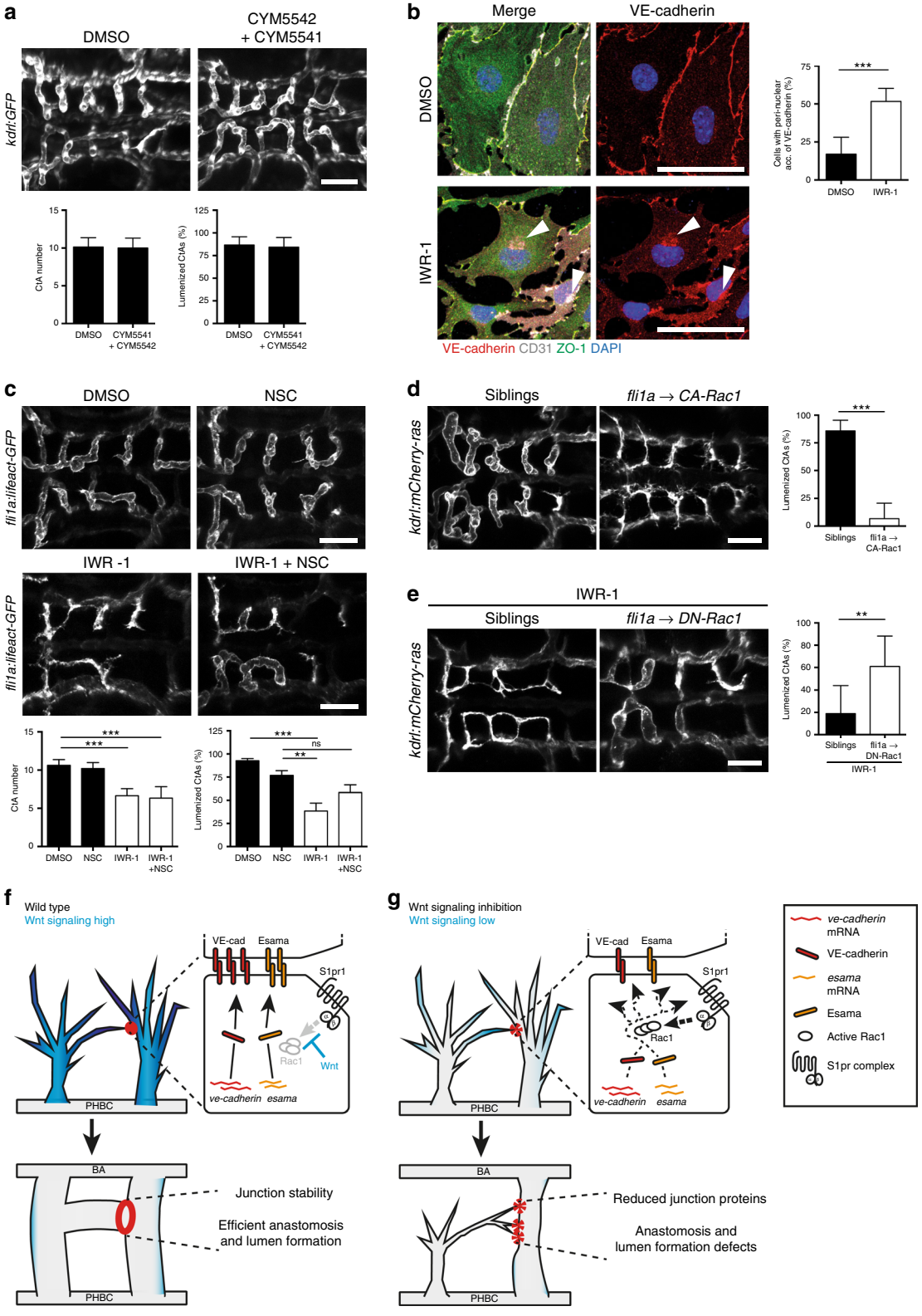

that Rac1 can act downstream of S1pr signaling in barriergenesis[27]. However, we demonstrate a different regulation in Wnt-responsive brain capillary ECs during capillary angiogenesis, which is similar to our observation of S1pr signaling regulation (Fig. 5). Our data in zebrafish and mouse BECs clearly show altered responsiveness of the ECs to Wnt inhibition depending on their developmental state. This indicates that S1pr-Rac1-mediated regulation of VE-cadherin is differently affecting the modulation of established junctions in mature blood vessels compared to junctions newly forming during brain angiogenesis.

Additionally, over-activation of Rac1 could destabilize junction molecule complexes, as has been shown for initial stages of pharyngeal pouch formation in zebrafish[50]. In this study, the authors suggested that Wnt signaling mediates activation of Rac1 by an unknown mechanism[50]; however, a possible role of S1pr signaling has not been addressed. The authors also observed a

Fig. 6 Wnt signaling regulates S1pr1 signaling downstream of receptor activation. **a** Treatment of zebrafish embryos with S1pr agonists did not result in CtA formation or anastomosis defects. Wild-type embryos were treated from 29 to 48 hpf with S1pr agonists (CYM5541 and CYM5542) or DMSO (DMSO: $n = 10$; agonists: $n = 10$). **b** High resolution imaging of IWR-1-treated mouse primary BECs revealed intracellular accumulation of VE-cadherin. BECs isolated from P3 animals were treated with IWR-1 or DMSO (DMSO: $n = 12$; IWR-1: $n = 12$; $N = 4$). **c** Inhibition of Rac1 rescued lumen formation defects of CtAs in Wnt-depleted embryos. Embryos were single or co-treated with IWR-1 and NSC23766 (NSC, Rac1 inhibitor) from 29 to 48 hpf. (DMSO: $n = 8$; NSC: $n = 10$; IWR-1: $n = 14$; IWR-1 + NSC: $n = 12$). **d** EC-specific overexpression of CA-Rac1 results in lumen formation defects. Analysis of *Tg(fli1a:Gal4)*^{ubs3}*;(UAS:CA-Rac1)*^{mu211} embryos and control siblings at 48 hpf (siblings: $n = 15$, CA-Rac1: $n = 17$). **e** EC-specific overexpression of DN-Rac1 partially rescues IWR-1-induced lumen formation defects. Treatment of *Tg(fli1a:Gal4)*^{ubs3}*;(UAS:DN-Rac1)*^{mu212} embryos and control siblings with IWR-1 from 29 to 48 hpf (siblings: $n = 17$, DN-Rac1: $n = 5$). **f**, **g** Molecular events of brain capillary anastomosis in wild type (**f**) and Wnt-depleted (**g**) embryos. Wnt signaling is highly active in wild-type brain capillary sprouts (**f**, dark blue), which allows for efficient localization of VE-cadherin (red) and Esama (yellow) to cell–cell junctions, thus resulting in rapid anastomosis and lumen formation. Following Wnt signaling inhibition (**g**), brain capillary anastomosis is compromised due to VE-cadherin and Esama mislocalization caused by premature S1pr1 signaling, which involves activation of Rac1. Confocal images of zebrafish embryos (**a**, **c**, **d**, **e**) show dorsal views (anterior to the left) and EC-labeling GFP or mCherry as indicated. Images of mouse BECs (**b**) display immunostaining for VE-cadherin (red), CD31 (white), ZO-1 (green), and DAPI (blue). All values represent mean ± SD. $^{*}p < 0.05$, $^{**}p < 0.01$, $^{***}p < 0.001$, One-way ANOVA; *n* number of analyzed embryos (**a**, **c**, **d**, **e**); *n*, number of analyzed embryos, *N*, number of biological replicates (**b**); BBB, blood-brain barrier, BECs, brain ECs, CtAs, central arteries; ECs, endothelial cells; ns, not significant; S1pr, sphingosine-1-phosphate receptor; Scale bars: **a**, **c**, **d**, **e** = 50 µm; **b** = 100 µm

reduced membrane localization of the adherens junction molecules E-Cadherin and Alcama after Wnt signaling inhibition by morpholino-mediated knockdown of Disheveled, which is in line with our findings during brain angiogenesis. We therefore speculate that similarly to brain capillary ECs, Wnt signaling regulates Rac1-mediated S1pr signaling and thereby modulate junction localization of adhesion molecules also during pharyngeal pouch formation.

During brain neo-vascularization, we and others report divers functions of Wnt signaling, which regulate many steps of brain capillary angiogenesis and BBB formation and cross-communicate with other signaling cues[51]. First, Wnt signaling is required for the formation of the brain capillary pre-tip cells within the parental vessel, which is dependent on a functional Gpr124-Reck co-receptor complex[12,15–18]. Second, Wnt signaling limits S1pr signaling during brain capillary sprouting and promotes brain capillary anastomosis through efficient VE-cadherin and Esama localization to the membrane (as shown in this work). And third, Wnt signaling leads to the induction of BBB components, such as glucose transporter Glut1 and Claudin family members, already during brain angiogenesis in order to subsequently establish a functional BBB after brain angiogenesis has been completed[10,26,48,52] and sealing of the BBB is likely to be promoted by S1pr signaling after the onset of blood circulation (Supplementary Fig. 5[30,41]). The complexity of the signaling network regulating EC behavior during brain angiogenesis and BBB formation is far from being understood. Our study provides a regulatory function of Wnt signaling during brain angiogenesis, which was only unraveled by interfering with Wnt signaling in a temporally and spatially restricted manner in combination with in vivo time-lapse imaging. We were able to identify a post-transcriptional level of regulation, which is essential for cell–cell junction formation and the modulation of EC barrier establishment or tightness. Therefore, interfering with Wnt or S1p signaling during treatment of infectious and neurodegenerative diseases as well as anti-cancer therapy remains a major clinical obstacle as adverse effects and cross-reactions are not well predictable[30,53–55]. The FDA approved sphingosine analog and agonist of S1pr1 and S1pr3–5 called Fingolimod (FTY720/Gilenya) has been reported to cause side effects of increased of vascular permeability in the lung and cardio-vascular complications. Moreover, cases with neuroencephalitis were noted when the drug was applied at higher doses. Therefore, the evaluation of the potential clinical impact for CNS development and pathology of these and future substances requires a greater understanding of signaling cues regulating EC properties and behavior.

Methods

Zebrafish husbandry and strains. Zebrafish (*Danio rerio*) husbandry and embryo maintenance were carried out under standard conditions at 28.5 °C[56]. Embryonic developmental stages were determined according to ref. [57].

Transgenic lines used in this study were *Tg(14TCF:loxP-STOP-loxP-dGFP)*^{mu20233}, *Tg(axin2*$_{BAC}$*:Venus-Pest)*^{mu28833}, *Tg(fli1a:dsRed)*^{um1358}, *Tg(fli1a:lifeact-GFP)*^{mu24059}, *Tg(fli1a:nGFP)*^{y760}, *Tg(fli1ep:Gal4ff)*^{ubs361}, *Tg(gata1:dsRed)*^{sd262}, *Tg(kdrl:cre)*^{s89863}, *Tg(kdrl:GFP)*^{s84364}, *Tg(kdrl:mKate2-CAAX)*^{ubs1623}, *Tg(kdrl:Hras-mCherry)*^{s89665}, *Tg(kdrl:tagBFP)*^{mu29366}, *Tg(UAS:Kaede)*^{rk867}, *Tg(UAS:VE-cadherinΔC-EGFP)*^{ubs1223} and *Tg(ve-cad*$_{BAC}$*:ve-cadTS)*^{uq11bh} (referred as VE-cadTS)[36]. Mutants used in this study were *esama*^{ubs1924}, *gpr124*^{s98412} and *ve-cadherin*^{ubs835}.

The *Tg(UAS:CA-Rac1)*^{mu211} and *Tg(UAS:DN-Rac1)*^{mu212} lines were generated by injection of plasmids, which were a gift from Gage Crump[50], and according to standard transgenesis protocol[68]. Both constructs harbor *α-crystallin:cerulean*, inducing blue fluorescence in the lenses at 48 hpf. To overexpress CA-Rac1 and DN-Rac1 in the vasculature the respective fish were mated to *Tg(fli1ep:Gal4ff)*^{ubs3}*;(kdrl:Hras-mCherry)*^{s896}. Please note, that in the case of DN-Rac1 overexpression, all embryos were presorted for established circulation in PHBC and BA prior to analysis by confocal microscopy as we most likely obtained multiple integrations of the construct and thereby varying phenotypes in the offspring embryos.

Generation of transgenic Wnt-manipulating lines. The *Tg(hsp70l:loxP-STOP-loxP-mCherry-dntcf)*^{mu201} line was generated by fusing the coding sequences of *mCherry*[69] in frame with *dntcf*[70] downstream of a heat shock inducible promoter (hsp70l[69]). A floxed STOP cassette (loxP-STOP-loxP, Hesselson 2009) was inserted upstream of *mCherry* by AflII-SpeI digest. Using the gateway system, *hsp70l:loxP-STOP-loxP-mCherry-dntcf* was cloned into the destination vector pTol2Dest[71].

The *Tg(hsp70l:loxP-STOP-loxP-mCherry)*^{mu279} line was generated by removing the *dntcf* sequence from *Tol2-hsp70l:loxP-STOP-loxP-mCherry-dntcf-Tol2* using AfeI-SnaBI digest followed by Klenow blunting and religation.

For both lines, standard transgenesis was performed[68].

Microinjections. For ubiquitous removal of the floxed STOP cassette by Cre recombinase, 2 nL of *cre* mRNA (200 pg/nL) were injected at single cell stage. Therefore the *cre* coding sequence[69] was cloned into pCS2+ and transcribed into mRNA by using the Sp6 mMessage mMachine kit (Ambion) following NotI-digest as previously described[33].

For overexpression of S1pr's, the coding sequences of *s1pr1*, *s1pr2*, *s1pr3a*, and *s1pr5a* were amplified from 24 hpf-cDNA and cloned into pCS2+ using the following primers (see also Supplementary Table 1): *s1pr1* fwd 5′-ATGGATGACCTAATCGCC-3′, *s1pr1* rev 5′-CGAGACGAAAAAGTTCACG-3′, *s1pr2* fwd 5′-ATGACTACTTGCCGTCTG-3′, *s1pr2* rev 5′-GGGATCTGCAAAC ACTTGG-3′, *s1pr3a* fwd 5′-ATGGATGACGAGCTTGAACC-3′, *s1pr3a* rev 5′-TCAGAACTTCCCCAAAGCG-3′, *s1pr5a* fwd 5′-GGTCAGCAGAAGTGAAA TGG-3′, *s1pr5a* rev 5′-CAGACTTGTTTACTTGGCAG-3′. Transcription into mRNA following NotI-digest was carried out using the Sp6 mMessage mMachine kit (Ambion) as described[33]. Thereafter, 2 nL of 75 ng/µL or 150 ng/µL *s1pr1* mRNA, 10 ng/µL *s1pr2* mRNA, 150 ng/µL *s1pr3a* or 150 ng/µL *s1pr5a* mRNA were injected at single cell stage as indicated for each experiment. For agonist experiments, 75 ng/µL s1pr1 mRNA was additionally supplemented with 200 µM Sphingosine-1-phospate (S1p, Tocris Bioscience, 1370).

For transient CRISPR-Cas9-mediated knockout of *s1pr1*, annealed template oligonucleotides were transcribed into gRNAs using MEGAshortscript T7 Kit (Ambion): *s1pr1* 5′- AAAGCACCGACTCGGTGCCACTTTTTCAAGTTGAT

AACGGACTAGCCTTATTTTAACTTGCTATTTCTAGCTCTAAAACTCTCT-GAAGAACCATTGCGTTATAGTGAGTCGTATTACGC-3′ (*s1pr1* target sequence: 5′-TCTCTGAAGAACCATTGCGT-3′). A total of 2 nL of 500 ng/µL gRNA and 300 ng/µL *nls-zCas9-nls* mRNA[72] or only *nls-zCas9-nls* mRNA as control were injected at single cell stage. Efficacy of the CRISPR-targeting was accessed by PCR using *s1pr1* fwd 5′-TCTATACTGCCAACATCCTG-3′ and rev 5′-CTGATGAGCATGAAGACCC-3′ (see also Supplementary Table 1) and subsequent restriction enzyme digest using Hpy188I. This leads to 136 bp and 69 bp fragments in control samples and additionally ~205 bp fragments in samples obtained from *s1pr1* CRISPR injected embryos.

Vascular-specific Cre-mediated recombination. For vascular-specific removal of floxed STOP-cassettes, transgenic fish (e.g. *Tg(hsp70l:loxP-STOP-loxP-mCherry-dntcf)*^{mu201}) were mated with *Tg(kdrl:cre)*^{s898}. The resulting embryos carrying both transgenes were used for analysis and in the case of heat shock inducible transgenes were labeled by iEC (e.g., mCherry^{iEC}, mCherry-dnTcf^{iEC}).

Heat shock and pharmacological treatments. In order to induce gene expression by heat shock, 26 hpf-old dechorionated embryos were incubated 40 min at 39 °C in pre-warmed E3 medium and analyzed at indicated developmental stages. For validation of the *Tg(hsp70l:loxP-STOP-loxP-mCherry-dntcf)*^{mu201} and *Tg(hsp70l:loxP-STOP-loxP-mCherry)*^{mu279} lines, embryos were incubated at 10 hpf and 15 hpf for 1 h at 39 °C and analyzed at 24 hpf.

For pharmacological treatments, dechorionated embryos were incubated from 5.5 to 24 hpf (for validation of S1pr antagonists), from 29 to 48 hpf or from 26 to 32 hpf in E3 medium supplemented with 150 µM Aphidicolin (A, Sigma-Aldrich)[33], 100 µM Chloroquine (Sigma-Aldrich)[73,74], 10 µM CYM5541 (Sigma-Aldrich), 10 µM CYM5542 (Tocris Bioscience), 80 µM Dynasore (Sigma-Aldrich)[74,75], 20 mM Hydroxyurea (HU, Sigma-Aldrich)[33], 20 µM IWR-1 (Sigma-Aldrich)[33], 50 µM JTE013 (JTE, Cayman Chemical), 10 µM MG132 (Sigma-Aldrich)[74,76], 100 µM NSC23766 (NSC, Sigma-Aldrich), 5 µg/mL Rho Activator II (Cytoskeleton)[59], 2 µg/mL Rho inhibitor CT03 (Cytoskeleton)[59], 100 µM TY52156 (TY, Tocris Bioscience) and 50 µM VPC23019 (VPC, Cayman Chemical). *Tg(hsp70l:loxP-STOP-loxP-mCherry-dntcf)*^{mu201} and *Tg(hsp70l:loxP-STOP-loxP-mCherry)*^{mu279} embryos were incubated directly after heat shock from 27 to 30 hpf with 12.5 µM and from 30 to 48 hpf with 25 µM VPC.

Microinjections of fluorescent dye (angiography). To analyze blood vessel perfusion, 2 nL 40 kDa FITC-Dextran 40 (1 mg/mL; TdB consultancy) were injected into the blood stream of anesthetized embryos at 48 hpf.

Immunohistochemistry of zebrafish embryos. Immunohistochemistry was carried out as previously described[77]. Additionally, primary and secondary antibody dilutions were supplemented 1:1 with Pierce™ Immunostain Enhancer (Thermo Fisher Scientific). Antibodies used in this study: 1:400 rabbit anti-zf-VE-cadherin[77], 1:1000 mouse anti–hZO-1 (Invitrogen, 339100[59]), 1:400 rabbit anti-Esama[23], 1:200 rabbit anti-dnTcf (anti-TCF7L1; Proteintech Group, 14519-1-AP), 1:2000 goat anti-rabbit IgG Alexa Fluor 594 (Invitrogen, A-21207), 1:2000 goat anti-mouse IgG Alexa Fluor 647 (Invitrogen, A-21235), 1:2000 goat anti-mouse IgG Alexa Fluor 488 (Invitrogen, A-11001).

Fluorescent in situ hybrisization (FISH). Fluorescent in situ hybrisization (FISH) was adapted from refs. [78,79]. Briefly: MeOH-fixed embryos were rehydrated, digested with Proteinase K (Roth, 7528.4, 10 µg/mL) for 12 min and refixed in 4% PFA. After washing with PBS containing 0.3% (v/v) Tween and pre-hybridization at 65 °C, embryos were incubated hybridization buffer containing digoxigenin (DIG)-labeled antisense probes at 65 °C for >12 h. Probe removal, blocking, and primary antibody incubation was performed according to the published protocol. Primary antibodies were POD-coupled anti-DIG (Roche, 1:400) and anti-GFP (Abcam, ab6556, 1:400), which was used for counter-staining GFP in transgenic embryos. After removal of the antibody solution, embryos were incubated for 60 min with TSA Plus Cy3 solution (Perkin Elmer, NEL744001KT), washed three times with PBS-Tween to remove excess staining solution and subjected to 1:500 goat anti-rabbit IgG Alexa Fluor 488 (Invitrogen) for 60 min. At last, embryos were washed with PBS-Tween >5 h and sequentially taken up in 75% Glycerol for confocal microscopy.

The antisense probes for *ve-cadherin*[80] and *esama*[24,81] were generated from plasmid templates using T3 or Sp6 polymerase and DIG-labelled UTP (2 h, 37 °C) and purified by precipitation[81].

Photoswitching and FACS isolation of brain capillary ECs. Photoswitching of *Tg(fli1:gal4)*^{ubs3}*;(UAS:kaede)*^{rk8} embryos was performed using a Zeiss LSM 710 confocal microscope (Carl Zeiss, objective lenses: Plan-Apochromat ×20/0.8 M27) after embryo anesthesia with a low dose of tricaine. Embryos were mounted laterally in 1% low-melting agarose in glass-bottom Petri dishes (MatTek Corporation, Ashland, MA). Photoconversion of Kaede fluorescent protein was performed by scanning the selected region of interest with a 405 nm diode laser (100% laser, 5 iterations, 50 s). After photoconversion, embryos were manually removed from the agarose and placed in fresh egg water (0.3 g/L Instant Ocean Salt, 75 mg/L $CaSO_4$; 1 mg/L Methylene Blue) additionally supplemented with N-Phenylthiourea (30 mg/L, Sigma-Aldrich) and covered with aluminum foil to protect from the light before trypsin treatment. After several washes in HBSS (Hank's Balanced Salt Solution, Gibco) without Ca^{2+}/Mg^{2+}, zebrafish embryos dissociation was performed at 28.5 °C during 30 min using 2 mL of trypsin-LE select (Gibco). Dissociation was stopped by added 200 µL of FBS solution. After centrifugation, pellet was resuspended with HBSS with Ca^{2+}/Mg^{2+} +5% FBS and filtered. Photoswitched ECs were isolated on FACS Aria II. Cells were immediately centrifuged, frozen by liquid nitrogen and stored at −80 °C.

RNA sequencing of zebrafish brain capillary ECs. For RNA-seq, RNA was isolated from FACS sorted zebrafish CtAs ECs cells using the miRNeasy micro Kit (Qiagen) combined with on-column DNase digestion (DNase-Free DNase Set, Qiagen) to avoid contamination by genomic DNA. RNA and library preparation integrity were verified with a BioAnalyzer 2100 (Agilent) or LabChip Gx Touch 24 (Perkin Elmer). RNA amount was adjusted on number of isolated cells by FACS and ~250–500 pg total RNA was used as input for SMART-Seq® v4 Ultra® Low Input RNA Kit (Takara Clontech) for cDNA pre-amplification. Obtained full-length cDNA was checked on LabChip and fragmented by Ultrasonication by E220 machine (Covaris). Final Library Preparation was performed by Low Input Library Prep Kit v2 (Takara Clontech). Sequencing was performed on the NextSeq500 instrument (Illumina) using v2 chemistry, resulting in minimum of 30M reads per library with 1 × 75 bp single end setup. The resulting raw reads were assessed for quality, adapter content, and duplication rates with FastQC (available online at: http://www.bioinformatics.babraham.ac.uk/projects/fastqc). Reaper version 13–100 was employed to trim reads after a quality drop below a mean of Q20 in a window of 10 nucleotides[82]. Only reads between 30 and 150 nucleotides were cleared for further analyses. Trimmed and filtered reads were aligned versus the Zebrafish genome version DanRer10 (GRCz10.87) using STAR 2.4.0a with the parameter "—outFilterMismatchNoverLmax 0.1" to increase the maximum ratio of mismatches to mapped length to 10%[83]. The number of reads aligning to genes was counted with featureCounts 1.4.5-p1 tool from the Subread package[84]. Only reads mapping at least partially inside exons were admitted and aggregated per gene. Reads overlapping multiple genes or aligning to multiple regions were excluded. The Ensemble annotation was enriched with UniProt data (release 06.06.2014) based on Ensembl gene identifiers (activities at the Universal Protein Resource (UniProt)).

RNA isolation from zebrafish embryos and RT-qPCR. RNA was isolated from zebrafish embryos with Trizol reagent (Thermo Fisher Scientific), and cDNA was generated using the SuperScript II reverse transcriptase kit (Invitrogen). Real-time quantitative PCR (RT-qPCR) was conducted using Power SYBR Green (Applied Biosystems) and the following primers (see also Supplementary Table 1): *axin2* fwd 5′-CCTGGAGGAGAGACTTCAAC-3′, *axin2* rev 5′-GAGCAAAGGCAGA-GAATGGG-3′, *β-actin* fwd 5′-CTGGACTTCGAGCAGGAGAT-3′, *β-actin* rev 5′-GCAAGATTCCATACCCAGGA-3′, *β-catenin* fwd 5′-GCCGCCACCAAA-CAGGAG-3′, *β-catenin* rev 5′-CAGCAGCACACGTCACCACG-3′, *ccnd1* fwd 5′-CTGTGCGACAGACGTCAACT-3′, *ccnd1* rev 5′-GGTGAGGTTCTGGGAT-GAGA-3′, *lef1* fwd 5′-GTTGGACAGATGACCCCTCC-3′, *lef1* rev 5′-CTGTTTCACCTGTGGGTTGAC-3′.

Mouse brain primary EC isolation and culture. For immunostaining or gene expression analysis of wild-type primary endothelial cells, C57BL/6J pups were used. To inactivate S1pr1 in the postnatal endothelium, *S1pr1*$^{lox/lox85}$ and *Cdh5(PAC)CreERT2*[86] mice were interbred. The resulting offspring were injected at P1 and P2 with 50 µg of 4-OHT and samples processed at P3.

Mouse brain primary microvascular fragment isolation and culture was performed as described[34]. In brief, brains were collected from mice at postnatal day 3 (P3) or adults (>8 weeks old) in ice-cold Dulbecco's Modified Eagle's Medium (DMEM, Life technologies 11965–092) supplemented with 1% penicillin/streptomycin (Gibco, 15140122) and L-Glutamine (Gibco, 25030081), hereafter termed dissection media. Brains were transferred to a Petri dish, where olfactory bulbs and cerebellum were removed. The hemispheres were mechanically disrupted to small pieces and further digested for 10 min at 37 °C in 0.5 mg/mL collagenase (Sigma-Aldrich, C6885) dissolved in dissection media (2 rounds of digestion for samples from adult animals). Next, the cell suspension was mixed with an equal volume of DMEM supplemented with 20% fetal bovine serum (FBS, Life Technologies), filtered through a 70 µm nylon cell strainer (Falcon, 352350) and centrifuged 5 min at 300 g. After centrifugation, the cell pellet was resuspended in dissection media supplemented with 0.5 mg/mL heparin (Sigma-Aldrich, H3149) and incubated for 40 min with CD31 (BD Pharmingen, 553370) -bound sheep anti-rat IgG magnetic Dynabeads (Life Technologies, 110.35) on a rotary wheel at room temperature. After incubation, microvascular fragments bound to magnetic beads were retrieved using a DynaMag-2 magnet (Life Technologies, 12321D), washed 5 times with heparin-supplemented dissection media and finally resuspended in TrypLE Select (Gibco, A12177-01) in order to dissociate them from the magnetic beads. After 12 min incubation at 37 °C, unbound beads were removed with the magnet and the suspension containing the microvascular fragments was mixed with EGM2-supplemented EBM2 media (Lonza, CC-3456 and CC-4176). After

centrifugation (10 min, 300×*g*) the microvascular fragments were resuspended in EGM2–EBM2 media supplemented with puromycin (Sigma-Aldrich, P9620, 10 µg/mL) and plated on collagen-I-coated µ-Slide 8-well ibiTreat cell culture chambers (Ibidi, 80826) or 24-well cell culture plates. Hereafter, cells were kept in culture at 37 °C and 5% CO_2. Twenty hours later, wells were washed three times with PBS to remove dead and unattached cells and fresh EGM2–EBM2 media supplemented with puromycin (5 µg/mL) was added. The next day, pharmacologic treatment started with drugs diluted in EGM2–EBM2 media.

IWR-1 (Sigma-Aldrich) and VPC23019 (VPC, Cayman Chemical) were dissolved in DMSO to a 10 mM concentration. Inhibition of Wnt signaling was achieved after 48 h treatment with 10 or 20 µM IWR-1 for endothelial cells from young pups or adult animals, respectively. Alternatively, 10 µM IWR-1-treated cells from young pups were exposed in parallel to 2 µM VPC to assess the effect of S1pr1 signaling blocking upon Wnt inhibition. Vehicle (DMSO) treated was used in all experiments as control.

Immunohistochemistry of mouse brain primary EC. After inhibitor treatment, cells growing in 8-well ibiTreat cell culture chambers were fixed in 4% paraformaldehyde (PFA, Sigma-Aldrich, P6148) for 15 min at room temperature, washed three times with PBS and permeabilized with 0.2% Triton X-100 (Sigma-Aldrich, T8787) in PBS for 15 min. After washing three times with PBS, cells were blocked by incubation with 2% normal donkey serum (Abcam, ab7475) in PBS in a humidified chamber for 30 min. Primary antibodies (goat polyclonal anti-CD31, R&D Systems, AF3628, 1:100; rat monoclonal anti-VE-cadherin clone 11D4, BD Biosciences, 555289, 1:100; and rabbit polyclonal anti-ZO-1, Invitrogen, 402200, 1:100) were diluted in blocking buffer and incubated with the cells in a humidified chamber overnight at 4 °C. Wells were then washed three times with PBS and secondary antibodies (donkey anti goat Alexa Fluor 488, Invitrogen, A11055, 1:400; donkey anti rat Alexa Fluor Cy3, Jackson Immuno Research, 712-165-153, 1:400; and donkey anti rabbit Alexa Fluor 647, Invitrogen, A31573, 1:400) together with DAPI (Sigma-Aldrich, D9542, 1 µg/mL) were diluted in blocking buffer and incubated at room temperature for 2 h. After secondary antibody incubation, cells were washed as described above and covered with PBS until imaging.

RT-qPCR of mouse brain primary ECs. After inhibitor treatment, cells growing in 24-well cell culture plates were collected in 350 µL RLT Plus Buffer (Qiagen, 1053393) supplemented with 1% β-mercaptoethanol (Sigma, M6250) and total RNA was isolated using the RNeasy Plus Micro Kit (Qiagen, 74034) following the manufacturer's instructions. Whole RNA was assessed in terms of quantity and quality using Bioanalyzer 2000 (Agilent), reverse transcribed and converted to complementary DNA (cDNA) using the iScript cDNA synthesis kit (BioRad, 170-8890). The following FAM-conjugated TaqMan gene expression probes (all from Thermo Fisher Scientific) were used: *VE-cadherin* (*Cdh5*, Mm00486938_m1), *Axin2* (Mm01265780_m1), *Lef1* (Mm01310389_m1), and *Ccnd1* (Mm00432360_m1). VIC-conjugated *Actb* (4352341E) TaqMan probe was used to normalize gene expression. Quantitative PCR (qPCR) reactions were performed on a CFX96 Touch Real-Time PCR Detection System (BioRad) using the Sso Advanced Universal Probes Supermix (BioRad, 1725281). All relative gene expression analyses were performed using the $2^{-\Delta\Delta Ct}$ method in a minimum of four animals per group with triplicate reactions for each gene evaluated.

Confocal microscopy. Confocal microscopy was performed using LSM780 and LSM880 microscopes (Carl Zeiss Microscopy GmbH; objective lenses: Plan-Apochromat ×20/0.8; LD C-Apochromat ×40/1.1 W Korr M27). For filopodia analysis in zebrafish at high resolution, images were acquired with the LSM880 Airyscan module. For life imaging of VE-cadherinTS embryos, the Online Fingerprinting mode of the LSM880 microscope was utilized. In general, PFA-fixed or living zebrafish embryos were embedded in 0.3% agarose, which was dissolved in E3 medium and additionally supplemented with N-Phenylthiourea (30 mg/L, Sigma-Aldrich) and Tricaine (19.2 mg/L, Sigma-Aldrich) for living embryos as previously described[59]. For time-lapse analysis, the agarose was additionally supplemented with IWR-1 or DMSO and a stable temperature of 28.5 °C was maintained using a heating chamber. Assembly of confocal stacks and time-lapse movies was conducted using Imaris 8/9 software (Bitplane). Quantification of signal intensity and volume was done using the Imaris surface-rendering algorithm.

Statistical analysis. For all quantifications, statistical analysis was performed using Prism6 software (GraphPad). Graphs show mean ± standard deviation (SD) or standard error of the mean (SEM) and *p*-values were calculated using unpaired two-tailed Student's *t*-test or one-way ANOVA for single and multiple comparisons as indicated for each experiment.

Animal models. All animal experiments were performed in compliance with the relevant laws and institutional guidelines, were approved by local animal ethics committees and were conducted at the University of Münster and the MPI for Molecular Biomedicine with permissions granted by the Landesamt für Natur, Umwelt und Verbraucherschutz (LANUV) of North Rhine-Westphalia.

Data availability

The authors declare that the data supporting the findings of this study are available within the paper and its supplementary information files. The RNA sequencing data of this study have been deposited in NCBI's Gene Expression Omnibus and are accessible through GEO Series accession number GSE121041. The rest of the data are available from the authors upon reasonable request.

Received: 16 March 2018 Accepted: 15 October 2018
Published online: 19 November 2018

References

1. Engelhardt, B. & Liebner, S. Novel insights into the development and maintenance of the blood-brain barrier. *Cell Tissue Res.* **355**, 687–699 (2014).
2. Vallon, M., Chang, J., Zhang, H. & Kuo, C. J. Developmental and pathological angiogenesis in the central nervous system. *Cell Mol. Life Sci.* **71**, 3489–3506 (2014).
3. Ruhrberg, C. & Bautch, V. L. Neurovascular development and links to disease. *Cell Mol. Life Sci.* **70**, 1675–1684 (2013).
4. Bussmann, J., Wolfe, S. A. & Siekmann, A. F. Arterial-venous network formation during brain vascularization involves hemodynamic regulation of chemokine signaling. *Development* **138**, 1717–1726 (2011).
5. Betz, C., Lenard, A., Belting, H. G. & Affolter, M. Cell behaviors and dynamics during angiogenesis. *Development* **143**, 2249–2260 (2016).
6. Ulrich, F., Ma, L. H., Baker, R. G. & Torres-Vazquez, J. Neurovascular development in the embryonic zebrafish hindbrain. *Dev. Biol.* **357**, 134–151 (2011).
7. Fujita, M. et al. Assembly and patterning of the vascular network of the vertebrate hindbrain. *Development* **138**, 1705–1715 (2011).
8. Xie, J., Farage, E., Sugimoto, M. & Anand-Apte, B. A novel transgenic zebrafish model for blood-brain and blood-retinal barrier development. *BMC Dev. Biol.* **10**, 76 (2010).
9. Jeong, J. Y. et al. Functional and developmental analysis of the blood-brain barrier in zebrafish. *Brain Res. Bull.* **75**, 619–628 (2008).
10. Daneman, R. et al. Wnt/ -catenin signaling is required for CNS, but not non-CNS, angiogenesis. *Proc. Natl Acad. Sci. USA* **106**, 6422–6422 (2009).
11. Stenman, J. M. et al. Canonical Wnt signaling regulates organ-specific assembly and differentiation of CNS vasculature. *Science* **322**, 1247–1250 (2008).
12. Vanhollebeke, B. et al. Tip cell-specific requirement for an atypical Gpr124- and Reck-dependent Wnt/beta-catenin pathway during brain angiogenesis. *Elife* **4**, e06489 (2015). https://doi.org/10.7554/eLife.06489
13. Tran, K. A. et al. Endothelial beta-catenin signaling is required for maintaining adult blood-brain barrier integrity and central nervous system homeostasis. *Circulation* **133**, 177–186 (2016).
14. Liebner, S. et al. Wnt/beta-catenin signaling controls development of the blood-brain barrier. *J. Cell Biol.* **183**, 409–417 (2008).
15. Ulrich, F. et al. Reck enables cerebrovascular development by promoting canonical Wnt signaling. *Development* **143**, 147–159 (2016).
16. Posokhova, E. et al. GPR124 functions as a WNT7-specific coactivator of canonical beta-catenin signaling. *Cell Rep.* **10**, 123–130 (2015).
17. Cho, C., Smallwood, P. M. & Nathans, J. Reck and Gpr124 are essential receptor cofactors for Wnt7a/Wnt7b-specific signaling in mammalian CNS angiogenesis and blood-brain barrier regulation. *Neuron* **95**, 1056–1073 e1055 (2017).
18. Eubelen, M. et al. A molecular mechanism for Wnt ligand-specific signaling. *Science* **361**, eaat1178 (2018).
19. Kuhnert, F. et al. Essential regulation of CNS angiogenesis by the orphan G protein-coupled receptor GPR124. *Science* **330**, 985–989 (2010).
20. Zhou, Y. & Nathans, J. Gpr124 controls CNS angiogenesis and blood-brain barrier integrity by promoting ligand-specific canonical wnt signaling. *Dev. Cell.* **31**, 248–256 (2014).
21. Giannotta, M., Trani, M. & Dejana, E. VE-cadherin and endothelial adherens junctions: active guardians of vascular integrity. *Dev. Cell* **26**, 441–454 (2013).
22. Vestweber, D. VE-cadherin: the major endothelial adhesion molecule controlling cellular junctions and blood vessel formation. *Arterioscler. Thromb. Vasc. Biol.* **28**, 223–232 (2008).
23. Lenard, A. et al. In vivo analysis reveals a highly stereotypic morphogenetic pathway of vascular anastomosis. *Dev. Cell* **25**, 492–506 (2013).
24. Sauteur, L., Affolter, M. & Belting, H. G. Distinct and redundant functions of Esama and VE-cadherin during vascular morphogenesis. *Development* **144**, 1554–1565 (2017).
25. Vestweber, D. How leukocytes cross the vascular endothelium. *Nat. Rev. Immunol.* **15**, 692–704 (2015).

26. Taddei, A. et al. Endothelial adherens junctions control tight junctions by VE-cadherin-mediated upregulation of claudin-5. *Nat. Cell Biol.* **10**, 923–934 (2008).
27. Prager, B., Spampinato, S. F. & Ransohoff, R. M. Sphingosine 1-phosphate signaling at the blood-brain barrier. *Trends Mol. Med.* **21**, 354–363 (2015).
28. Yanagida, K. & Hla, T. Vascular and immunobiology of the circulatory sphingosine 1-phosphate gradient. *Annu. Rev. Physiol.* **79**, 67–91 (2017).
29. Kono, M. et al. The sphingosine-1-phosphate receptors S1P1, S1P2, and S1P3 function coordinately during embryonic angiogenesis. *J. Biol. Chem.* **279**, 29367–29373 (2004).
30. Yanagida, K. et al. Size-selective opening of the blood-brain barrier by targeting endothelial sphingosine 1-phosphate receptor 1. *Proc. Natl Acad. Sci. USA* **114**, 4531–4536 (2017).
31. Gaengel, K. et al. The sphingosine-1-phosphate receptor S1PR1 restricts sprouting angiogenesis by regulating the interplay between VE-cadherin and VEGFR2. *Dev. Cell* **23**, 587–599 (2012).
32. Chen, B. et al. Small molecule-mediated disruption of Wnt-dependent signaling in tissue regeneration and cancer. *Nat. Chem. Biol.* **5**, 100–107 (2009).
33. Hübner, K. et al. Wnt signaling positively regulates endothelial cell fate specification in the Fli1a-positive progenitor population via Lef1. *Dev. Biol.* **430**, 142–155 (2017).
34. He, L. et al. Analysis of the brain mural cell transcriptome. *Sci. Rep.* **6**, 35108 (2016).
35. Sauteur, L. et al. Cdh5/VE-cadherin promotes endothelial cell interface elongation via cortical actin polymerization during angiogenic sprouting. *Cell Rep.* **9**, 504–513 (2014).
36. Lagendijk, A. K. et al. Live imaging molecular changes in junctional tension upon VE-cadherin in zebrafish. *Nat. Commun.* **8**, 1402 (2017).
37. Conway, D. E. et al. Fluid shear stress on endothelial cells modulates mechanical tension across VE-cadherin and PECAM-1. *Curr. Biol.* **23**, 1024–1030 (2013).
38. Lee, M. J. et al. Vascular endothelial cell adherens junction assembly and morphogenesis induced by sphingosine-1-phosphate. *Cell* **99**, 301–312 (1999).
39. Paik, J. H. et al. Sphingosine 1-phosphate receptor regulation of N-cadherin mediates vascular stabilization. *Genes Dev.* **18**, 2392–2403 (2004).
40. Sanchez, T. et al. Induction of vascular permeability by the sphingosine-1-phosphate receptor-2 (S1P2R) and its downstream effectors ROCK and PTEN. *Arterioscler. Thromb. Vasc. Biol.* **27**, 1312–1318 (2007).
41. Xiong, Y., Yang, P., Proia, R. L. & Hla, T. Erythrocyte-derived sphingosine 1-phosphate is essential for vascular development. *J. Clin. Invest.* **124**, 4823–4828 (2014).
42. Garcia, J. G. et al. Sphingosine 1-phosphate promotes endothelial cell barrier integrity by Edg-dependent cytoskeletal rearrangement. *J. Clin. Invest.* **108**, 689–701 (2001).
43. Zhao, Y. D. et al. Bone marrow progenitor cells induce endothelial adherens junction integrity by sphingosine-1-phosphate-mediated Rac1 and Cdc42 signaling. *Circ. Res.* **105**, 696–704, 698 p following 704 (2009).
44. Radeva, M. Y. & Waschke, J. Mind the gap: mechanisms regulating the endothelial barrier. *Acta. Physiol.* **222**, e12860 (2018). https://doi.org/10.1111/apha.12860
45. Grainger, S. et al. Wnt9a is required for the aortic amplification of nascent hematopoietic stem cells. *Cell Rep.* **17**, 1595–1606 (2016).
46. Chanda, B., Ditadi, A., Iscove, N. N. & Keller, G. Retinoic acid signaling is essential for embryonic hematopoietic stem cell development. *Cell* **155**, 215–227 (2013).
47. Nicenboim, J. et al. Lymphatic vessels arise from specialized angioblasts within a venous niche. *Nature* **522**, 56–61 (2015).
48. Hupe, M. et al. Gene expression profiles of brain endothelial cells during embryonic development at bulk and single-cell levels. *Sci. Signal.* **10**, eaag2476 (2017).
49. O'Sullivan, S. & Dev, K. K. Sphingosine-1-phosphate receptor therapies: advances in clinical trials for CNS-related diseases. *Neuropharmacology* **113**, 597–607 (2017).
50. Choe, C. P. et al. Wnt-dependent epithelial transitions drive pharyngeal pouch formation. *Dev. Cell* **24**, 296–309 (2013).
51. Reis, M. & Liebner, S. Wnt signaling in the vasculature. *Exp. Cell Res.* **319**, 1317–1323 (2013).
52. Umans, R. A. et al. CNS angiogenesis and barriergenesis occur simultaneously. *Dev. Biol.* **425**, 101–108 (2017).
53. Sharma, S., Mathur, A. G., Pradhan, S., Singh, D. B. & Gupta, S. Fingolimod (FTY720): first approved oral therapy for multiple sclerosis. *J. Pharmacol. Pharmacother.* **2**, 49–51 (2011).
54. Lu, B., . & Green, B. A. & Farr, J. M. & Lopes, F. C. & Van Raay, T. J. Wnt drug discovery: weaving through the screens, patents and clinical trials. *Cancers* **8**, E82 (2016).
55. Kahn, M. Can we safely target the WNT pathway? *Nat. Rev. Drug. Discov.* **13**, 513–532 (2014).
56. Westerfield, M. *The Zebrafish Book*. (University of Oregon Press, Eugene, OR, 1993).
57. Kimmel, C. B., Ballard, W. W., Kimmel, S. R., Ullmann, B. & Schilling, T. F. Stages of embryonic-development of the zebrafish. *Dev. Dynam* **203**, 253–310 (1995).
58. Covassin, L. D. et al. A genetic screen for vascular mutants in zebrafish reveals dynamic roles for Vegf/Plcg1 signaling during artery development. *Dev. Biol.* **329**, 212–226 (2009).
59. Hamm, M. J., Kirchmaier, B. C. & Herzog, W. Sema3d controls collective endothelial cell migration by distinct mechanisms via Nrp1 and PlxnD1. *J. Cell Biol.* **215**, 415–430 (2016).
60. Lawson, N. D. & Weinstein, B. M. In vivo imaging of embryonic vascular development using transgenic zebrafish. *Dev. Biol.* **248**, 307–318 (2002).
61. Herwig, L. et al. Distinct cellular mechanisms of blood vessel fusion in the zebrafish embryo. *Curr. Biol.* **21**, 1942–1948 (2011).
62. Traver, D. et al. Transplantation and in vivo imaging of multilineage engraftment in zebrafish bloodless mutants. *Nat. Immunol.* **4**, 1238–1246 (2003).
63. Bertrand, J. Y. et al. Haematopoietic stem cells derive directly from aortic endothelium during development. *Nature* **464**, 108–111 (2010).
64. Jin, S. W., Beis, D., Mitchell, T., Chen, J. N. & Stainier, D. Y. Cellular and molecular analyses of vascular tube and lumen formation in zebrafish. *Development* **132**, 5199–5209 (2005). https://doi.org/10.7554/eLife.20253
65. Chi, N. C. et al. Foxn4 directly regulates tbx2b expression and atrioventricular canal formation. *Genes Dev.* **22**, 734–739 (2008).
66. Matsuoka, R. L. et al. Radial glia regulate vascular patterning around the developing spinal cord. *eLife* **5**, e20253 (2016).
67. Hatta, K., Tsujii, H. & Omura, T. Cell tracking using a photoconvertible fluorescent protein. *Nat. Protoc.* **1**, 960–967 (2006).
68. Helker, C. S. et al. The zebrafish common cardinal veins develop by a novel mechanism: lumen ensheathment. *Development* **140**, 2776–2786 (2013).
69. Hesselson, D., Anderson, R. M., Beinat, M. & Stainier, D. Y. Distinct populations of quiescent and proliferative pancreatic beta-cells identified by HOTcre mediated labeling. *Proc. Natl Acad. Sci. USA* **106**, 14896–14901 (2009).
70. Dorsky, R. I., Sheldahl, L. C. & Moon, R. T. A transgenic Lef1/beta-catenin-dependent reporter is expressed in spatially restricted domains throughout zebrafish development. *Dev. Biol.* **241**, 229–237 (2002).
71. Villefranc, J. A., Amigo, J. & Lawson, N. D. Gateway compatible vectors for analysis of gene function in the zebrafish. *Dev. Dyn.* **236**, 3077–3087 (2007).
72. Jao, L. E., Wente, S. R. & Chen, W. Efficient multiplex biallelic zebrafish genome editing using a CRISPR nuclease system. *Proc. Natl Acad. Sci. USA* **110**, 13904–13909 (2013).
73. Ganesan, S., Moussavi Nik, S. H., Newman, M. & Lardelli, M. Identification and expression analysis of the zebrafish orthologues of the mammalian MAP1LC3 gene family. *Exp. Cell Res.* **328**, 228–237 (2014).
74. Sempou, E., Biasini, E., Pinzon-Olejua, A., Harris, D. A. & Malaga-Trillo, E. Activation of zebrafish Src family kinases by the prion protein is an amyloid-beta-sensitive signal that prevents the endocytosis and degradation of E-cadherin/beta-catenin complexes in vivo. *Mol. Neurodegener.* **11**, 18 (2016).
75. Liu, Z. et al. Fscn1 is required for the trafficking of TGF-beta family type I receptors during endoderm formation. *Nat. Commun.* **7**, 12603 (2016).
76. Winder, S. J., Lipscomb, L., Angela Parkin, C. & Juusola, M. The proteasomal inhibitor MG132 prevents muscular dystrophy in zebrafish. *PLoS Curr.* **3**, RRN1286 (2011).
77. Blum, Y. et al. Complex cell rearrangements during intersegmental vessel sprouting and vessel fusion in the zebrafish embryo. *Dev. Biol.* **316**, 312–322 (2008).
78. Auman, H. J. et al. Functional modulation of cardiac form through regionally confined cell shape changes. *PLoS Biol.* **5**, e53 (2007).
79. Schoenebeck, J. J., Keegan, B. R. & Yelon, D. Vessel and blood specification override cardiac potential in anterior mesoderm. *Dev. Cell* **13**, 254–267 (2007).
80. Larson, J. D. et al. Expression of VE-cadherin in zebrafish embryos: a new tool to evaluate vascular development. *Dev. Dyn.* **231**, 204–213 (2004).
81. Thisse, C. & Thisse, B. High-resolution in situ hybridization to whole-mount zebrafish embryos. *Nat. Protoc.* **3**, 59–69 (2008).
82. Davis, M. P., van Dongen, S., Abreu-Goodger, C., Bartonicek, N. & Enright, A. J. Kraken: a set of tools for quality control and analysis of high-throughput sequence data. *Methods* **63**, 41–49 (2013).
83. Dobin, A. et al. STAR: ultrafast universal RNA-seq aligner. *Bioinformatics* **29**, 15–21 (2013).
84. Liao, Y., Smyth, G. K. & Shi, W. featureCounts: an efficient general purpose program for assigning sequence reads to genomic features. *Bioinformatics* **30**, 923–930 (2014).

85. Allende, M. L., Yamashita, T. & Proia, R. L. G-protein-coupled receptor S1P1 acts within endothelial cells to regulate vascular maturation. *Blood* **102**, 3665–3667 (2003).
86. Wang, Y. et al. Ephrin-B2 controls VEGF-induced angiogenesis and lymphangiogenesis. *Nature* **465**, 483–486 (2010).

Acknowledgements

We thank Dietmar Vestweber and Stefan Offermanns for discussions and experimental suggestions. We thank Ben Hogan and Ann-Kathrin Lagendijk for the VE-cadherinTS fish. We thank Timothy Hla for the S1pr1-flox mice. We are grateful to Reinhild Bussmann for excellent fish husbandry, Stefan Volkery for imaging assistance, Stefan Guenther for the RNA sequencing, Jung-Mo Kim for sharing mice and Katja Müller and Hendrik Arf for technical assistance. This work was supported by the Deutsche Forschungsgemeinschaft (FOR2325: HE4585/3-1 and AD324/3-1) and Japan Society for the Promotion of Science (JSPS) Overseas Research Fellowships (awarded to Y.W.). Work in the B.V. laboratory was supported by the FNRS (MIS F.4543.15), the Concerted Research Action (ARC), the Fondation ULB, the Queen Elisabeth Medical Foundation (Q.E.M.F.), and the FRFS-WELBIO (CR-2017S-05)

Author contributions

K.H. performed experiments and together with W.H., analyzed the data, created the figures and wrote the manuscript. P.C., S.G., and B.V. performed and analyzed the RNA sequencing experiment, C.W., H.G.B., and M.A. analyzed *ve-cadherin* and *esama* mutants, R.D.-H. and R.A. performed and discussed primary mouse brain E.C. experiments, Y.W. and M.H. performed S1pr overexpression and agonist experiments, and K. G. generated dnTcf zebrafish lines. All authors provided experimental suggestions, critical comments, and reviewed the manuscript.

Additional information

Supplementary Information accompanies this paper at https://doi.org/10.1038/s41467-018-07302-x.

Competing interests: The authors declare no competing interests.

Reprints and permission information is available online at http://npg.nature.com/reprintsandpermissions/

Publisher's note: Springer Nature remains neutral with regard to jurisdictional claims in published maps and institutional affiliations.

Supplementary Information

Wnt/β-catenin signaling regulates VE-cadherin-mediated anastomosis of brain capillaries by counteracting S1pr1 signaling

(Hübner *et al.*)

Supplementary Figure 1

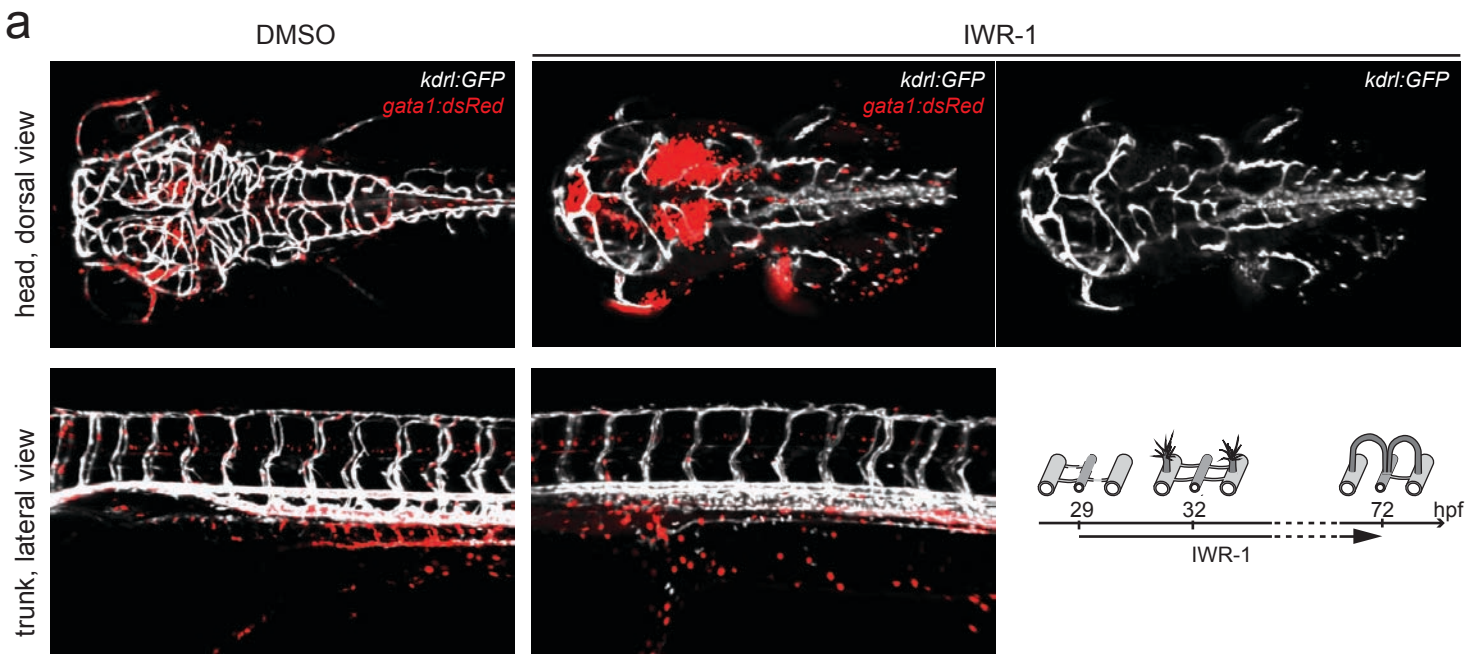

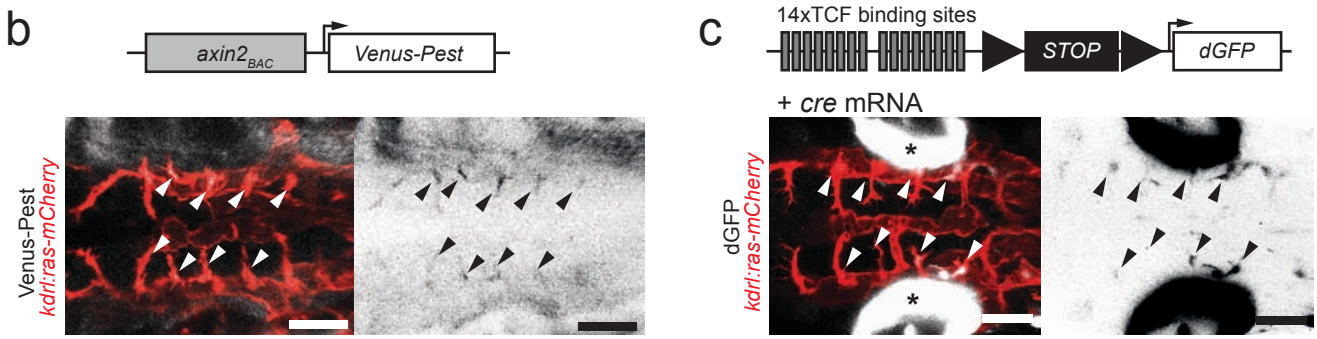

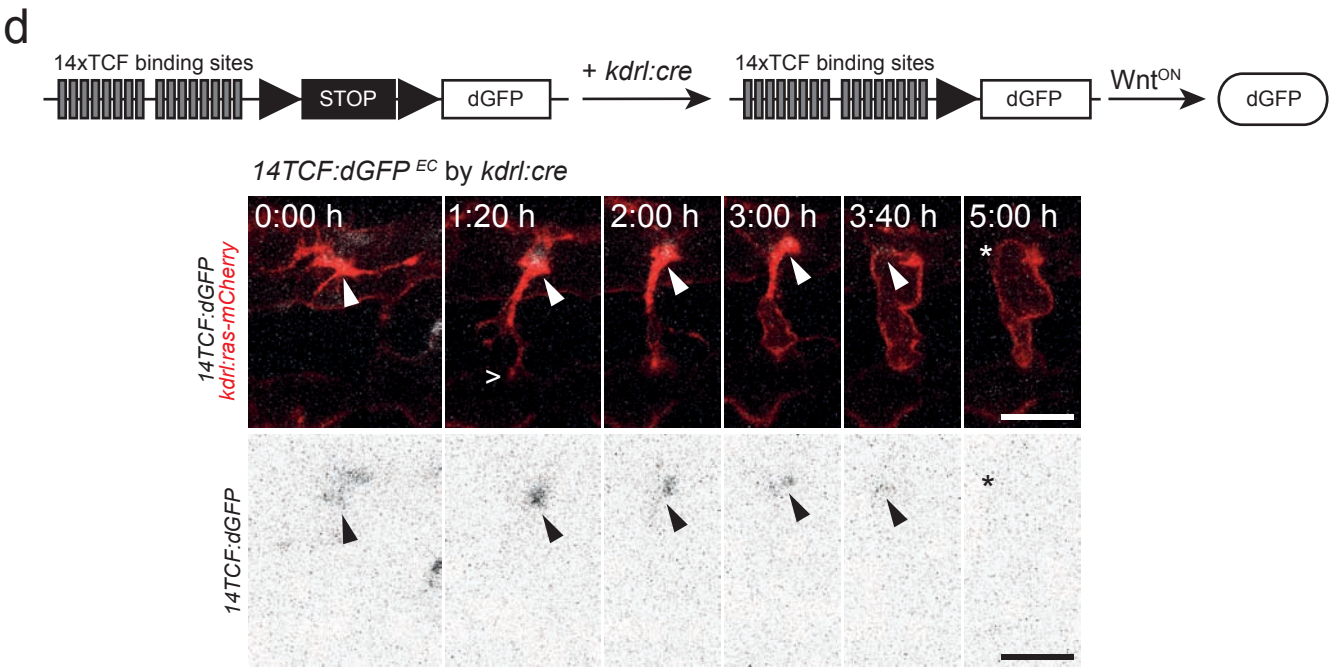

Supplementary Figure 1

Wnt signaling is active in brain ECs during angiogenesis

a) Wnt signaling inhibition by IWR-1 treatment caused severe vascular defects and hemorrhages in the brain, but not in the trunk of zebrafish embryos. Confocal images showing dorsal views of the head (anterior to the left) or lateral views of the trunk (anterior to the left) of 72 hpf-old embryos with ECs labeled with GFP (white, by *Tg(kdrl:GFP)*^{s843}) and erythrocytes labeled with dsRed (red, by *Tg(gata1:dsRed)*^{sd2}), which were treated with IWR-1 or DMSO from 29 to 72 hpf.

b,c) At 34 hpf, Wnt signaling reporters are expressed in all CtA sprouts in the hindbrain, indicating active Wnt signaling during sprout migration (arrowheads in b,c). Confocal images of embryos (dorsal views) co-expressing *Tg(kdrl:ras-mCherry)*^{s896} for labeling ECs (red) and β-catenin dependent Wnt signaling reporters expressing short-lived fluorophores: *Tg(axin2*$_{BAC}$*:Venus-Pest)*^{mu288} (b) and *Tg(14TCF:loxP-STOP-loxP-dGFP)*^{mu202} injected with *cre* mRNA (c). Asterisk in c marks Venus-Pest expression in the ear in *Tg(axin2*$_{BAC}$*:Venus-Pest)*^{mu28} embryos.

d) Vascular specific excision of the STOP cassette in *Tg(14TCF:loxP-STOP-loxP-dGFP)*^{mu202} embryos by *kdrl:cre*. Expression of dGFP indicates active Wnt signaling in ECs. Expression of dGFP was detected in CtA ECs starting during tip cell formation within the PHBC until lumen formation finished. Still images from a confocal time lapse movie of *Tg(14TCF:loxP-STOP-loxP-dGFP)*^{mu202}*; (kdrl:cre)*^{s898} double transgenic embryos with ECs labeled by *Tg(kdrl:ras-mCherry)*^{s896}. The dGFP channel is represented in inverted colors for better visualization. Arrows mark dGFP signal in CtA sprouts and open arrow indicates cell-cell-contact formation. Note, that the Wnt signaling responsive transgene (*14TCF:loxP-STOP-loxP-dGFP*) is heterozygous, which lead to weaker fluorescence signal compared to the homozygous transgene expression in Fig. 1b; CtA, central artery; ECs, endothelial cells; hpf, hours post fertilization; PHBC, primordial hindbrain channel.

Supplementary Figure 2

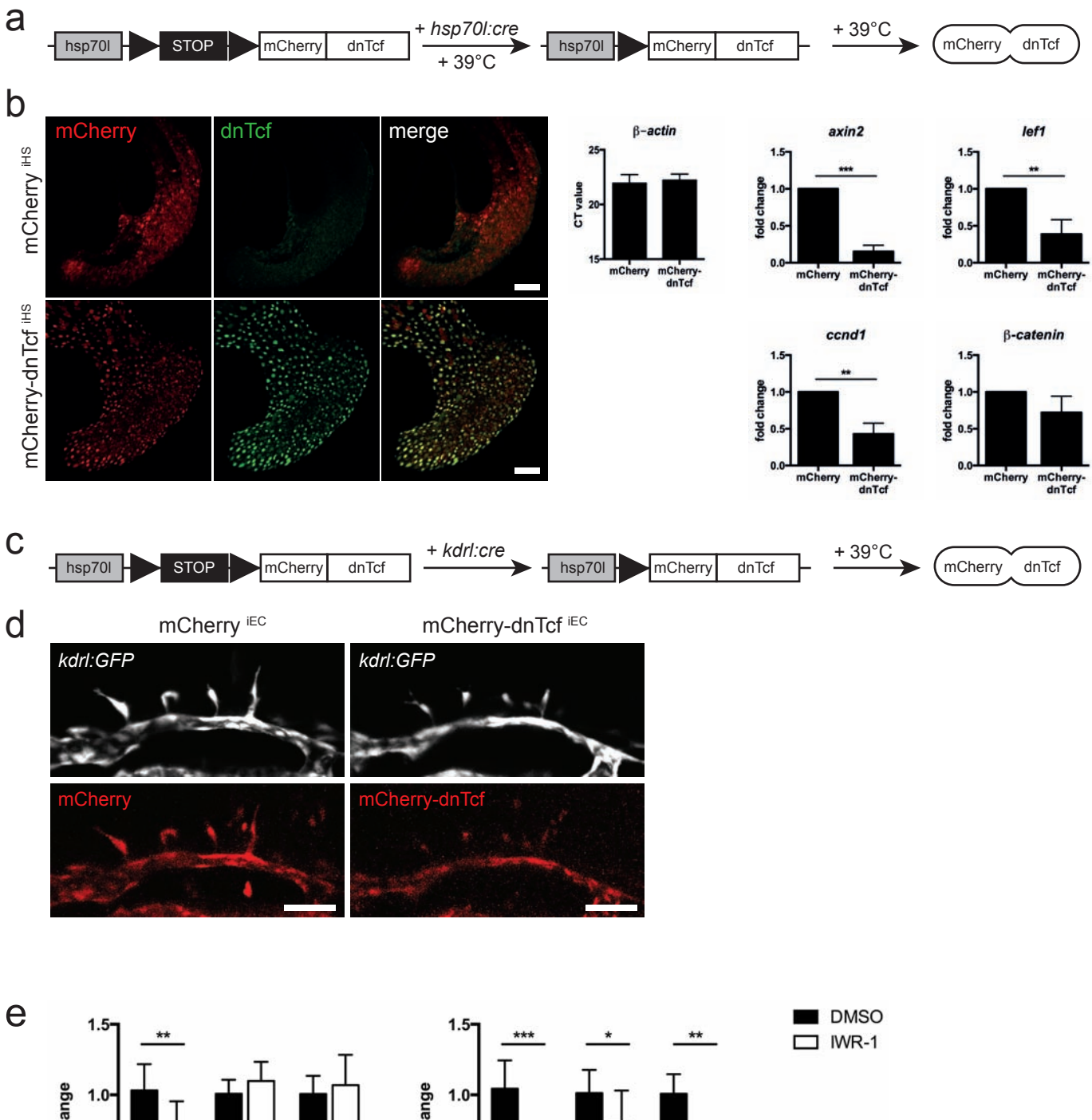

Supplementary Figure 2

Validation of transgenic Wnt-manipulating lines

a) For dnTcf expression in all cells, *Tg(hsp70l:loxP-STOP-loxP-mCherry-dntcf)*^{mu201} embryos were injected with *cre* mRNA and subjected to heat shock to induce mCherry-dnTcf expression (referred as mCherry-dnTcf^{iHS}).

b) Overexpression of dnTcf robustly blocks expression of Wnt target genes. Induction of mCherry-dnTcf in all cells by heat shock can be detected by immunostaining in 24 hpf-old *Tg(hsp70l:loxP-STOP-loxP-mCherry-dntcf)*^{mu201} but not in *Tg(hsp70l:loxP-STOP-loxP-mCherry)*^{mu279} embryos. Wnt signaling target genes *axin2*, *lef1* and *ccnd1* were down regulated after mCherry-dnTcf expression, but the expression of *β-catenin* was not significantly affected. Values represent mean ± SD. *p<0.05, **p<0.01, ***p<0.001, Student's t-test of three independent experiments.

c) For EC-specific expression of dnTcf, *Tg(hsp70l:loxP-STOP-loxP-mCherry-dntcf)*^{mu201} embryos were mated to *Tg(kdrl:cre)*^{s898} and mCherry-dnTcf expression was induced by heat shock at 26 hpf (referred as mCherry-dnTcf^{iEC}).

d) Expression of mCherry^{iEC} or mCherry-dnTcf^{iEC} co-localized with GFP expression from *Tg(kdrl:GFP)*^{s843} in CtAs and PHBC of 32 hpf-old embryos. Therefore, the heat shock protocol is suitable to induce mCherry-dnTcf during CtA angiogenesis.

e) Analysis of expression levels of Wnt target genes in DMSO or IWR-1 treated mouse primary BECs isolated from P3 or adult animals by RT-qPCR (P3: *n*=4, adult: *n*=7). Values in represent mean ±SD, *p<0.05, **p<0.01, ***p<0.001, *n*, number of biological replicates.

Confocal images of zebrafish embryos show lateral views (anterior to the left). BECs, brain ECs, CtA, central artery; ECs, endothelial cells; PHBC, primordial hindbrain channel; Scale bars: 50 μm.

Supplementary Figure 3

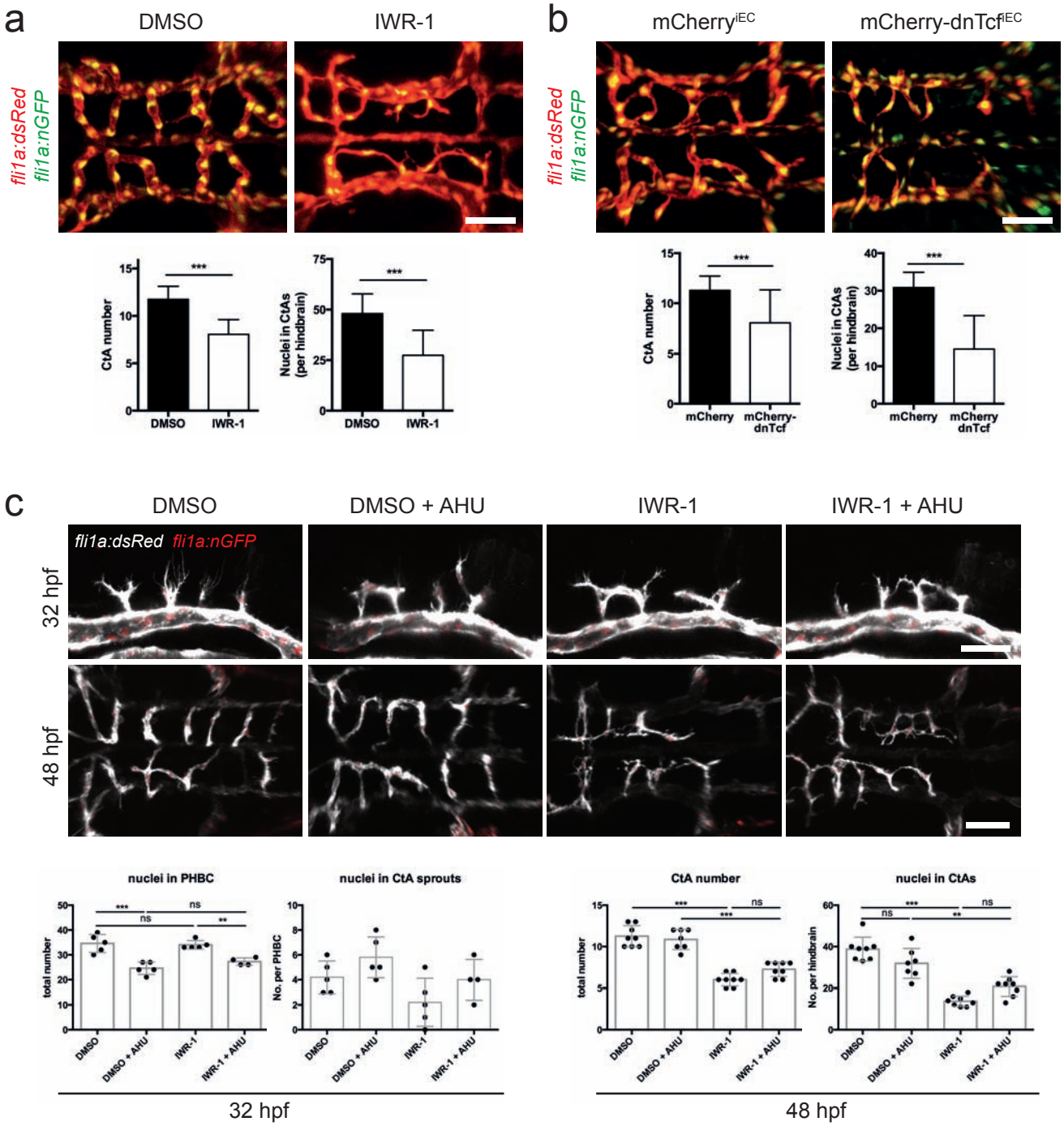

Supplementary Figure 3

Wnt signaling impacts EC number independent of proliferation

a,b) Inhibition of Wnt signaling by IWR-1 treatment (a) or by EC-specific dnTcf expression induced by heat shock at 26 hpf (b) affected EC numbers in CtAs.

a) IWR-1 treatment from 29 to 48 hpf resulted in decreased total number of CtAs and also reduced EC number within CtAs compared to control (DMSO: CtA number *n*=35, EC number *n*=39; IWR-1: CtA number *n*=20 EC number *n*=22).

b) Expression of mCherry-dnTcf^{iEC} resulted in decreased total number of CtAs and reduced EC number within CtAs compared to mCherry^{iEC} (mCherry^{iEC}: CtA number *n*=39, EC number *n*=40; mCherry-dnTcf^{iEC}: CtA number *n*=12, EC number *n*=14).

c) Decreased EC numbers after Wnt signaling inhibition did not result from decreased EC proliferation. Embryos were treated with DMSO (control), IWR-1, AHU or IWR-1+AHU from 26 to 32 hpf or from 29 to 48 hpf. Inhibition of proliferation by AHU decreased the number of ECs in the PHBC at 32 hpf (*n*=5), but had no effect on the EC number within CtAs at 48 hpf, which was only affected by IWR-1 treatment (*n*=5). Confocal images show dorsal views of 48 hpf-old embryos and lateral views of 32 hpf-old embryos (anterior to the left) with GFP expression from *Tg(fli1a:nGFP)^{y7}* and dsRed expression from *Tg(fli1a:dsRed)^{um13}*. Values represent mean ±SD. *p<0.05, **p<0.01, ***p<0.001, Student's t-test (a,b) or One-way ANOVA (c); *n*, number of analyzed embryos; CtAs, central arteries; ECs, endothelial cells; PHBC, primordial hindbrain channel; Scale bars: 50 µm.

Supplementary Figure 4

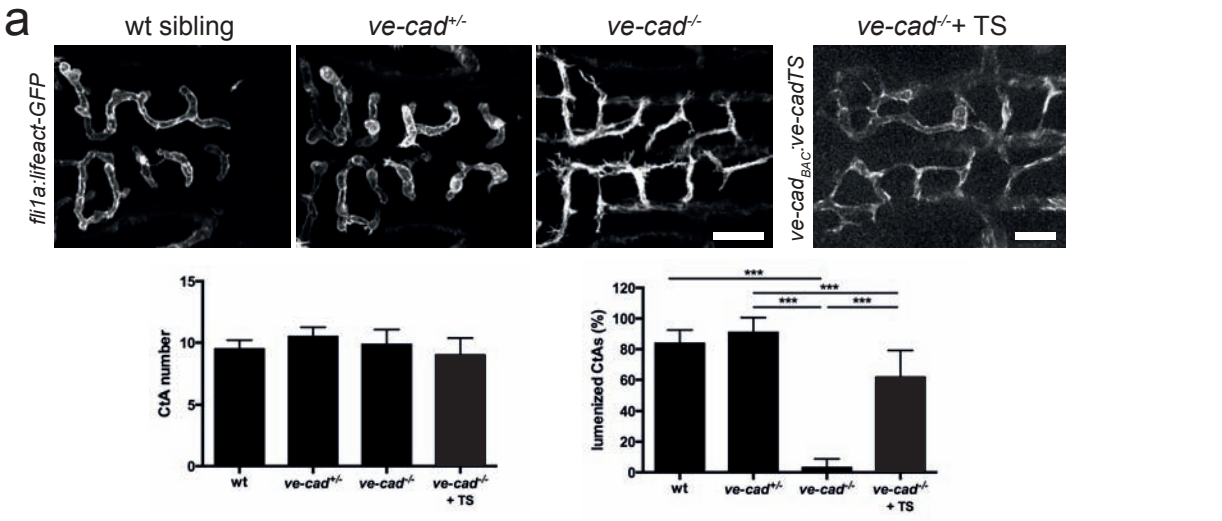

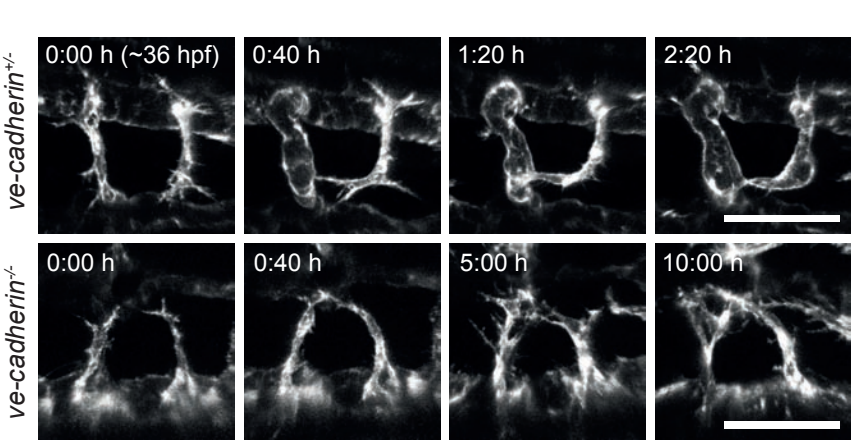

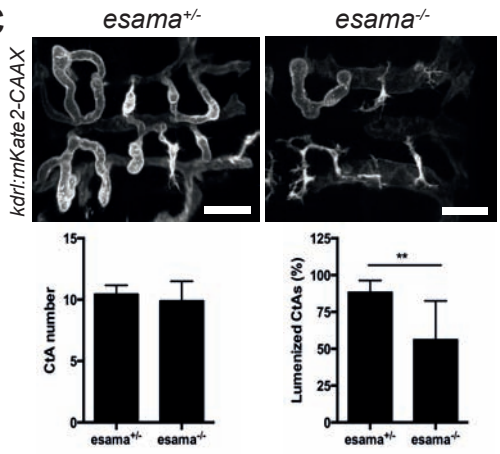

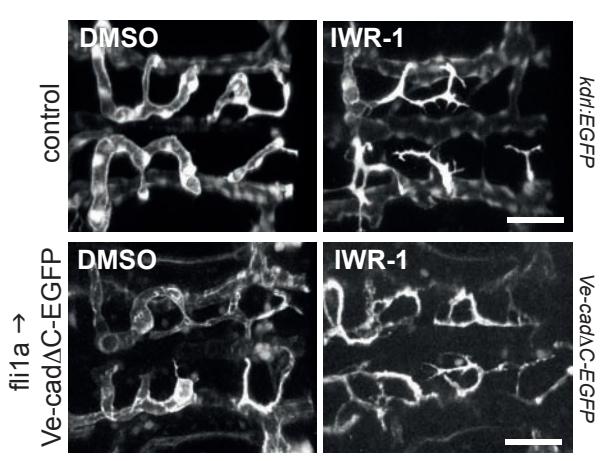

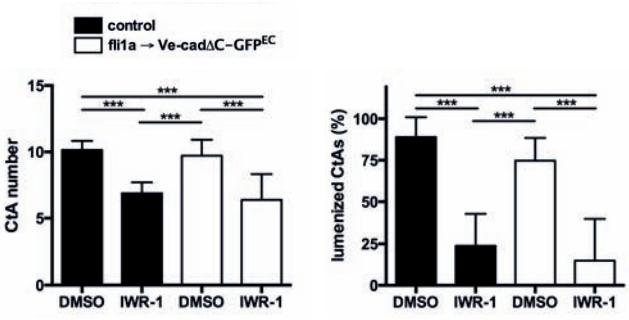

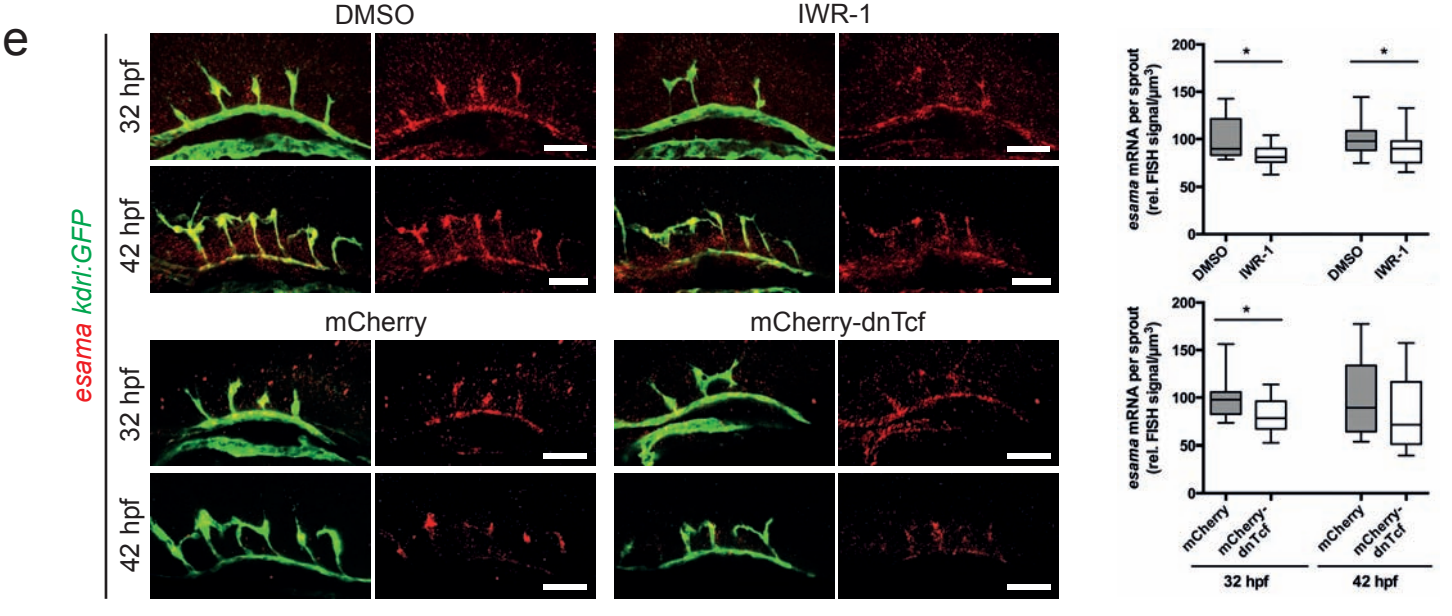

Supplementary Figure 4

VE-cadherin and Esama are required for CtA anastomosis

a) Lumen formation was completely impaired in homozygous *ve-cadherin*^{ubs8} mutant embryos at 48 hpf, while the number of CtAs remained unaffected. Expression of an intracellular modified VE-cadherinTS in *ve-cadherin*$^{ubs8/ubs8}$ mutants partially restored the lumen formation defects (wt: *n*= 2; *ve-cadherin*$^{ubs8/+}$: *n*=8; *ve-cadherin*$^{ubs8/ubs8}$: *n*=7; *ve-cadherin*$^{ubs8/ubs8}$ + TS: *n*=22).

b) Still images from time-lapse movies of *ve-cadherin*^{ubs8} mutant embryos expressing *Tg(fli1a:lifeact-GFP)*^{mu240}*.* In homozygous *ve-cadherin*^{ubs8} mutants anastomosis of CtAs was completely abolished. Heterozygous siblings did not exhibit anastomosis defects (*ve-cadherin*$^{ubs8/ubs8}$: *n* = 4; siblings: *n* = 4).

c) Homozygous *esama*^{ubs19} mutants showed decreased proportion of lumenized CtAs, but no changes in CtA numbers (*esama*$^{+/ubs19}$: *n*=9; *esama*$^{ubs19/ubs19}$: *n*=10).
Confocal images show dorsal views (anterior to the left) and GFP expression of *Tg(fli1a:lifeact-GFP)*^{mu240} (a,b) or mKate expression of *Tg(kdrl:mKate-CAAX)*^{ubs16} (c).

d) Overexpression of a truncated VE-cadherin version (VE-cadΔC-EGFP) did not restore lumen formation defects in Wnt-depleted embryos. *Tg(kdrl:GFP)*^{s843} (control) or *Tg(fli1a:Gal4)*^{ubs3}*;(UAS: VE-cadΔC-EGFP)*^{ubs12} embryos were treated from 29 to 48 hpf with IWR-1 or DMSO (control: DMSO: *n*=7, IWR-1: *n*=8; VE-cadΔC: DMSO: *n*=14, IWR-1: *n*=13). Values in a-d represent mean ± SD. *p<0.05, **p<0.01, ***p<0.001, Student's t-test; *n*, number of analyzed embryos.

e) Inhibition of Wnt signaling by incubation with IWR-1 or heat shock induced EC-specific dnTcf expression did not severely affect *esama* mRNA expression at 32 or 42 hpf. Expression of *esama* in CtA sprouts was slightly decreased after IWR-1 treatment or mCherry-dnTcf^{iEC} expression (32hpf: DMSO: *n*=15, *N*=5 and IWR-1: *n*=9, *N*=5, mCherry^{iEC}: n=16, N=6 and mCherry-dnTcf^{iEC}: n=10, N=5; 42hpf: DMSO: n=24, N=5 and IWR-1: *n*=16, *N*=5, mCherry: *n*=16, *N*=5 and mCherry-dnTcf: *n*=9, *N*=4). Confocal images show lateral views (anterior to the left) of *Tg(kdrl:GFP)*^{s843} embryos following display whole mount fluorescent *in situ* hybridization in combination with anti-GFP immunostaining. Quantifications were represented by Box-and-Whisker plots with median (center line), 25th and 75th percentiles (bounds of box) and Min-to-Max (whiskers), *p<0.05, **p<0.01, ***p<0.001, Student's t-test; *n*, number of CtA volumes analyzed; *N*, number of embryos analyzed; CtAs, central arteries; ECs, endothelial cells; PHBC, primordial hindbrain channel, TS, tension sensor; Scale bars: 50 μm.

Supplementary Figure 5

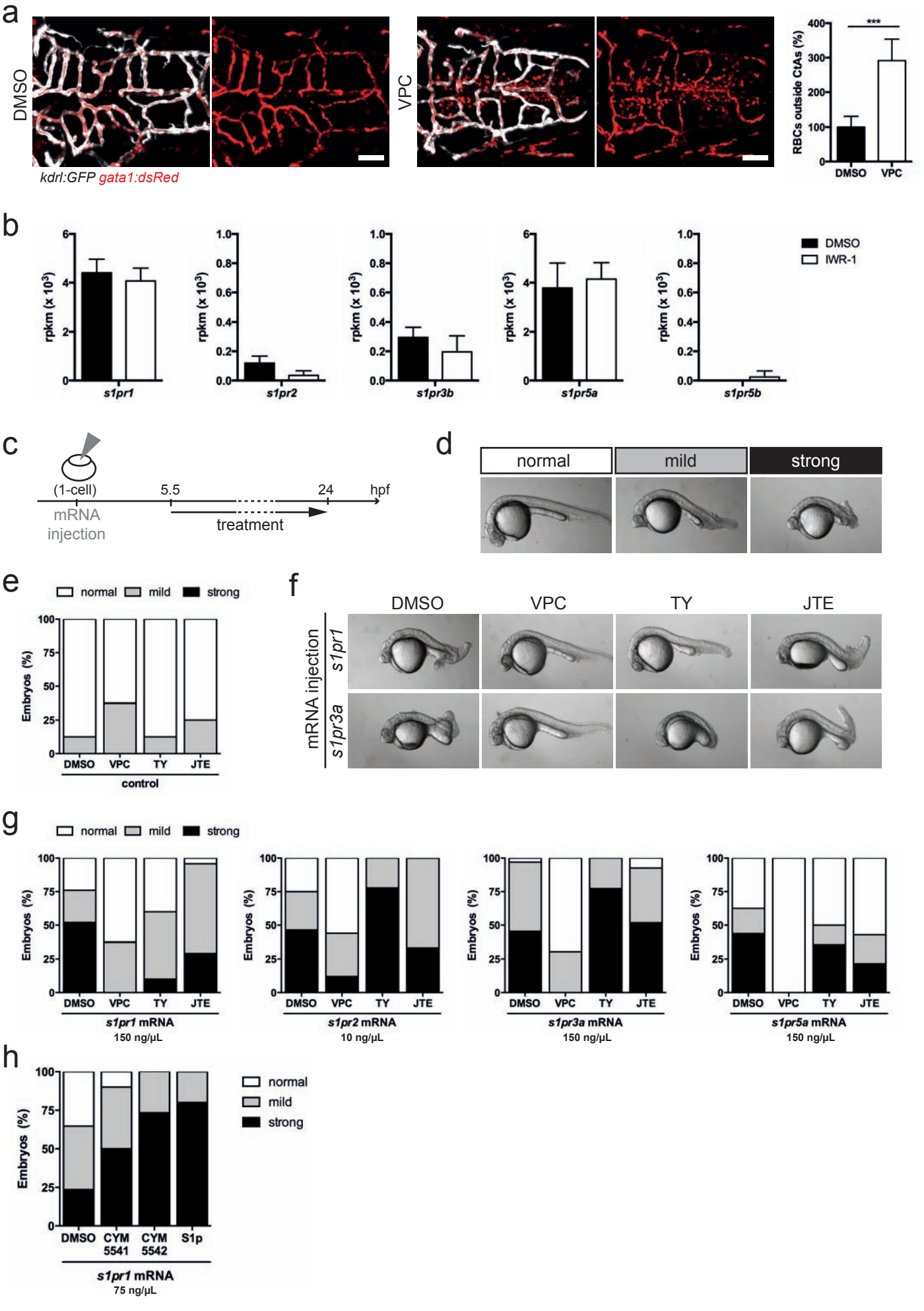

Supplementary Figure 5

Pharmacological targeting of S1pr receptors in zebrafish

a) Pharmacological inhibition of S1pr signaling causes extravasation of erythrocytes (red blood cells, RBCs). Embryos expressing GFP in ECs (by *Tg(kdrl:GFP)*^{s843}) and dsRed in RBCs (by *Tg(gata1:dsRed)*^{sd2}) were treated with VPC23019 (VPC) or DMSO from 48 to 72 hpf (DMSO: *n*=9; VPC: *n*=9).

b) Expression levels of *s1pr's* expressed in CtA ECs were not significantly changed by inhibition of Wnt signaling (RNA sequencing, see methods).

c-g) S1pr's (S1pr1, S1pr2, S1pr3a and S1pr5a) were overexpressed by mRNA injection into single-cell stage embryos. Rescue experiments were performed by treatment with VPC23019 (VPC, described S1pr1 and S1pr3 antagonist), TY52156 (TY, described S1pr3 antagonist) and JTE013 (JTE, described S1pr2 antagonist) from 5.5 hpf to 24 hpf (c,f,g). Embryos were sorted in categories according to phenotype (d): "normal" (white): wild type appearance, "mild": little developmental delay, minor anterior-posterior body axis formation defects (>60% of head and tail formed, intact eye and capacity of embryonic reflex),"strong": severe developmental delays, profound anterior-posterior axis defects (<60% of head and tail formed, obvious deformation or complete lack of tissues and organs, such as brain, eye and tail). VPC (described as S1pr1/S1pr3 antagonist) rescued phenotypic defects of all *s1pr* overexpression scenarios (f,g), TY (described as S1pr3 antagonist) specifically rescued *s1pr1* overexpression in zebrafish. The described S1pr2 antagonist JTE, did not restore phenotypic defects in the tested overexpression scenarios (e: control: DMSO: *n*=8, VPC: *n*=8, TY: *n*=8, JTE: *n*=8; f,g: *s1pr1* mRNA: DMSO: *n*=25, VPC: *n*=16, TY: *n*=20, JTE: *n*=24; *s1pr2* mRNA: DMSO: *n*=28, VPC: *n*=25, TY: *n*=27, JTE: *n*=30; *s1pr3a* mRNA: DMSO: *n*=33, VPC: *n*=33, TY: *n*=22, JTE: *n*=27; *s1pr5a* mRNA: DMSO: *n*=16, VPC: *n*=8, TY: *n*=14, JTE: *n*=14).

h) After mRNA injection overexpressed S1pr1 can be stimulated by S1p co-injection or treatment with pharmacological agonists. S1pr3 agonist CYM5541 or S1pr1 agonist CYM5542 aggravate phenotypic defects in comparison to control (*s1pr1* mRNA: DMSO: *n*=17, CYM5541: *n*=20, CYM5542: *n*=15, S1p: *n*=30). Brightfield images (d,f) show lateral views (anterior to the left) of representative zebrafish embryos at 24 hpf.

Values represent mean ±SD. *p<0.05, **p<0.01, ***p<0.001, student's t-test; *n*, number of analyzed embryos.

Supplementary Figure 6

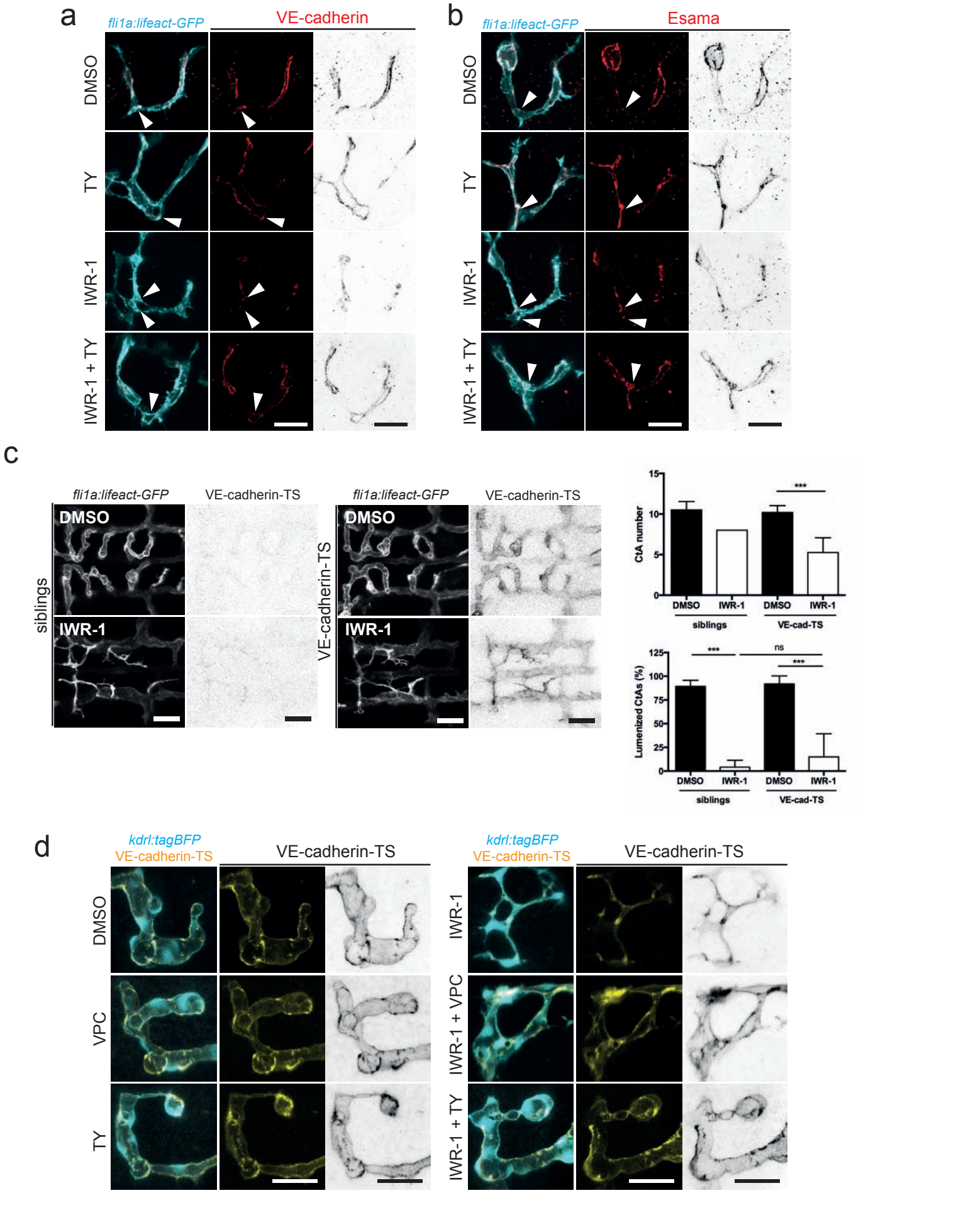

Supplementary Figure 6

Wnt and S1pr signaling regulate VE-cadherin localization

a,b) Inhibition of S1pr1 signaling together with blocking Wnt signaling rescued VE-cadherin (a) and Esama (b) protein levels at the cell-cell junctions. Immunostaining was performed for VE-cadherin (a, red) and Esama (b, red) of 42 hpf-old embryos after single or co-treatment with IWR-1 and TY. Junction localization of VE-cadherin and Esama (arrows show anastomosis rings) was reduced after IWR-1 treatment, not affected by TY treatment and restored in co-treated embryos.

c) Expression of the VE-cad-TS in wild type embryos does not restore or worsen the lumen formation defects caused by Wnt signaling inhibition. *Tg(ve-cad$_{BAC}$:ve-cadTS)^{uq11bh}* embryos (and control siblings) were treated with DMSO or IWR-1 from 29 to 48 hpf (sibling: DMSO: *n*=6, IWR-1: *n*=3; VE-cad-TS: DMSO: *n*=5, IWR-1: *n*=8). Values represent mean ±SD. *p<0.05, **p<0.01, ***p<0.001, One-way ANOVA; *n*, number of analyzed embryos.

d) Blocking of S1pr signaling rescued localization of VE-cad-TS in cell-cell junctions as well as lumen formation in Wnt-depleted embryos. Life imaging of VE-cad-TS embryos (*Tg(ve-cad$_{BAC}$:ve-cadTS)^{uq11bh}*) at 48 hpf following single or co-treatment with IWR-1 and S1pr antagonist VPC or S1pr1 antagonist TY starting from 29 hpf.

Confocal images show dorsal views (anterior to the left) and ECs labeled by *Tg(fli1a:lifeact-GFP)^{mu240}* (a-c) or *Tg(kdrl:tagBFP)^{mu293}* (d). CtAs, central arteries; S1pr, Sphingosine-1-phosphate receptor, TS, tension sensor, VE-cad, VE-cadherin; Scale bars: (a,b,d) 30 µm, (c) 50 µm.

Supplementary Figure 7

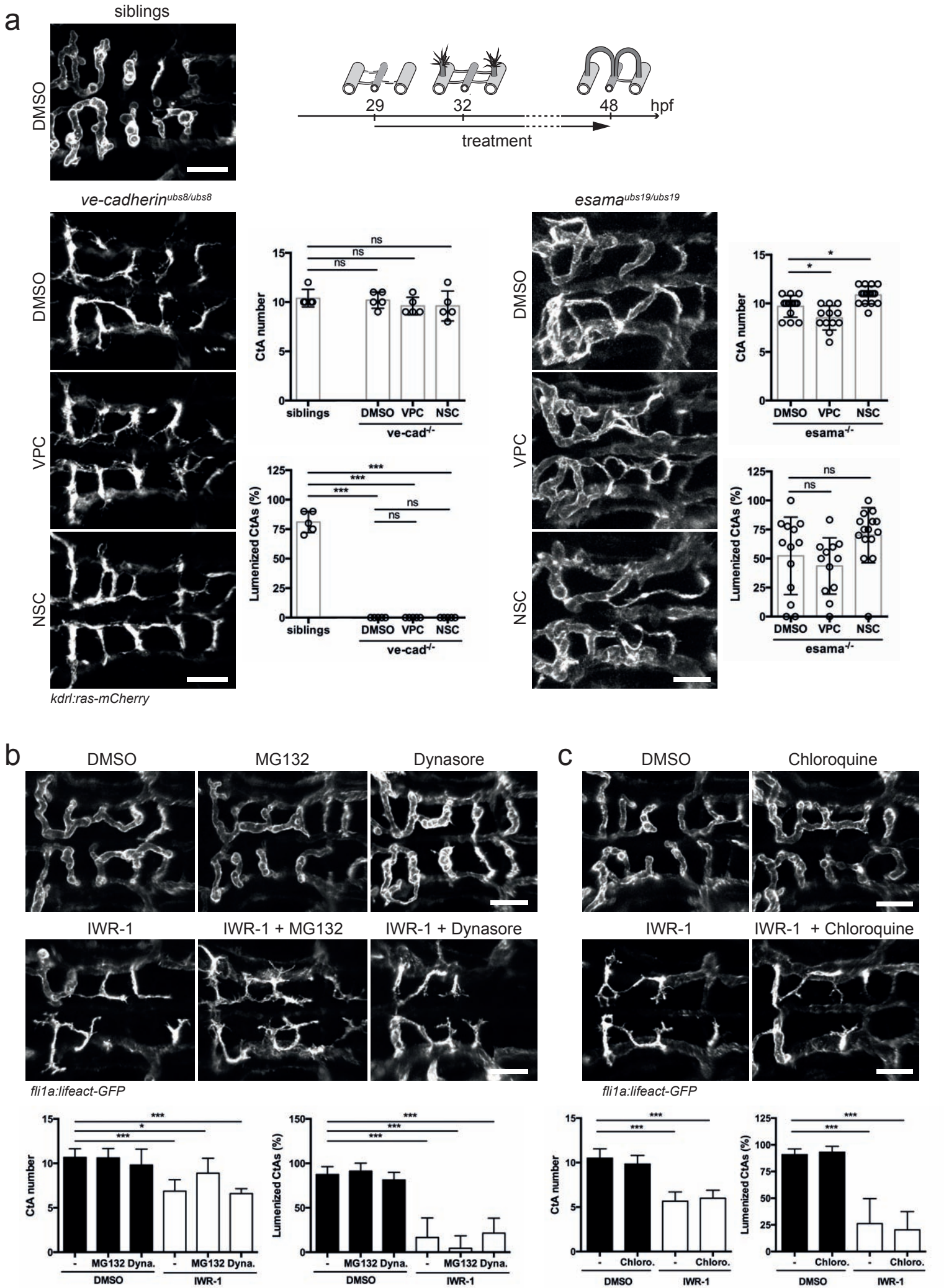

Supplementary Figure 7

Wnt and S1pr1 signaling act upstream of VE-cadherin function

a) Pharmacologic inhibition of S1pr signaling or Rac1 activity does not rescue CtA formation defects in *ve-cadherin* or *esama* mutant embryos. Treatment of *ve-cadherin* or *esama* mutant embryos with DMSO, VPC (S1pr antagonist) or NSC (Rac1 inhibitor) from 29 to 48 hpf (siblings: *n*=5; *ve-cadherin*$^{-/-}$: DMSO: *n*=5, VPC: *n*=5, NSC: *n*=5; *esama*$^{-/-}$: DMSO: *n*=13, VPC: *n*=15, NSC: *n*=12).

b,c) Embryos were single or co-treated with IWR-1, MG132 (proteasome inhibitor,b), Dynasore (dynamin inhibitor, b) or Chloroquine (lysosome inhibitor, c) from 29 to 48 hpf. Treatment with IWR-1 reduced CtA number and proportion of lumenized CtAs compared to control. Co-treatment with MG132, Dynasore or Chloroquine could not restore lumen formation defects caused by IWR-1 (b: DMSO: *n*=10; MG132: *n*=10; Dynasore: *n*=5; IWR-1: *n*=10; IWR-1 + MG132: *n*=10; IWR-1 + Dynasore: *n*=5; c: DMSO: *n*=6; Chloroquine: *n*=6; IWR-1: *n*=6; IWR-1 + Chloroquine: *n*=6).

Confocal images show dorsal views (anterior to the left) and ECs labeled by *Tg(kdrl:ras-Cherry)*^{s896} (a). or *Tg(fli1a:lifeact-GFP)*^{mu240} (b,c). Values represent mean ± SD. *p<0.05, **p<0.01, ***p<0.001, One-way ANOVA; *n*, number of analyzed embryos; CtAs, central arteries; S1pr, Sphingosine-1-phosphate receptor; Scale bars: 50 µm.

Supplementary Figure 8

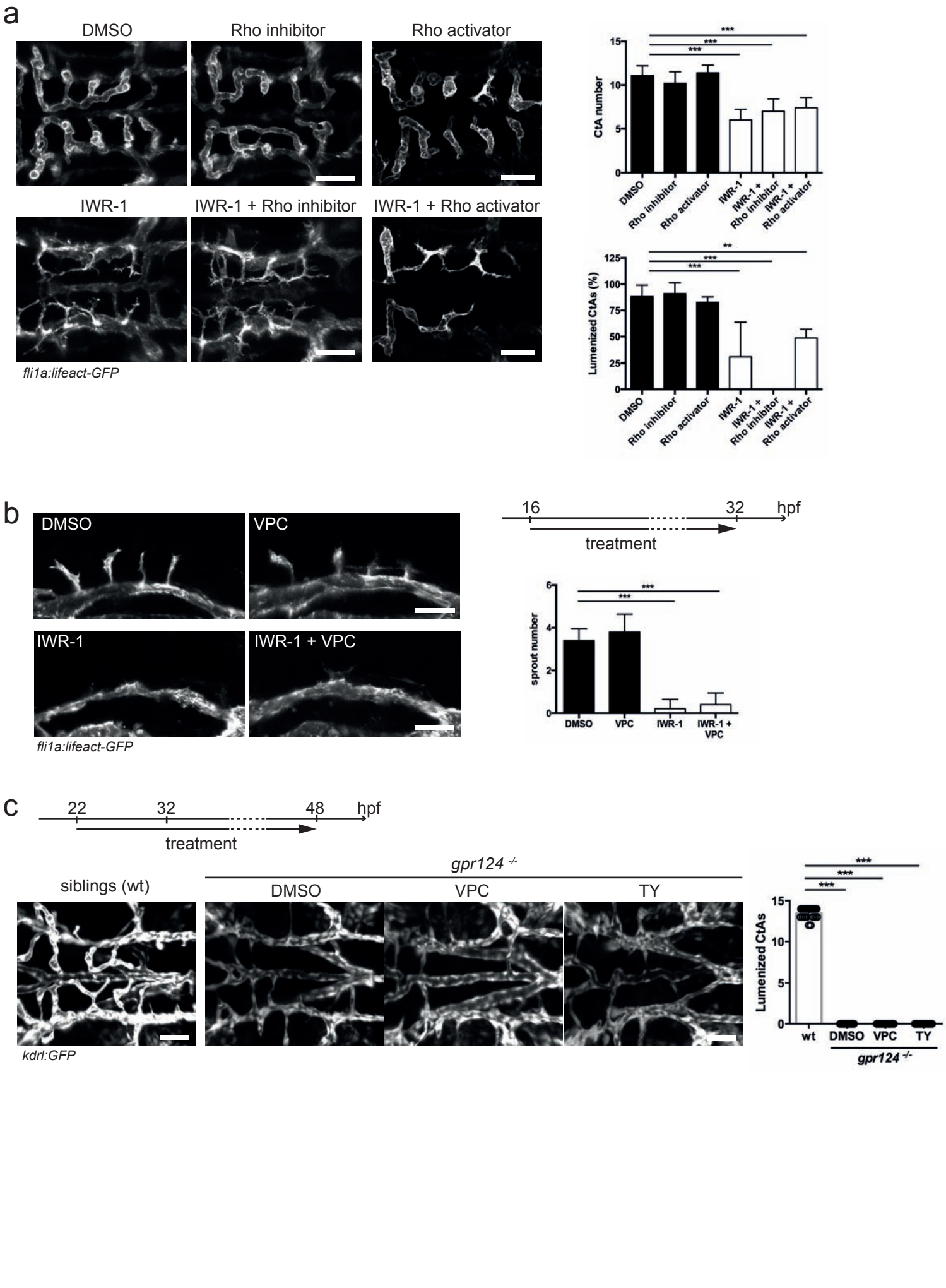

Supplementary Figure 8

Manipulation of Rho does not rescue Wnt-depleted embryos

a) Embryos were single or co-treated with IWR-1, Rho inhibitor or Rho activator from 29 to 48 hpf. CtA number and proportion of lumenized CtAs were reduced after treatment with IWR-1 and could not be rescued by co-treatment with Rho activator or Rho inhibitor (DMSO: *n*=10; Rho inhibitor: *n*=5; Rho activator: *n*=5; IWR-1: *n*=9; IWR-1 + Rho inhibitor: *n*=4; IWR-1 + Rho activator: *n*=5).

b) Pharmacologic inhibition of S1pr signaling does not rescue CtA sprouting defects in Wnt-depleted embryos. *Tg(fli1a:lifeact-GFP)^{mu240}* embryos were single or co-treated with IWR-1 and VPC starting from 16 ss (17 hpf) to 32 hpf. CtA tip cell formation was abolished in IWR-1 and IWR-1+VPC co-treated embryos, but not affected in VPC single-treated embryos in comparison to control (DMSO: *n*=5; VPC: *n*=5; IWR-1: *n*=5; IWR-1 + VPC: *n*=5).

c) Pharmacologic inhibition of S1pr signaling does not rescue CtA formation defects in *gpr124* mutant embryos. Treatment of gpr124 mutant embryos with DMSO, VPC or TY from 22 to 48 hpf (wt: *n*=10; *gpr124$^{-/-}$*: DMSO: *n*=10, VPC: *n*=8, TY: *n*=8).

Confocal images show dorsal views (a,c) or lateral views (b) (anterior to the left) and GFP expression from *Tg(fli1a:lifeact-GFP)^{mu240}*(a,c) or *Tg(kdrl:GFP)^{s843}*(b). Values represent mean ± SD. *p<0.05, **p<0.01, ***p<0.001, one-way ANOVA; *n*, number of analyzed embryos; CtAs, central arteries; S1pr, Sphingosine-1-phosphate receptor; Scale bars: 50 µm.

Supplementary Table 1

Primer	**Sequence (5' –> 3')**
s1pr1 fwd	ATGGATGACCTAATCGCC
s1pr1 rev	CGAGACGAAAAAGTTCACG
s1pr2 fwd	ATGACTACTTGCCGTCTG
s1pr2 rev	GGGATCTGCAAACACTTGG
s1pr3a fwd	ATGGATGACGAGCTTGAACC
s1pr3a rev	TCAGAACTTCCCCAAAGCG
s1pr5a fwd	GGTCAGCAGAAGTGAAATGG
s1pr5a rev	CAGACTTGTTTACTTGGCAG
s1pr1 CRISPR genotyping fwd	TCTATACTGCCAACATCCTG
s1pr1 CRISPR genotyping rev	CTGATGAGCATGAAGACCC
qPCR *axin2* fwd	CCTGGAGGAGAGACTTCAAC
qPCR *axin2* rev	GAGCAAAGGCAGAGAATGGG
qPCR *β-actin* fwd	CTGGACTTCGAGCAGGAGAT
qPCR *β-actin* rev	GCAAGATTCCATACCCAGGA
qPCR *β-catenin* fwd	GCCGCCACCAAACAGGAG
qPCR *β-catenin* rev	CAGCAGCACACGTCACCACG
qPCR *ccnd1* fwd	CTGTGCGACAGACGTCAACT
qPCR *ccnd1* rev	GGTGAGGTTCTGGGATGAGA
qPCR *lef1* fwd	GTTGGACAGATGACCCCTCC
qPCR *lef1* rev	CTGTTTCACCTGTGGGTTGAC

A.2.2. Angulo-Urarte et al., 2018, Nature communications

Endothelial cell rearrangements during vascular patterning require PI3-kinase-mediated inhibition of actomyosin contractility.

Summary:

Angulo-Urarte et al. investigated the contribution of the PI3K pathway to endothelial cell rearrangements *in vivo* and *in vitro* during vascular development. They show, that blocking PI3Kα signaling leads to impaired junctional remodeling and defective cell rearrangements. Additionally, cells grow in aberrant layers. Failure in rearrangements is reflected in the disability to stabilize new cell-cell contacts at sites of anastomosis. Furthermore, they uncovered a downstream pathway, namely NUAK1/MYPT1/MLCP, that drives cell rearrangements by inhibition of actomyosin contractility.

Aim of the collaboration and my contribution:

Aim of collaboration was to investigate junctional dynamics upon PI3K- inhibition using live *in vivo* time-lapse imaging. I treated embryos transgenically expressing EGFP-ZO1 with GDC0326 subjected to time-lapse imaging. Since embryos presented a dramatic increase in cell apoptosis that led to zebrafish embryonic death, I injected a morpholino against p53 prior to inhibitor treatment. This was to overcome unspecified off-target effects. Finally, I performed over-night time lapse imaging and post-acquisition image preparation.

nature COMMUNICATIONS

ARTICLE

DOI: 10.1038/s41467-018-07172-3 OPEN

Endothelial cell rearrangements during vascular patterning require PI3-kinase-mediated inhibition of actomyosin contractility

Ana Angulo-Urarte[1], Pedro Casado[2], Sandra D. Castillo[1], Piotr Kobialka[1], Maria Paraskevi Kotini[3], Ana M. Figueiredo[1], Pau Castel[4], Vinothini Rajeeve[2], Maria Milà-Guasch[1], Jaime Millan[5], Cora Wiesner[3], Helena Serra[1], Laia Muixi[1], Oriol Casanovas[6], Francesc Viñals[6,7], Markus Affolter[3], Holger Gerhardt[8,9,10], Stephan Huveneers[11], Heinz-Georg Belting[3], Pedro R. Cutillas[2] & Mariona Graupera[1,12]

Angiogenesis is a dynamic process relying on endothelial cell rearrangements within vascular tubes, yet the underlying mechanisms and functional relevance are poorly understood. Here we show that PI3Kα regulates endothelial cell rearrangements using a combination of a PI3Kα-selective inhibitor and endothelial-specific genetic deletion to abrogate PI3Kα activity during vessel development. Quantitative phosphoproteomics together with detailed cell biology analyses in vivo and in vitro reveal that PI3K signalling prevents NUAK1-dependent phosphorylation of the myosin phosphatase targeting-1 (MYPT1) protein, thereby allowing myosin light chain phosphatase (MLCP) activity and ultimately downregulating actomyosin contractility. Decreased PI3K activity enhances actomyosin contractility and impairs junctional remodelling and stabilization. This leads to overstretched endothelial cells that fail to anastomose properly and form aberrant superimposed layers within the vasculature. Our findings define the PI3K/NUAK1/MYPT1/MLCP axis as a critical pathway to regulate actomyosin contractility in endothelial cells, supporting vascular patterning and expansion through the control of cell rearrangement.

[1] Vascular Signalling Laboratory, ProCURE, Oncobell Program, Institut d´Investigació Biomèdica de Bellvitge (IDIBELL), Gran Via de l'Hospitalet 199, 08908 L´Hospitalet de Llobregat, Barcelona, Spain. [2] Centre for Haemato-Oncology, Barts Cancer Institute, Queen Mary University of London, London EC1M 6BQ, UK. [3] Biozentrum der Universität Basel, Klingelbergstrasse 50/70, 4056 Basel, Switzerland. [4] Helen Diller Family Comprehensive Cancer Center, University of California-San Francisco, 1450 3rd Street, San Francisco, CA 94158, USA. [5] Centro de Biología Molecular Severo Ochoa, CSIC-UAM, Calle Nicolás Cabrera, 28049 Madrid, Spain. [6] Translation Research Laboratory, ProCURE, Oncobell Program, IDIBELL, Gran Via de l'Hospitalet 199, 08908 L´Hospitalet de Llobregat, Barcelona, Spain. [7] Departament de Ciències Fisiològiques II, Universitat de Barcelona, Carrer de la Feixa Llarga, 08907 L´Hospitalet de Llobregat, Barcelona, Spain. [8] Max-Delbrueck Center for Molecular Medicine (MDC), Robert-Rössle-Straße 10, 13125 Berlin, Germany. [9] The German Center for Cardiovascular Research (DZHK), Oudenarder Str. 16, 13347 Berlin, Germany. [10] The Berlin Institute of Health (BIH), Berlin 10178, Germany. [11] Department of Medical Biochemistry, Amsterdam UMC, University of Amsterdam, Amsterdam Cardiovascular Sciences, Meibergdreef 9, 1105 AZ Amsterdam, Netherlands. [12] CIBERONC, Instituto de Salud Carlos III, Av. de Monforte de Lemos, 5, 28029 Madrid, Spain. These authors contributed equally: Pedro Casado, Sandra D. Castillo. Correspondence and requests for materials should be addressed to M.G. (email: mgraupera@idibell.cat)

Tissue growth and homoeostasis require the establishment of a functional hierarchical tubular network of blood vessels[1]. Blood vessels are mainly formed by a process known as sprouting angiogenesis in which new vascular sprouts arise from parental vessels, grow, and fuse to an adjacent sprout or a pre-existing vessel[1,2]. Newly formed sprouts are highly dynamic with endothelial cells interchanging their relative position within the vascular tube[3–7]. This collective cell migration across the vascular tubes relies on cell rearrangement; yet the regulation of this cell behaviour during the formation and patterning of blood vessels is poorly understood.

Endothelial cell rearrangement occurs through the reorganization of cell–cell junctional contacts thereby allowing the modification of cell−cell adhesion strengths[7–10]. In endothelial cells, there are two types of vascular endothelial-cadherin (Cdh5/VE-cadherin)-based junctional patterns, namely continuous or straight, and discontinuous or serrated[7,9,10]. Straight junctional VE-cadherin organization is mainly found in stable and mature junctions, whereas the serrated VE-cadherin junctional pattern is considered as immature or remodelling junctions[9,10]. Although these VE-cadherin junctional patterns are not visible in the endothelium during zebrafish developmental angiogenesis[11], computational models have proposed that spatial heterogeneity of these junctional patterns is necessary for cells to rearrange in vivo[7]. Yet, how these junctional profiles impact on the capacity of endothelial cells to rearrange remains poorly understood. Formation, remodelling, and stabilization of cell−cell adhesions in cultured endothelial cells are mediated by actin structures[12]. At mature junctions, linear VE-cadherin is aligned to parallel cortical actin bundles. Instead, serrated immature junctions are connected to perpendicular or radial tensile actin cables[9,10]. The switch between stable and immature junctions is mediated by actomyosin contraction-based pulling forces at the cell–cell junctions[9,10,13].

Among the different players of the angiogenic process, class I PI3-kinases (PI3K) have emerged as a critical node[14], for both the physiology of endothelial cells[15,16] and the pathogenesis of venous malformations[17,18], the most common type of vascular malformations. PI3Ks are lipid kinases that signal downstream of a variety of cell surface receptors and regulate cellular functions including growth, proliferation, migration, and metabolism[19]. Upon activation, these enzymes generate the lipid phosphatidylinositiol-3,4,5-triphosphate, a second messenger that triggers signalling pathways, such as those mediated by the serine/threonine kinase AKT and its substrates[20]. Of the class I PI3K isoforms, PI3Kα has been shown to be the only isoform required for endothelial-mediated vascular development[15]. Several studies have demonstrated that PI3Kα signalling primary regulates cell motility during angiogenesis in mouse and zebrafish[15,21,22].

Our study uncovers a PI3K downstream pathway, namely NUAK1/MYPT1/MLCP, as a critical node in the regulation of cell rearrangement during vessel growth. We have found that blockade of PI3Kα signalling impairs junctional remodelling, inhibits cell rearrangement and drives endothelial cells to grow in superimposed aberrant layers. We identify that a failure of cells to rearrange results in cell stretching and inability to remodel and stabilize new cell–cell contacts upon anastomosis. Through a combination of in vivo and in vitro approaches together with an unbiased and deep quantitative phosphoproteomic screening, we have discovered that PI3Kα mediates cell rearrangement by inhibiting actomyosin contractility through NUAK1/MYPT1/MLCP.

Results

PI3Kα mediates rearrangement of endothelial cells. Here, we investigated how endothelial cell rearrangements within the vascular sprouts contribute to vessel expansion and patterning. We and others have shown that the PI3Kα isoform regulates endothelial cell motility (Supplementary Fig. 1, Supplementary Movies 1 and 2, and refs. [15,21,22]). Therefore, we predicted that cell rearrangement would be altered upon blockage of this signalling node. To validate our hypothesis, we first studied vessel growth in zebrafish embryos treated with a PI3Kα isoform-specific inhibitor (GDC-0326; ref. [23]). We focused our studies between 27 and 38 h post fertilization (hpf), when intersegmental vessels (ISVs) that arise from the dorsal aorta reach the dorsal roof and form the dorsal longitudinal anastomotic vessels (DLAVs)[24]. Treatment with GDC-0326 efficiently inhibited PI3K signalling (Supplementary Fig. 2a) and this led to aberrant endothelial cell junctional patterns. Junctions were frequently disconnected in the dorsal region of the ISV axis and the junctional elongation was reduced in both ISVs and DLAV (Fig. 1a, b). We also observed the presence of ring-shaped junctions in these embryos that suggests lack of tight contact between adjacent endothelial cells (Fig. 1a). Moreover, GDC-0326-treated embryos showed a delay in the growth of ISVs (Supplementary Fig. 2b-d), without an overall delay in embryo development (Supplementary Fig. 2e). These aberrant junctional patterns are indicative of defects in cell rearrangements[11]. Conversely, in vehicle-treated embryos, ISV outgrowth was accompanied by a normal extensive junctional remodelling leading to a pattern of highly elongated endothelial cell junctions (Fig. 1a, b).

In order to translate our observations into a mammalian model, we inactivated PI3Kα in endothelial cells using genetic approaches and we studied retinal angiogenesis. To maximize *Pik3ca* deletion and avoid compensations by other PI3K isoforms we studied $Pik3ca^{KD/flox}$ mice, in which one *Pik3ca* allele is a constitutive kinase-dead (KD)[25], and the other is a lox-P-flanked *Pik3ca* allele[15]. $Pik3ca^{KD/flox}$ mice were crossed into the *Pdgfb-iCreER* transgenic mouse, which expresses a tamoxifen-inducible CRE recombinase specifically in endothelial cells[26] (further referred to as $Pik3ca^{KD/i\Delta EC}$) (Supplementary Table 1 provides details of the mouse models used). To ensure that *Pik3ca flox* allele is completely knocked out in our experimental settings, we assessed PI3Kα half-life in $Pik3ca^{flox/flox}$ mice crossed into the *Pdgfb-iCreER* (referred to as $Pik3ca^{i\Delta EC/i\Delta EC}$). Complete depletion of the PI3Kα protein was achieved at 96 h after 4-hydroxytamoxifen (4-OHT) treatment (Supplementary Fig. 3a). Thus, to reach complete PI3Kα depletion in vivo, we administered 4-OHT at postnatal day (P) 1 and P2 and investigated $Pik3ca^{KD/i\Delta EC}$ retinas at P7. As compared to control retinas, $Pik3ca^{KD/i\Delta EC}$ P7 retinas showed a decrease in phospho-S6 (pS6) (S240/4) and an enhanced nuclear FOXO1 staining confirming the inactivation of the PI3K pathway (Supplementary Fig. 3b, c).

In line with our previous findings in zebrafish embryos, we observed that endothelial cells in $Pik3ca^{KD/i\Delta EC}$ retinas showed an increased number of junctional gaps (Fig. 1c–e; yellow arrowheads). Furthermore, in a proportion of vascular tubes, the junction gaps resulted either in isolated rings or single-dots of VE-cadherin, indicating lack of tight contacts between endothelial cells (Fig. 1c; red asterisks). To investigate this phenotype in further detail, we analysed VE-cadherin-based cell−cell junctions in cultured endothelial cells from $Pik3ca^{KD/i\Delta EC}$ mice by immunostaining for β-catenin and F-actin (Fig. 1f). These experiments showed that $Pik3ca^{KD/i\Delta EC}$ endothelial cells failed to establish mature cell−cell junctions; instead, most of the junctions remained immature and connected to radial actin fibres (Fig. 1f–h). Together these data indicate that PI3Kα signalling is involved in cell−cell junctional remodelling in endothelial cells, a process required for cellular rearrangements within the vasculature.

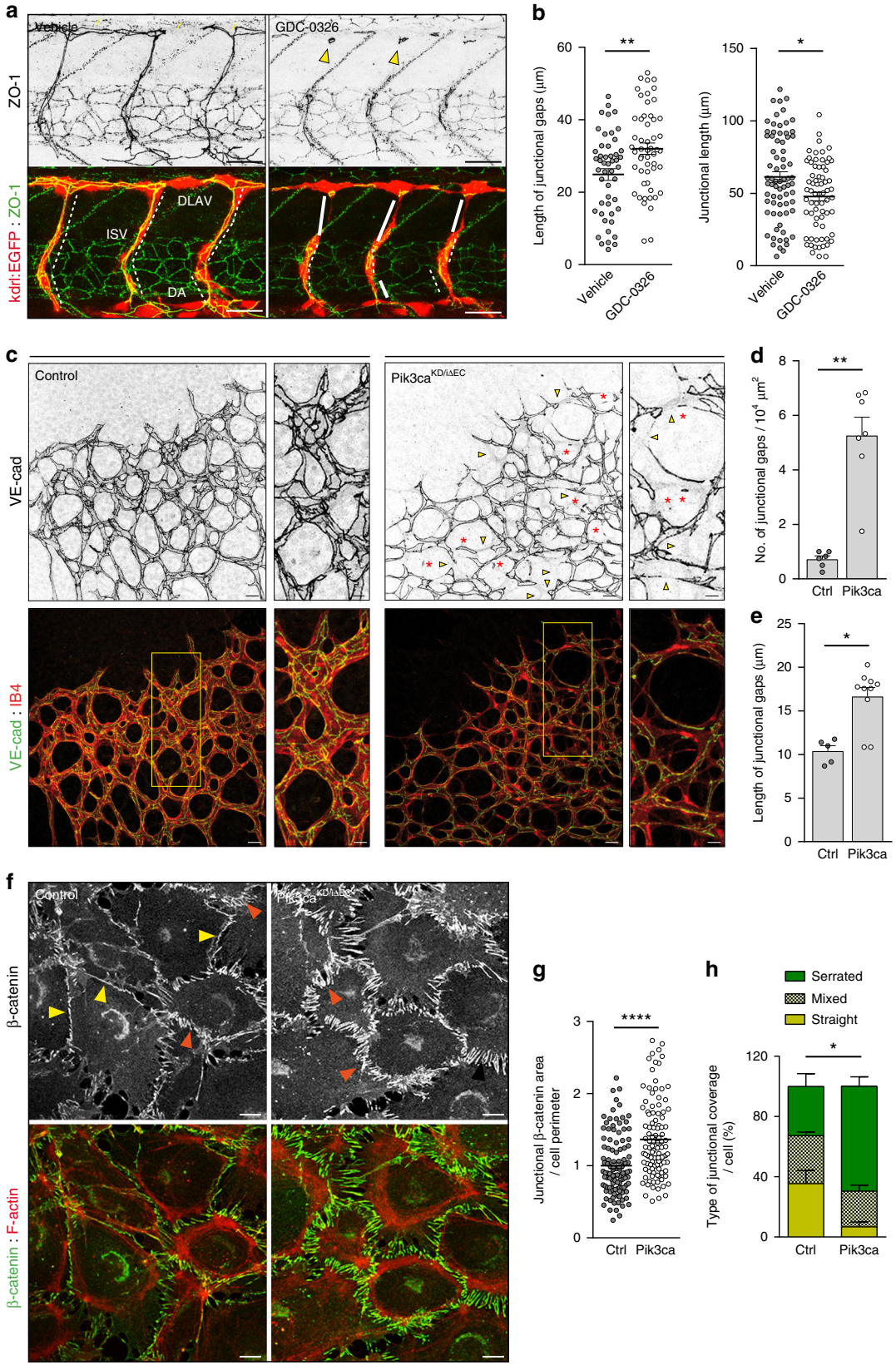

Defects in cell rearrangements lead to anastomosis failure. P7 *Pik3ca*$^{KD/i\Delta EC}$ retinas exhibited a significant reduction in vascular radial outgrowth (Fig. 2a and Supplementary Fig. 4a) with no detectable differences in sprouting activity (Supplementary Fig. 4c, d). This phenotype was further increased at P10, with the sprouting front of *Pik3ca*$^{KD/i\Delta EC}$ retinas neither reaching the periphery of the retina nor invading deeper retinal layers (Fig. 2a and Supplementary Fig. 4b). However, P7 *Pik3ca*$^{KD/i\Delta EC}$ retinas showed an increase in vessel density with vascular tubes growing in multiple layers (Fig. 2a–c; Supplementary Fig. 4e and

Fig. 1 Defects in junctional remodelling upon inactivation of PI3Kα in endothelial cells. **a** Lateral views of intersomitic vessels (ISV) in vehicle and GDC-0326 (50 μM)-treated transgenic Tg(*kdrl:EGFP*)^{s843} (shown in red) embryos stained for ZO-1 (green) at 33 h post fertilization (hpf). Single ZO-1 staining is shown in upper row. DA refers to dorsal aorta and DLAV refers to dorsal longitudinal anastomotic vessels. White lines indicate ZO-1 negative staining; punctuate white lines indicate elongation of junction; yellow arrowheads show ring-shape junctions. **b** Quantification of the length of the dorsal part of the ISVs without ZO-1 (left graph) and length of the ISVs with continuous ZO-1 staining (right graph) in vehicle and GDC-0326 treated embryos ($n \geq 54$ ISVs per treatment). **c** Representative maximum intensity projections of anti-VE-cadherin (green) and isolectin B4 (IB4, red) immunostained control and *Pik3ca*$^{KD/i\Delta EC}$ mouse retinas at P7. Single channel is shown in upper row. Yellow islets show higher magnification of selected regions shown to the right. Yellow arrowheads indicate vascular segments without VE-cadherin staining; red asterisks indicate VE-cadherin-positive isolated rings or single-dots within the vascular tubes, indicating cell−cell junctional contacts that have not elongated. **d**, **e** Quantitative number of VE-cadherin-negative vessels (junctional gaps) per unit area ($n \geq 5$ retinas per genotype) (**d**) and length of vessel structures without VE-cadherin (length of junctional gaps) ($n \geq 6$ retinas per genotype) (**e**). **f** Confocal immunofluorescence images of primary mouse endothelial cells isolated from control and *Pik3ca*$^{KD/i\Delta EC}$ mice stained for β-catenin (green) and F-actin (red) after being treated with 4-OHT for 72 h and re-plated on gelatin-coated slides for 24 h. Yellow arrowheads indicate straight junctional pattern; orange arrowheads indicate serrated junctional pattern. **g** Graph shows the average of β-catenin-positive area along junctional linescans ($n \geq 109$ cells from six independent experiments). **h** Quantification of percentages of cells with serrated, straight or mixed junctions ($n = 5$ independent experiments). Scale bars, 30 μm (**a**), 20 μm (**c**), 10 μm (**c** small panel, **f**). Data in **b**, **d**, **e**, **g**, **h** represent mean ± SEM (error bars). $^{*}P < 0.05$, $^{**}P < 0.01$, $^{****}P < 0.0001$ were considered statistically significant. Statistical analysis was performed by the two-sided Mann–Whitney test

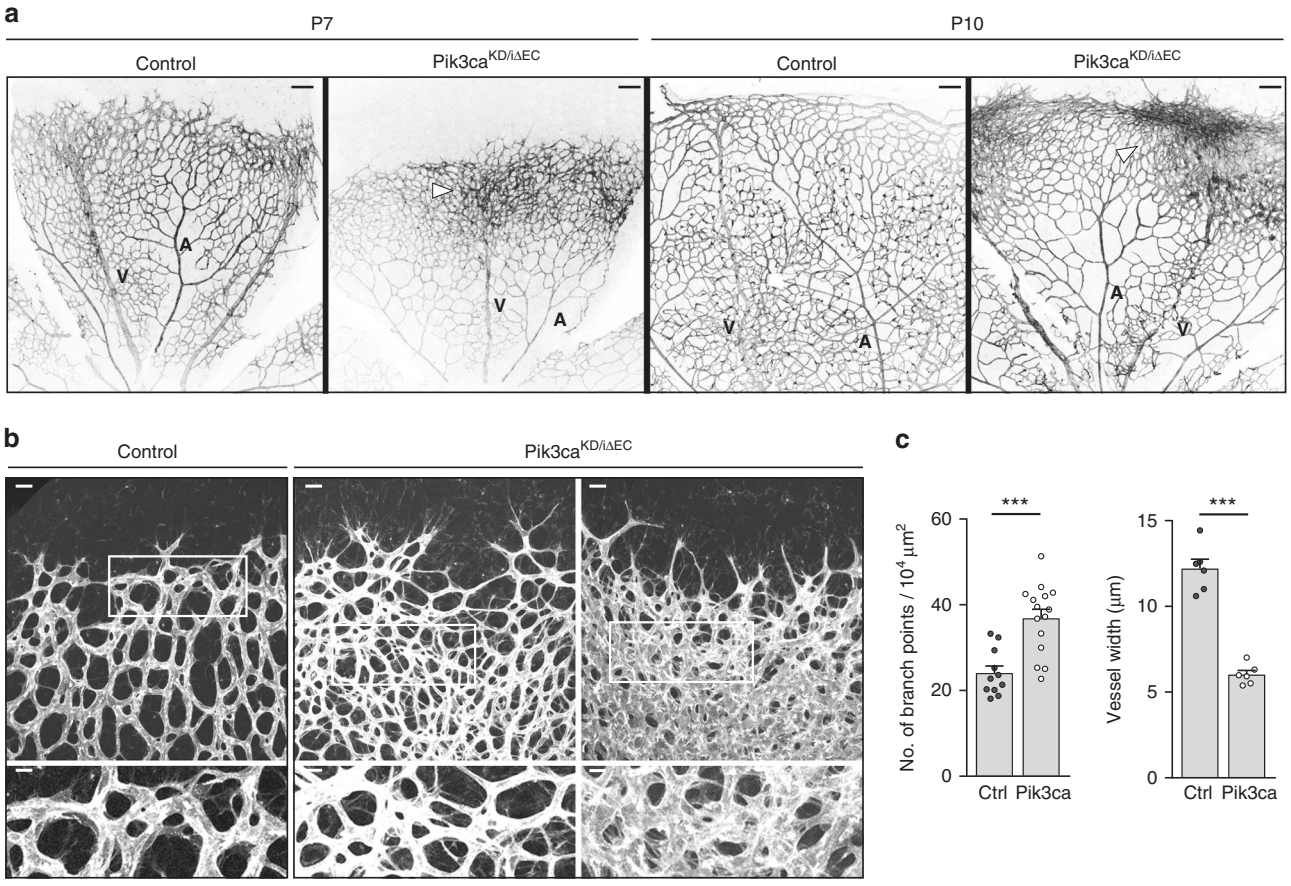

Fig. 2 Endothelial PI3Kα regulates vascular growth. **a** Representative images of whole mount retinas stained with IB4 from control and *Pik3ca*$^{KD/i\Delta EC}$ mouse littermates at P7 and at P10. Veins (V) and arteries (A) are indicated. White arrowheads show areas where the vascular plexus is superimposed. **b** Representative high-magnification images of whole mount retinas stained with IB4 from control and *Pik3ca*$^{KD/i\Delta EC}$ mouse littermates at P7. Two independent areas for *Pik3ca*$^{KD/i\Delta EC}$ retinas are shown. White islets show higher magnification of selected regions shown below. **c** Quantification of number of branch points per unit area and vessel width per unit area of control (Ctrl) and *Pik3ca*$^{KD/i\Delta EC}$ (*Pik3ca*) retinas ($n \geq 6$ retinas per genotype). Scale bars, 100 μm (**a**), 20 μm (**b**, upper panels), 10 μm (**b**, lower panels). Data represent mean ± SEM (error bars). $^{***}P < 0.001$. Statistical analysis was performed by the two-sided Mann–Whitney test

Supplementary Movies 3 and 4); this superposition was more pronounced at P10 (Supplementary Fig. 4b, f). Also, the vascular tubes in *Pik3ca*$^{KD/i\Delta EC}$ retinas showed smaller calibre (Fig. 2b, c). Analysis of *Pik3ca*$^{KD/WT}$ and *Pik3ca*$^{i\Delta EC/i\Delta EC}$ retinas (Supplementary Table 1) showed that the former appeared normal, whereas *Pik3ca*$^{i\Delta EC/i\Delta EC}$ retinas looked similar to *Pik3ca*$^{KD/i\Delta EC}$ retinas but with milder vascular defects (Supplementary Fig. 4a, b).

Current models of enhanced vessel density involve an increase in the number of endothelial cells[16,17,27,28]. However, immunostaining of endothelial cell nuclei revealed a significant reduction in the total number of endothelial cells (Fig. 3a, b) and in

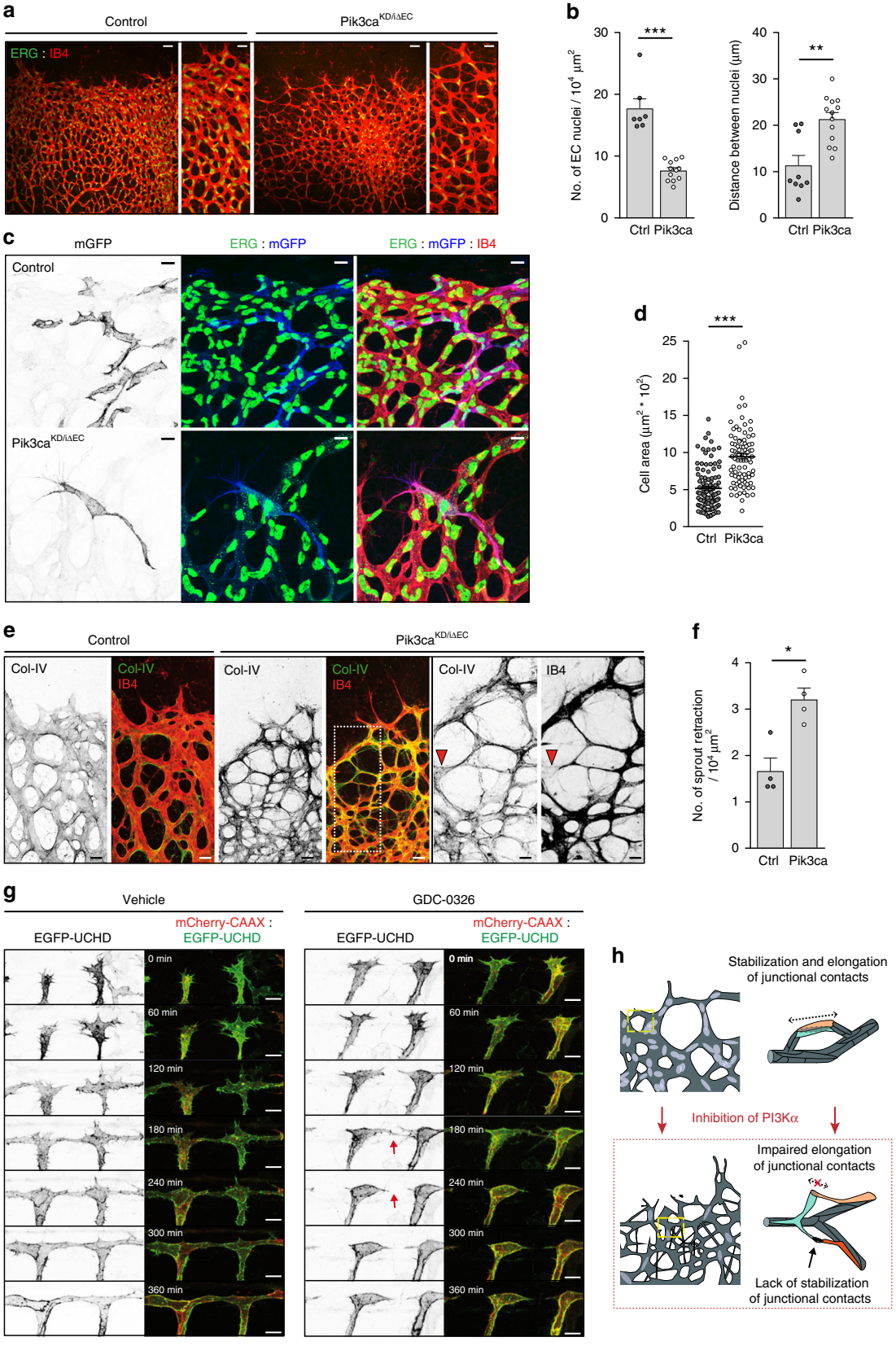

endothelial cells in S-phase in *Pik3ca*$^{KD/i\Delta EC}$ retinas (Supplementary Fig. 5a, b). Endothelial cells were highly stretched in *Pik3ca*$^{KD/i\Delta EC}$ retinal vessels, with the distance between adjacent endothelial cell nuclei increased by twofold (Fig. 3a, b). This suggests that these cells failed to elongate alongside each other, a process known as cell pairing[29], and as a consequence the cells overstretched. Given the lower number of endothelial cells in GDC-0326-treated embryos and in *Pik3ca*$^{KD/i\Delta EC}$ retinas, a reduction in cell number might interfere with cell rearrangement during sprouting angiogenesis

Fig. 3 Cell stretching defects and anastomosis failure in *Pik3ca*$^{KD/i\Delta EC}$ vessels. **a** Representative images of retinas stained for ERG (green) and IB4 (red) from control and *Pik3ca*$^{KD/i\Delta EC}$ P7 pups. Higher magnification are shown to the right. **b** Quantification of endothelial cells per unit area assessed by ERG positivity and of the distance between two adjacent endothelial cell nuclei ($n \geq 6$ retinas per genotype). **c** Immunostaining of single-cell labelling with membrane-bound GFP (mGFP, blue), endothelial nuclei (ERG, green) and blood vessel (IB4, red). Retinas from *Pdgfb-iCre;Pik3ca*$^{WT/flox}$ were used as control. **d** Quantification of cell size of individual mGFP-positive cells in control and *Pik3ca*$^{KD/i\Delta EC}$ retinas. At least 89 individual mGFP-positive cells from four independent retinas per genotype were quantified. **e** Images of control and *Pik3ca*$^{KD/i\Delta EC}$ P7 retinas stained for collagen IV (green) and IB4 (red). Single channels are also shown. White punctuated islet in the image of a *Pik3ca*$^{KD/i\Delta EC}$ retina shows higher magnification of selected region to the right. Red arrowheads indicate a retracting sprout. **f** Quantification of retracting sprouts per area ($n = 4$ retinas per genotype). **g** Images from a time-lapse movie (starting at 30 hpf) showing lateral views of ISV morphogenesis in transgenic Tg(*UAS:EGFP-UCHD*)^{ubs18};(*kdrl:mCherry-CAAX*)^{S916} embryos treated with vehicle (left panel) or GDC-0326 (50 μM) (right panel). Endothelial cell membrane is visualized in red and the actin cytoskeleton is visualized by F-actin binding domain of utrophin in green. Single channels are also shown. Red arrow shows a retracting event between two endothelial cells. **h** Schematic illustration showing the vascular defects driven by inactivation of PI3Kα (designed by Ana Angulo-Urarte). During vessel growth remodelling, stabilization, and elongation (punctuated arrow) of adherent junctional contacts is required between neighbouring endothelial cells to rearrange. Upon inactivation of PI3Kα, endothelial cells fail to stabilize (black arrow) and elongate (crossed punctuated arrow) junctional contacts. Scale bars, 40 μm (**a**), 20 μm (**a** amplified panels, **e**), 10 μm (**c**, **e** amplified panels) 15 μm (**g**). Data in **b**, **d**, and **f** represent mean ± SEM (error bars). $^{*}P < 0.05$, $^{**}P < 0.01$, $^{***}P < 0.001$. Statistical analysis was performed by the two-sided Mann−Whitney test

(as shown in Fig. 1). To test this possibility, we inhibited cell proliferation with systemic administration of mitomycin C at P5, 48 h before harvesting the retinas at P7, followed by assessing cell proliferation and vascular patterning. As previously described[30], 5-ethynyl-2′-deoxyuridine (EdU) incorporation showed a prominent block in endothelial cell proliferation in mitomycin C-treated retinas, leading to an overall reduction in endothelial cells (Supplementary Fig. 5c-f). However, no major differences in VE-cadherin junctional pattern were observed (Supplementary Fig. 5e, f). Similar results were observed in zebrafish embryos upon administration of the cell cycle blockers aphidicolin (APH) or hydroxyurea (HU) (Supplementary Fig. 6a-g). These data indicate that inhibition of cell proliferation per se does not impair cell rearrangement.

We hypothesized that the increase in vascular branches observed in *Pik3ca*$^{KD/i\Delta EC}$ retinas (Fig. 2b, c) was the result of stretched endothelial cells extending multiple protrusions. To visualize single-cell morphology, we used R26-mTmG reporter mice, which express a membrane-bound green fluorescent protein (GFP) upon *Cre* recombination[31]. We crossed R26-mTmG reporter mice with *Pik3ca*$^{KD/i\Delta EC}$ mice and reduced the tamoxifen dose in order to induce mosaic inactivation of PI3Kα (Supplementary Fig. 7a). Analysis of single cells confirmed stretched cell-shapes upon inactivation of PI3Kα (Fig. 3c, d). Cell pairing is an important process for the formation of multicellular vascular tubes; thus the absence of cell pairing might result in defects in lumen formation. Staining for intracellular adhesion molecule 2 (ICAM2), a marker of the apical side of vessels, confirmed frequent lumenal gaps in *Pik3ca*$^{KD/i\Delta EC}$ retinal vessels. The lack of ICAM2 staining in *Pik3ca*$^{KD/i\Delta EC}$ retinas was principally observed in thin tubular structures (Supplementary Fig. 7b, c; yellow asterisks), supporting the notion that the nonluminized tubes are only cell protrusions. Inactivation of PI3Kα also led to an increase in collagen IV empty sleeves in newly formed sprout connections (Fig. 3e, f), showing a lack of stabilization of new contacts and a failure to anastomose. In zebrafish embryos treated with GDC-0326, time-lapse analysis of DLAV formation confirmed that initial contacts between adjacent sprouts occurred but they failed to stabilize, resulting in frequent cell retraction and sprout disconnections (Fig. 3g; Supplementary Movies 5 and 6).

Together, our data show that PI3Kα is necessary for cells to rearrange by regulating remodelling, elongation and stabilization of junctional contacts. Lack of cell rearrangements results in stretched endothelial cells which extend multiple protrusions that fail to anastomose and grow in superimposed aberrant layers (Fig. 3h). While proliferation defects likely contribute to impaired cell rearrangement upon inhibition of PI3K, our data indicate that PI3K signalling primarily regulates junctional remodelling and cell rearrangement.

PI3Kα inhibition upregulates phospho-MYPT1. To define the molecular and signalling changes occurring upon inactivation of PI3Kα in endothelial cells, we performed untargeted mass spectrometry (MS)-based phosphoproteomics analyses in primary mouse endothelial cells from *Pik3ca*$^{flox/flox}$ (control) and *Pik3ca*$^{KD/i\Delta EC}$ mice. We analysed four biological replicates per genotype, each of which was treated with vehicle (ethanol) for 24 h or 4-OHT for 24 and 96 h (Fig. 4a). We identified a total of 6836 phosphopeptides in the 24 samples analysed, which were quantified using a previously described label-free methodology[32], generating 328,128 data points. This analysis identified: (i) 224 differently regulated phosphopeptides in the *Pik3ca*$^{KD/flox}$ endothelial cells relative to control; (ii) 122 deregulated phosphopeptides in *Pik3ca*$^{KD/i\Delta EC}$ endothelial cells upon 24 h treatment with 4-OHT; and (iii) 202 deregulated phosphopeptides in *Pik3ca*$^{KD/i\Delta EC}$ endothelial cells upon 96 h treatment with 4-OHT (Fig. 4b, c).

We clustered the phosphorylation sites that were significantly deregulated at 96 h post 4-OHT treatment by gene ontology (Supplementary Fig. 3a). Of particular relevance for the cell rearrangement phenotype observed, we found a total of 23 phosphosites from 14 cytoskeleton-related proteins that were differently modulated between *Pik3ca*$^{KD/i\Delta EC}$ and control endothelial cells. These included the myosin light chain phosphatase (MLCP), CDC42, RAC1, junctional proteins, focal adhesions, intermediate filaments, and microtubules (Fig. 4d).

Among the different candidates, *Pik3ca*$^{KD/i\Delta EC}$ endothelial cells showed an upregulation on the S445 phosphosite (pS445) of the phosphatase 1 regulatory subunit 12 A (Ppp1r12A) also known as MYPT1 (Fig. 4d). This protein was of particular interest because, together with PP1β and M20, it composes the MLCP complex and regulates the dephosphorylation of the myosin light-chain (MLC) 2 (refs. [33–36]), which is required for the contraction of actomyosin (illustration is shown in Supplementary Fig. 8a). We validated the increase of pS445 MYPT1 in *Pik3ca*$^{KD/i\Delta EC}$ endothelial cells by western blot (Fig. 4e; Supplementary Fig. 8b, c). Also, we confirmed the PI3Kα-mediated regulation of pS445 MYPT1 in wild-type endothelial and HEK-293 cells treated with GDC-0326 (Fig. 4e; Supplementary Fig. 8b, c).

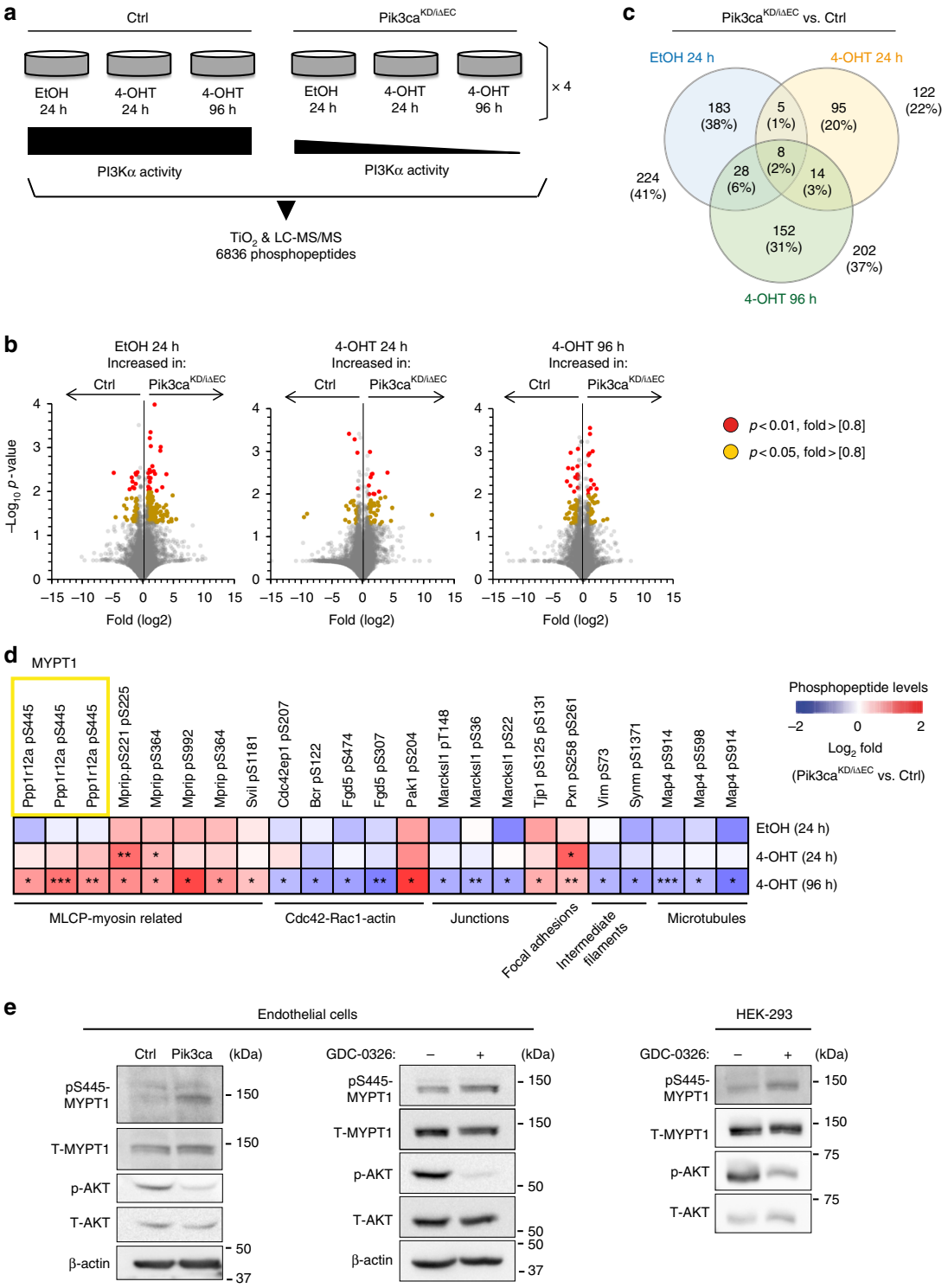

PI3Kα is required to suppress actomyosin contractility. Zagoroska et al. found that S445 MYPT1 phosphorylation triggers the binding of MYPT1 to 14-3-3, thereby blocking the ability of the MLCP complex to dephosphorylate MLC2 in S19 and T18/S19 (ref. [35]). Thus, we predicted that inhibition of PI3Kα, and the resultant increase of MYPT1 S445 phosphorylation, might promote the detachment of MLCP from the actomyosin machinery, thereby increasing actomyosin contractility. Indeed, we detected that the ability of MYPT1 to bind β-actin in an overlay assay was reduced upon inhibition of PI3Kα (Fig. 5a). By knocking down MYPT1 protein expression with small interference RNA (siRNA), we found that phosphorylation of MLC2 at S20 (S19 in humans) was increased upon MYPT1 downregulation in endothelial cells (Fig. 5b–d).

Enhanced phosphorylation of MLC2 on S20 was also found upon both genetic and pharmacologic inhibition of PI3Kα in mouse endothelial cells (Supplementary Fig. 9a, b). Moreover, pS20 MLC2 staining was enriched at the subcortical region of *Pik3ca*$^{KD/i\Delta EC}$ endothelial cells (Fig. 6a–c; Supplementary Fig. 9c). This was correlated with subcortical accumulation of F-actin

Fig. 4 Phosphoproteomics elucidate downstream effectors of PI3Kα in endothelial cells. **a** Schematic illustration of the untargeted label-free mass spectrometry analysis. The study was conducted in *Pik3ca*$^{flox/flox}$ (control) and *Pdgfb-iCre;Pik3ca*$^{KD/flox}$ (*Pik3ca*$^{KD/i\Delta EC}$) mouse lung endothelial cells under exponential growing conditions upon preincubation with vehicle (EtOH) or 4-OHT for the indicated time points. The vehicle condition for analysis of the heterozygous inactivation of PI3Kα (*Pik3ca*$^{KD/flox}$ without induction of CRE activity) was included as a further control and four different mice were analysed in each condition (a total of 24 samples). **b** Volcano plots exhibiting changes in phosphopeptides across genotypes. The *Y* axis represent the negative $\log_{10}$ of *P* value and the *X* axis shows the $\log_2$ of the fold change between control and *Pik3ca*$^{KD/i\Delta EC}$ endothelial cells treated with vehicle (EtOH) for 24 h, 4-OHT for 24 h or 4-OHT for 96 h. Red and yellow dots represent significantly regulated phosphopeptides ($P < 0.01$ and $P < 0.05$ respectively) with a fold-change higher than 0.8 or lower than −0.8. **c** Venn diagram showing the number and percentage of phosphopeptides which are significantly upregulated or downregulated between experimental groups. Number and percentage of overlapping phosphopeptides between groups are also shown. **d** Heatmap indicating fold-changes in the phosphorylation of proteins related to the cytoskeleton. Phosphopeptides identified to be down- or upregulated in *Pik3ca*$^{KD/i\Delta EC}$ vs. Ctrl are shown in blue and red, respectively across EtOH and 4-OHT treatments. Values shown represent mean fold-change over Ctrl. **e** Western blot validation of pS445 MYPT1 in mouse lung endothelial cells and HEK-293 cells upon genetic and pharmacological inhibition of PI3Kα. Control and *Pik3ca*$^{KD/i\Delta EC}$ endothelial cells were treated with 4-OHT for 72 h, re-platted for 24 h and subjected to immunoblotting. Wild-type endothelial cells and HEK-293 cells were treated with vehicle or GDC-0326 for 48 h and subjected to immunoblotting. Quantification of at least three independent experiments is shown in Supplementary Figure 8

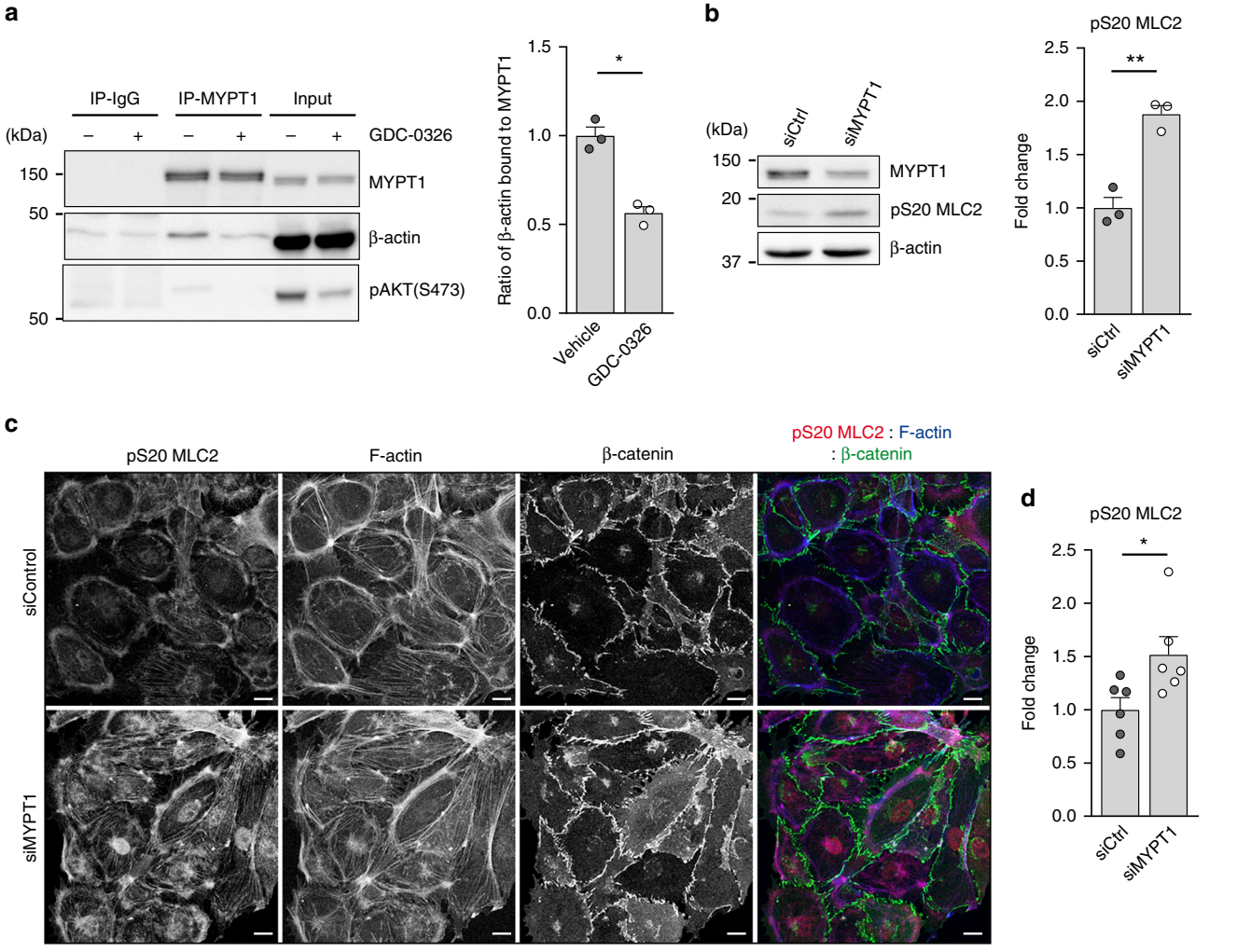

Fig. 5 MYPT1 promotes dephosphorylation of MLC2 in endothelial cells. **a** Immunoblot analysis of HEK-293 cells treated with vehicle or GDC-0326 for 48 h using the indicated antibodies. Endogenous MYPT1 was immunoprecipitated and its ability to interact with actin was assessed in an overlay assay. Bars to the right show quantification of actin bound to total MYPT1 from three independent experiments. **b** Western blot analysis of MYPT1, pS20 MLC2 and β-actin in lysates of wild-type mouse lung endothelial cells transfected with siControl (siCtrl) or siMYPT1. Bars to the right show quantification of pS20 MLC2 normalized to β-actin from three independent experiments. **c** Images of endothelial cells transfected with siCtrl or siMYPT1, seeded on gelatin-coated plates 72 h post-transfection, and immunostained for β-catenin (green), pS20 MLC2 (red) and F-actin (blue). **d** Quantification of total cell pS20 MLC2 immunostaining intensity (shown as integrated density) of images shown in **c** ($n \geq 6$ independent experiments). Scale bars, 15 µm (**c**). Data in **a**, **b**, and **d** represent mean ± SEM (error bars). $^*P < 0.05$, $^{**}P < 0.01$. Statistical analysis was performed in **a**, and **b** by the two-sided Student's *t* test and in **d** by the two-sided Mann–Whitney test

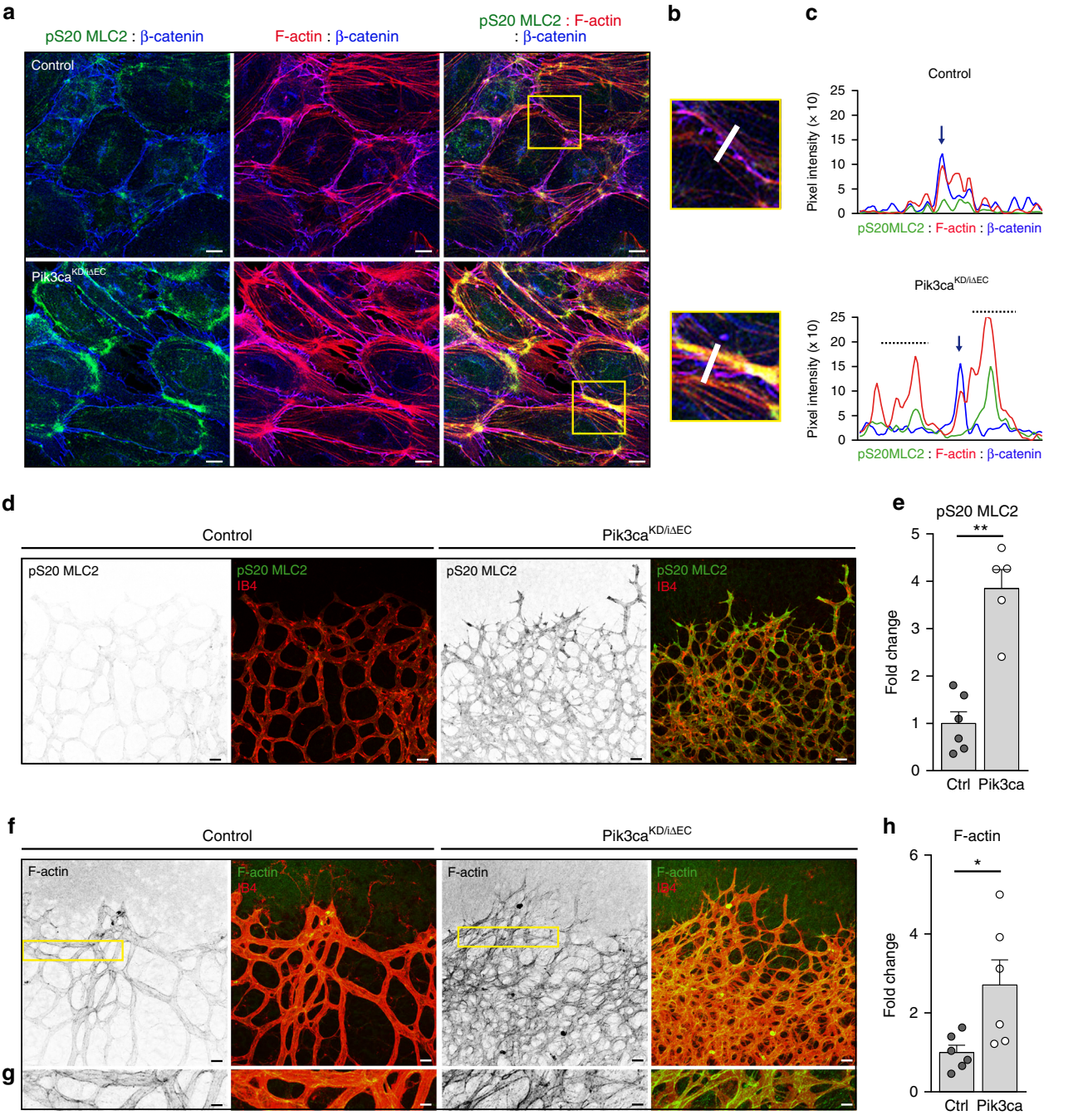

Fig. 6 Inactivation of PI3Kα results in increased actomyosin contractility. **a** pS20 MLC2 (green), F-actin (red) and β-catenin (blue) immunostaining of endothelial cells isolated from control and *Pik3ca*$^{KD/i\Delta EC}$ mice treated with 4-OHT for 72 h and re-plated on gelatin-coated slides for 24 h. **b** Yellow islets show higher magnification of selected regions in **a**. **c** Representative fluorescence intensities of pS20 MLC2, β-catenin and F-actin immunostaining corresponding to the area depicted by the white line in **b**. Vertical blue arrows indicate endothelial junction between two endothelial cells. Punctuated lines highlight subcortical area. **d** pS20 MLC2 (green) and IB4 (red) staining of control and *Pik3ca*$^{KD/i\Delta EC}$ P7 retinas. **e** Quantification of the intensity of pS20 MLC2 staining per vascular area (shown as integrated density) ($n \geq 5$ retinas per genotype). **f** F-actin (green) and IB4 (red) staining of control and *Pik3ca*$^{KD/i\Delta EC}$ P7 retinas. **g** High magnification of selected regions shown in (**f**) illustrates the increase in F-actin intensity induced in *Pik3ca*$^{KD/i\Delta EC}$ endothelium. **h** Quantification of F-actin staining per vascular area (shown as integrated density) ($n \geq 6$ retinas per genotype). Scale bars, 15 µm (**a**), 20 µm (**d**, **f**), 10 µm (**g**). Data in **e** and **g** represent mean ± SEM (error bars). $^{*}P < 0.05$, $^{**}P < 0.01$. Statistical analysis was performed by the two-sided Mann–Whitney test

(Fig. 6a–c; Supplementary Fig. 9d). Instead, control cells showed stress fibres evenly distributed between the cytoplasm and the subcortical area of the cell (Fig. 6a–c). Analysis of *Pik3ca*$^{KD/i\Delta EC}$ retinal vessels confirmed an increase in the intensity of pS20 MLC2 (Fig. 6d, e) and F-actin staining (Fig. 6f, g). Together, these experiments show that PI3Kα activity is required to downregulate actomyosin contractility and may also explain why *Pik3ca*$^{KD/i\Delta EC}$ endothelial cells fail to stabilize junctions in vivo (Fig. 1).

NUAK1 inhibition restores PI3Kα-driven vascular phenotypes. Two non-related protein kinases are able to phosphorylate

MYPT1 on S445, namely NUAK family kinase 1 (NUAK1)[35] and large tumour suppressor kinase 1 (LATS1)[37]. Up to date, only NUAK1 has been reported to regulate phosphorylation of MLC2[35]. Based on these findings, we tested whether restoring MLCP activity by blocking NUAK1 reduces pS20 MLC2 and suppresses actomyosin contractility. Treatment of endothelial cells with a selective NUAK1 inhibitor (NUAKi)[38] reduced phosphorylation of MLC2 and F-actin staining (Fig. 7a). Inhibition of ROCK, the main kinase that phosphorylates MLC2, was not sufficient to completely abrogate actomyosin contractility in *Pik3ca*$^{KD/i\Delta EC}$ endothelial cells (Supplementary Fig. 10a, b). In contrast, ROCK inhibitor completely abrogated pS20 MLC2 and disrupted stress fibres in control cells (Supplementary Fig. 10a, b). This further supports the role of PI3Kα in the regulation of the phosphorylation of MLC2 in an MYPT1/MLCP-dependent manner.

Next, we attempted to rescue the vascular phenotypes triggered by the inactivation of PI3Kα in vivo by treating newborn mice with NUAKi. While inhibition of NUAK1 did not impact on the outgrowth of the vasculature, it normalized the hyperbranched vascular plexus and the vessel width and prevented the three-dimensional growth in *Pik3ca*$^{KD/i\Delta EC}$ retinas (Fig. 7c, d and Supplementary Fig. 10c). In line with the observations in cultured endothelial cells, administration of ROCK inhibitor in vivo did not rescue the *Pik3ca*$^{KD/i\Delta EC}$ retinal phenotype (Supplementary Fig 10d-f). This further supports that PI3K signalling does not regulate pMLC2 in a ROCK-dependent manner. Altogether, these data demonstrate that regulation of the NUAK1/MYPT1/MLC2 axis by PI3Kα is required to inhibit actomyosin contractility in cultured endothelial cells and in growing vessels in vivo (Fig. 7e).

Discussion

In this study, we present evidence demonstrating that the PI3K downstream pathway, the NUAK1/MYPT1/MLCP axis, controls actin dynamics in endothelial cells. We uncover that failure of endothelial cells to rearrange results in vascular tubes composed of stretched cells, which grow in a superimposed fashion and fail to stabilize upon anastomosis. Our data support that a tight regulation of endothelial cell movement, beyond tip cells, is necessary for the adequate patterning of the vascular plexus. Cell rearrangement is critical for any process that implies collective cell migration such as in epithelial sheets and neural crest cells during development, and in cancer cells during collective invasion[39,40]. Thus, our discoveries may be translated to the cellular and molecular dynamics orchestrating these critical pathophysiological processes.

The combination of a PI3Kα-selective inhibitor together with an endothelial-specific inducible genetic system has allowed us to fully abrogate PI3Kα activity during vessel development and unravel functions of this signalling hub. We show here that inhibition of PI3Kα hinders endothelial cell pairing and triggers defects in cell elongation. These aberrant cellular behaviours ultimately result in stretches of unicellular vascular tubes devoid of lumen. Thus, our data demonstrate that rearrangement of endothelial cells is required to form well-organized, multicellular vascular tubes. Our experimental strategies also reveal cell proliferation defects in PI3Kα-inhibited endothelial cells. Although it is possible that such defects contribute to the overall phenotype, the observation that blockade of proliferation per se does not interfere with junctional patterns argues for impaired junctional remodelling and cell motility as an independent defect in *Pik3ca*$^{KD/i\Delta EC}$ retinas. Previous data showing that partial decrease in PI3K output selectively decreases endothelial cell migration with no defects in cell proliferation further support this interpretation[15,22]. *Pik3ca*$^{KD/i\Delta EC}$ retinas show an atypical phenotype consisting of hyperbranching but reduced numbers of endothelial cells. In contrast, canonical reduction of endothelial cell proliferation in vivo, by over-activation of Notch or depletion of VEGFR2, results in a hypobranched plexus[41–43]. Our data thus highlight that increased numbers of branches is not always associated with an increase in endothelial cell proliferation as previously described. Taken together, the present data establish that PI3Kα is an important regulator of sprouting angiogenesis and confirm that angiogenic endothelial cells are exquisitely regulated by this signalling hub.

Previous studies have described that PI3K signalling regulates planar cell rearrangement in epithelial cells by stimulating junctional lengthening and stability[44,45]. Our data show that inactivation of PI3K signalling also impairs junctional remodelling in cultured endothelial cells and identify that this also occurs during vessel growth in vivo. Aberrant junctional patterns are indicative of defects in cell rearrangements[11]. Therefore, this suggests that cell rearrangement defects in our PI3Kα-inhibited in vivo models are caused by impaired junctional remodelling. We also identify that the spatial heterogeneity of junctional patterns required for cells to rearrange is lost in *Pik3ca*$^{KD/i\Delta EC}$ endothelial cells, with a concomitant shift towards serrated immature junctions. While current understanding of junctional patterns associates serrated junctions with highly motile cells and straight junctions with non-moving cells[46], our data suggest that the loss of junctional pattern heterogeneity, regardless of the type, blocks cell rearrangement. This agrees with previous results based on computational models which indicate that cells rearrange when differential adhesion strengths are found between neighbouring cells[7].

Mechanistically, we show that PI3Kα mediates endothelial cell rearrangement by inhibiting actomyosin contractility at the subcortical edge of the cells. This is in line with previous reports documenting that inactivation of PI3K in vitro leads to both enhanced actin contractility[47] and aberrant actin pattern[48]. Together, this supports the notion that actomyosin activity has to be low for cell rearrangements to occur. This is not unique of endothelial cells as it has also been observed in *Drosophila* epithelial tracheal tubes and in tumour cells[49,50]. Upon contraction, the actomyosin machinery transmits force to cell−cell contacts and regulates junctional remodelling[12,50]. This process is required for cells to change their adhesion strengths and propel cell movement. We observe that inhibition of PI3K impairs junction stabilization and actomyosin contractility, and in turn reduces cell migration. PI3K is at the crossroad of many extracellular inputs[14]; thus it is not surprising that other mechanisms activate PI3K signalling to stimulate endothelial cell migration during vessel growth[51]. Indeed, during angiogenesis, fibronectin, a critical component of the extracellular matrix of endothelial cells, mediates cell migration through the activation of PI3K[51]. Given that aberrant adhesion of endothelial cells to the extracellular matrix compromises the formation of stable adherent junctions in vivo[52], we speculate that the regulation of cell−cell adhesion and cell−matrix adhesion by PI3K synergize to mediate cell rearrangement during vessel growth.

The growth of the junctional ring upon establishing new contacts is also impaired upon inactivation of PI3K in both mouse retinas and in zebrafish embryos. This fits with the observation that junctional elongation requires cortical tension from the actomyosin cytoskeleton[11,53]. We postulate that during angiogenesis, a tight equilibrium between stimulation and suppression of actomyosin contractility is required to allow proper growth of the newly formed junctional contact points. This also explains why reduced phosphorylation of MLC2 is associated with junctional defects in angiogenesis[54,55]. Together, our data indicate that the regulation of junctional remodelling and stability by PI3Kα signalling underscores changes in both cell−cell

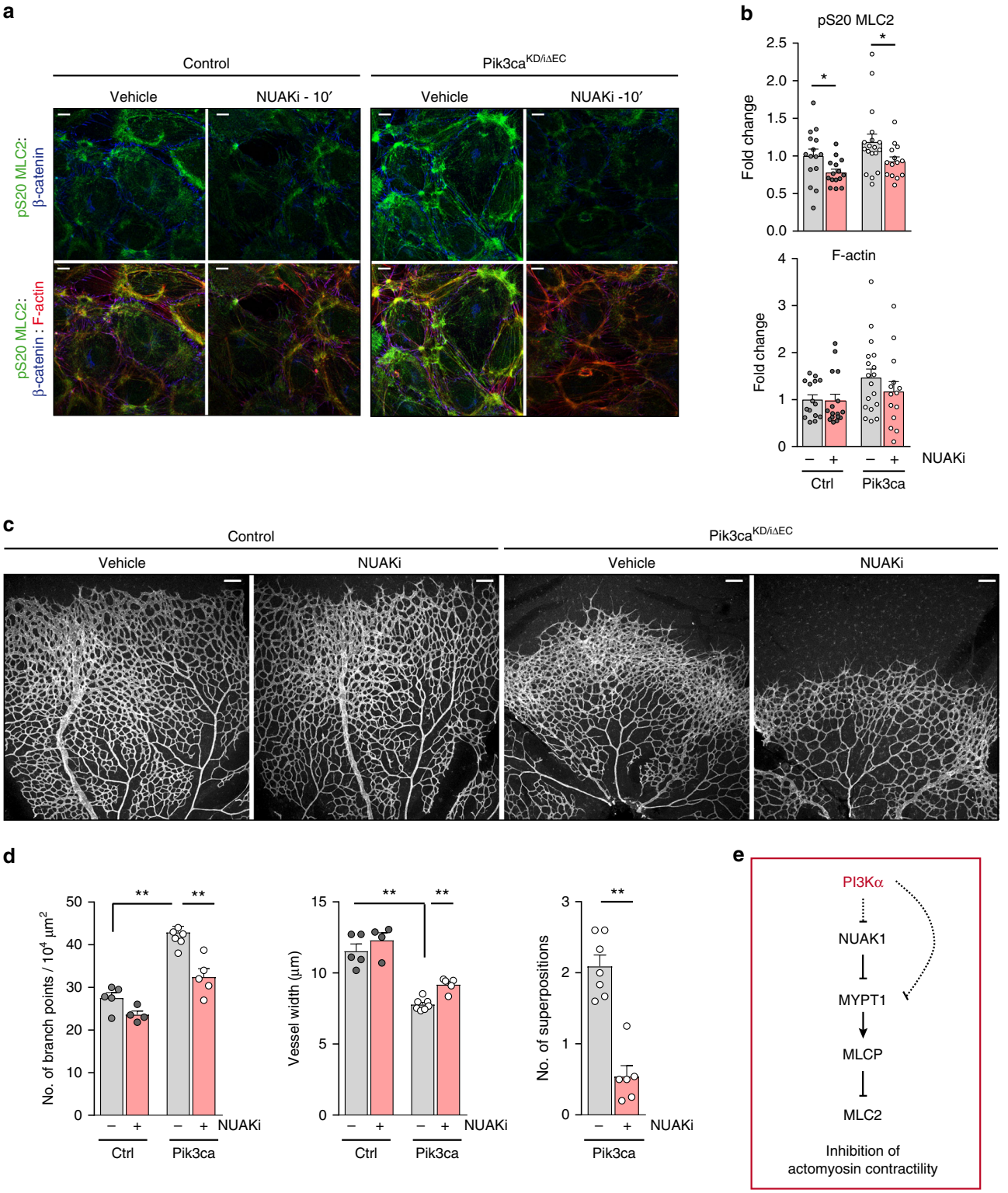

Fig. 7 Blockade of NUAK1 restores the endothelial phenotypes imposed by PI3Kα inactivation. **a** Confocal images of control and *Pik3ca*$^{KD/i\Delta EC}$ endothelial cells treated with 4-OHT for 72 h, re-plated on gelatin-coated slides for 24 h and treated with 10 µM WZ4003 (NUAK1 inhibitor; NUAKi) or DMSO as control for 10 min, and stained for pS20 MLC2, β-catenin and F-actin. **b** Quantification of subcortical pS20 MLC2 (upper graph) and F-actin (lower graph) immunostaining intensities (shown as integrated density) ($n \geq 14$ images of three independent experiments). **c** IB4-stained control and *Pik3ca*$^{KD/i\Delta EC}$ retinas treated with DMSO as control or WZ4003 (NUAKi) at P6 (16:00), and isolated at P7 (1000 hours). **d** Quantification of branch points per unit area, vessel width per unit area, and superimposed vascular tubes per unit area ($n \geq 4$ retinas per genotype and treatment). **e** Molecular mechanism by which PI3Kα suppresses actomyosin contractility. Scale bars, 15 µm (**a**), 100 µm (**c**). Data in **b** and **d** represent mean ± SEM (error bars). $^*P < 0.05$, $^{**}P < 0.01$. Statistical analysis was performed by the two-sided Mann–Whitney test

adhesion properties and junctional growth upon new cell−cell contacts. Given the similarity between the vascular defects in *Pik3ca*$^{KD/i\Delta EC}$ retinas and GDC-0326-treated zebrafish and those observed in *cdh5*-mutant zebrafish embryos and mouse retinas, we propose that PI3Kα and VE-cadherin cooperate to regulate cell rearrangement and contact expansion.

We have identified a molecular pathway regulated by PI3K signalling that points towards a role of PI3K in regulating actin dynamics. Specifically, we have discovered that inactivation of PI3Kα leads to enhanced phosphorylation of MYPT1 at S445, a site which can be phosphorylated by NUAK1 (ref. [35]). We demonstrate that blocking NUAK1 restores both actomyosin contractility and the vascular patterning defects triggered by inactivation of PI3Kα In contrast, NUAKi does not restore the outgrowth of the vasculature in *Pik3ca*$^{KD/i\Delta EC}$ retinas. This might be explained by the inability of NUAKi to restore endothelial cell proliferation; thereby further supporting that cell rearrangement defects and altered cell proliferation in *Pik3ca*$^{KD/i\Delta EC}$ retinas are two non-related events. At the moment, it is still not fully clear how PI3K signalling inhibits NUAK1. Given that AKT inhibits liver kinase B1 (LKB1) through phosphorylation-dependent nuclear retention[56] and LKB1 activates NUAK1, it is tempting to speculate that PI3Kα blocks the ability of LKB1 to phosphorylate NUAK1. By preventing the phosphorylation of MYPT1 on S445 by NUAK1, PI3Kα then promotes MLCP phosphatase activity (Fig. 7e). Supporting this idea, genetic endothelial depletion of LKB1 opposes *Pik3ca*$^{KD/i\Delta EC}$ vascular phenotypes, with enhanced retinal angiogenesis and increased endothelial cell proliferation and migration[57]. However, taking into account the complexity of the PI3K signalling cascade, other pathways may also contribute to the vascular defects seen in the *Pik3ca*$^{KD/i\Delta EC}$ vasculature.

Taken together, our study discovers the PI3Kα/MYPT1/MLCP signalling axis as a critical hub in endothelial cell rearrangement and highlights the key role of cell rearrangement in the orchestration of collective cell migration during angiogenesis. The regulation of actomyosin remodelling by PI3K signalling has been observed in a variety of primary and tumour cells; yet the molecular mechanism behind this regulation has not been fully understood. Therefore, our findings may be translated into other developmental and pathological situations.

Methods

Reagents. All chemicals, unless otherwise stated, were from Sigma-Aldrich. Growing mediums for cultured cells were from Gibco.

Zebrafish. Maintenance of zebrafish (*Danio rerio*) and experimental procedures involving zebrafish embryos were carried out at the Biozentrum/Universität Basel according to Swiss national guidelines of animal experimentation (TSchV). Zebrafish lines were maintained under licences 1014 H and 1014G1 issued by the Veterinäramt-Basel-Stadt. The fish were maintained using standard procedures and embryos obtained via natural spawning[58], and embryos were staged by hours post-fertilization (hpf) at 28.5 (ref. [59]). All experiments were performed in accordance with federal guidelines and were approved by the Kantonales Veterinäramt of Kanton Basel-Stadt (Switzerland). The following zebrafish lines were used: Tg(*kdrl:EGFP-nls*)^{ubs1} (ref. [29]), Tg(*fli1ep:mCherry-nls*)^{ubs10} (ref. [60]), Tg(*kdrl:EGFP*)^{s843} (ref. [61]), Tg(*kdrl:mCherry-CAAX*)^{s916} (ref. [62]), and Tg(*UAS:EGFP-UCHD*)^{ubs18} (ref. [11]). For pharmacological inhibition of PI3Kα, dechorionated zebrafish embryos were treated with dimethylsulphoxide (DMSO) or 50 µM GDC-0326 inhibitor (Genentech[23]) in E3 medium supplemented with 0.003% 1-phenyl-2-thiourea from 22 hpf or 27 hpf, as indicated in the Results section. E3 medium containing DMSO or 50 µM GDC-0326 was changed every 4 h. To overcome unspecified off-target effects induced by the combination of PI3Kα inhibitor and laser exposure, all experiments were done in a p53 morpholino background. P53 morpholino (Gene Tools) was dissolved in DEPC water containing 0.2% phenol red and 5 ng were injected to 1−2 cell-stage embryos. In order to block cell cycle during angiogenesis[63], 26−28 hpf zebrafish embryos were treated with 20 mM hydroxyurea (HU) and 150 µM aphidicolin (APH). Embryo treatment lasted throughout live imaging or until the embryos were fixed in 2 % PFA and prepared for immunofluorescence.

Mice. Mice were maintained under specific pathogen-free conditions and kept in individually ventilated cages. Experiments were conducted in accordance with the guidelines and laws of the Catalan Departament d'Agricultura, Ramaderia i Pesca (Catalunya, Spain) under the Project License number: DMAH 6809, following protocols approved by the local Ethics Committees of IDIBELL-CEEA. All PI3Kα mutant mice and littermate controls were bred in the C57/BL/6 genetic background (Supplementary Table 1). For the analysis of angiogenesis in the postnatal mouse retina, CRE-mediated recombination was induced in newborn mice by intraperitoneal (i.p.) injections of 25 µg of 4-OHT (2.5 µl of a 10 mg ml^{-1} solution in absolute ethanol) at P1 and P2. Eyes were harvested at P7 and P10 for analysis. Control animals were littermate *Pik3ca*$^{flox/flox}$ pups without CRE expression and injected with 4-OHT. For mosaic inactivation of PI3Kα, R26-mTmG reporter mouse[31] was crossed with *Pik3ca*$^{KD/i\Delta EC}$ mice and 0.8 µg of 4-OHT (2.5 µl of a 0.33 mg ml^{-1} solution in absolute ethanol) was injected i.p. at P1, and eyes were harvested at P7. CRE-mediated recombination was assessed by the expression of membrane-bound GFP. Injected retinas from R26-mTmG;*Pdgfb-iCreER*;*Pik3ca*$^{flox/WT}$ mice were used as control for the analysis. The R26-mTmG allele was kept heterozygous. To block proliferation, wild-type pups were i.p. injected with 10 µg g^{-1} of animal of mitomycin C solution (Sigma, #M4287) as described in ref. [30] at P5. At P7, all pups were i.p. injected with EdU (Invitrogen) to assess proliferation (EdU staining protocol below). For pharmacological rescue experiment studies the following protocols were used: ROCK was inhibited in half of the pups from the same litter by i.p. injection of 30 mg kg^{-1} of animal of Y-27632 (Calbiochem, #688000) dissolved in DMSO at P6 (18:00) and P7 (10:00), and eyes were harvested at P7 (14:00). NUAK1 was inhibited in half of the pups by a single subcutaneous injection of 30 mg kg^{-1} of animal of WZ4003 (Selleckchem, #S7317) at P6 (16:00 hours), and eyes were harvested at P7 (10:00). Control mice were injected with DMSO only.

Cells. Mouse lungs were digested with Dispase (Life Technologies, #17105-041; 4 units ml^{-1}) for 1 h at 37 °C, followed by positive selection with anti-mouse vascular endothelial-cadherin (Pharmingen, #555289) antibody coated with magnetic beads (Dynal Biotech, #110-35). Cells were seeded on a 12-well plate and were coated with gelatin (0.5%) in DMEM/F12 supplemented with 20% foetal calf serum and EC growth factor (PromoCell, #C30140) and 1% penicillin/streptomycin. After the first passage, the cells were re-purified with vascular endothelial-cadherin antibody-coated magnetic beads. Cells were cultured until passage 5. Human umbilical vein endothelial cells (HUVECs, Lonza, #C2519A) were cultured in EBM-2 culture medium supplemented with EGM-2 BulletKit (Lonza, #CC-3162) on 0.5% gelatin-coated plates and culture up to passage 5. Human embryonic kidney cells (HEK-293, ATCC, CRL-1573) were cultured in DMEM (Lonza, #12-733F) supplemented with 10% of inactivated FBS and 1% penicillin/streptomycin. To induce gene deletion in mouse lung endothelial cells 4-OHT (1 µM) or vehicle (ethanol) was added to the cultured medium for 24 h, followed by replacing the medium without 4-OHT or vehicle. All the experiments were performed 96 h after the addition of 4-OHT or vehicle. For pharmacological inhibition of ROCK and NUAK1 kinases, cells were cultured for 24 h followed by treatment with vehicle (DMSO), 10 µM ROCK inhibitor for 10 or 30 min, or 10 µM NUAK1 inhibitor for 10 min. For pharmacological inhibition of PI3Kα, cells were treated with vehicle (DMSO) and 1 µM GDC-0326 inhibitor (Genentech) for 48 h.

siRNA transfection. Solution A (493 µl of Opti-MEM (Gibco, #51985026) with 7.5 µl of 20 µM control (Dharmacon, #D-001206-13) or 20 µM MYPT1 (Dharmacon, #M-063177-02 SMART pool siRNA oligomer)) and solution B (493 µl of Opti-MEM with 7.5 µl of lipofectamine RNAi Max (Thermo Fisher Scientific, #13778075)) were prepared and incubated for 5 min at room temperature (RT) in separated tubes following the manufacturer's instructions. Subsequently, solution B was added to solution A and incubated for 20 min at RT, followed by adding A + B solution to endothelial cells (750,000 cells) in suspension resuspended in 500 µl of Opti-MEM without antibiotics on cover-slips in six-well plates (three cover-slips per well previously coated with 0.5% gelatin). The medium was changed the day after, and cells were either fixed for immunofluorescence assays or lysed for western blotting 72 h after transfection.

Protein extraction, immunoprecipitation and immunoblotting. Zebrafish embryos were subjected to a deyolking protocol to avoid the interference of yolk proteins in our analyses. Dechorionated embryos were collected in a 1.5 ml tube filled with 1 ml deyolking buffer (55 mM NaCl, 1.8 mM KCl and 1.25 mM $NaHCO_3$). By pipetting with a narrow tip the yolk sac was disrupted. The embryos were shaken for 5 min at 200 × *g* to dissolve the yolk. Cells were pelleted at 300 × *g* for 30 s and the supernatant discarded. Two additional washes were performed by adding 1 ml of wash buffer (110 mM NaCl, 3.5 mM KCl, 2.7 mM $CaCl_2$, 10 mM Tris/Cl pH 8.5), shaking 2 min at 200 × *g* and pelletting the cells as before. For protein extraction, deyolked zebrafish embryos, mouse lung endothelial cells and HEK-293 cells were lysed in 50 mM Tris HCl pH 7.4, 5 mM EDTA, 150 mM NaCl and 1 % Triton X-100 supplemented with 2 mg ml^{-1} aprotinin, 1 mM sodium fluoride, 1 mM pepstatin, 1 ng ml^{-1} leupeptin, 1 mM phenylmethysulfonyl-fluoridem, 10 g ml^{-1} Na-p-tosyl-L-lysine chloro-methyl ketone hydrochloride, 1 mM sodium orthovanadate, 1 µM okadaic acid and 1 mM DTT followed by

clearance of lysates by centrifugation. Supernatants were resolved on 8, 10 or 12% SDS–PAGE gels, transferred onto nitrocellulose or PVDF membranes. Membranes were blocked in 5% (w/v) skimmed milk, incubated with specific primary antibodies overnight at 4 °C in 2% BSA in 0.1% Tween-20 TBS buffer (further referred to as TBST), then washed three times with TBST and incubated with peroxidase-conjugated secondary antibodies in 5% (w/v) skimmed milk in TBST at RT for 1 h. The following primary antibodies were used: p-AKT (Ser 473) (Cell Signaling Technology, #4060, diluted 1:1000), AKT (Cell Signaling Technology, #9272, diluted 1:2000), VE-cadherin (Santa Cruz Biotechnology, #sc-6458, diluted 1:500), p85 (Millipore, #ABS234, diluted 1:2000), PI3Kα (monoclonal clone U3A[64]), Ser445 MYPT1 (MRC Reagents, #S508C[35], 1 μg ml^{-1}), MYPT1 (MRC Reagents, #S110D, ref. [35], 1 μg ml^{-1} with a 10 μg ml^{-1} of a dephosphopeptide variant of the antigen used to raise the antibody), pS19/S20 MLC2 (Rockland Antibodies, #039600-401-416, diluted 1:500), β-actin (Abcam, #ab49900, diluted 1:10,000) and α-tubulin (Sigma-Aldrich, #T6074, diluted 1:10,000). The following secondary antibodies from DAKO were used in a 1:5000 dilution: swine anti-rabbit (#P0399), rabbit anti-goat (#P0449), rabbit anti-mouse (#P0260), and rabbit anti-sheep (#P0163).

MYPT1 immunoprecipitation (IP) was performed using a sheep polyclonal MYPT1 antibody (MRC Reagents, #S110D) covalently coupled to protein G-Sepharose (GE Healthcare, #17-0618-01) (1 μg of antibody per 1 μl of beads) with a dimethyl pimelimidate cross-linking procedure[35]. Cells treated with DMSO or GDC-0326 for 48 h were lysed with IP buffer (50 mM Tris pH 8.0, 150 mM NaCl, 0.1% SDS, 1% NP40, 0.5% sodium deoxycolate, 2 mg ml^{-1} aprotinin, 1 mM pepstatin A, 1 ng ml^{-1} leupeptin, 10 g ml^{-1} TLCK, 1 mM PMSF, 1 mM NaF, 1 mM $NaVO_3$ and 1 μM okadaic acid) and clarified by centrifugation at maximum speed for 15 min at 4 °C. Cell lysate (1 mg) was incubated with 5 μg of coupled antibody for 1 h at 4 °C. Immunoprecipitates were washed four times with IP buffer and resuspended in 1× SDS Sample Buffer. Immunoprecipitates and cell lysates (50 μg) were subjected to electrophoresis on 8−12% SDS–PAGE and transferred to nitrocellulose membranes. For sheep antibodies, the membranes were incubated for 30 min with TBST containing 10% (w/v) skimmed milk. The membranes were then immunoblotted in 10% (w/v) skimmed milk in TBST with the MYPT1 primary antibody (1 μg ml^{-1}) overnight at 4 °C. The incubation with phosphospecific MYPT1 sheep antibody was performed with the addition of 10 μg ml^{-1} of a dephosphopeptide variant of the antigen used to raise the antibody. Uncropped scans are shown in Supplementary Figures 11-13.

Live 2D wound healing assay. Mouse lung endothelial cells and HUVECs were plated on six-well plate dishes coated with 0.5% gelatin to grow to confluence for 24 h. Cell monolayers were scratched with a p200 pipette tip to induce cell migration. Phase-contrast images were performed every 10 min using a widefield microscope (NIKON Eclipse TI) equipped with a ×10air objective and an Andor Zyla 4.2 plus sCMOS camera. An Okolab cage incubator and humidified CO_2 gas chamber set to 37 °C and 5% CO_2 were used during the imaging process.

Immunofluorescence analysis in zebrafish, retinas and cells. For immunofluorescence and imaging of zebrafish embryos, dechorionated zebrafish embryos were fixed in 2% paraformaldehyde and 0.1% Tween 20 in PBS overnight at 4 °C. After fixation, embryos were washed four times with 0.1% Tween 20 in PBS (hereafter refer to as PBST) for 5 min, permeabilized with 0.5% Triton-X-100 in PBS at room temperature (RT) for 15−30 min, and blocked with 1% BSA, 5% goat serum (Gibco, #16210-064) and 0.2% Triton X-100 in PBS at 4 °C overnight by continuous shaking. Thereafter, embryos were incubated with mouse anti-human ZO-1 (Zymed, #33-9111, diluted 1:200) in 500 μl of blocking buffer at 4 °C overnight, washed in PBST at least six times for over 3 h, and incubated with Alexa-633 goat anti-mouse IgG (Invitrogen, #A-21053, diluted 1:1000) in 500 μl of blocking buffer overnight at 4 °C. Embryos were finally washed in PBST at 4 °C overnight with continuous shaking. Fixed or live fluorescence positive zebrafish embryos were selected using a Leica MZ FLIII fluorescent, anaesthetized in E3 supplemented with 1× tricaine pH 7 (0.08%) and mounted in a 35 mm glass-bottomed dish (0.17 mm; MatTek), using 0.7% low melting agarose containing 1× tricaine. For live imaging, the mounting agarose was additionally supplemented with 0.003 % phenylthiourea (PTU) and inhibitor if the case.

Mouse eyes were fixed in 4% PFA in PBS for 1 h on ice and washed in PBS for at least 10 min. Retinas were isolated and fixed with 4% PFA in PBS for 1 h on ice. After washing the retinas with PBS three times, they were incubated with blocking buffer (1% BSA, 0.3% Triton X-100 in PBS) overnight at 4 °C. Then, retinas were incubated with the specific primary antibodies diluted in blocking buffer overnight at 4 °C. Primary antibodies against the following proteins were used: pSer240/244-S6 (Cell Signaling Technology, #2215, diluted 1:100), FOXO1 (Cell Signaling Technology, #2880S, diluted 1:100), VE-cadherin (BD Bioscience, #555289, diluted 1:50), ERG (Abcam, #AB92513, diluted 1:400), Collagen IV (Chemicon international, #AB756P, diluted 1:50), ICAM-2 (BD Bioscience, #553326, diluted 1:100), pS19/S20 MLC2 (Rockland Antibodies, #039600-401-416, diluted 1:100). Retinas were washed three times in PBST and then in Pblec buffer (1% Triton X-100, 1 mM $CaCl_2$, 1 mM $MgCl_2$ and 1 mM $MnCl_2$ in PBS, pH 6.8) for 30 min at RT. Thereafter the retinas were incubated for 2 h at RT or overnight at 4 °C in Pblec buffer containing Alexa-conjugated secondary antibodies (diluted 1:200) and Alexa-conjugated Isolectin GS-B4 (IB4, Invitrogen, #I21411, #I21412, I32450, diluted 1:300), washed three times with PBST and flat-mounted on microscope glass slides with Mowiol (Calbiochem, #475904). For F-actin staining, Alexa-Fluor 568-conjugated phalloidin (Invitrogen, #A12380, diluted 1:400) was used. The following secondary antibodies Alexa-Fluor conjugated were used (1:300 dilution): Alexa-Fluor 488 goat anti-rat (Invitrogen, #A11006), Alexa-Fluor 488 goat anti-rabbit (Invitrogen, #A11008), Alexa-Fluor 568 goat anti-rabbit (Invitrogen, #A11011), Alexa-Fluor 647 donkey anti-rabbit (Invitrogen, #A31573). The labelling of proliferative endothelial cells with EdU was performed at P7. Pups were injected i.p. with 60 μl of EdU (0.5 mg ml^{-1} in PBS, Invitrogen, #C10340) 2 h before they were sacrificed. EdU-positive cells were detected in the retinal vasculature with the Click-iT EdU Alexa Fluor-647 Imaging Kit (Invitrogen, #C10340).

Endothelial cells were seeded on cover-slips in six-well plates coated with 0.5% gelatin. 24 h later, corresponding treatment was done and cells were washed once with cold PBS (supplemented with 1 mM $CaCl_2$ and 0.5 mM $MgCl_2$) and fixed in 4% PFA for 15 min at RT. Cells were then washed with PBS and permeabilized in 0.1% Triton X-100 in PBS for 30 min at RT and incubated in blocking solution (3% BSA, 5% goat serum, 0.1% Triton X-100 in PBS) for 1 h at RT. Cover-slips were removed from the culture plate and were incubated in the appropriate dilution of primary antibodies in blocking solution ON at 4 °C in a wet chamber. Primary antibodies against the following proteins were used: pS19/S20 MLC2 (Rockland Antibodies, #039600-401-416, diluted 1:100) and β-catenin (BD Bioscience #610153, diluted 1:200). The following day, cover-slips were washed three times with PBS at RT and incubated in the appropriate dilution of Alexa-Fluor 488 goat anti-rabbit (Invitrogen, #A11008, diluted 1:200), Alexa-Fluor 568 goat anti-mouse (Invitrogen, #A21236, diluted 1:200) and Alexa-Fluor 633-conjugated phalloidin (Invitrogen, #A22287, diluted 1:400) in PBS for 2 h at RT in a wet chamber. Three washes with PBS were performed, adding 1 μg ml^{-1} of 4′,6-diamidino-2-phenylindole (DAPI; Molecular Probes, #D1306) in the last one.

Imaging analysis and quantification. All quantifications obtained from confocal (Leica SP5) or widefield microscopes (Nikon Eclipse 80i or Nikon Eclipse TI) were performed using Image J software (http://fiji.sc/). Zebrafish movies were analysed with ImageJ software. Photoshop and Illustrator (Adobe) software were used for image processing.

In the zebrafish, images were taken at ×40(NA = 1.1) water immersion objective, maximum intensity projections were used for quantification and five ISVs were quantified per embryo. Measurements of ISVs length were made straight from the edge of the aorta to the leading edge of the sprout and the number of endothelial nuclei in that length was quantified. The number of endothelial nuclei in the DLAV and DA was quantified per segment within five ISVs. Junctional length and junctional gaps length were measured in embryos stained for ZO-1. Only flat-mounted embryos were selected for quantification avoiding crooked ones.

In the retina, vascular parameter were quantified in at least four images of comparable vascular areas per retina and of at least three mice of each genotype or experimental conditions. All images shown in the figures are maximum intensity projections unless otherwise specified. For the quantification of retinal vessel progression overview, widefield images of IB4-stained retinal vasculature were obtained with the ×10 objective (Nikon Eclipse 80i microscope). The distance of vessel growth from the centre of the optic nerve to the edge of the angiogenic front was measured per each retina leaflet. The mean of all leaflet measurements was obtained per retina and compared between control and mutant groups. For all other quantifications high-resolution confocal images at ×40 oil immersion objective was used. The number of filopodia and sprouts were quantified at the angiogenic front. The total number of filopodia and sprouts were normalized to a vessel length of 100 μm at the angiogenic front. Endothelial branch points, vessel width, superimposed vascular tubes, number of junctional gaps, length of junctional gaps, distance between nuclei, endothelial cell numbers, collagen IV empty sleeves and lumen disconnections were quantified behind the angiogenic front in fields sized 100 μm × 100 μm. For quantification of cell shape, single GFP-positive cells located behind the sprouting front were only considered. Vessel width, distance between neighbouring cells, length of junctional gaps and area of GFP-positive cells was determined using ImageJ software with the proper scale set up. To assess the proliferation rate, double-positive EdU/ERG endothelial nuclei were counted in field of 200 μm × 200 μm behind the vascular sprouting front and the total number was divided by the total number of endothelial cells (ERG-positive nuclei). For quantification of pS20 MLC2 and F-actin immunostaining, signal intensity within IB4 positive area in images taken with the ×40 oil immersion objective was measured. In brief, manual threshold was set to obtain binary images of IB4 staining. IB4-positive area was measured and defined as a region of interest (ROI). Integrated density of pS20 MLC2 or F-actin was measured in the IB4-positive area for each image. Then, to calculate the corrected total fluorescence (CTF), the following formula was used: CTF = Integrated Density – (Area selected for IB4 positivity × Mean fluorescence of background readings). The background readings were taken from three areas close to the vasculature but negative for IB4. 3D reconstructions were generated by using the Leica LAS-X.

In phase-contrast wound healing assays, quantification of cell migration was made by measuring the percentage of cell-free area. Cells from the first, second and third row were manually tracked using the Manual Tracking plugin and cell velocity, directionality and travelled distance were calculated with the chemotaxis tool plugin.

In cultured endothelial cells, maximum intensity projections of confocal images with the ×63 oil immersion objective were acquired. Signal intensity of pS20 MLC2 and F-actin immunostaining/cell was quantified using the junctional staining of β-catenin to select individual endothelial cells (ROI A1). Using the enlarge command two concentric areas were drawn in each cell (distance of −2.5 µm (ROI A2) and −7.5 µm (ROI A3) from the junctional β-catenin positive staining). Integrated density was measured. For measuring total intensity levels: area from ROIs A1 was used as templates to measure total integrate intensity of pS20 MLC2 and F-actin staining in individual endothelial cells. For measuring subcortical levels: Integrate density from ROIs A2 to ROI A3 was calculated in individual endothelial cells. The mean of the integrate density of four cells per image, and at least four images per genotype and treatment were used for the quantification. β-catenin junctional positive area/cell perimeter was calculated per individual cell. For that, a manual threshold was set to obtain binary images. Then, total β-catenin area—β-catenin nuclear area in individual cells was calculated to obtain β-catenin junctional positive area. Junctional staining of β-catenin was used to measure the perimeter of individual cells. At least four cells per image and four images per genotype were used for the quantification. To measure the type of junctional coverage, percentage of junctional pattern was considered. ≥60% serrated pattern/cell = serrated, ≥ 60% of straight junctional pattern/cell = straight, ≈50% of each pattern/cell = mixed. Five cells per image and at least five images per genotype were used for the quantification.

Mass spectrometry. Primary endothelial cells were washed twice with cold PBS supplemented with 1 mM Na_3VO_4 and 1 mM NaF and lysed with 300 µl of urea buffer (8 M Urea in 20 mM in HEPES pH 8.0 supplemented with 1 mM Na_3VO_4, 1 mM NaF, 1 mM $Na_4P_2O_7$ and 1 mM sodium β-glycerophosphate) for 30 min. All mass spectrometry solvents were prepared in LC-MS grade water (LGC Promochem, #SO-9368-B025). We used published methods for phosphoproteome analyses[32,65,66]. In brief, 250 µg of protein were reduced and alkylated by sequential incubation with 10 mM DTT and 16.6 mM iodoacetamide for 1 h. Urea concentration was diluted to 2 M with 20 mM HEPES (pH 8.0), and 80 µl of trypsin beads (50% slurry of TLCK-trypsin (Thermo-Fisher Scientific, #20230)) preconditioned with three washes of 20 mM HEPES (pH 8.0) were added to the samples, followed by incubating the tubes for 16 h at 37 °C with agitation. Trypsin beads were removed by centrifugation at 2000 × *g* for 5 min at 5 °C. Following trypsin digestion, peptide solutions were desalted using 10 mg OASIS-HLB cartridges (Waters, #186000383). Briefly, OASIS cartridges were accommodated in a vacuum manifold (−5 mmHg), activated with 1 ml ACN (LGC Promochem, #SO-9340-B025) and equilibrated with 1.5 ml of washing solution (1% ACN, 0.1% TFA (LGC Promochem, #SO-9668-B001)). After loading the samples, cartridges were washed with 1 ml of washing solution. Phosphopeptides were eluted with 500 µl of glycolic acid buffer 1 (1 M glycolic acid (Acros Organics, #154515000), 50% ACN, 5% TFA) and subjected to phosphoenrichment. Phosphopeptides were enriched using TiO_2 (GL Sciences, #5020-75010). Sample volumes were normalized to 1 ml using glycolic acid buffer 2 (1 M glycolic acid, 80% ACN, 5% TFA), 50 µl of TiO_2 beads (50% slurry in 1% TFA) were added to the peptide mixture, incubated for 5 min at RT with agitation and centrifuged for 30 s at 1500 × *g*. For each sample, 80% of the supernatant was transferred to fresh tubes and stored in ice and the remaining 20% used to resuspend the bead pellets that were loaded into an empty prewashed PE-filtered spin-tips (Glygen, #TF2EMT.96) and packed by centrifugation at 1500 × *g* for 3 min. After loading the remaining volume of the supernatant by centrifugation at 1500 × *g* for 3 min, spin tips were sequentially washed with 100 µl of glycolic acid buffer 2, ammonium acetate buffer (100 mM ammonium acetate in 25% ACN) and 10% ACN by RT centrifugation for 3 min at 1500 × *g*. For phosphopeptide recovery, additional 50 µl of 5% ammonia solution (LGC Promochem, HPA-0070-B010) followed by centrifugation for 5 min at 1500 × *g* was repeated four times. Eluents were snap frozen in dry ice, dried in a speed vac (RVC 2-25, Martin Christ Gefriertrocknungsanlagen GmbH, Osterode am Harz, Germany) and peptide pellets stored at −80 °C. Peptide pellets were resuspended in 12 µl of reconstitution buffer (20 fmol/µl enolase (Waters, #186002325) in 3% ACN, 0.1% TFA) and 5 µl were loaded onto an LC-MS/MS system consisting of a Dionex UltiMate 3000 RSLC directly coupled to an Orbitrap Q-Exactive Plus mass spectrometer (Thermo Fisher Scientific). Peptides were trapped in a µ-pre-column (Acclaim PepMap 100, Themo Fisher Scientific, #160454) and separated in an analytical column (Acclaim PepMap 100, Thermo Fisher Scientific, #164569) using A (3% ACN, 0.1% FA (Thermo Fisher Scientific, # F-1850-PB08)) and B (100% ACN, 0.1% FA) solutions as mobile phases. The following parameters were used: 3−23% B gradient for 120 min and a flow rate of 0.3 µl min^{-1}. As they eluted from the nano-LC system, peptides were infused into the online connected Q-Exactive Plus system operating with a 2.1 s duty cycle. Acquisition of full scan survey spectra (m/z 375−1500) with a 70,000 FWHM resolution was followed by data-dependent acquisition in which the 20 most intense ions were selected for HCD (higher energy collisional dissociation) and MS/MS scanning (200−2000 m/z) with a resolution of 17,500 FWHM. A 30 s dynamic exclusion period was enabled with an exclusion list with 10 ppm mass window. Overall duty cycle generated chromatographic peaks of approximately 30 s at the base, which allowed the construction of extracted ion chromatograms (XICs) with at least ten data points.

Peptide identification and quantification. Mascot Daemon 2.5.0 was used to automate peptide identification from MS data. Peak list files (MGFs) from RAW data were generated with Mascot Distiller v2.5.1.0 and searched into the Mascot search engine (v2.5) in order to match MS/MS data to theoretical peptide fragmentation data[67]. The searches were performed against the SwissProt Database (uniprot_sprot_2014_08.fasta) with an FDR of 1% (specific FDR for each phosphopeptide identification is included in Supplementary Data 1). A maximum of 2 trypsin missed cleavages and a mass tolerance of ±10 ppm for the MS scans and ± 25 mmu for the MS/MS scans were allowed. Carbamidomethyl Cys as fixed modification, and phosphorylation at Ser, Thr, and Tyr, PyroGlu on N-terminal Gln and oxidation of Met as variable modifications were considered. The accuracy of phosphosite location within the identified peptides was assessed using delta score values as described by Savitski et al.[68]. Delta scores for each phosphopeptide are reported in Supplementary Data 1. In-house developed software (Pescal) was used for label-free peptide quantification[69]. Pescal constructs extracted ion chromatograms (XIC) for each identified peptide and measures the area of the XICs for all the peptides identified across all samples. Thresholds for XIC generation were ±7 ppm and ±2 min m/z and retention time windows, respectively and undetectable peptides were given an intensity value of 0. Values of two technical replicates per sample were averaged and intensity values for each peptide were normalized to total sample intensity. Normalized quantitative data were used to calculate fold changes between groups and statistical significance (assessed by Student's *t* test) when necessary. The construction of volcano plots and heatmaps was automated with a script generated in R software using the ggplot package. Venn diagrams were constructed using the software Venny (v2.1, http://bioinfogp.cnb.csic.es/tools/venny).

Statistics. Data were analysed using GraphPad Prism software and were presented as mean ± SEM (error bars). Sample size and experimental replicates were indicated in figure legends. Statistical analysis was performed by the nonparametric Mann−Whitney's test or the parametric Student's *t* test. ns not significant; $^{*}P < 0.05$; $^{**}P < 0.01$; $^{***}P < 0.001$; and $^{****}P < 0.001$ were considered statistically significant.

Code availability. The mass spectrometry data is deposited in the PRIDE repository (www.ebi.ac.uk/pride/archive/) with the dataset identifier PXD007060. The codes used for analysing the mass spectrometry data are annotated in Supplementary Table 2.

Reporting Summary. Further information on research design is available in the Nature Research Reporting Summary linked to this article.

Data availability

The mass spectrometry data that support the findings of this study have been deposited and are publicly available at the ProteomeXchange Consortium via the PRIDE[70] partner repository (www.ebi.ac.uk/pride/archive/) with the dataset identifier PXD007060. The rest of the data and materials generated within this study are available from the corresponding author upon request. A reporting summary for this article is available as a Supplementary Information file.

Received: 13 December 2017 Accepted: 19 October 2018
Published online: 16 November 2018

References

1. Potente, M., Gerhardt, H. & Carmeliet, P. Basic and therapeutic aspects of angiogenesis. *Cell* **146**, 873–887 (2011).
2. Adams, R. H. & Alitalo, K. Molecular regulation of angiogenesis and lymphangiogenesis. *Nat Rev. Mol. Cell Biol.* **8**, 464–478 (2007).
3. Jakobsson, L. et al. Endothelial cells dynamically compete for the tip cell position during angiogenic sprouting. *Nat Cell Biol.* **12**, 943–953 (2010).
4. Phng, L. K. et al. Formin-mediated actin polymerization at endothelial junctions is required for vessel lumen formation and stabilization. *Dev. Cell* **32**, 123–132 (2015).
5. Arima, S. et al. Angiogenic morphogenesis driven by dynamic and heterogeneous collective endothelial cell movement. *Development* **138**, 4763–4776 (2011).
6. Pitulescu, M. E. et al. Dll4 and Notch signalling couples sprouting angiogenesis and artery formation. *Nat Cell Biol.* **19**, 915–927 (2017).
7. Bentley, K. et al. The role of differential VE-cadherin dynamics in cell rearrangement during angiogenesis. *Nat Cell Biol.* **16**, 309–321 (2014).
8. Lenard, A. et al. In vivo analysis reveals a highly stereotypic morphogenetic pathway of vascular anastomosis. *Dev. Cell* **25**, 492–506 (2013).
9. Huveneers, S. et al. Vinculin associates with endothelial VE-cadherin junctions to control force-dependent remodeling. *J. Cell Biol.* **196**, 641–652 (2012).

10. Millan, J. et al. Adherens junctions connect stress fibres between adjacent endothelial cells. *BMC Biol.* **8**, 11 (2010).
11. Sauteur, L. et al. Cdh5/VE-cadherin promotes endothelial cell interface elongation via cortical actin polymerization during angiogenic sprouting. *Cell Rep.* **9**, 504–513 (2014).
12. Dorland, Y. L. & Huveneers, S. Cell−cell junctional mechanotransduction in endothelial remodeling. *Cell. Mol. Life Sci.* **74**, 279–292 (2017).
13. Dejana, E. & Orsenigo, F. Endothelial adherens junctions at a glance. *J. Cell Sci.* **126**, 2545–2549 (2013).
14. Graupera, M. & Potente, M. Regulation of angiogenesis by PI3K signaling networks. *Exp. Cell Res.* **319**, 1348–1355 (2013).
15. Graupera, M. et al. Angiogenesis selectively requires the p110alpha isoform of PI3K to control endothelial cell migration. *Nature* **453**, 662–666 (2008).
16. Serra, H. et al. PTEN mediates Notch-dependent stalk cell arrest in angiogenesis. *Nat Commun.* **6**, 7935 (2015).
17. Castillo, S. D. et al. Somatic activating mutations in Pik3ca cause sporadic venous malformations in mice and humans. *Sci. Transl. Med.* **8**, 332ra343 (2016).
18. Castel, P. et al. Somatic PIK3CA mutations as a driver of sporadic venous malformations. *Sci. Transl. Med.* **8**, 332ra342 (2016).
19. Vanhaesebroeck, B., Guillermet-Guibert, J., Graupera, M. & Bilanges, B. The emerging mechanisms of isoform-specific PI3K signalling. *Nat Rev. Mol. Cell Biol.* **11**, 329–341 (2010).
20. Manning, B. D. & Toker, A. AKT/PKB signaling: navigating the network. *Cell* **169**, 381–405 (2017).
21. Herbert, S. P. et al. Arterial-venous segregation by selective cell sprouting: an alternative mode of blood vessel formation. *Science* **326**, 294–298 (2009).
22. Nicoli, S., Knyphausen, C. P., Zhu, L. J., Lakshmanan, A. & Lawson, N. D. miR-221 is required for endothelial tip cell behaviors during vascular development. *Dev. Cell* **22**, 418–429 (2012).
23. Heffron, T. P. et al. The rational design of selective benzoxazepin inhibitors of the alpha-isoform of phosphoinositide 3-kinase culminating in the identification of (S)-2-((2-(1-isopropyl-1H-1,2,4-triazol-5-yl)-5,6-dihydrobenzo[f]imidazo[1,2-d][1,4]oxazepin-9-yl)oxy)propanamide (GDC-0326). *J. Med. Chem.* **59**, 985–1002 (2016).
24. Isogai, S., Horiguchi, M. & Weinstein, B. M. The vascular anatomy of the developing zebrafish: an atlas of embryonic and early larval development. *Dev. Biol.* **230**, 278–301 (2001).
25. Foukas, L. C. et al. Critical role for the p110alpha phosphoinositide-3-OH kinase in growth and metabolic regulation. *Nature* **441**, 366–370 (2006).
26. Claxton, S. et al. Efficient, inducible Cre-recombinase activation in vascular endothelium. *Genesis* **46**, 74–80 (2008).
27. Hellstrom, M. et al. Dll4 signalling through Notch1 regulates formation of tip cells during angiogenesis. *Nature* **445**, 776–780 (2007).
28. Tammela, T. et al. VEGFR-3 controls tip to stalk conversion at vessel fusion sites by reinforcing Notch signalling. *Nat Cell Biol.* **13**, 1202–1213 (2011).
29. Blum, Y. et al. Complex cell rearrangements during intersegmental vessel sprouting and vessel fusion in the zebrafish embryo. *Dev. Biol.* **316**, 312–322 (2008).
30. Ubezio, B. et al. Synchronization of endothelial Dll4-Notch dynamics switch blood vessels from branching to expansion. *eLife* **5**, e12167 (2016).
31. Muzumdar, M. D., Tasic, B., Miyamichi, K., Li, L. & Luo, L. A global double-fluorescent Cre reporter mouse. *Genesis* **45**, 593–605 (2007).
32. Montoya, A., Beltran, L., Casado, P., Rodriguez-Prados, J. C. & Cutillas, P. R. Characterization of a TiO(2) enrichment method for label-free quantitative phosphoproteomics. *Methods* **54**, 370–378 (2011).
33. Grassie, M. E., Moffat, L. D., Walsh, M. P. & MacDonald, J. A. The myosin phosphatase targeting protein (MYPT) family: a regulated mechanism for achieving substrate specificity of the catalytic subunit of protein phosphatase type 1delta. *Arch. Biochem. Biophys.* **510**, 147–159 (2011).
34. Alessi, D., MacDougall, L. K., Sola, M. M., Ikebe, M. & Cohen, P. The control of protein phosphatase-1 by targetting subunits. The major myosin phosphatase in avian smooth muscle is a novel form of protein phosphatase-1. *Eur. J. Biochem.* **210**, 1023–1035 (1992).
35. Zagorska, A. et al. New roles for the LKB1-NUAK pathway in controlling myosin phosphatase complexes and cell adhesion. *Sci. Signal.* **3**, ra25 (2010).
36. Matsumura, F. & Hartshorne, D. J. Myosin phosphatase target subunit: many roles in cell function. *Biochem. Biophys. Res. Commun.* **369**, 149–156 (2008).
37. Chiyoda, T. et al. LATS1/WARTS phosphorylates MYPT1 to counteract PLK1 and regulate mammalian mitotic progression. *J. Cell Biol.* **197**, 625–641 (2012).
38. Banerjee, S. et al. Characterization of WZ4003 and HTH-01-015 as selective inhibitors of the LKB1-tumour-suppressor-activated NUAK kinases. *Biochem. J.* **457**, 215–225 (2014).
39. Friedl, P. & Gilmour, D. Collective cell migration in morphogenesis, regeneration and cancer. *Nat. Rev. Mol. Cell Biol.* **10**, 445–457 (2009).
40. Pandya, P., Orgaz, J. L. & Sanz-Moreno, V. Actomyosin contractility and collective migration: may the force be with you. *Curr. Opin. Cell Biol.* **48**, 87–96 (2017).
41. Benedito, R. et al. The notch ligands Dll4 and Jagged1 have opposing effects on angiogenesis. *Cell* **137**, 1124–1135 (2009).
42. Zarkada, G., Heinolainen, K., Makinen, T., Kubota, Y. & Alitalo, K. VEGFR3 does not sustain retinal angiogenesis without VEGFR2. *Proc. Natl Acad. Sci. USA* **112**, 761–766 (2015).
43. Phng, L. K. et al. Nrarp coordinates endothelial Notch and Wnt signaling to control vessel density in angiogenesis. *Dev. Cell* **16**, 70–82 (2009).
44. Bardet, P. L. et al. PTEN controls junction lengthening and stability during cell rearrangement in epithelial tissue. *Dev. Cell* **25**, 534–546 (2013).
45. Giampietro, C. et al. The actin-binding protein EPS8 binds VE-cadherin and modulates YAP localization and signaling. *J. Cell Biol.* **211**, 1177–1192 (2015).
46. Kametani, Y. & Takeichi, M. Basal-to-apical cadherin flow at cell junctions. *Nat. Cell Biol.* **9**, 92–98 (2007).
47. Tsuji-Tamura, K. & Ogawa, M. Inhibition of the PI3K-Akt and mTORC1 signaling pathways promotes the elongation of vascular endothelial cells. *J. Cell Sci.* **129**, 1165–1178 (2016).
48. Brachmann, S. M. et al. Role of phosphoinositide 3-kinase regulatory isoforms in development and actin rearrangement. *Mol. Cell. Biol.* **25**, 2593–2606 (2005).
49. Ochoa-Espinosa, A., Harmansa, S., Caussinus, E. & Affolter, M. Myosin II is not required for Drosophila tracheal branch elongation and cell intercalation. *Development* **144**, 2961–2968 (2017).
50. Hidalgo-Carcedo, C. et al. Collective cell migration requires suppression of actomyosin at cell-cell contacts mediated by DDR1 and the cell polarity regulators Par3 and Par6. *Nat Cell Biol.* **13**, 49–58 (2011).
51. Stenzel, D. et al. Integrin-dependent and -independent functions of astrocytic fibronectin in retinal angiogenesis. *Development* **138**, 4451–4463 (2011).
52. Fraccaroli, A. et al. Endothelial alpha-parvin controls integrity of developing vasculature and is required for maintenance of cell-cell junctions. *Circ. Res.* **117**, 29–40 (2015).
53. Gaengel, K. et al. The sphingosine-1-phosphate receptor S1PR1 restricts sprouting angiogenesis by regulating the interplay between VE-cadherin and VEGFR2. *Dev. Cell* **23**, 587–599 (2012).
54. Yamamoto, H. et al. Integrin beta1 controls VE-cadherin localization and blood vessel stability. *Nat Commun.* **6**, 6429 (2015).
55. Abraham, S. et al. VE-Cadherin-mediated cell-cell interaction suppresses sprouting via signaling to MLC2 phosphorylation. *Curr. Biol.* **19**, 668–674 (2009).
56. Liu, L., Siu, F. M., Che, C. M., Xu, A. & Wang, Y. Akt blocks the tumor suppressor activity of LKB1 by promoting phosphorylation-dependent nuclear retention through 14-3-3 proteins. *Am. J. Transl. Res.* **4**, 175–186 (2012).
57. Zhang, W. et al. Deletion of endothelial cell-specific liver kinase B1 increases angiogenesis and tumor growth via vascular endothelial growth factor. *Oncogene* **36**, 4277–4287 (2017).
58. Whitlock, K. E. & Westerfield, M. The olfactory placodes of the zebrafish form by convergence of cellular fields at the edge of the neural plate. *Development* **127**, 3645–3653 (2000).
59. Kimmel, C. B., Ballard, W. W., Kimmel, S. R., Ullmann, B. & Schilling, T. F. Stages of embryonic development of the zebrafish. *Dev. Dyn.* **203**, 253–310 (1995).
60. Heckel, E. et al. Oscillatory flow modulates mechanosensitive klf2a expression through trpv4 and trpp2 during heart valve development. *Curr. Biol.* **25**, 1354–1361 (2015).
61. Jin, S. W., Beis, D., Mitchell, T., Chen, J. N. & Stainier, D. Y. Cellular and molecular analyses of vascular tube and lumen formation in zebrafish. *Development* **132**, 5199–5209 (2005).
62. Hogan, B. M. et al. Vegfc/Flt4 signalling is suppressed by Dll4 in developing zebrafish intersegmental arteries. *Development* **136**, 4001–4009 (2009).
63. Fukuhara, S. et al. Visualizing the cell-cycle progression of endothelial cells in zebrafish. *Dev. Biol.* **393**, 10–23 (2014).
64. Klippel, A., Escobedo, J. A., Hirano, M. & Williams, L. T. The interaction of small domains between the subunits of phosphatidylinositol 3-kinase determines enzyme activity. *Mol. Cell. Biol.* **14**, 2675–2685 (1994).
65. Gruhler, A. et al. Quantitative phosphoproteomics applied to the yeast pheromone signaling pathway. *Mol. Cell Proteom.* **4**, 310–327 (2005).
66. Larsen, M. R., Thingholm, T. E., Jensen, O. N., Roepstorff, P. & Jorgensen, T. J. Highly selective enrichment of phosphorylated peptides from peptide mixtures using titanium dioxide microcolumns. *Mol. Cell. Proteom.* **4**, 873–886 (2005).
67. Perkins, D. N., Pappin, D. J., Creasy, D. M. & Cottrell, J. S. Probability-based protein identification by searching sequence databases using mass spectrometry data. *Electrophoresis* **20**, 3551–3567 (1999).
68. Savitski, M. M. et al. Confident phosphorylation site localization using the Mascot Delta Score. *Mol. Cell. Proteom.* **10**, M110 003830 (2011).

69. Cutillas, P. R. Targeted in-depth quantification of signaling using label-free mass spectrometry. *Methods Enzymol.* **585**, 245–268 (2017).
70. Vizcaino, J. A. et al. 2016 update of the PRIDE database and its related tools. *Nucleic Acids Res.* **44**, D447–D456 (2016).

Acknowledgements

We thank members of the Vascular Signalling Laboratory for helpful discussion and Alba Martínez for the technical support. We thank Arkaitz Carracedo (CIC-bioGUNE, Bilbao) for critical review of the manuscript. We thank the Biozentrum Imaging Core Facility and Carmen Casal in the IDIBELL Imaging Core Facility for their support. We thank CERCA Programme/Generalitat de Catalunya for institutional support. This work was funded by Ministerio de Ciencia, Innovación y Universidades, which is part of Agencia Estatal de Investigación (AEI, Spain) through the projects SAF2014-59950-P, SAF2017-82072-ERC, and SAF2017-89116-R co-funded by European Regional Developmental Fund (ERDF), a way to build Europe; by the Catalan Government through the projects 2014-SGR and 2017-SGR; and by la Fundació Bancària "La Caixa". This project has received funding from the European Union's Seventh Framework Programme FP7/2007-2013 under the Marie Sklodowska-Curie grant agreement no. 317250 (for A.M.F.), and from the European Union's Horizon 2020 research and innovation programme under the Marie Sklodowska-Curie grant agreements no. 675392 (for P.K.) and no. 749731 (for S.D.C.). S.D.C. was also supported by the Generalitat de Catalunya with a Beatriu de Pinós fellowship (BP16-00001). P. Castel was supported by the Jane Coffin Childs Memorial Fund for Medical Research. M.A. laboratory is supported by the Kantons Basel-Stadt and Basel-Land and by grants from the Swiss National Science Foundation. C.W. was supported by the Biozentrum Basel International PhD Program Fellowships for Excellence. H.G. is supported by an ERC consolidator grant Reshape 311719. P.R.C. and P. Casado research is supported by grants from CRUK (C15966/A24375), Barts and The London Charity (297/2249) and BBSRC (BB/M006174/1). S.H. is supported by the Netherlands Organization of Scientific Research (NWO-VIDI grant 016.156.327). J.M. is supported by SAF2017-88187-R (MINECO), B2017/BMD-3817 (Comunidad de Madrid) and ENDOCORNEA2, Convenio Colaboración CSIC-Quirón FJD. 2.

Author contributions

A.A.-U., P.R.C. and M.G. conceived the project; A.A.-U., P. Casado, S.D.C., P.K., M.P.K., A.M.F., P. Castel., V.R., M.M.-G., C.W., H.S., and L.M. performed experiments and analysed data with the supervision of J.M., O.C., F.V., M.A., H.G., S.H., H.-G.B., P.R.C. and M.G. A.A.-U., S.D.C. and M.G. wrote the manuscript. J.M., O.C., F.V., M.A., H.G., S.H., H.-G. B., P.R.C. and M.G. provided funding.

Additional information

Supplementary Information accompanies this paper at https://doi.org/10.1038/s41467-018-07172-3.

Competing interests: M.G., O.C., and F.V. are recipients of an unrestricted research grant from Roche Pharma for the support of ProCURE program. The remaining authors declare no competing interests.

Reprints and permission information is available online at http://npg.nature.com/reprintsandpermissions/

Publisher's note: Springer Nature remains neutral with regard to jurisdictional claims in published maps and institutional affiliations.

Supplementary Information

Angulo-Urarte et al.

Endothelial cell rearrangements during vascular patterning require PI3-kinase-mediated inhibition of actomyosin contractility

Supplementary Figure 1

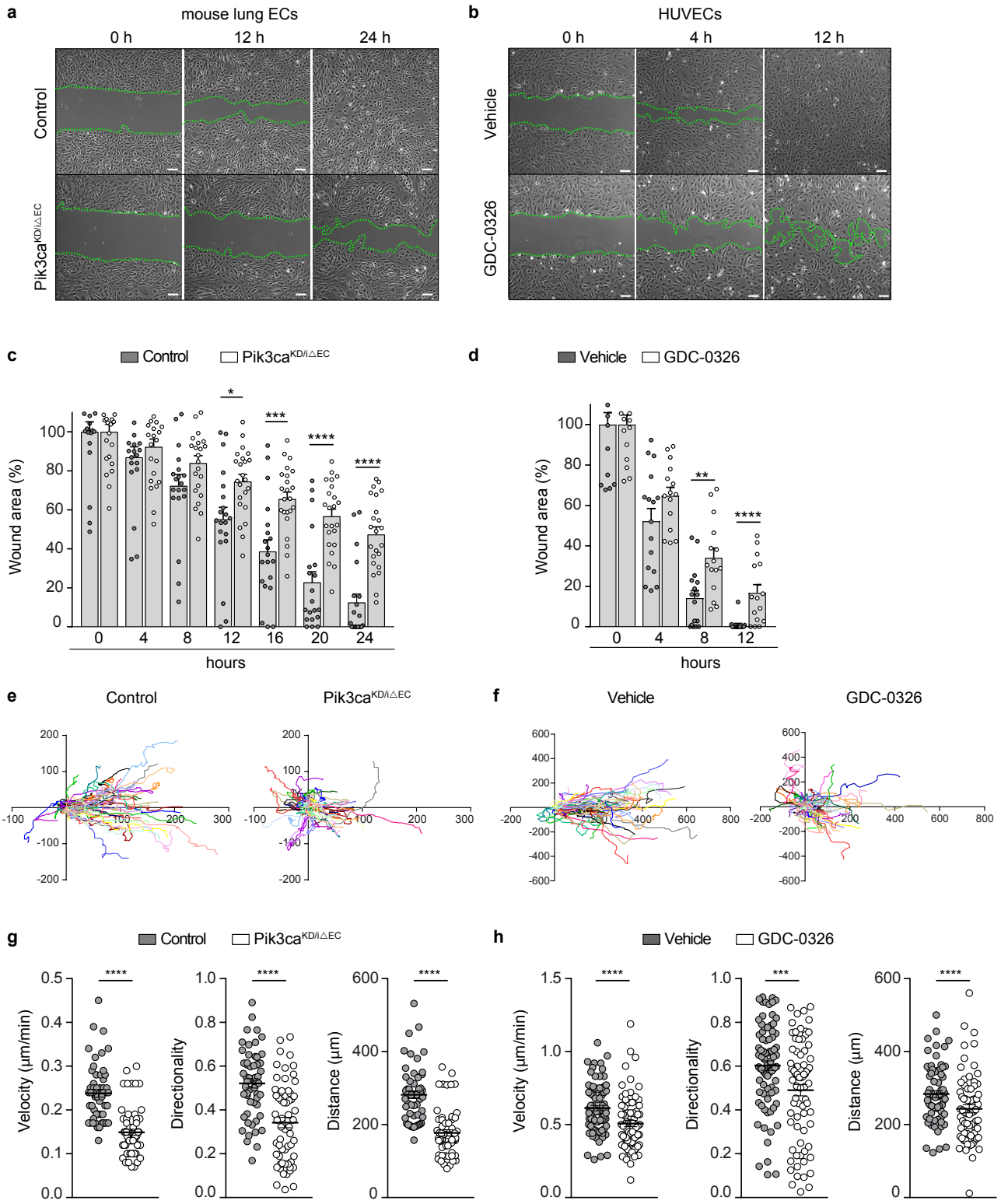

Supplementary Figure 1. Inactivation of PI3Kα impairs collective cell migration. (**a**) Representative phase contrast images of primary mouse endothelial cells isolated from control (top) and *Pik3ca*$^{KD/i\Delta EC}$ (bottom) mice immediately after performing the scratch, and 12 h and 24 h later. Cells were treated with 4-OHT for 96 h before performing the scratch. (**b**) Representative phase contrast images of vehicle (DMSO, top) and GDC-0326 (1 μM, bottom) -treated HUVECs immediately after performing the scratch, and 4 h and 12 h later. Cells were treated with DMSO or GDC-0326 for 24 h before performing the scratch. Green dashed lines highlight open scratch-area in **a** and **b**. (**c, d**) Quantification of wound closure area at the indicated time-points after the scratch. n≥ 20 scratch areas per condition from three independent experiments in **c,** and n≥ 15 scratch areas per treatment from two independent experiments in **d**. (**e**, **f**) Plots depicting cell migration of control and *Pik3ca*$^{KD/i\Delta EC}$ primary mouse endothelial cells during 20 h in a wound healing assay (**e**), and during 8 h in vehicle and GDC-0326 treated HUVECs (**f**). X and Y axis in the plots represent distance in μm. (**g**, **h**) Mean velocity directionality and travelled distance of individual cells measured during 20 h in **g** and 8 h in **h** after performing the scratch. n≥ 55 cells per condition from three independent experiments in **g,** and n≥ 104 cells per treatment from three independent experiments in **h**. Scale bars, 100 μm (**a, b**). Data in **c, d, g,** and **h** represent mean ± S.E.M. (error bars). *P<0.05, **P<0.01, ***P<0.001, and ****P<0.0001. Statistical analysis was performed with the two-sided Mann–Whitney test.

Supplementary Figure 2

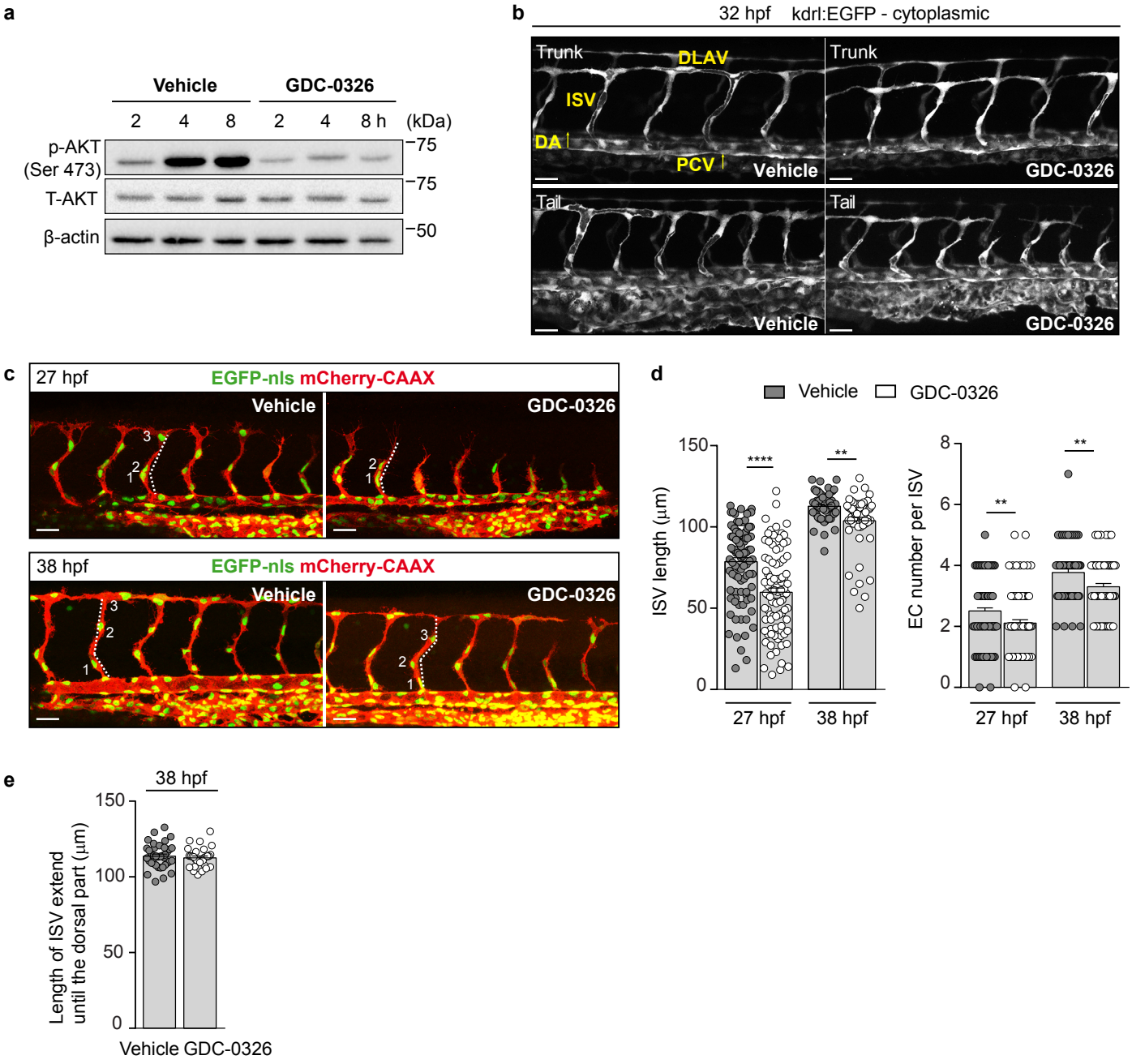

Supplementary Figure 2. Inactivation of PI3Kα in zebrafish embryos. (**a**) Wild type sibling zebrafish embryos were treated with vehicle (DMSO) or GDC-0326 (50 μM) at 22 hpf for 2 h, 4 h and 8 h followed by immunoblotting with the indicated antibodies. (**b**) Representative images of vehicle and GDC-0326 (50 μM) treated Tg(*kdrl:EGFP*)^{s843} zebrafish embryos from 22 to 32 hpf. DA refers to dorsal aorta, PCV refers to posterior cardinal vein, ISV refers to intersomitic vessels, and DLAV refers to dorsal longitudinal anastomotic vessels. (**c**) Representative images of vehicle and GDC-0326 (50 μM) treated Tg(*kdrl:EGFP-nls*)^{ubs1}/(*kdrl:mCherry-CAAX*)^{s916} transgenic embryos from 22 to 27 hpf (upper panel) or to 38 hpf (lower panel). ISV length (white punctuated lines) and nucleus number per ISV measurements are exemplified. Numbers indicate endothelial cell nuclei. (**d**) Quantitative analysis of vessel length and number of endothelial cells per ISV in zebrafish embryos shown in **c** (n≥ 52 ISVs per treatment). (**e**) Quantitative analysis of ISV length from the ISVs that have reached the top roof and started to form the DLAV at 38 hpf. Scale bars, 30 μm (**b, c**). Data in **d** and **e** represent mean ± S.E.M. (error bars). **P<0.01 and ****P<0.0001. Statistical analysis was performed with the two-sided Mann–Whitney test.

Supplementary Figure 3

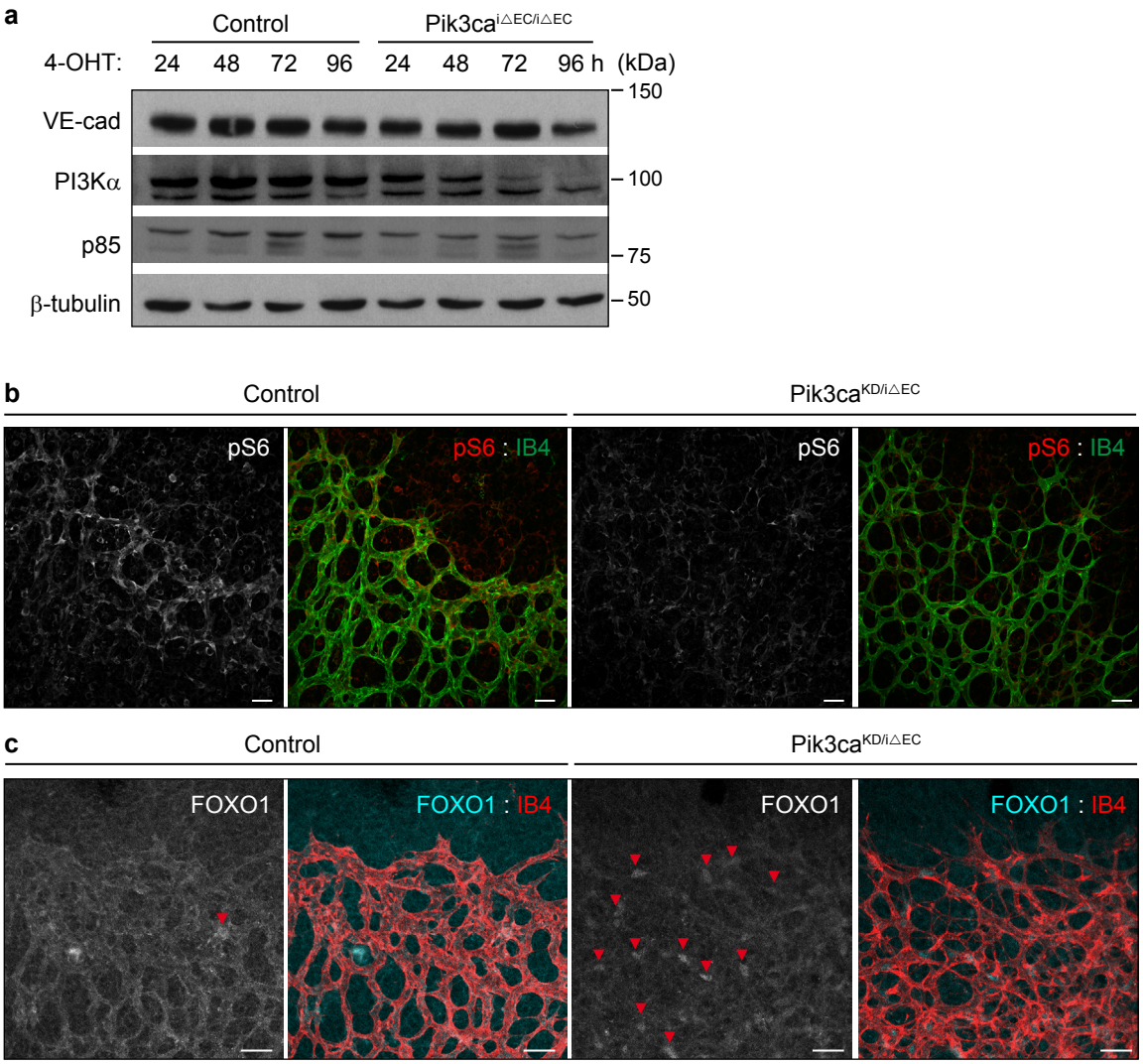

Supplementary Figure 3. Inactivation of PI3Kα in the mouse retinas. (**a**) Control and *Pik3ca*$^{i\Delta EC/i\Delta EC}$ mouse lung endothelial cells were incubated with 4-OHT for 24 h, 48 h, 72 h or 96 h, followed by immunoblotting using the indicated antibodies. (**b**) Representative images of pS6 240/242 (red) and IB4 (green)-stained P7 retinas of control and *Pik3ca*$^{KD/i\Delta EC}$ genotypes. (**c**) Confocal images of FOXO1 (cyan) and IB4 (red)-stained P7 retinas of control and *Pik3ca*$^{KD/i\Delta EC}$ genotypes. Scale bars, 30 μm (**b, c**).

Supplementary Figure 4

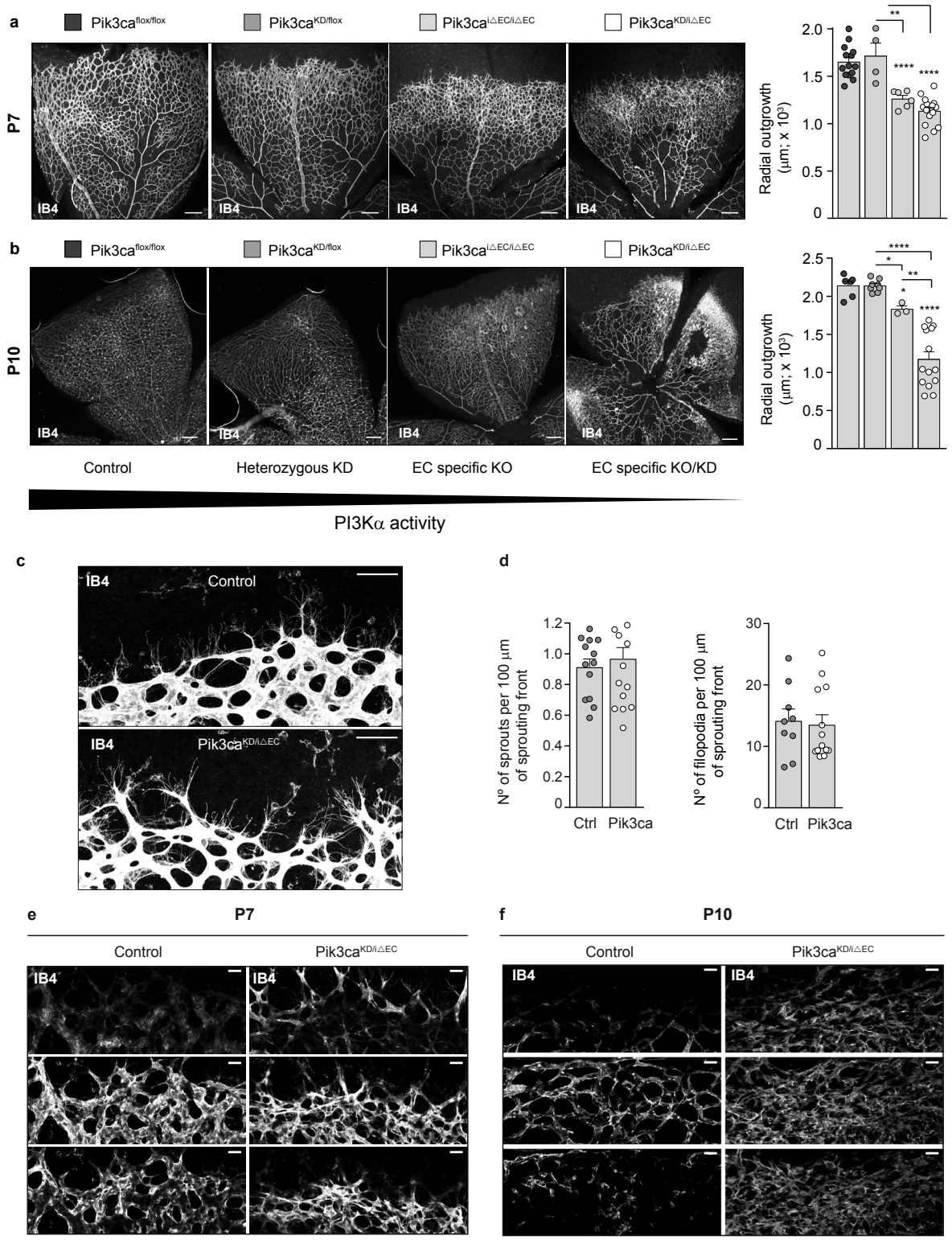

Supplementary Figure 4. Endothelial inactivation of PI3Kα leads to abnormal vessel growth. (**a**) Whole mount visualization of blood vessels by IB4 staining of P7 retinas from control, *Pik3ca*$^{KD/flox}$, *Pik3ca*$^{\Delta EC/i\Delta EC}$ and *Pik3ca*$^{KD/i\Delta EC}$ mouse littermates injected with 4-OHT at P1 and P2. Bars to the right show quantification of radial expansion of the vascular plexus in P7 retinas of respective genotypes. n≥ 4 retinas per genotype. (**b**) Whole mount visualization of blood vessels by IB4 staining of P10 retinas from control, *Pik3ca*$^{KD/flox}$, *Pik3ca*$^{\Delta EC/i\Delta EC}$, and *Pik3ca*$^{KD/i\Delta EC}$ mouse littermates injected with 4-OHT at P1 and P2. Bars to the right show quantification of the radial expansion of the vascular plexus in P10 retinas of respective genotypes. n≥ 3 retinas per genotype. (**c**) Whole mount visualization of blood vessels by IB4 staining of control and *Pik3ca*$^{KD/i\Delta EC}$ retinas at P7. (**d**) Quantitative analysis of number of sprouts (n≥ 13 retinas per genotype) and filopodial extensions (n≥ 9 retinas per genotype) of images shown in **c**. (**e**, **f**) Representative images corresponding to the top, middle and bottom layer of control and *Pik3ca*$^{KD/i\Delta EC}$ P7 (**e**) and P10 (**f**) retinas visualized by IB4 staining. The same number and width of Z-stacks was taken per retina of each genotype. Scale bars, 150 μm (**a**), 200 μm (**b**), 50 μm (**c**), 20 μm (**e, f**). Data in **a, b**, and **d** represent mean ± S.E.M. (error bars). *P<0.05, **P<0.01, ***P<0.001, and ****P<0.0001. Statistical analysis was performed with the two-sided Mann–Whitney test.

Supplementary Figure 5

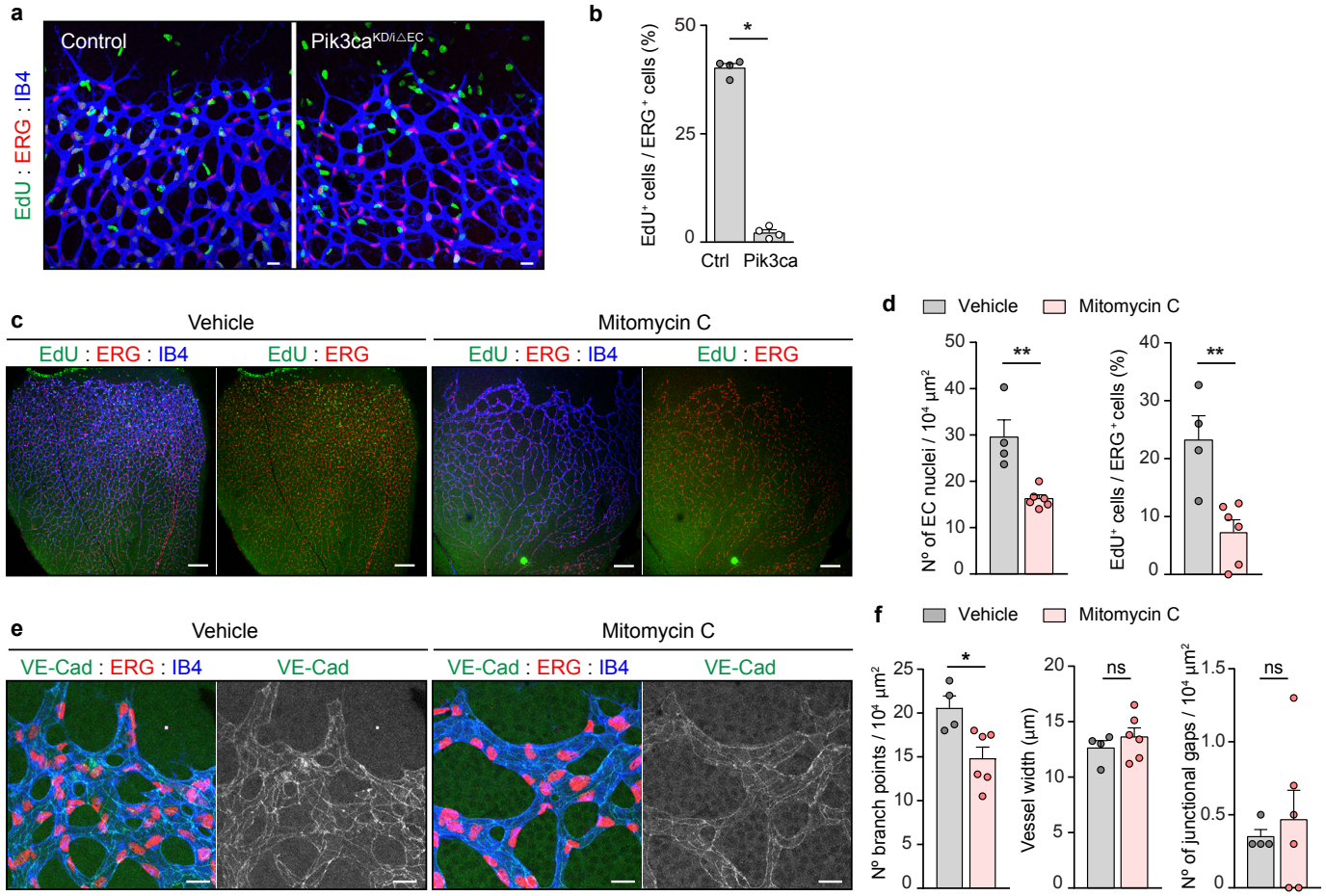

Supplementary Figure 5. Reduced proliferation does not interfere with junctional pattern in postnatal retinas. (**a**) EdU (green), ERG (red) and IB4 (blue) staining of control and *Pik3ca*$^{KD/i\Delta EC}$ P7 retinas. (**b**) Quantification of EdU-positive endothelial cells per total number of endothelial cells in control and *Pik3ca*$^{KD/i\Delta EC}$ P7 retinas (n≥4 retinas per genotype). (**c**) EdU (green), ERG (red) and IB4 (blue) staining of whole mount retinas from wild type mouse littermates treated with vehicle (DMSO) or mitomycin C at P5, and isolated at P7. (**d**) Quantification of endothelial cells per unit area assessed by ERG positivity (left panel) and of EdU positive endothelial cells per total number of endothelial cells (n≥ 4 retinas per treatment). (**e**) Representative images of whole mount retinas stained for VE-cadherin (green), ERG (red) and IB4 (blue) from wild type mouse littermates treated with vehicle or mitomycin C at P5 and isolated at P7. (**f**) Quantification of branch points, vessel width, and number of junctional gaps per unit area of images shown in **e** (n≥ 6 retinas per treatment). Scale bars, 20 µm (**a, e**), 140 µm (**c**). Data in **d**, **f** represent mean ± S.E.M. (error bars). ns: not significant,*P<0.05, **P<0.01. Statistical analysis was performed with the two-sided Mann–Whitney test.

Supplementary Figure 6

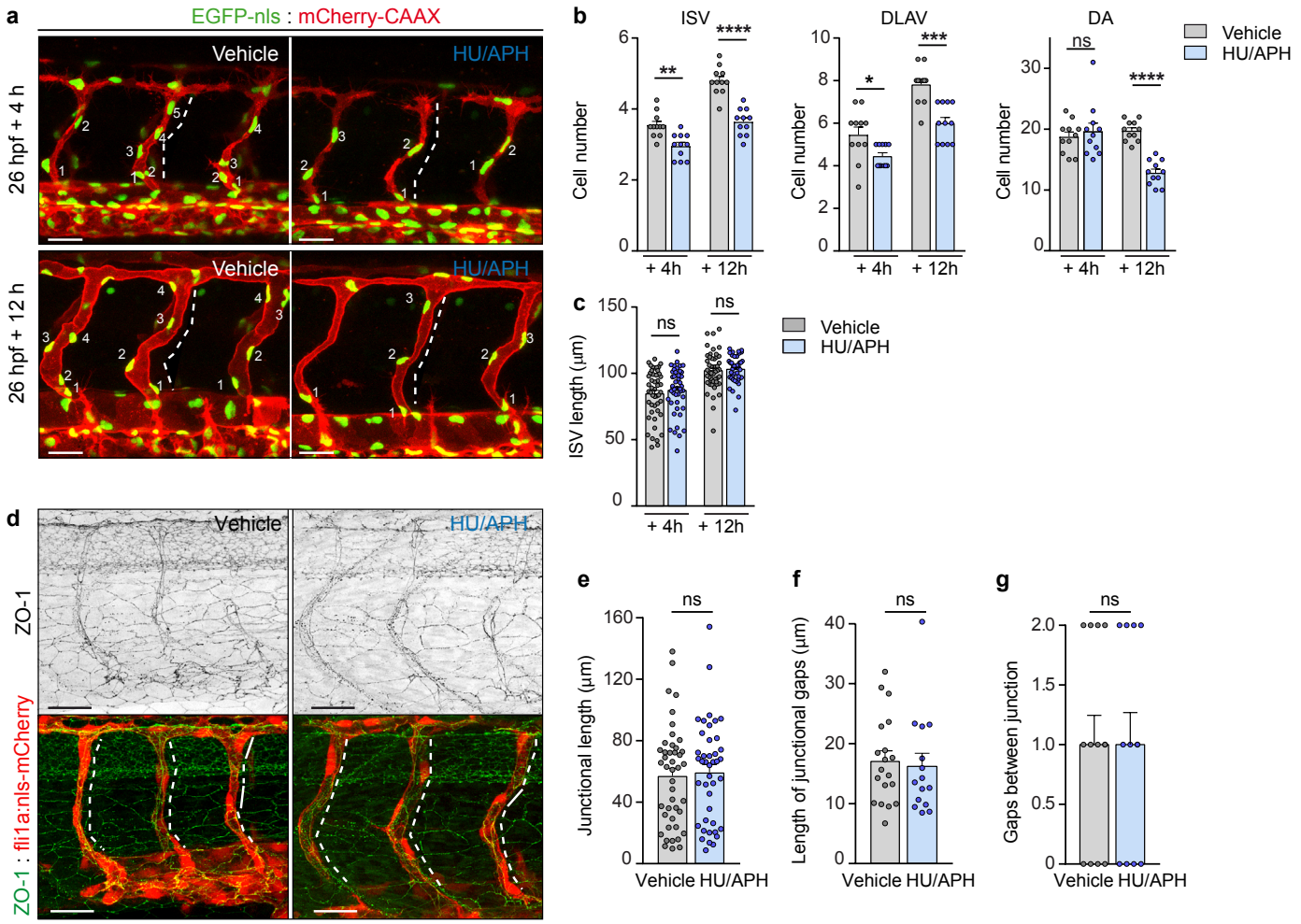

Supplementary Figure 6. Reduced proliferation does not interfere with junctional pattern in zebrafish embryos. (**a**) Images of vehicle and HU/APH-treated Tg(*kdrl:EGFP-nls*)^{ubs1}/(*kdrl:mCherry-CAAX*)^{s916} transgenic embryos from 26 hpf + 4 h (treatment) (upper panel) or to 26 hpf + 12 h treatment (lower panel). ISV length (white punctuated lines) and nucleus number per ISV measurements are exemplified. Number indicates endothelial cell nuclei. (**b**) Analysis of number of endothelial cells per ISV, DLAV and dorsal aorta (within 5 ISVs) in vehicle and HU/APH-treated zebrafish embryos (n=11 embryos per treatment, 5 ISVs per embryo, three independent experiments). (**c**) Analysis of ISV length (n≥42 ISVs per treatment, from 11-12 embryos analyzed from three independent experiments) in vehicle and HU/APH-treated zebrafish embryos. (**d**) Lateral views of intersomitic vessels (ISV) in vehicle or HU/APH treated transgenic Tg(*fli1ep:mCherry-nls*)^{ubs10} (shown in red) embryos stained for ZO-1 (green) at 33-34 hpf. Single ZO-1 staining is shown in row 1. White lines indicate ZO-1 negative staining (junctional gaps); white punctuate lines indicate elongation of junction. (**e**) Quantification of the length of the ISVs with continuous ZO-1 staining (n≥42 ISVs per treatment, from 11-12 embryos analyzed from three independent experiments). (**f**) Quantification of the length of the dorsal part of the ISVs without ZO-1 (length of junctional gaps) (ISVs without junctional gaps were excluded, n≥15 ISVs per treatment, from 11-12 embryos analyzed from three independent experiments). (**g**) Average number of gaps per ISV in vehicle and HU/APH-treated embryos (n=11 embryos per treatment, 5 ISVs per embryo, three independent experiments). Scale bars, 30 µm (**a, d**). Data in **b**, **c**, **e**, **f** and **g** represent mean ± S.E.M. (error bars). ns: not significant, **P<0.01, ***P<0.001, ****P<0.0001. Statistical analysis was performed with the two-sided Mann–Whitney test.

Supplementary Figure 7

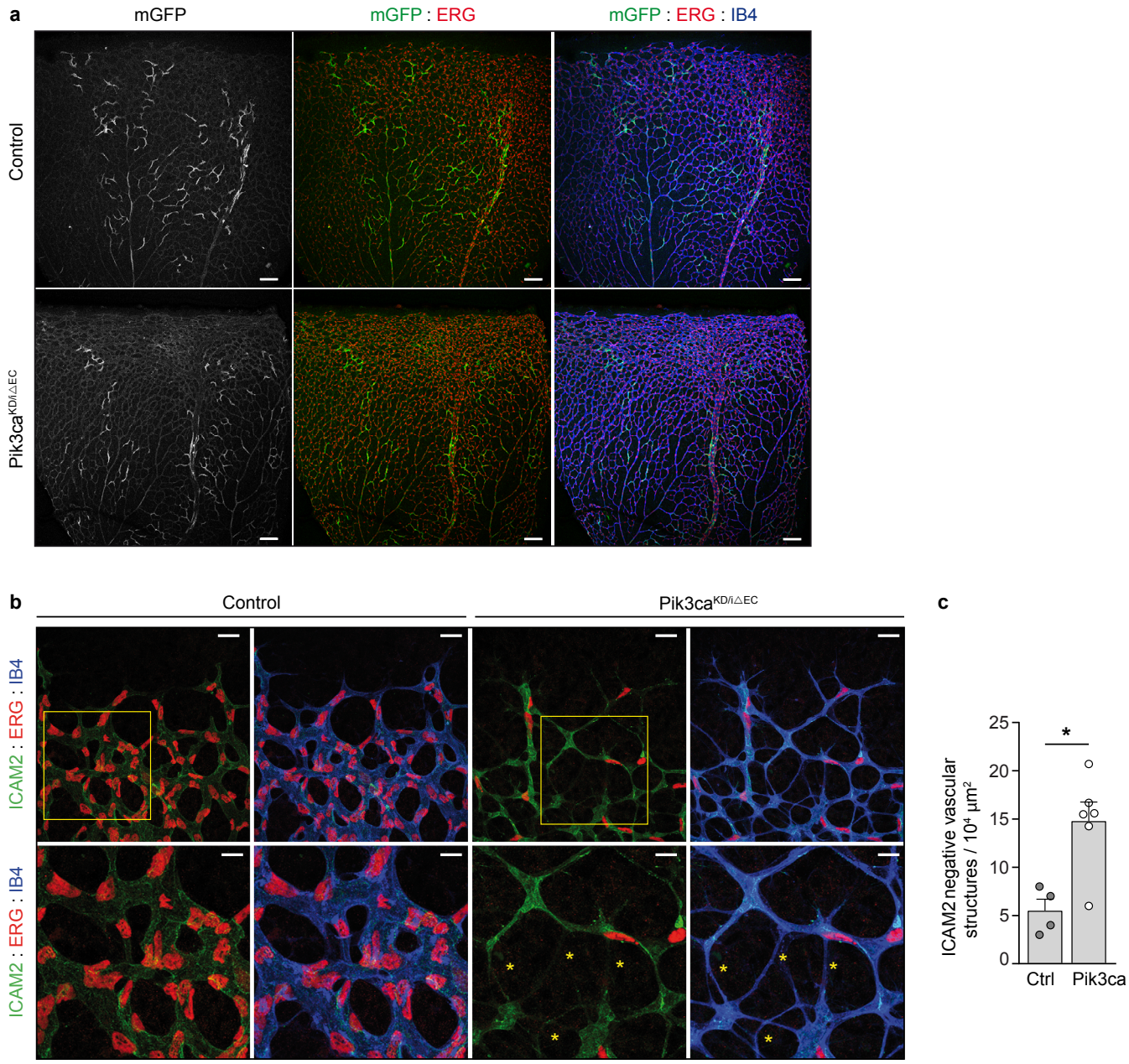

Supplementary Figure 7. Aberrant shape and lumen formation in *Pik3ca*$^{KD/i\Delta EC}$ endothelium. (**a**) Overview of immunostaining of single-cell labelling using Cre-induced expression of membrane-bound GFP (mGFP, shown in green in the image), endothelial nuclei (ERG, shown in red) and blood vessel (IB4, shown in blue). (**b**) Control and *Pik3ca*$^{KD/i\Delta EC}$ P7 retinas showing ICAM2 (green), ERG (red), and IB4 (blue). Yellow asterisks indicate IB4 positive/ICAM2 negative protrusions. (**c**) Quantification of ICAM2 negative vessels per unit area of images shown in **b** (n=4 retinas per genotype). Scale bars, 100 μm (**a**), 40 μm (**b**, upper panel), 10 μm (**b**, lower panel). Data represent mean ± S.E.M. (error bars). *P<0.05. Statistical analysis was performed with the two-sided Mann–Whitney test.

Supplementary Figure 8

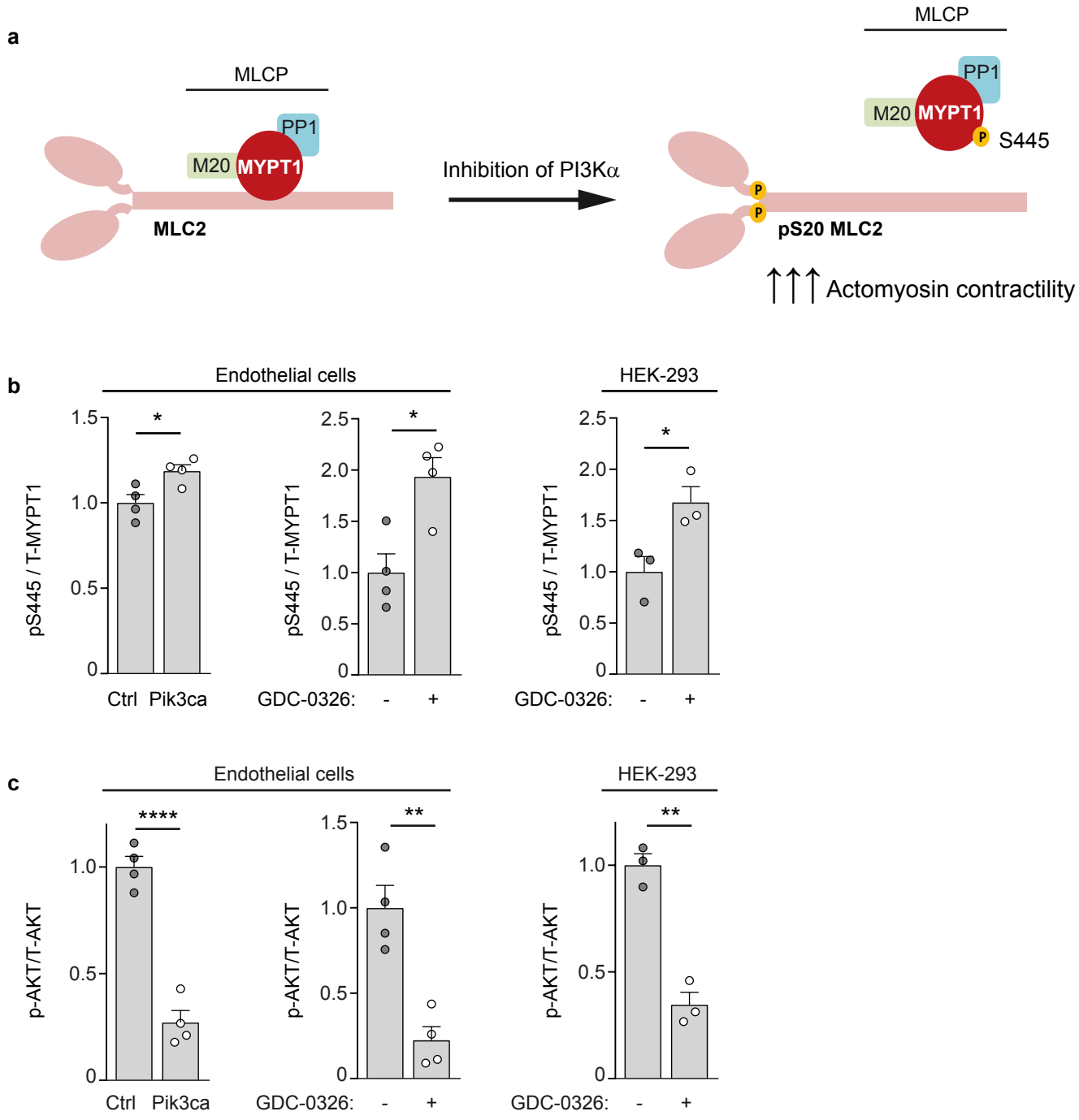

Supplementary Figure 8. Analysis of phosphoproteomic screening. (**a**) Schematic representation of the expected impact of inhibition of PI3Kα signalling on pS20 MLC2 and actomyosin contractility. MLCP is a trimeric heteroenzyme (PP1 catalytic subunit, MYPT1 regulatory subunit, and M20 subunit) that inactivates non-muscle myosin II by the dephosphorylation of MLC2. We observed that inhibition of PI3Kα results in phosphorylation of MYPT1 on the S445 residue favouring the delocalization of the MLCP complex from its substrate leading to an increase in the phosphorylation of MLC2 on S20, and as result, an increase in actomyosin contractility. Designed by Piotr Kobialka and Mariona Graupera. (**b, c**) Quantification of the relative immunoreactivity of pS445 MYPT1 normalized to total MYPT1 (**b**) and of pS473 AKT normalized to total AKT (**c**) from western blots shown in Fig. 4e and represented as the mean of at least three independent experiments. Data represent mean ± S.E.M. (error bars). *P<0.05, **P<0.01, and ****P<0.0001. Statistical analysis was performed by the two-sided Student´s t test.

Supplementary Figure 9

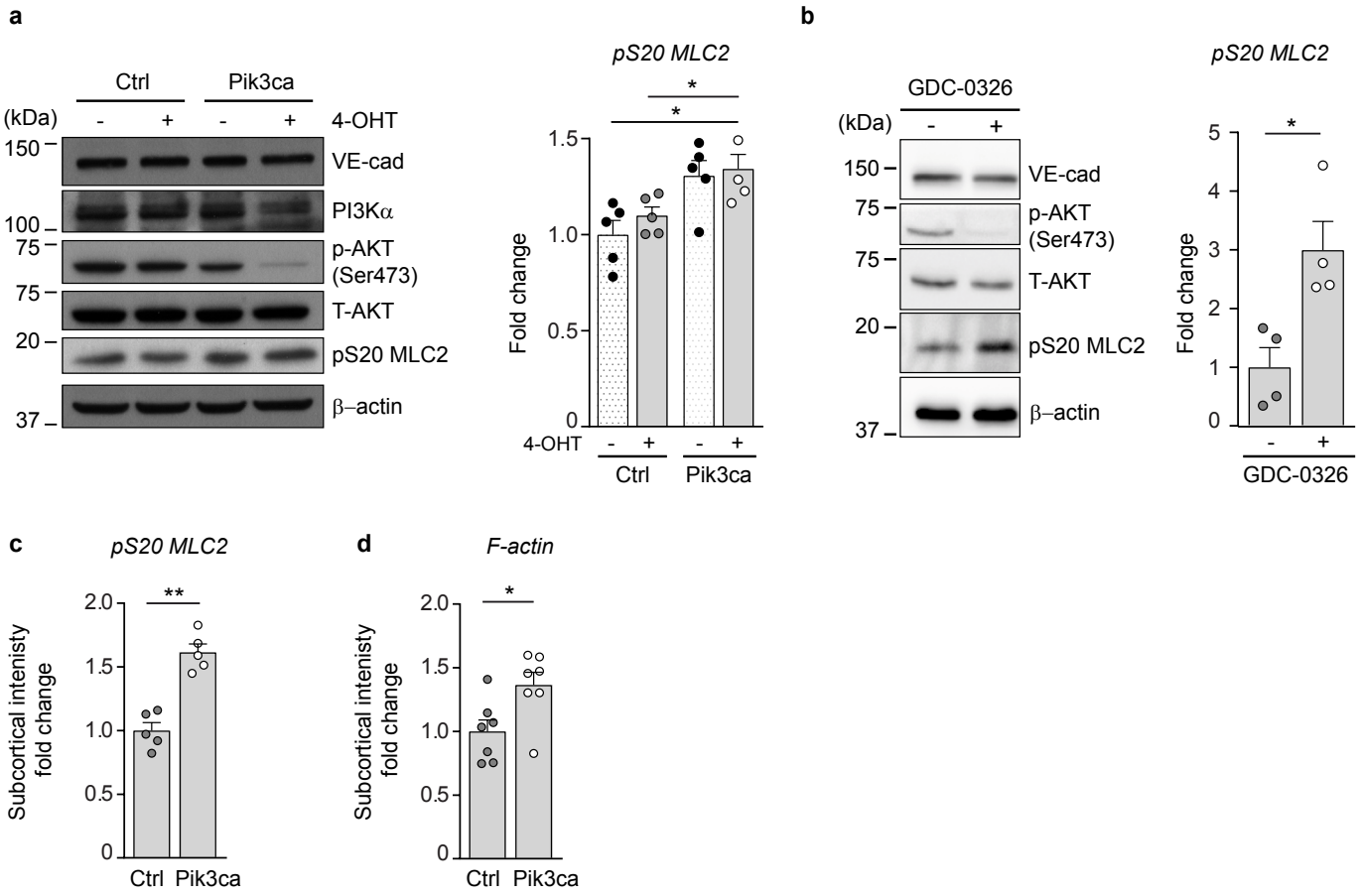

Supplementary Figure 9. Impact of inactivation of PI3Kα on pS20 MLC2 and its localization in endothelial cells. (**a**) Control and *Pik3ca*$^{KD/i\Delta EC}$ endothelial cells treated with 4-OHT for 96 h, followed by immunoblotting using the indicated antibodies. Quantification of pS20 MLC2 is shown to the right (n=5 independent experiments). (**b**) Wild type mouse lung endothelial cells were incubated with vehicle (DMSO) or GDC-0326 (1 μm) for 48 h followed by immunoblotting using the indicated antibodies. Quantification of pS20 MLC2 is shown to the right (n=4 independent experiments). (**c**, **d**) Quantification of pS20 MLC2 (**c**) and F-actin (**d**) immunostaining intensity at the subcortical location (shown as integrated density) of control and *Pik3ca*$^{KD/i\Delta EC}$ endothelial cells treated with 4-OHT for 96 h (n≥5 independent experiments). Data in **a, b, c** and **d** represent mean ± S.E.M. (error bars). *P<0.05 and **P<0.01. Statistical analysis was performed with the two-sided Mann–Whitney test.

Supplementary Figure 10

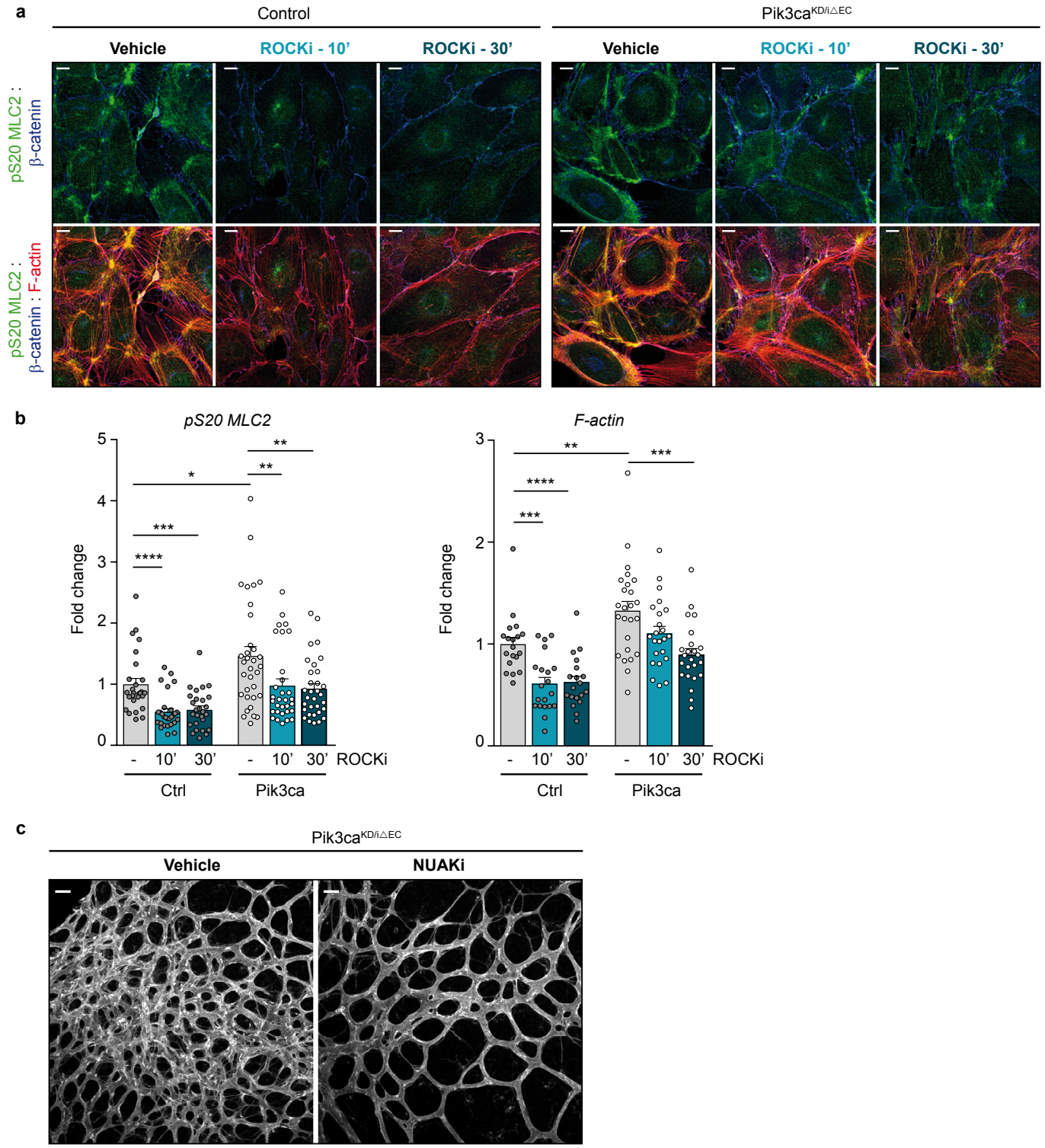

This figure continues in the next page.

Supplementary Figure 10 extension

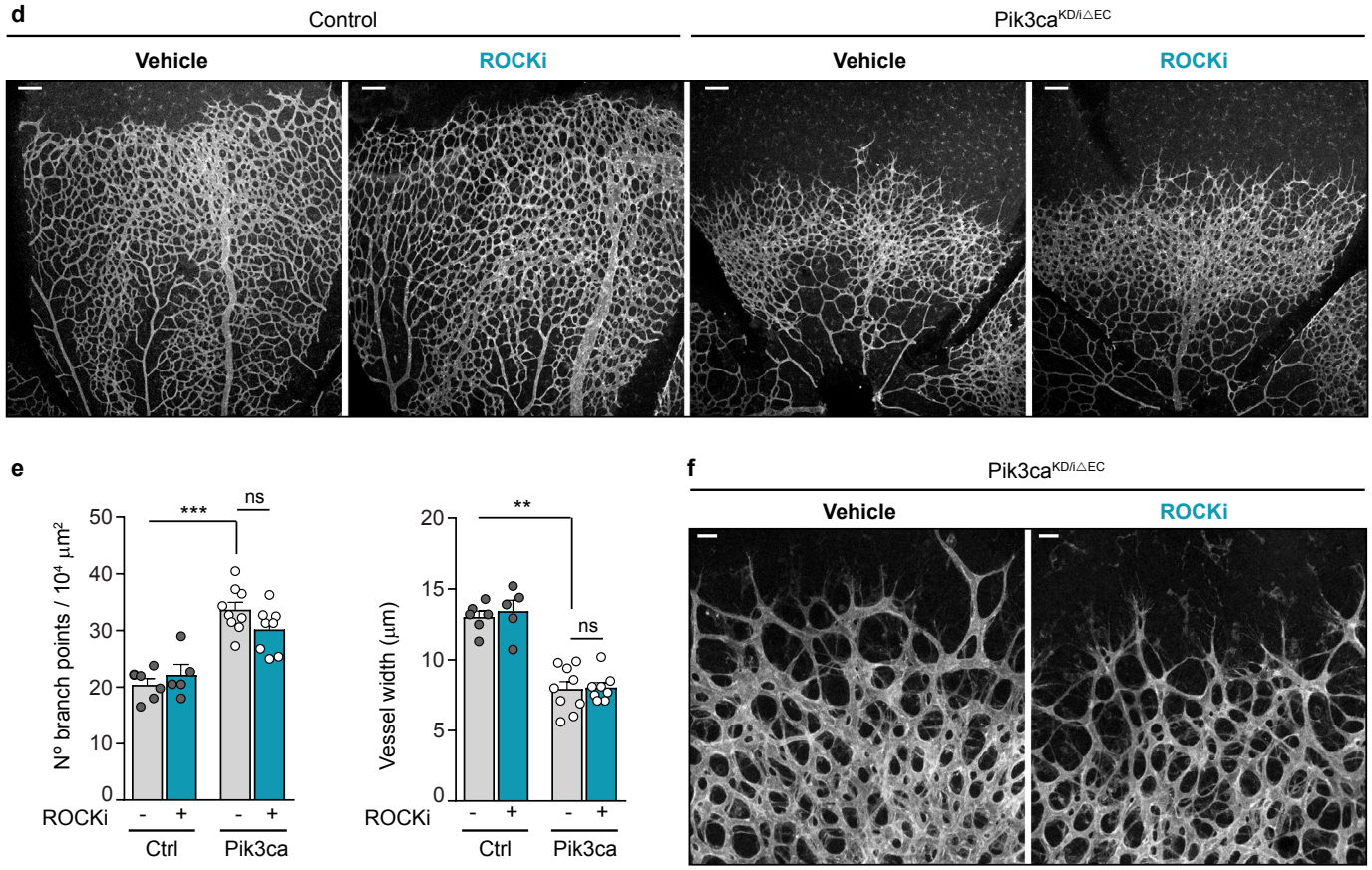

Supplementary Figure 10. Inactivation of ROCK does not restore the endothelial phenotypes imposed by PI3Kα inactivation. (**a**) Assessment of pS20 MLC2 (green), F-actin (red), and β-catenin (blue) of control and *Pik3ca*$^{KD/i\Delta EC}$ endothelial cells treated with 4-OHT for 96 h and incubated with DMSO as control or 10 μM Y-27632 (ROCK inhibitor; ROCKi) for 10 or 30 min. (**b**) Subcortical quantification of pS20 MLC2 (left panel) and F-actin (right panel) immunostaining intensities (shown as integrated density) of images shown in **a**. (n≥ 28 images of at least three independent experiments). (**c**) High magnification confocal images of *Pik3ca*$^{KD/i\Delta EC}$ P7 retinas treated with DMSO or WZ4003 (NUAKi) at P6. (**d**) IB4-stained control and *Pik3ca*$^{KD/i\Delta EC}$ P7 retinas treated with DMSO or Y-27632 (ROCKi) at P6 and P7 (10 am). (**e**) Quantification of branch points per unit area and vessel width per unit area (n≥5 retinas per genotype and treatment). (**f**) High magnification confocal images of *Pik3ca*$^{KD/i\Delta EC}$ P7 retinas treated with DMSO or Y-27632. Scale bars, 15 μm (**a**), 20 μm (**c**), 100 μm (**d**), 20 μm (**f**). Data in **b** and **e** represent mean ± S.E.M. (error bars). ns: not significant, *P<0.05, **P<0.01, ***P<0.001, and ****P<0.0001. Statistical analysis was performed with the two-sided Mann–Whitney test.

Supplementary Figure 11

a Supplementary Figure 2a

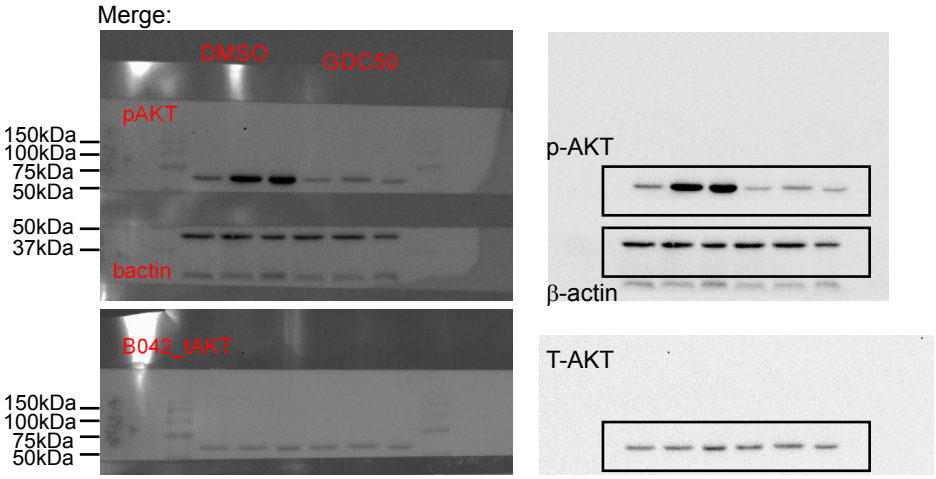

b Supplementary Figure 3a

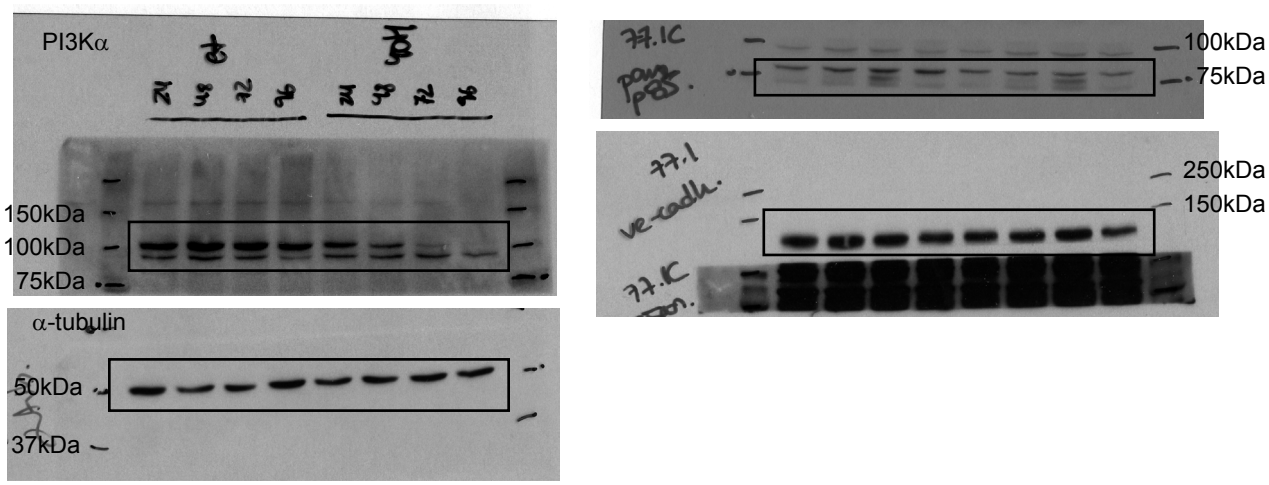

Supplementary Figure 11. Uncropped western blots. (**a**) Blots related to Supplementary Figure 2a. Left panels show the merge with the molecular markers and the right panels show the boxes indicating the cropped sections used in the corresponding figures. (**b**) Blots related to Supplementary Figure 3a. Boxes indicate the cropped sections used in the corresponding figures.
Of note, for some immunoblotting assays membranes were cut into several pieces to incubate with different antibodies.

Supplementary Figure 12

a Figure 4e

Panel 1

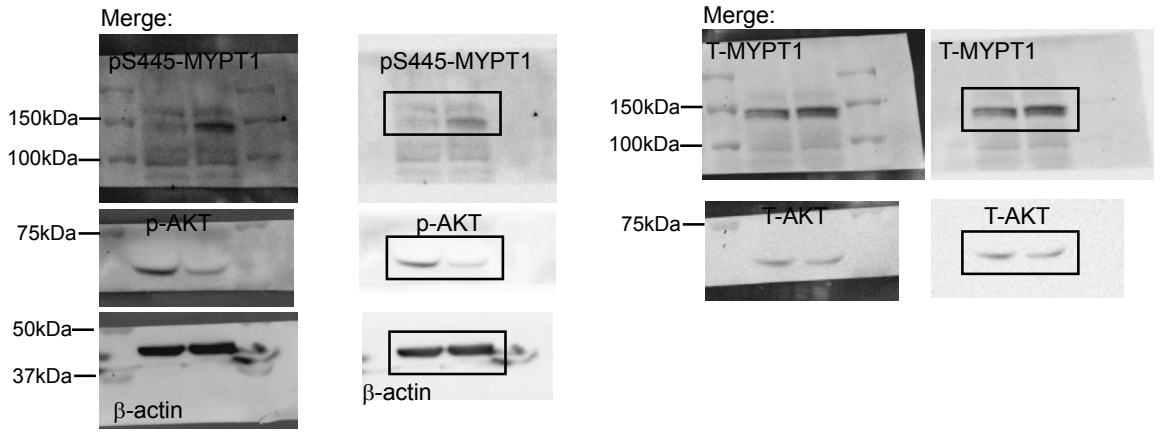

Panel 2

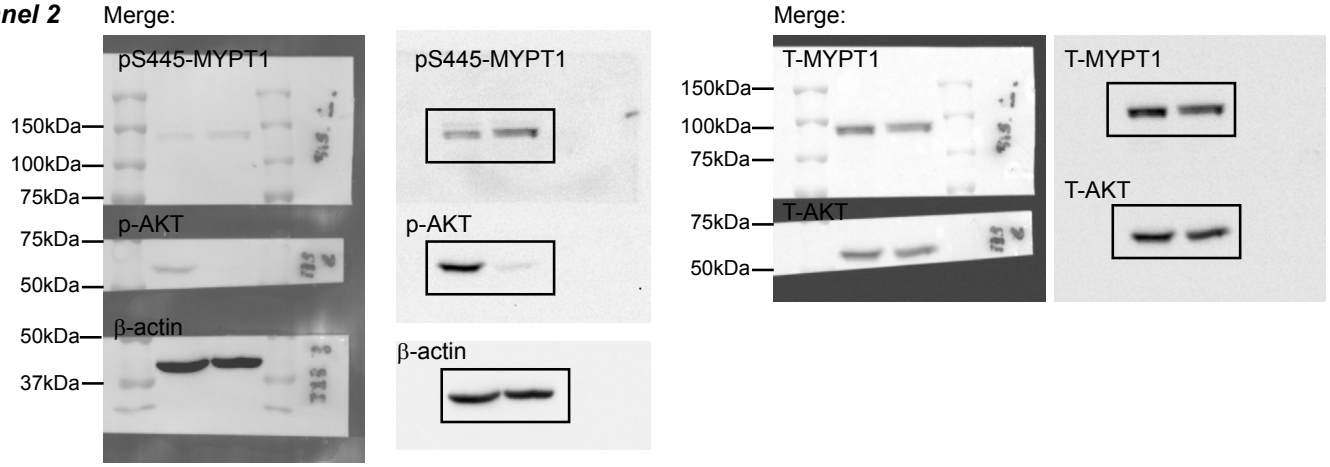

Panel 3

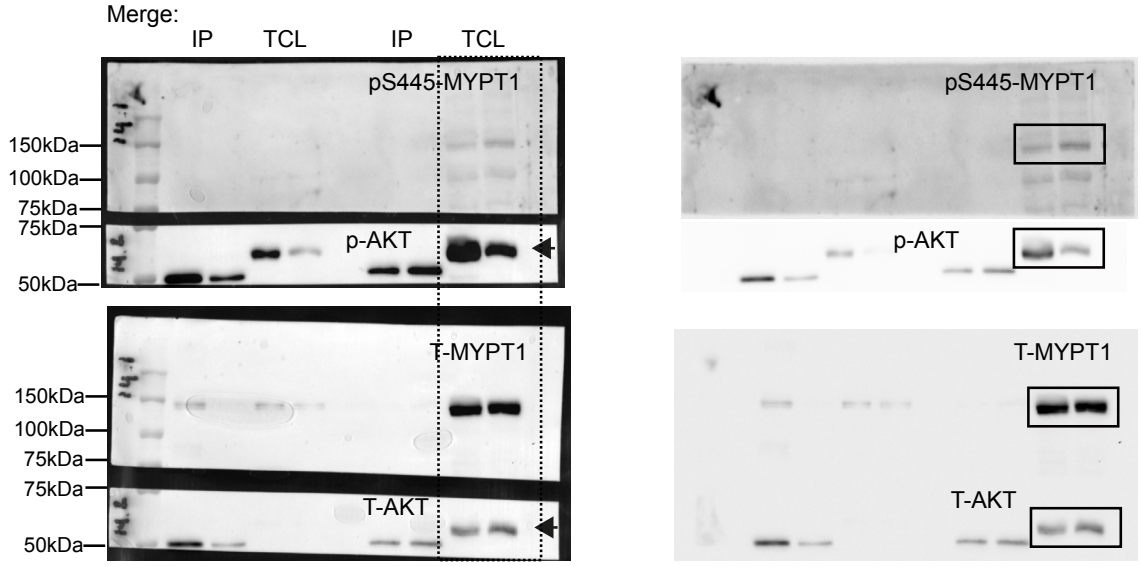

Supplementary Figure 12. Uncropped western blots. Blots related to Figure 4e. Left panels show the merge with the molecular markers and the right panels show the boxes indicating the cropped sections used in the corresponding figures. Of note, for some immunoblotting assays membranes were cut into several pieces to incubate with different antibodies.

Supplementary Figure 13

a Figure 5a

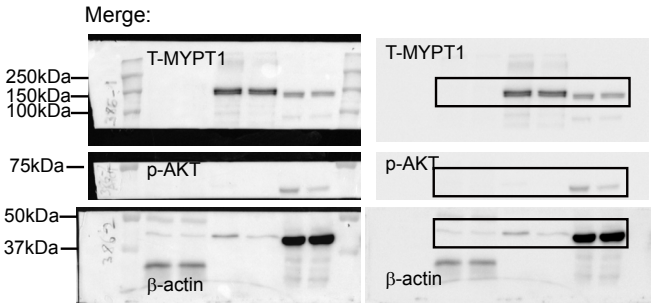

b Figure 5b

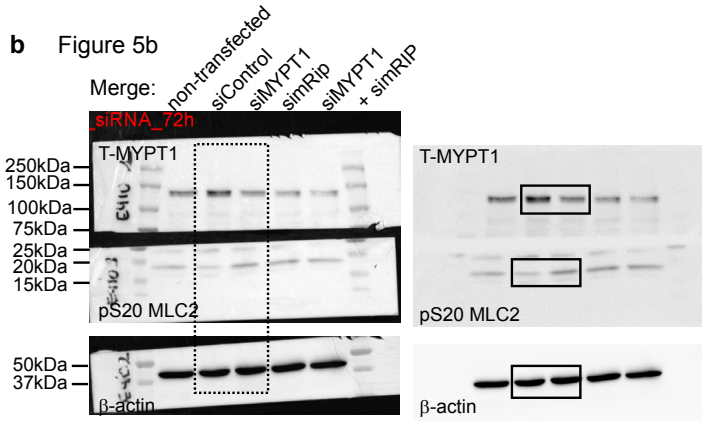

c Supplementary Figure 9a

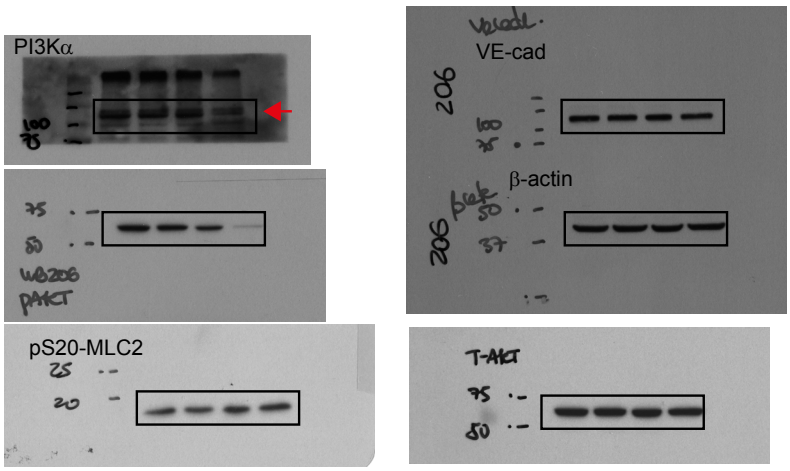

d Supplementary Figure 9b

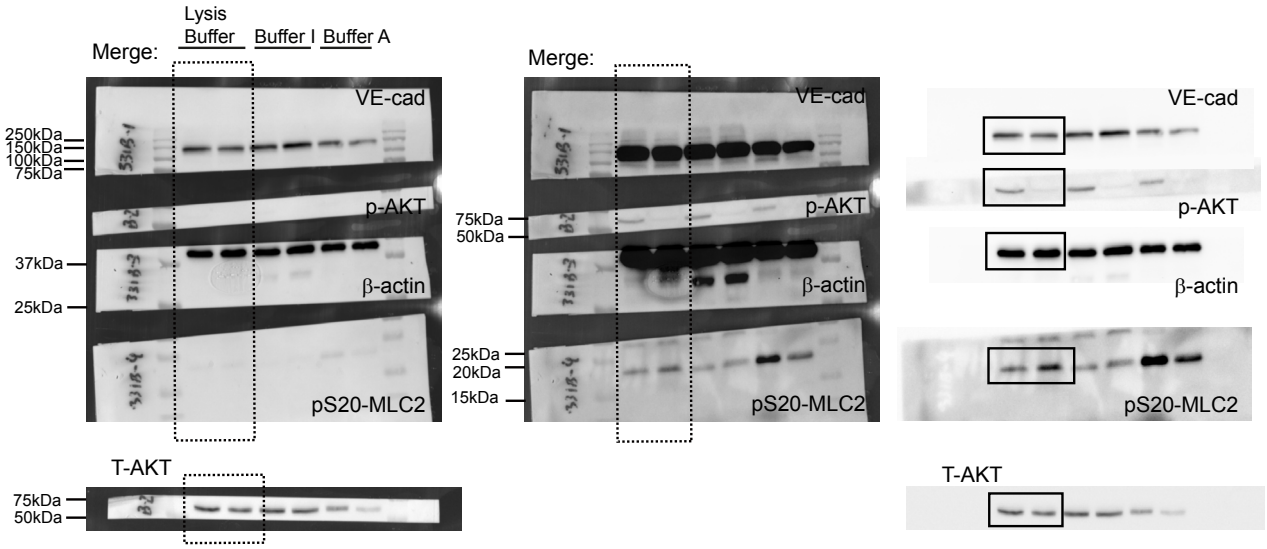

Supplementary Figure 13. Uncropped western blots. (**a**) Blots related to Figure 5a. (**b**) Blots related to Figure 5b. (**c**) Blots related to Supplementary Figure 9a. (**d**) Blots related to Supplementary Figure 9b. Left panels show the merge with the molecular markers and the right panels show the boxes indicating the cropped sections used in the corresponding figures. Of note, for some immunoblotting assays membranes were cut into several pieces to incubate with different antibodies.

Supplementary Table 1. Summary of genetic models use to study *Pik3ca* inactivation

Mouse model	Name after 4-OHT treatment	Description
Pik3ca$^{flox/flox}$	Control	Control. No Cre recombinase expression
Pik3ca$^{KD/flox}$	*Pik3ca*$^{KD/flox}$	Heterozygous kinase dead (KD). One *Pik3ca* alelle expresses constitutively a kinase dead form of the PI3Kα protein. Half of the PI3Kα protein is inactive.
Pdgfb-iCreER Pik3ca$^{flox/flox}$	*Pik3ca*$^{i\Delta EC/i\Delta EC}$	Endothelial specific knockout mouse (KO). Endothelial specific deletion of both *Pi3kca* alleles after 4-HOT administration
Pdgfb-iCreER Pik3ca$^{KD/flox}$	*Pik3ca*$^{KD/i\Delta EC}$	Kinase dead allele and endothelial specific knockout allele. One *Pik3ca* allele expresses constitutively a kinase dead form of the PI3Kα protein and the other is deleted after 4-OHT administration. Main model of study in this manuscript.

Supplementary Table 2. Codes used for the analysis of the mass spectrometry data.

Sample Name	Animal ID	Genotype	Treatment	Replicate
R_b1822p5_S10_SF622_24h_ETH_Phos_R1.raw	SF622	Control	24h ethanol	1
R_b1822p5_S10_SF622_24h_ETH_Phos_R2.raw	SF622	Control	24h ethanol	2
R_b1822p5_S11_SF622_24h_4HTA_Phos_R1.raw	SF622	Control	24h 4OHT	1
R_b1822p5_S11_SF622_24h_4HTA_Phos_R2.raw	SF622	Control	24h 4OHT	2
R_b1822p5_S12_SF622_96h_4HTA_Phos_R1.raw	SF622	Control	96h 4OHT	1
R_b1822p5_S12_SF622_96h_4HTA_Phos_R2.raw	SF622	Control	96h 4OHT	2
R_b1822p5_S13_SF602_24h_ETH_Phos_R1.raw	SF602	Control	24h ethanol	1
R_b1822p5_S13_SF602_24h_ETH_Phos_R2.raw	SF602	Control	24h ethanol	2
R_b1822p5_S14_SF602_24h_4HTA_Phos_R1.raw	SF602	Control	24h 4OHT	1
R_b1822p5_S14_SF602_24h_4HTA_Phos_R2.raw	SF602	Control	24h 4OHT	2
R_b1822p5_S15_SF602_96h_4HTA_Phos_R1.raw	SF602	Control	96h 4OHT	1
R_b1822p5_S15_SF602_96h_4HTA_Phos_R2.raw	SF602	Control	96h 4OHT	2
R_b1822p5_S16_SF603_24h_ETH_Phos_R1.raw	SF603	Control	24h ethanol	1
R_b1822p5_S16_SF603_24h_ETH_Phos_R2.raw	SF603	Control	24h ethanol	2
R_b1822p5_S17_SF603_24h_4HTA_Phos_R1.raw	SF603	Control	24h 4OHT	1
R_b1822p5_S17_SF603_24h_4HTA_Phos_R2.raw	SF603	Control	24h 4OHT	2
R_b1822p5_S18_SF603_96h_4HTA_Phos_R1.raw	SF603	Control	96h 4OHT	1
R_b1822p5_S18_SF603_96h_4HTA_Phos_R2.raw	SF603	Control	96h 4OHT	2
R_b1822p5_S19_SF604_24h_ETH_Phos_R1.raw	SF604	Pik3CA$^{KD/Flox}$	24h ethanol	1
R_b1822p5_S19_SF604_24h_ETH_Phos_R2.raw	SF604	Pik3CA$^{KD/Flox}$	24h ethanol	2
R_b1822p5_S1_SF619_24h_ETH_Phos_R1.raw	SF604	Pik3CA$^{KD/Flox}$	24h ethanol	1
R_b1822p5_S1_SF619_24h_ETH_Phos_R2.raw	SF604	Pik3CA$^{KD/Flox}$	24h ethanol	2
R_b1822p5_S20_SF604_24h_4HTA_Phos_R1.raw	SF604	Pik3CA$^{KD/Flox}$	24h 4OHT	1
R_b1822p5_S20_SF604_24h_4HTA_Phos_R2.raw	SF604	Pik3CA$^{KD/Flox}$	24h 4OHT	2
R_b1822p5_S21_SF604_96h_4HTA_Phos_R1.raw	SF604	Pik3CA$^{KD/Flox}$	96h 4OHT	1
R_b1822p5_S21_SF604_96h_4HTA_Phos_R2.raw	SF604	Pik3CA$^{KD/Flox}$	96h 4OHT	2
R_b1822p5_S22_SF607_24h_ETH_Phos_R1.raw	SF607	Pik3CA$^{KD/Flox}$	24h ethanol	1
R_b1822p5_S22_SF607_24h_ETH_Phos_R2.raw	SF607	Pik3CA$^{KD/Flox}$	24h ethanol	2
R_b1822p5_S23_SF607_24h_4HTA_Phos_R1.raw	SF607	Pik3CA$^{KD/Flox}$	24h 4OHT	1
R_b1822p5_S23_SF607_24h_4HTA_Phos_R2.raw	SF607	Pik3CA$^{KD/Flox}$	24h 4OHT	2
R_b1822p5_S24_SF607_96h_4HTA_Phos_R1.raw	SF607	Pik3CA$^{KD/Flox}$	96h 4OHT	1
R_b1822p5_S24_SF607_96h_4HTA_Phos_R2.raw	SF607	Pik3CA$^{KD/Flox}$	96h 4OHT	2
R_b1822p5_S2_SF619_24h_4HTA_Phos_R1.raw	SF619	Pik3CA$^{KD/Flox}$	24h 4OHT	1
R_b1822p5_S2_SF619_24h_4HTA_Phos_R2.raw	SF619	Pik3CA$^{KD/Flox}$	24h 4OHT	2
R_b1822p5_S3_SF619_96h_4HTA_Phos_R1.raw	SF619	Pik3CA$^{KD/Flox}$	96h 4OHT	1
R_b1822p5_S3_SF619_96h_4HTA_Phos_R2.raw	SF619	Pik3CA$^{KD/Flox}$	96h 4OHT	2
R_b1822p5_S4_SF624_24h_ETH_Phos_R1.raw	SF624	Control	24h ethanol	1
R_b1822p5_S4_SF624_24h_ETH_Phos_R2.raw	SF624	Control	24h ethanol	2
R_b1822p5_S5_SF624_24h_4HTA_Phos_R1.raw	SF624	Control	24h 4OHT	1
R_b1822p5_S5_SF624_24h_4HTA_Phos_R2.raw	SF624	Control	24h 4OHT	2
R_b1822p5_S6_SF624_96h_4HTA_Phos_R1.raw	SF624	Control	96h 4OHT	1
R_b1822p5_S6_SF624_96h_4HTA_Phos_R2.raw	SF624	Control	96h 4OHT	2
R_b1822p5_S7_SF621_24h_ETH_Phos_R1.raw	SF621	Pik3CA$^{KD/Flox}$	24h ethanol	1
R_b1822p5_S7_SF621_24h_ETH_Phos_R2.raw	SF621	Pik3CA$^{KD/Flox}$	24h ethanol	2
R_b1822p5_S8_SF621_24h_4HTA_Phos_R1.raw	SF621	Pik3CA$^{KD/Flox}$	24h 4OHT	1
R_b1822p5_S8_SF621_24h_4HTA_Phos_R2.raw	SF621	Pik3CA$^{KD/Flox}$	24h 4OHT	2
R_b1822p5_S9_SF621_96h_4HTA_Phos_R1.raw	SF621	Pik3CA$^{KD/Flox}$	96h 4OHT	1
R_b1822p5_S9_SF621_96h_4HTA_Phos_R2.raw	SF621	Pik3CA$^{KD/Flox}$	96h 4OHT	2

A.2.3. Paatero et al., 2018, Nature communications

Junction-based lamellipodia drive endothelial cell rearrangements in vivo via a VE-cadherin-F-actin based oscillatory cell-cell interaction.

Summary:

Paatero et al. describe a novel mechanism, in which endothelial cells use junction-based lamellipodia (JBL) for cellular rearrangement and concomitant cell elongation. JBL are characterized as F-actin dependent structures emanating from cell junctions in the direction of movements. They show an oscillatory behavior and are highly dependent on VE-cadherin and its interaction with the actin cytoskeleton. They hypothesize, that JBL provide the physical means for cell rearrangements and that it might be a general mechanism of endothelial cells employed during vascular remodeling.

My contribution:

For this publication, I was experimentally analyzing the role of Rac1 during junctional rearrangements. Prior to imaging, I treated embryos transgenically expressing EGFP-ZO1 with a Rac1 inhibitor (NSC23766) or DMSO and performed high resolution time-lapse imaging during the process of junctional ring elongation. Analysis proved the formation of double junctions to be a hallmark during the JBL cycle and provided the basis for experiments performed in this thesis. The results obtained are integrated in the manuscript in Figure 6 e and are also part of my thesis (depicted in Figure 26). Additionally, I was extensively involved in proof-reading and giving suggestions for improvements until final submission of the manuscript.

nature COMMUNICATIONS

ARTICLE

DOI: 10.1038/s41467-018-05851-9 OPEN

Junction-based lamellipodia drive endothelial cell rearrangements in vivo via a VE-cadherin-F-actin based oscillatory cell-cell interaction

Ilkka Paatero[1,2], Loïc Sauteur[1], Minkyoung Lee[1], Anne K. Lagendijk[3], Daniel Heutschi[1], Cora Wiesner[1], Camilo Guzmán[3], Dimitri Bieli[1], Benjamin M. Hogan[3], Markus Affolter[1] & Heinz-Georg Belting[1]

Angiogenesis and vascular remodeling are driven by extensive endothelial cell movements. Here, we present in vivo evidence that endothelial cell movements are associated with oscillating lamellipodia-like structures, which emerge from cell junctions in the direction of cell movements. High-resolution time-lapse imaging of these junction-based lamellipodia (JBL) shows dynamic and distinct deployment of junctional proteins, such as F-actin, VE-cadherin and ZO1, during JBL oscillations. Upon initiation, F-actin and VE-cadherin are broadly distributed within JBL, whereas ZO1 remains at cell junctions. Subsequently, a new junction is formed at the front of the JBL, which then merges with the proximal junction. Rac1 inhibition interferes with JBL oscillations and disrupts cell elongation—similar to a truncation in *ve-cadherin* preventing VE-cad/F-actin interaction. Taken together, our observations suggest an oscillating ratchet-like mechanism, which is used by endothelial cells to move over each other and thus provides the physical means for cell rearrangements.

[1] Department of Cell Biology, Biozentrum, University of Basel, Basel 4056, Switzerland. [2] Turku Centre for Biotechnology, University of Turku and Åbo Akademi University, Turku 20520, Finland. [3] Division of Genomics of Development and Disease, Institute for Molecular Bioscience, The University of Queensland, St Lucia, QLD 4072, Australia. These authors contributed equally: Loïc Sauteur, Minkyoung Lee. Correspondence and requests for materials should be addressed to M.A. (email: markus.affolter@unibas.ch) or to H.-G.B. (email: heinz-georg.belting@unibas.ch)

Organ morphogenesis is driven by a wealth of tightly orchestrated cellular behaviors, which ensure proper organ assembly and function. The cardiovascular system is one of the most ramified vertebrate organs and is characterized by an extraordinary plasticity. It forms during early embryonic development, and it expands and remodels to adapt to the needs of the growing embryo. In adult life, this plasticity allows flexible responses, for example, during inflammation and wound healing[1,2].

At the cellular level, blood vessel morphogenesis and remodeling are accomplished by endothelial cell behaviors including cell migration, cell rearrangement and cell shape changes[3–5]. This repertoire of dynamic behaviors allows endothelial cells to rapidly respond to different contextual cues, for example during angiogenic sprouting, anastomosis, diapedesis or regeneration. In particular, it has been shown that endothelial cells are very motile, not only during sprouting, but also within established vessels, where they migrate against the blood flow[6,7].

Endothelial cell migration has been extensively studied in different in vivo and in vitro systems mainly focusing on angiogenic tip cell behavior and the interaction of endothelial cells with the extracellular matrix (ECM)[8,9]. However, endothelial cells can also shuffle positions within an angiogenic sprout[10], and these cellular rearrangements require the junctional adhesion protein VE-cadherin/CDH5[11–13]. Moreover, in vivo analyses in avian and fish embryos have shown that endothelial cells can migrate within patent blood vessels emphasizing that regulation of endothelial cell adhesion and motility is critical during vascular remodeling processes[6,7,14,15].

Although many aspects of sprouting angiogenesis and vascular remodeling rely on endothelial cell interactions[3], the exact role of endothelial cell junctions (and in particular that of VE-cad) in these processes is not well understood. Indeed, rather than supporting an active function for VE-cad in dynamic cell behaviors, most studies point to a restrictive or permissive role, consistent with the maintenance of endothelial integrity[16–18]. On the other hand, the observation that loss of VE-cad function can inhibit cell rearrangements suggests an active contribution to this process[12,13].

To decipher the cellular and molecular mechanisms, which enable cells to move within the endothelium, we have focused on the process of anastomosis during the formation of the dorsal longitudinal anastomotic vessel (DLAV) in the zebrafish embryo by high-resolution time-lapse microscopy. This process occurs in a relatively stereotypical manner and involves a convergence movement of endothelial cells, which is illustrated by extensive cell junction elongation[19]. Ultimately, this process alters tube architecture and converts unicellular vessels to multicellular vessels[20]. By in vivo time-lapse imaging of several junctional components and pharmacological interference with F-actin dynamics, we are able to describe a actin-based mechanism, which allows endothelial cells to move along each other while maintaining junctional integrity. In particular, we describe a rearrangement mechanism, which is initiated by junction-based lamellipodia (JBL) leading to the formation of distal, VE-cad based attachment sites, which in turn serve as an anchor point for junction elongation. We propose that the oscillating behavior of JBL, which depends on F-actin polymerization as well as contractility, provides a general mechanism of endothelial cell movement during blood vessel formation and vascular remodeling.

Results

Changes of vessel architecture during blood vessel formation. Blood vessel formation is associated with prominent cell shape changes and cell rearrangements. The DLAV presents a well-defined in vivo model to analyze how a wide repertoire of endothelial cell activities leads to the formation of a new blood vessel, starting with establishment of an interendothelial contact point, followed by the formation of a continuous luminal surface and the transformation from a unicellular to a multicellular tubular architecture. Unicellular and multicellular tubes are easily discerned by junctional patterns, whereas unicellular tubes display isolated rings separated by segments without any junction, multicellular tubes have a continuous network of multiple junctions along their longitudinal axis (Fig. 1a). To gain more insight into this transformation process, we used a reporter line expressing a full-length VE-cadherin fluorescent protein fusion (VE-cad-Venus)[21] (Fig. 1b–e, Supplementary Movie 1) and performed in vivo time-lapse experiments between 27 and 40 h post fertilization (hpf). These experiments showed that most DLAVs were initially unicellular tubes, and that the majority (69%, $n = 26$ (8 embryos)) of DLAV segments were transformed to a multicellular configuration before 40 hpf (Fig. 1b–e, Supplementary Fig. 1a). The transformation from the initial tip cell contact to a multicellular vessel, with a continuous cell–cell junction network, took several hours (median 190 min, segments $n = 14$ (8 embryos), Supplementary Fig.1b), with high variability between individual segments. During this time window, the endothelial cell–cell junctions expanded extensively from initial spot-like structures to elongated junctions covering the entire DLAV segment. However, movement of the junctions was also seen in perfused vessels (Supplementary Fig. 1c). The cellular rearrangements are thus occurring both in nascent non-lumenized vessels and also in inflated, perfused vessels.

The thickness of remodeling junctions is polarized. When we analyzed ring-shaped junctions in the DLAV of VE-cad-Venus embryos in more detail, we observed that the junctions were not uniform in thickness along their circumference in unicellular vessels. In medial regions, the junctions formed significantly thicker, and more diffuse, pattern than on the lateral sides (Fig. 1f, j), coinciding with the general direction of endothelial cell movements during anastomosis. In contrast, we did not observe such junctional polarity in multicellular vessels (Fig. 1j). We confirmed these observations by immunostainings for the junctional proteins VE-cadherin and ZO1, which showed that in the newly formed junctions in unicellular configuration, the medial junctional domains were consistently thicker than the lateral domains (Fig. 1g–i, k). Again, this polarity of junctional thickness was not seen in vessel areas of more mature multicellular architecture (Fig. 1k).

Remodeling junctions form junction-based lamellipodia. To gain insight into the nature of this junctional polarity, we performed live-imaging experiments on Cdh5-Venus expressing transgenic embryos at high temporal resolution. Here, we observed that the polarized junctional thickenings are formed by dynamic lamellipodia-like protrusions (Fig. 2a, b, Supplementary Movie 2). In addition, we used a F-actin visualizing EGFP-UCHD transgenic fish line in a similar setup (Fig. 2c, d, Supplementary Movie 3). Remarkably, F-actin and VE-cadherin, both showed similar oscillatory dynamics with a median duration of 6 min (Fig. 2e). Moreover, the protrusions were oriented along the vessel axis (Fig. 2f), which is consistent with the increased junctional thickness of medial junctional domains.

To test whether this dynamic junctional behavior is restricted to the process of anastomosis or is a more general behavior, we further analyzed the F-actin fluctuations during junctional remodeling in the dorsal aorta. Here, we found that the relative intensity of EGFP-UCHD was increased at the site of forming protrusions (Fig. 3a, b, Supplementary Movie 4), indicating

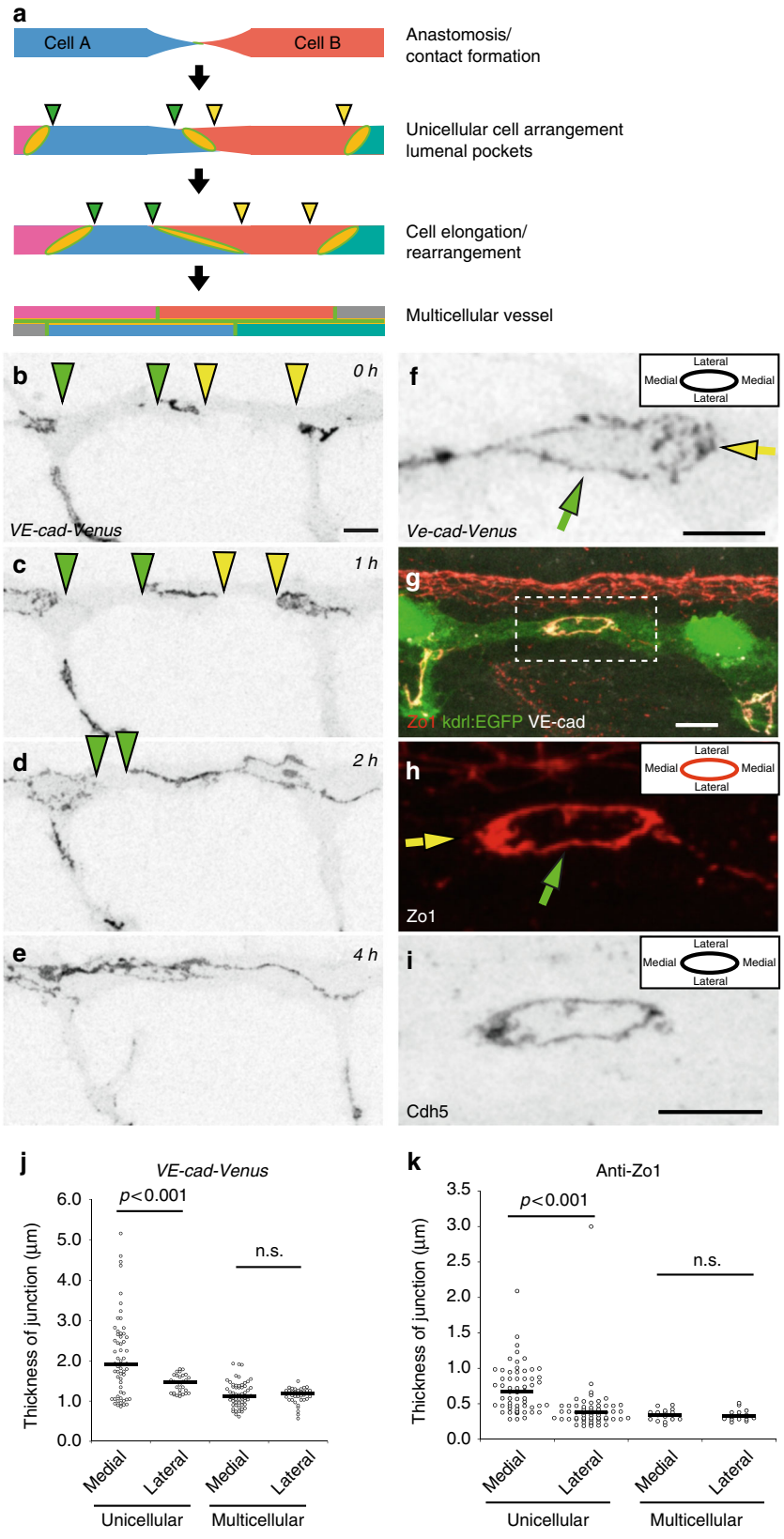

recruitment of additional F-actin. We further analyzed the dynamic behavior of junctional F-actin using kymographs (Fig. 3c, d) and found that the fluctuations in intensity occurred in rather rhythmic patterns, and at the same junctional site, protrusions were generated repeatedly within regular intervals, indicative for oscillations in F-actin intensity in the remodeling junction.

The polarized occurrence and directionality of protrusions along the direction of vessel growth suggests that they are involved in endothelial cell movements. To address this, we

Fig. 1 Polarized thickness in remodeling junctions. **a** Schematic model of cellular rearrangements during formation and maturation of dorsal longitudinal anastomosing vessel (DLAV) in zebrafish. At first, the tip cells (Cell A and B) of two anastomosing endothelial sprouts contact and form a de novo junction. Next, a vessel with unicellular architecture is formed, where junctions are not interconnected but are visible as separate rings. Then, through cellular rearrangement and elongation, the junctions elongate along vessel axis until junctions are interconnected and vessel reaches the final multicellular architecture. The edges of the junctional gaps in the unicellular vessels are marked with green and yellow triangles. **b**–**e** Still pictures of a time-lapse movie (Supplementary Movie 1) showing EC junctions of *Tg*(BAC(*cdh5:cdh5-ts*)) embryo, which expresses VE-cad-Venus fusion protein, during transition from unicellular to multicellular vessel during DLAV formation, in inversed contrast starting around 28 hpf. The edges of the junctional gaps in the unicellular vessels are marked with green and yellow triangles. **f** Close-up image of VE-cad-Venus embryos. The diffuse thickening of medial domain of the junction is marked with a yellow arrow. **g**–**i** Whole-mount immunofluorescence staining of the DLAV using anti-ZO1, anti-VE-cad (rat) of 28–30 hpf (*Tg*(*kdrl:EGFP*^{s843})) embryos. **h** The yellow arrow points to the medial junctional domain and the green arrow to the lateral junctional domain. **j** Quantification of junctional thickness measurements. $n = 44$ unicellular junctions and 48 multicellular junctions from 5 VE-cad-Venus *Tg*(BAC(*cdh5:cdh5-ts*)) embryos. Non-parametric Kruskal–Wallis test was used. **k** Quantification of the junctional thickness measurements from immunostainings of *Tg*(*kdrl:EGFP*^{s843}) embryos. $n = 58$ unicellular junctions and 17 multicellular junctions from 8 embryos. Non-parametric Kruskal–Wallis test was used. Scale bars 10 μm

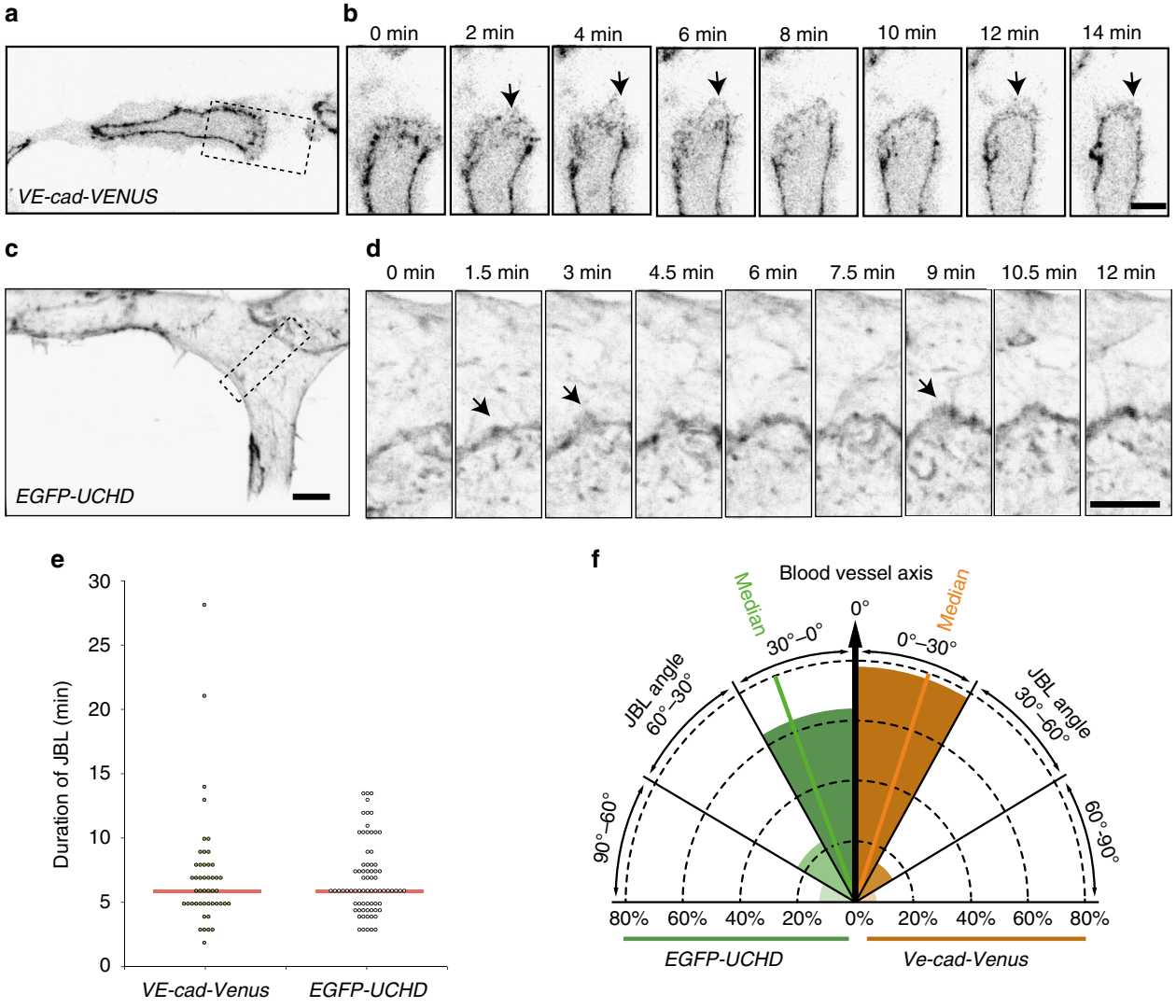

Fig. 2 Active VE-cad and F-actin behavior of junction-based lamellipodia. **a**, **b** Still images from a movie (Supplementary Movie 2) of a VE-cad-Venus expressing embryo *Tg(BAC(cdh5:cdh5-ts))*, showing the DLAV at 30 hpf in inversed contrast. **b** A magnification of the inset in **a**. Arrows point to JBL. **c**, **d** Still images from a movie (Supplementary Movie 3) of a EGFP-UCHD expressing embryo (*Tg(fli:Gal4ff*^{ubs3}, *UAS:EGFP-UCHD*^{ubs18})) showing the DLAV at 30 hpf in inversed contrast. **d** A magnification of the inset in **c**. Arrows point to JBL. **e** Scatter plot of quantitation of the duration of the JBL with the VE-cad-Venus transgene ($n = 48$ in 6 embryos) and EGFP-UCHD movies ($n = 74$ in 6 embryos), red line represents the median. **f** Quantitation of JBL angle in the DLAV in respect to the blood vessel axis (0°) using the EGFP-UCHD transgene ($n = 103$ from 6 embryos) or Cdh5-Venus transgene ($n = 41$ from 5 embryos). Scale bars 5 μm

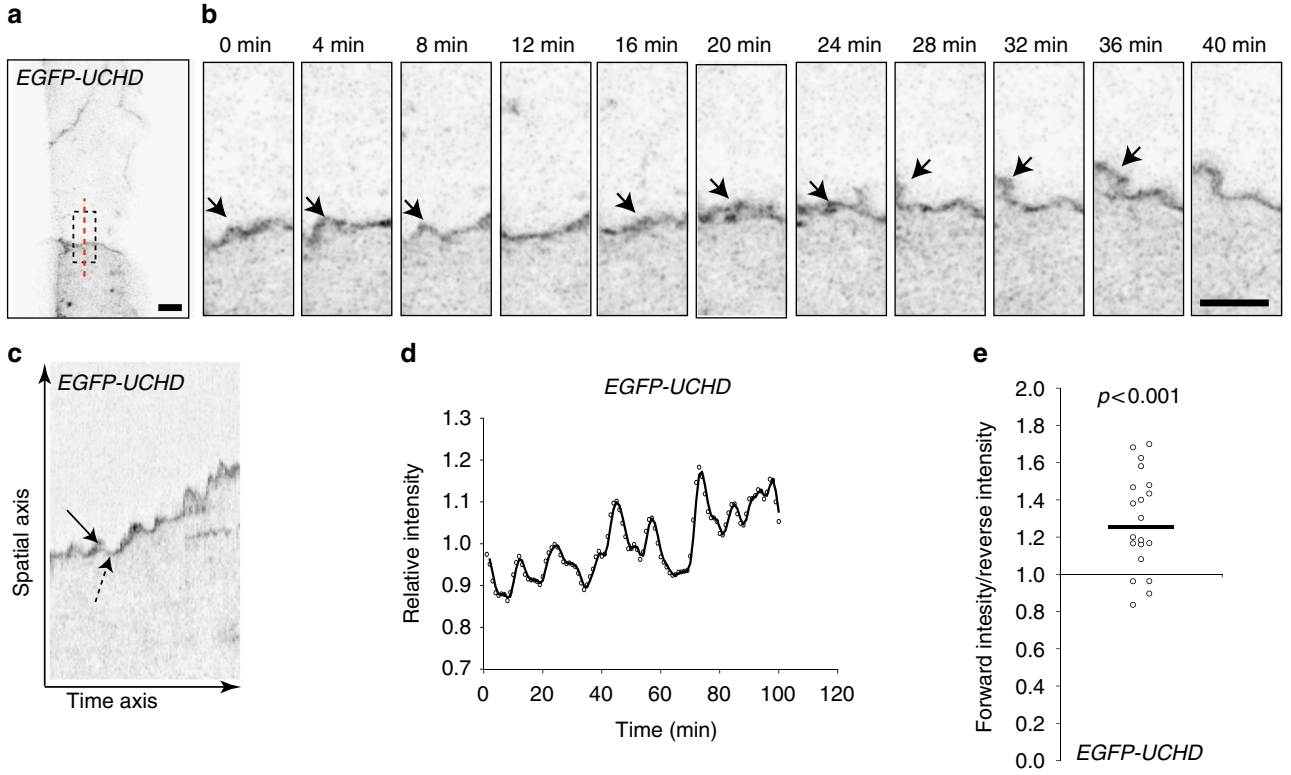

Fig. 3 Oscillatory F-actin dynamics during remodeling of cell–cell junctions. **a**, **b** Still images from a movie (Supplementary Movie 4) showing JBL formation in the dorsal aorta of an EGFP-UCHD expressing 2dpf embryo (*Tg(fli:Gal4ff^{ubs3}; UAS:EGFP-UCHD^{ubs18})*), shown in inversed contrast. **b** A magnification of the inset in **a** and the red dashed line indicates the site for kymograph in **c**. Arrows point to a JBL, seen as a local thickening of the junction. **c** Kymograph across the junction. Solid arrow denotes forward movement and dashed arrow backward movement of the junction. **d** Intensity plotting of a EGFP-UCHD JBL kymograph. **e** Scatter plot of the relative EGFP-UCHD intensity during forward and backward movements ($n = 20$ events, 4 movies). EGFP-UCHD intensity value in a forward movement was divided with intensity value during subsequent reverse movement. Non-parametric one sample Wilcoxon signed rank test was used as statistical test. Scale bars 5 µm

analyzed the potential association between local junctional movements and the occurrence of F-actin protrusions in the dorsal aorta (Fig. 3c, d). Analysis of F-actin intensities showed that higher intensities were associated with local forward movement of junctions than with reverse movement (Fig. 3e).

Taken together, we observe an F-actin-based protrusive endothelial behavior, which occurs during junctional remodeling in vivo. Because of their similarity to 'classical' lamellipodia, their oscillating behavior and structural connection with endothelial cell junctions, we call these protrusions junction-based lamellipodia or JBL.

JBL form at the front end of elongating junctions. Blood vessel anastomosis is driven by the convergence movement of two tip cells and is associated with an elongation of their mutual cell junction. The formation of JBL at the junctional poles suggested that these dynamic structures may generate tractive forces, which contribute to junction elongation. However, cell junctions demarcate the interface between two cells and our above analyses did not differentiate, whether cells form JBL at their respective junctional front or rear ends or both. To analyze the contributions of individual cells to F-actin protrusions, we generated a transgenic zebrafish line expressing a photoconvertible mCLAV-UCHD fusion protein in endothelial cells. For mosaic analysis, we photoconverted mCLAV-UCHD in single SeA sprouts 2–3 h prior to contact initiation between tip cells from neighboring segments and recorded the behavior of the junctional F-actin later during anastomosis and formation of the DLAV (Fig. 4a). In vivo photoconversion resulted in efficient green-to-red conversion (Fig. 4b), allowing the analysis of differentially labeled F-actin pools during DLAV formation (Fig. 4c). Photoconverted and non-converted mCLAV-UCHD-labeled endothelial cell junctions and showed matching patterns within the anastomotic junctional ring—except for the poles of the anastomotic ring where F-actin based protrusions were forming. Here, the colocalization of the two markers was suspended and we found elevated levels of either of the two F-actin pools at the front end of the junction with respect to cell movement (green JBL over red cell, or vice versa, 24 out of 28 events, $p < 0.001$). This oriented localization is consistent with an involvement of JBL in the forward movement of tip cells during anastomotic convergence movements.

F-actin protrusions precede junctional movements. Since the above observations suggest a step-wise mechanism of cell–cell interaction during JBL function, we set out to explore the spatio-temporal relationship between F-actin dynamics and the dynamics of other junctional components. To this end we generated transgenic fish lines expressing red F-actin (mRuby2-UCHD), which allows a direct comparison with other fluorescently labeled junctional components (e.g., EGFP-ZO1 and VE-cad-Venus) (Fig. 5a, b and c, d, respectively; Supplementary movies 5 and 6). Both VE-cad-Venus and EGFP-ZO1 followed the junctional F-actin front (11 and 9 movies analyzed, respectively); however, a different distribution pattern was observed during JBL formation. VE-cadherin localized diffusely at the front, largely overlapping with the F-actin protrusions (Fig. 5b, 60–120 s.). In contrast, EGFP-ZO1 showed a more defined localization and initially remained associated with the junction at the

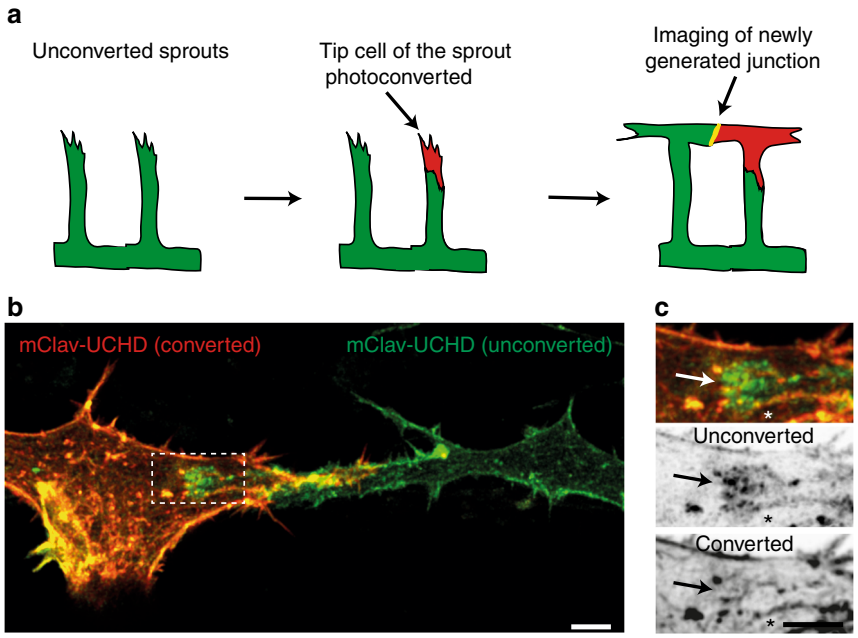

Fig. 4 JBL formation at the distal tip of the junction during DLAV anastomosis. **a** Schematic representation of the mClav2-UCHD photoconversion experiment. **b** Image of photoconverted and unconverted mClav2-UCHD cells in the DLAV of an *Tg(fli:Gal4ff^{ubs3};UAS:mClav2-UCHD^{ubs27})* embryo, at 32 hpf. **c** A close up of the inset in **b**. Arrows point to differentially labeled JBL and asterisk (*) marks the junction outside JBL. Scale bar 5 µm

proximal end of the protrusion (Fig. 5d, 0–36 s.). However, at later time points (Fig. 5d, 72 s.), we observed EGFP-ZO1 accumulation also at the front edge of the JBL, indicating the formation of a new junction at this site (Fig. 5d). To directly differentiate the distribution of VE-cadherin and ZO1, we injected a mCherry-ZO1 encoding plasmid into VE-cad-Venus recipients. The differential localization of both proteins confirmed our previous observations and showed that ZO1 distribution is largely restricted to cell junctions. In contrast, VE-cad was also found within areas outside of these junctions (Fig. 5e, f, Supplementary Movie 7).

Therefore, the respective distribution of ZO1 and VE-cad represent different aspects of JBL formation and illustrates a stepwise mechanism of JBL function. First, F-actin based JBL emanate from EC junctions, which are maintained. The JBL contains diffusely distributed VE-cad. This population of VE-cad precedes formation of the new junction in front of the JBL and may therefore provide adhesive properties for the JBL prior to formation of the new junction. Interestingly, a gradual movement of the old junction towards the new junction was observed in the EGFP-ZO1 movies (Fig. 5d). This indicates that the proximal junction is not resolved in situ, but is actually pulled forward and eventually merges with the distal junction.

F-actin is required for JBL formation and junction elongation. To elucidate the molecular mechanism underlying JBL function during endothelial cell movements, we examined the requirement of F-actin dynamics by pharmacological interference. Latrunculin B and NSC23766 (a Rac1 inhibitor) are potent inhibitors of F-actin polymerization and lamellipodial F-actin remodeling, respectively[22,23]. We used acute treatments to avoid secondary effects and performed live-imaging on rearranging endothelial cell junctions. Inhibition of F-actin polymerization led to pronounced defects in JBL formation. In 5 movies, we observed only 13 JBL, compared to 50 JBL in control embryos (Fig. 6a, b, Supplementary Movies 8 and 9). Moreover, those JBL, which did form in the presence of Latrunculin B, lasted longer, indicating additional defects in lamellipodial dynamics. Inhibition of Rac1 did not interfere as strongly with JBL formation as inhibition of F-actin polymerization. Here, we observed 49 JBL in 10 movies. However, these JBL displayed prolonged duration indicating defects in JBL dynamics (Fig. 6a, b, Supplementary Movie 10).

To test whether interfering with F-actin and JBL dynamics has consequences for endothelial cell rearrangements, we analyzed the effect of Latrunculin B and NSC23766 on junction elongation. Both compounds inhibited the elongation of the junction during DLAV formation (Fig. 6c, d) indicating that proper function of JBL is necessary for junctional elongation during anastomosis.

Although the gross morphology of JBL—based on VE-cad-Venus—looked relatively normal upon Rac1 inhibition, we wondered whether localization of other junctional proteins was affected. During the late phase of JBL oscillation, ZO1 is often localized in two lines outlining the distal (new) and proximal (old) junctions (Fig. 5d). When we compared EGFP-ZO1 distribution in control and NSC23766 treated embryos, we found that distal junctions were forming, showing that Rac1 inhibition did not abrogate de novo junction formation (Fig. 6e). Furthermore, despite the appearance of double junctions, we still did not observe any junction elongation in these instances.

As the above results suggested that Rac1 is primarily involved in the regulation of JBL dynamics rather than their structural properties, we analyzed the dynamics of junctional F-actin intensity oscillations (Supplementary Fig. 3b-d). In control embryos we observed a periodic pattern of JBL dynamics, but in NSC23766-treated embryos the periodicity was reduced (Supplementary Fig. 3e), indicating that junctional F-actin oscillations become less coordinated upon Rac1 inhibition.

VE-cadherin/F-actin interaction is required for JBL function. Next, we wanted to explore the role of VE-cad in JBL function, because several lines of evidence suggested that VE-cad may play

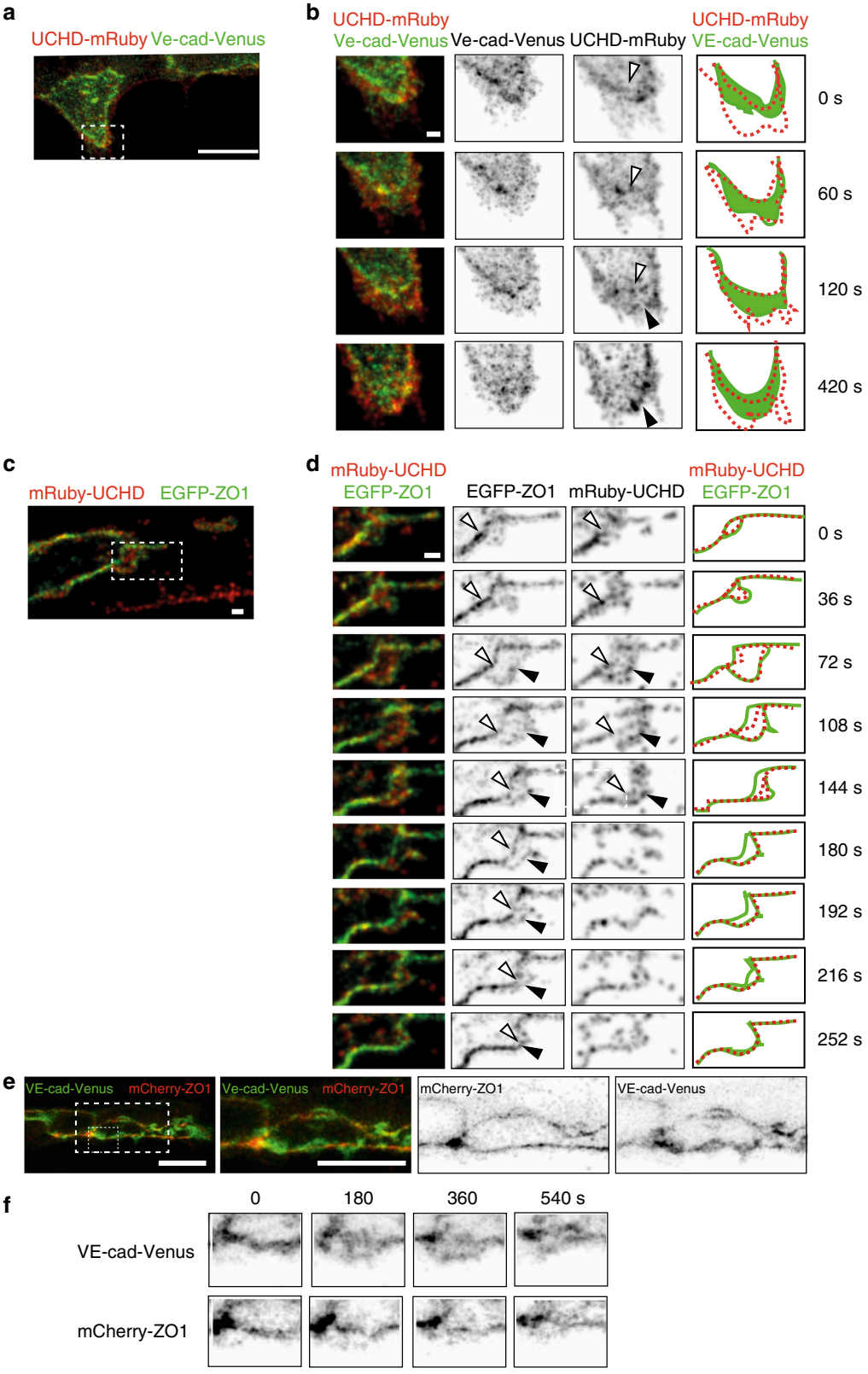

an important role in this process. In ve-cadherin zebrafish null mutants (*ve-cad/cdh5*^{ubs8}), blood vessel architecture is generally disrupted and discontinuous lumens prohibit blood flow[13,24]. These defects are caused by an inability of mutant ECs to perform coordinated cell junction elongation, which is required for multicellular tube formation during angiogenesis. Furthermore, the *ve-cad* mutant defects in junction elongation can be copied by the inhibition of F-actin polymerization[13].

Our finding that VE-cad accumulates in JBL prior to junction formation is consistent with the above observations, and collectively, they indicate a functional interaction between VE-cad and F-acting during junction elongation. To address this

Fig. 5 Distinct dynamics of VE-cadherin, F-actin and ZO1 during JBL formation. **a**, **b** Still images (Supplementary Movie 5) of an embryo showing the DLAV around 32 hpf in an embryo expressing both mRuby2-UCHD and VE-cad-Venus *Tg(fli:Gal4ff^{ubs3};UAS:mRuby2-UCHD^{ubs20};BAC(cdh5:cdh5-Venus))*. **b** A time series magnification of the inset in **a**. Individual channels are shown in inversed contrast. Similar observations were made in 11 movies. Open arrow head points to established junctions and black arrowhead to pioneering junction. **c** and **d**) Still images of an embryo showing DLAV around 32 hpf (Supplementary Movie 5) in an embryo expressing EGFP-ZO1 and mRuby2-UCHD (*Tg(fli:Gal4ff^{ubs3};UAS:mRuby2-UCHD^{ubs20};UAS:EGFP-hZO1^{ubs5})*). Imaged at rate of 12 s/stack. Similar observations were made in 9 movies. Open arrow head points to established junctions and black arrowhead to pioneering junction. **e** Images of endothelial cells in a VE-cad-Venus expressing embryo injected with mCherry-ZO1 encoding plasmid *Tg(BAC(cdh5:cdh5-ts)); fli1ep:mCherry-ZO1))* ($n = 7$ embryos). **f** Close-up from panel **e**. Both channels are shown in inverted contrast. Scale bars 1 µm (**b**–**d**) and 10 µm (**a**, **e**)

possibility, we generated a targeted mutation in *ve-cad* (*cdh5^{ubs25}*), which results in a "tailless" protein, lacking a portion of the cytoplasmic domain of VE-cad including the ß-catenin binding site, essential for VE-cad/F-actin interaction (Supplementary Fig. 4).

Despite the deletion, the VE-cadherin protein correctly localizes in the endothelial cell–cell junctions (Fig. 7h, k and Supplementary Fig. 4e). Homozygous *ve-cad^{ubs25}* mutants are embryonic lethal and display phenotypes similar to those of null mutants, including tip cell/stalk cell dissociation and defective blood circulation (Supplementary Fig. 5a-e)[13]. However, some of the defects are less pronounced and we observed blood flow in the DA and—in rare cases—in the DLAV (Supplementary Fig. 5a, Supplementary Movie 11). This shows that the extracellular domain of VE-cad mediates some inter-endothelial adhesion, which leads to a hypomorphic phenotype.

To assess the requirement for VE-cadherin/F-actin interaction for JBL formation, we first examined whether the junctional rings of VE-cad truncation (*cdh5^{ubs25}*) mutants displayed polarized thickness during anastomosis. Immunofluorescent staining for ZO1 revealed that medial junctions of mutants were narrower compared to heterozygotes, while the thickness of the lateral sides was not affected (Fig. 7a, b). We then tested whether the dynamics of F-actin protrusions were affected in VE-cad truncation (*cdh5^{ubs25}*) mutants. Time-lapse analyses in embryos expressing EGFP-UCHD indicated that F-actin protrusions oscillated more slowly in *cdh5^{ubs25}* mutants compared to wild-types in a manner similar to how protrusions behaved in the presence of the Rac1 inhibitor (Fig. 7c). Furthermore, by measuring the time-intervals between the end and the beginning of a JBL cycle, we found that this "lag phase" is more than doubled (Supplementary Fig. 4f) suggesting that full-length VE-cad is required for the initiation of JBL formation.

To test whether these defects in JBL have consequences for vascular morphogenesis, we examined the junctional architecture of forming SeA. In *cdh5^{ubs25}* mutants, we observed increased interjunctional gaps, which indicate a defect in multicellular tube formation due to a failure in junction elongation (Fig. 7d–l). We also compared relative nuclear movements, which are associated with stalk cell elongation. Consistent with the observed defects in junctional rearrangement, *cdh5^{ubs25}* mutants displayed significantly slower rearrangement of EC cell nuclei compared to wild-types (Fig. 7m, n). Taken together, these findings show that VE-cadherin plays an important role in F-actin dynamics and that the VE-cadherin/F-actin interaction is essential for JBL function, junction elongation and endothelial cell rearrangements in vivo.

Discussion

In this study, we have investigated the mechanisms by which junctional dynamics contribute to endothelial cell movements during blood vessel formation in vivo.

By time-lapse imaging of different structural components of endothelial cell junctions, we observe a dynamic and differential deployment of these proteins during junctional remodeling, which leads to the formation of transient lamellipodia-like protrusions, that we call JBL. Together with our analyses of F-actin dynamics and VE-cad function, our findings suggest a mechanism of cellular and molecular interactions, which allows endothelial cells to use each other as adhesive substrates and for force transmission during cell migration and elongation (Fig. 8). In essence, JBL act by a ratchet-like mechanism, which consists of F-actin-based protrusions and VE-cad based interendothelial cell adhesion. While F-actin protrusions provide the motive force, VE-cad based adhesion serves as an intercellular clutch.

Our time-lapse experiments show that junction elongation is associated with oscillating JBL, which occur at a frequency of about one every 6 min. This oscillatory behavior, their polarized localization at the leading edge of the junction, their role in cell movements together with their dependency on F-actin polymerization as well as Rac1 GTPase activity indicates that these protrusions share a functional basis with "classical" lamellipodia[25]. However, and in contrast with "classical" lamellipodia, the protrusions, which we are describing, emanate from inter-endothelial cell junctions and require VE-cad for adhesion and force transmission.

Here, we describe the role of JBL during angiogenesis in the zebrafish, where they promote endothelial cell elongation and rearrangements. It remains to be seen, whether JBL are unique to endothelial cells or employed more widely during morphogenetic processes of different cell types. Cadherin-based cell interactions have been shown to be essential for dynamic cell movements in several morphogenetic processes (reviewed by refs. [26,27]). In some aspects, the mechanism of JBL function appears to be similar to the one described for border cell migration during *Drosophila* oogenesis[28]. Here, actin-based cell protrusions and E-cadherin interactions between border and nurse cells are thought to be important to form an anchor point at the leading edge of border cells.

Oscillatory junctional protrusions of endothelial cells have also been described in cultured HUVECs[29,30]. Here, so-called junction-associated intermittent lamellipodia (JAIL) form in similar intervals as JBL. However, several characteristic differences suggest that JAIL and JBL represent different cellular activities. As the name indicates, JAIL formation is preceded by the local dissolution of the existing junction, which is thought to trigger the formation of an actin-based protrusion followed by the formation and stabilization of a new junction. In contrast, JBL formation is not associated with the dissolution of an existing junction. This leads to the formation of a characteristic double junction (proximal and distal) at the pole of the junctional ring (Fig. 8). Conceptually, maintenance of cell junctions should be a prerequisite for endothelial cell rearrangements in a perfused vessel in order to maintain the vascular seal and to prevent hemorrhage. We therefore predict that in the in vivo situation (i.e. developmental angiogenesis), JBL may be more prevalent than JAIL.

The distinct temporal and spatial distribution of VE-cad, F-actin and ZO1 during JBL oscillation suggested that these proteins also partake in JBL function. In agreement with this view, interference with VE-cadherin function, as well as F-actin dynamics inhibited JBL dynamics and junction elongation.

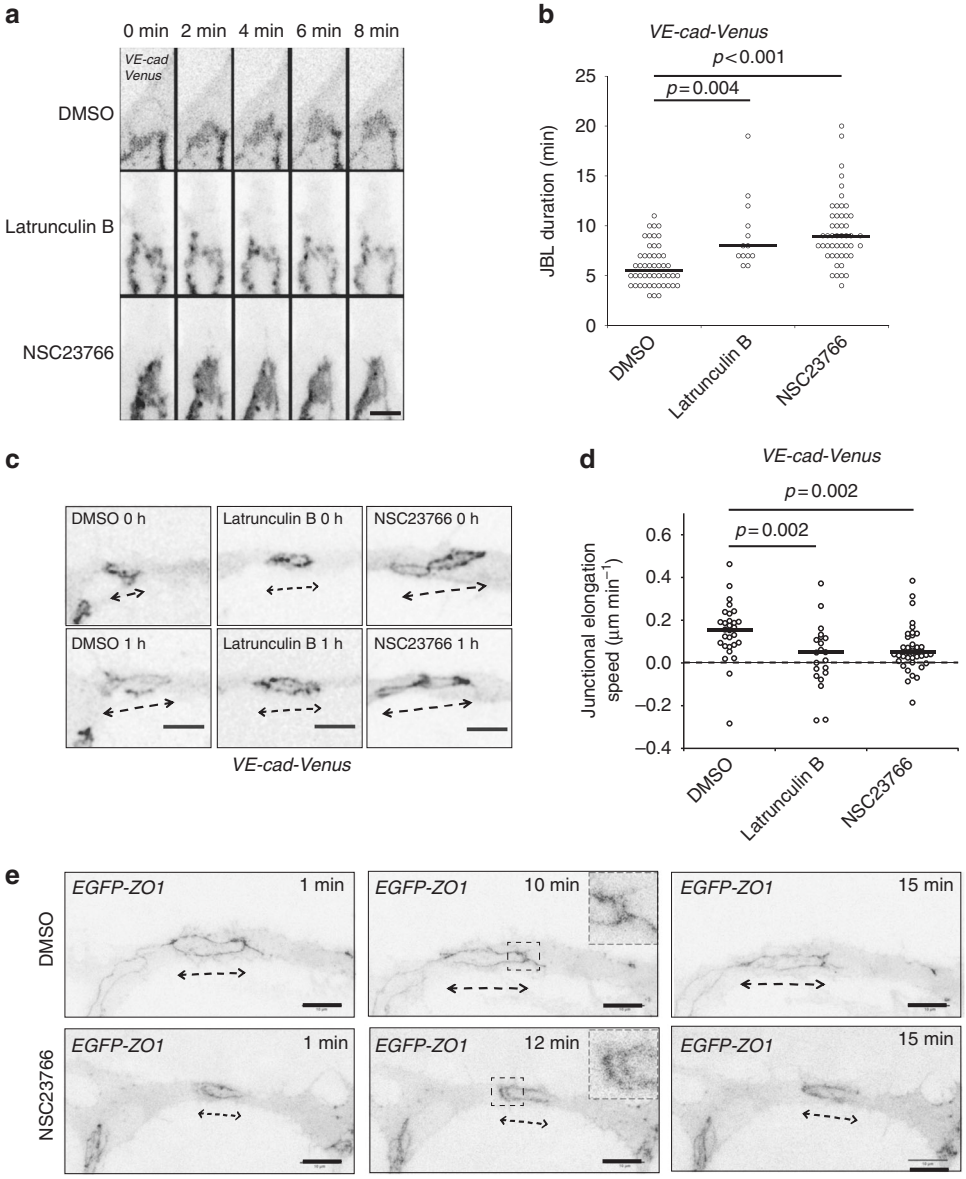

Fig. 6 Junction elongation and JBL formation are functionally linked. **a** Still images from a movie of an VE-cad-Venus expressing embryo *Tg*(BAC(*cdh5:cdh5-ts*)) during anastomosis in the DLAV (around 32 hpf), in the presence of DMSO (1%), Latrunculin B (150 ng ml^{-1}) or NSC23766 (900 µM). **b** Scatter plot quantitation of the duration of the JBL. DMSO, $n = 50$ (6 movies); Latrunculin B, $n = 13$ (5 movies); NSC23766, $n = 49$ (10 movies); black lines show median values. Non-parametric Kruskal–Wallis statistical test was used. **c** Confocal images of a *Tg(BAC(cdh5:cdh5-ts))* embryo during junctional elongation after DLAV anastomosis. Top panels $t = 0$ and bottom panels after 1 h incubation. **d** Quantification of the junctional elongation velocity in the presence of different chemicals using *Tg(BAC(cdh5:cdh5-ts))* embryos. DMSO (1%), $n = 29$ junctions (11 embryos); Latrunculin B (150 ng ml^{-1}), $n = 21$ (6 embryos); NSC23766 (300 µM), $n = 41$ (11 embryos). Dotted line indicated no movement observed, black lines are medians. Non-parametric Kruskal–Wallis statistical test was used. **e** Confocal images of anastomosing DLAV of EGFP-ZO1 embryos (*Tg(fli:Gal4ff^{ubs3};UAS:EGFP-hZO1^{ubs5})*) treated with DMSO or NSC23766. Scale bar 10 µm

Previous studies have emphasized the importance for VE-cadherin in dynamic endothelial cell interactions including cell rearrangements[11,12] and cell elongation[13]. We generated a *ve-cad* mutation, which disrupts VE-cad/F-actin interaction. The phenotype observed in these mutants is slightly milder than in the null mutant suggesting that the mutant protein still allows interendothelial adhesion. Nevertheless, the increase of discontinuous junctions in SeAs illustrates an inability of mutant endothelial cells to generate multicellular tubes, which in turn suggests defects in cell rearrangements. Consistent with this view, *ve-cad^{ubs25}* show reduced spatial distribution of cell nuclei in the SeA. Furthermore, analysis of JBL showed that polarity and oscillatory behavior are disturbed in *ve-cad^{ubs25}* mutants. Taken together, these results show that VE-cadherin actively contributes to morphogenetic cell movements via its interaction with the F-actin cytoskeleton.

The connection between VE-cad and F-actin in JBL function is also supported by F-actin interference experiments. Blocking F-actin polymerization by latrunculin-B effectively inhibits JBL formation and those JBL, which do form, show decreased oscillation. Furthermore, junctional rings do not elongate during this treatment. Inhibition of Rac1 by NSC23766 treatment did not lead to obvious defects in JBL formation, but in a reduction in their oscillation frequency as well as a defect in junction elongation. During NSC23766 treatment JBL looked relatively normal. When using a EGFP-ZO1 reporter, we also observed "double

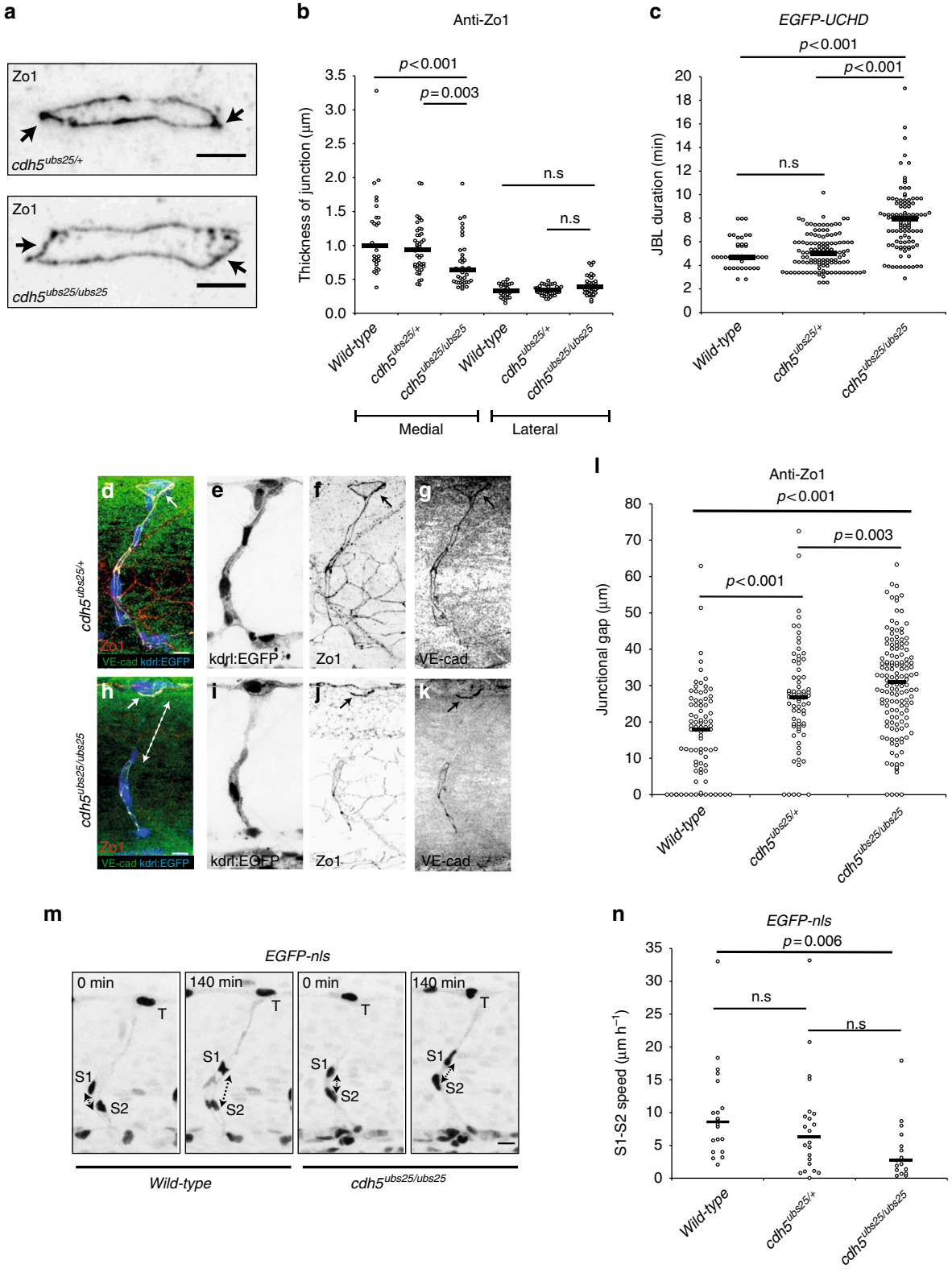

junctions", indicating that JBL are able to form a distal junction and that Rac1 may be required during later stages of JBL function.

A recent study has shown that JAIL formation requires polarized Rac1 at endothelial cell junctions in HUVECs[30]. It is therefore surprising that Rac1 inhibition does not block formation of JBL in zebrafish embryos. It is possible that even at high doses, we do not achieve full Rac1 inhibition in vivo. Alternatively, Rac1 may have a different function in JBL than in JAIL and formation of either protrusion may require different regulators.

Taken together, we have uncovered a hitherto non-described junction-based mechanism of active cell movements, which can be used by endothelial cell (and possibly other cell types) to rearrange and adapt their shape as needed. Inhibition of JBL

Fig. 7 Truncation of Ve-cadherin inhibits both JBL and endothelial cell remodeling. **a** Images of anti-ZO1 immunostained junctions in *cdh5*$^{ubs25/+}$ and *cdh5*$^{ubs25/ubs25}$ embryos. Arrows point to medial site of the junction. **b** Quantitation of the medial and lateral junctional thickness, based on immunostaining for ZO1; *cdh5*$^{ubs25/+}$, $n = 44$ junctions (17 embryos); *cdh5*$^{ubs25/ubs25}$, $n = 40$ (11 embryos); wild-type $n = 28$ (9 embryos). Black lines are medians. Non-parametric Kruskal–Wallis statistical test was used. **c** Quantitation of the duration of JBL based on EGFP-UCHD signal; *cdh5*$^{ubs25/+}$, $n = 122$ (8 embryos), *cdh5*$^{ubs25/ubs25}$ $n = 103$ (8 embryos) and wild-type $n = 43$ (3 embryos). All embryos carry the UAS:EGFP-UCHD transgene *Tg(fli:GFF*^{ubs3}*;UAS:EGFP-UCHD*^{ubs18}). **d**–**l** *Tg(kdrl:EGFP*^{s843}*);cdh5*$^{ubs25/+}$ (**d**–**g**) and *Tg(kdrl:EGFP*^{s843}*);cdh5*$^{ubs25/ubs25}$ (**h**–**k**) embryos stained for VE-cadherin (rabbit antibody, green) and ZO1 (red). Individual channels are shown in inversed contrast. Both wild-type and mutant VE-cad show junctional localization (solid arrow in panels **d**, **f**, **h**, and **j**). The junctional gap in the VE-cadherin staining of a SeA in a mutant embryo (*cdh5*$^{ubs25/ubs25}$) is marked with dashed double arrow in panel **h**. **l** Quantification of the length of junctional gaps in control (*cdh5* $^{ubs25/+}$, $n = 72$ gaps, 23 embryos) and mutant (*cdh5*$^{ubs25/ubs25}$, $n = 139$ gaps, 33 embryos) embryos. Black lines are medians. Non-parametric Mann–Whitney statistical test was used. **m** Still images from a confocal time-lapse of endothelial nuclei (*Tg; kdrl:nlsEGFP*^{ubs1}) in wild-type or *cdh5*$^{ubs25/ubs25}$ embryos during SeA formation. T tip cell, S1 stalk cell 1, S2 stalk cell 2; double-headed arrow indicates the distance of S1 and S2 nuclei. **n** Quantification of movement of stalk cell 1 (S1) nuclei in relation to stalk cell 2 (S2) nuclei during cell rearrangements in SeA; *cdh5*$^{ubs25/+}$, $n = 22$ SeA (4 embryos); *cdh5*$^{ubs25/ubs25}$, $n = 17$ SeA (4 embryos); wild-type $n = 20$ SeA (4 embryos). Black lines are medians. Non-parametric Kruskal–Wallis statistical test was used. Scale bars 5 µm (**a**), 10 µm (**d**, **h**, **m**)

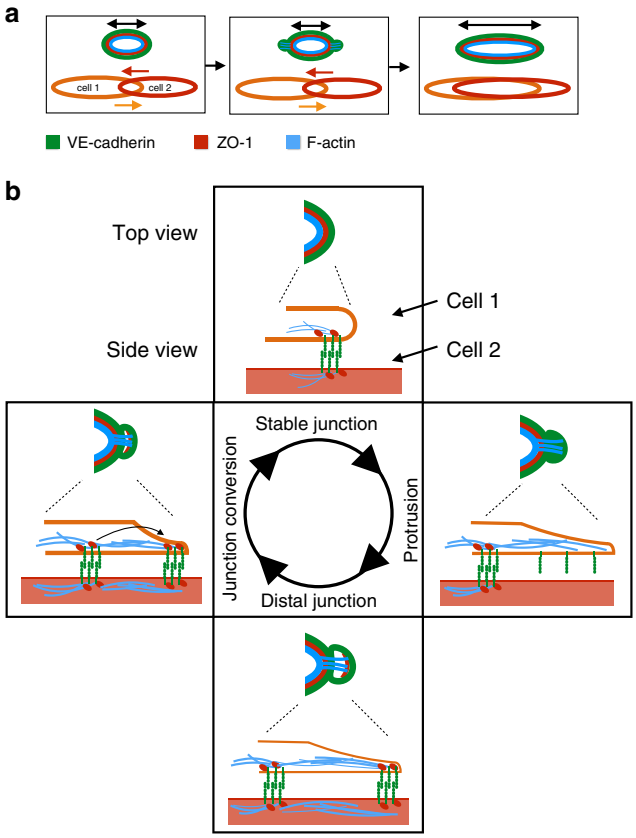

Fig. 8 A Ratchet-like molecular mechanism of junction remodeling. **a** Stepwise elongation of an endothelial cell junction during anastomosis. As two endothelial cells move over each other (bottom), the junction becomes elongated. The three proteins investigated in this study are indicated in different colors. **b** Proposed oscillatory mechanism of JBL function. A single cycle is depicted. F-actin protrusions emanate distally from a stable junction. These protrusions also contain diffuse VE-cadherin, but not ZO1. At the distal end of the protrusion, F-actin, ZO1 and VE-cadherin are components of a newly formed junction with VE-cadherin-mediated contact to the underlying cell. Eventually, dynamic F-actin remodeling pulls the proximal junction towards the new junction

function blocks these processes and results in a failure to form multi-cellular tubes and prevents formation of a patent vasculature. The salient feature of our proposed JBL model is that endothelial cells use each other as migratory substrates via VE-cadherin. Our model suggests that VE-cadherin provides an extracellular clutch, by generating an intercellular adhesion patch, which serves as an anchor for intracellular actomyosin contractions. This cell–cell interaction may be analogous to integrin-ECM-based adhesion patches of classical lamellipodia. Furthermore, these VE-cadherin adhesion complexes give rise to a distal junction with an underlying F-actin arc. Similar F-actin arcs have been described to be essential for the function of lamellipodia during migration of human endothelial cells (HUVECs) in vitro[31]. Future studies will aim to uncover the exact mechanisms of traction force generation and transmission during JBL-driven junction elongation. While F-actin dynamics are essential for junction elongation, we have never observed prominent stress fibers in this process, suggesting that F-actin-based traction forces are acting locally rather than over the longitudinal extent of the endothelial cells.

Although we have focused our studies on JBL formation and function in the process of blood vessel anastomosis, we observed JBL also within larger caliber vessels such as the dorsal aorta at stages, when endothelial cells are extensively rearranging and undergoing cell shape changes[21]. Our studies therefore indicate that endothelial cells employ JBL as a general means for rearrangements and shape changes during blood vessel assembly and vascular remodeling. Using interendothelial adhesion for force transmission allows dynamic endothelial activities while maintaining the vascular seal. We therefore envision that JBL may underlie many morphogenetic endothelial cell behaviors during blood vessel expansion, normalization, regression and endothelial shear stress response. Remodeling and reorganization of adherens junctions is essential for developmental morphogenesis[32,33]. Whether similar JBL occur also in different tissues, besides vasculature and endothelial cells, remains to be elucidated.

Methods

Fish strains and maintenance. Maintenance of fish and experimental procedures involving zebrafish embryos were carried out at the Biozentrum/Universität Basel according to Swiss national guidelines of animal experimentation (TSchV). Zebrafish lines were generated and maintained under licenses 1014H and 1014G1 issued by the Veterinäramt-Basel-Stadt. Fish strains carrying following transgenes and mutations were used in this study: *kdrl:EGFP*^{s843} [34], *VE-cad-Venus* (*BAC(cdh5-cdh5-TS)*, *fli:GFF*^{ubs3} [19], *UAS:EGFP-hZO1*^{ubs5} [19], *UAS:EGFP-UCHD*^{ubs18} [13], *UAS:mRuby2-UCHD*^{ubs20} (this study), *UAS:mCLAV2-UCHD*^{ubs27} (this study), *UAS:mRFP*[35], *cdh5*^{ubs25} (this study), and *Tg(kdrl:EGFPnls)*^{ubs1} [36]. The fish were maintained using standard procedures and embryos obtained via natural spawning[37].

Generation of transgenic fish lines. The EGFP sequence of pT24xnrUAS:EGFP-UCHD was replaced by the sequence of mRuby2 (amplified from pcDNA3-mRuby2 was a gift from Michael Lin; Addgene plasmid #40260)[38] or by the sequence of mClav2 (amplified from pmClavGR2-NT; Allele Biotechnology) to generate the final plasmids pT24xnrUAS:mRuby2-UCHD and pT24xnrUAS:mClav2-UCHD respectively. These final plasmids were injected individually, together with *tol2* RNA into Tg(*fli1:Gal4ff*)^{ubs3} embryos and that were raised to adulthood and eventually stable transgenic fish lines *Tg(UAS:mRuby2-UCHD)*^{ubs20} *and Tg(UAS:mClav2-UCHD)*^{ubs27} were isolated and maintained.

Transient expression of mCherry-ZO1 in zebrafish embryos. To transiently express mCherry-ZO1 in endothelial cells of zebrafish embryo, ~50 pg of plasmid *fli1ep:mCherry-ZO1*[39] was injected together with Tol2-transposase mRNA into 1–4 cell stage embryos (Tg(*BAC*(*cdh5:cdh5-ts*))). Twenty-four hours after injection healthy embryos expressing mCherry were selected, mounted in low-melting point agarose and imaged using Leica SP5 confocal microscope.

Generation of ve-cadherin mutants. The ve-cadherin truncation allele (*cdh5*^{ubs25}) was generated using CRISPR/CAS technology[40]. We sequenced exon 12 of *cdh5* (encoding the cytoplasmic domain) of ABC, Tubingen (TU) and tupfel;long-fin (TL) strains and found a potential target sequence in ABC (5′-GGGACCTGCA CTCTATGCCATGG-3′). Target guide RNA and Cas9 protein were synthetized by standard procedures[40] and co-injected into ABC/TU embryos. Offspring of G0 fish containing germline mutations were screened by PCR analysis for the loss of a *NcoI* restriction site, which is present on the wild-type allele. For subsequent genotyping, multiplex PCR was performed using allele-specific primers:

VE-cad-fwd: 5′-GAAACCCATATCAAACAGACCTGC-3′,
VE-cad-rev: 5′-CAGAGCCGTCTACTCCATAAAGC-3′,
VE-cad-ubs25-fwd: 5′-GACCTGCACTCTATGGAA-3′,
VE-cad-wild-type-rev: 5′-GCAGGAGGTTTCTTTACC-3′.

The genotyping protocol of *cdh5*^{ubs8} has been described earlier[13]. Following primers were used:

cdh5-FWD: 5′-TTGGTGTAACTGACAATGGGG-3′
cdh5-REV: 5′-ACAGTCTTGGTGTTACCATTGGG-3′
cdh5-WT-FWD: 5′-ATCCCCGTTTTCGATTCTGAC-3′
cdh5-ubs8-REV: 5′-CTGATGGATCCAGATTGGAATC-3′

Live imaging of zebrafish embryos. Embryos were anesthesized using Tricaine (MS-222, 160 mg l^{-1}, #E10521 Sigma-Aldrich) and embedded in 0.7% low-melting point agarose (Sigma-Aldrich) supplemented with Tricaine in glass-bottom dish. After the agarose solidified, it was overlaid with E3-medium supplemented with Tricaine. All the imaging was performed at 28.5 °C. The imaging was performed using Leica SP5 Matrix confocal microscope equipped with resonance scanner using ×63 NA 1.2 or ×40 NA 1.1 water immersion objectives. For imaging of JBL, the time points were 60–120 s intervals and in case of double-color imaging, 12–60 s.

For the pharmacological experiments, the treatment of embryos with inhibitors (DMSO 1%, Latrunculin B (150 ng ml^{-1}), NSC23766 (300–900 µM)) begun 1 h prior to embedding into low-melting point-agarose and confocal imaging. The inhibitors were present throughout the whole experiment.

Generation of polyclonal rat anti-zf-VE-CAD antibodies. A cDNA fragment encoding a polypeptide comprising the extracellular domain of zebrafish VE-cad (Ala22 to Lys464) was expressed in *E. coli* using the T7 expression system. The protein was purified on Ni-charged IMAC resin (BioRad) under denaturing conditions. Antiserum was raised in rats by ThermoFisher Scientific using standard immunization procedures.

Immunofluorescence analysis. Embryos were fixed with 2% paraformaldehyde (Electron Microscopy Sciences) in PBST (PBS + 0.1% Tween-20) at room temperature for 90 min, and immunostained using following protocol: Fixation with 2% PFA/PBST (PBS + 0.1% Tween-20) for 90 min at room temperature followed by washes with PBST. After permeabilization (PBST + 0.5% Triton X-100, 30 min), the samples were blocked (PBST + 0.1% Triton X100 + 10% normal goat serum + 1%BSA + 0.01% Sodium Azide, overnight, 4 °C). Subsequently, primary antibodies were added (diluted in Pierce Immunostain enhancer, #46644, Thermofisher Scientific) and incubated overnight at 4 °C. After several washes with PBST at room temperature, the secondary antibodies were added (1:2000 dilution in Pierce staining Enhancer) and incubated overnight at 4 °C. After several washes with PBST at room temperature, the embryos were mounted onto glass-bottom dishes using low-melting point agarose.

Mouse anti-hZO1 (dilution 1:400, Invitrogen #33–9100; use in zebrafish in ref. [36], rat anti-VE-cad (dilution 1:500) and rabbit anti-VE-cad (dilution 1:500) primary antibodies were used. Rat anti-VE-cad was validated by immunofluorescence by using *ve-cad* null mutant (*cdh5*^{ubs8}, *Tg(kdlr:EGFP*^{s843})) embryos[13] as control for specificity (Supplementary Fig. 2). Rabbit anti-VE-cad has been described and validated previously[36] and also validated with *ve-cad* null mutants[13]. Fluorescent secondary antibodies Alexa-568 goat anti-mouse IgG, Alexa-633 goat anti-rat IgG, and Alexa-633 goat anti-rabbit IgG (all from Invitrogen) were used.

Photoconversion experiment. Twenty-four hours post fertilization zebrafish embryos (*Tg(Fli:GFF*^{ubs3}*;UAS:mClav2-UCHD*^{ubs27}) were embedded in 0.7% low-melting point agarose onto 35 mm glass bottom dishes. Tip cells of vascular sprouts of segmental arteries were photoconverted on a Leica SP5 confocal microscope using a ×40 NA 1.1 water immersion objective. Photoconversion was performed with a 405 nm laser (20% power) until no further increase in converted UCHD-mClav2 signal was observed (conversion time 10–30 s). After this the embryos were allowed to develop for ~4 h before imaging of anastomosis events in DLAV.

Junction elongation experiment. Junctional elongation was analyzed by observing anastomosis and elongation of isolated junctional rings during DLAV formation. Inhibitor treatments Latrunculin B (150 ng ml^{-1}), NSC23766 (300–900 µM) or DMSO (1%) were applied 1 h before mounting of embryos into 0.7% low-melting point agarose and imaging the junctions for 1–2 h on a Leica SP5 (×40 NA 1.1 water immersion objective).

Cell rearrangement experiment. Embryos carrying nuclear GFP (Tg(*kdrl:EGFPnls*^{ubs1})) were used. Confocal Z-stacks were obtained as described above in 12–14 min intervals. To control small variations in the developmental phases of the individual SeA, $t = 0$ min was the time point when tip cell had reached the dorsal side and started to sprout in anteroposterior directions. The endpoint for analysis was 10 time points later ($t = 10$; 120–140 min). At $t = 0$ and $t = 10$ the distance (d) of stalk cell S1 and S2 was measured using FIJI. Speed of movement of S1 and S2 in relative to each other was calculated using equation:

$$\text{speed} = \frac{|d_{t0} - d_{t10}|}{\Delta t} \quad (1)$$

Image analysis and preparation. Image analysis and measurements were performed using FIJI. Deconvolution was performed using Huygens Remote Manager software[41]. Maximum Z-projections were used. Noise was reduced using Gaussian filtering (radius 1.0) and background subtracted (rolling ball radius 50) using FIJI. Contrast and brightness of images were linearly adjusted. Kymographs were generated from the sum Z-projections of time-lapse series using FIJI. Perpendicular straight line across the junction was drawn and kymograph generated using reslice tool. Colocalization analysis was performed using FIJI. First, background was subtracted (rolling ball radius 25), regions of interests (ROIs) of separate cell–cell junctions were selected and then colocalization analysis was done on these ROIs using Colocalization Test plugin with Fay image randomization ((written by Tony Collins, McMaster University, Hamilton, Canada). Publication figures were prepared using FIJI, OMERO Fig. and Adobe Illustrator.

Statistical analyses. Statistical analyses were performed using Microsoft Excel, IBM SPSS statistics 22 and GraphPad Prism version 6.05 for Windows software. Non-parametric two-sided Kruskal–Wallis *H*-test, Mann–Whitney *U*-test and binomial probability (photoconversion experiments, test probability 0.5) were used. The data reasonably met the assumptions of the tests. In Fig. 1e, f, where the data was non-normal and heteroscedastic similar *p*-values were obtained with Kruskal–Wallis *H*-test, Welch's *t*-test and median test.

No statistical power analysis was used to determine samples size. Systematic randomization was not used. Experiments with cdh5^{ubs25} (Fig. 7) were performed essentially blinded as the genotype was determined after data capture and analysis. In all other experiments blinding was not used. Samples of low technical quality were excluded from the subsequent analyses. In all figures (exception Fig. 2f and Supplementary Fig. 3d) the individual data points are plotted and median indicated with horizontal line as has been recommended[42]. In Fig. 2f, Supplementary Fig. 1a and c, the data are binned and the number of events in the given bin is plotted.

To formally analyze periodicity of F-actin intensity fluctuations, we calculated the autocorrelation function (ACF) using IBM SPSS statistics 22 software. Next, we analyzed the level of noise in the fluctuations (phase diffusion) that gradually reduces the oscillation of the ACF. To quantify this effect, we fitted each of the ACFs using a sinusoidal function enveloped by an exponential decay using Igor Pro 6.37 (WaveMetrics Inc, Lake Oswego, OR, USA). The function used was:

$$\text{ACF}(t) = \text{A} \times \sin(f \times t + \theta) \times e^{\left(\frac{-t}{\tau}\right)} \quad (2)$$

where t is the lagtime of the ACF, A is amplitude, f the frequency, θ is the phase, and τ is the characteristic lifetime of the decay.

Data availability

The data that support the findings of this study are available from the corresponding authors upon reasonable request.

Received: 7 April 2017 Accepted: 26 July 2018
Published online: 31 August 2018

References

1. Carmeliet, P. Angiogenesis in health and disease. *Nat. Med.* **9**, 653–660 (2003).
2. Potente, M., Gerhardt, H. & Carmeliet, P. Basic and therapeutic aspects of angiogenesis. *Cell* **146**, 873–887 (2011).
3. Betz, C., Lenard, A., Belting, H.-G. & Affolter, M. Cell behaviors and dynamics during angiogenesis. *Development* **143**, 2249–2260 (2016).

4. Schuermann, A., Helker, C. S. M. & Herzog, W. Angiogenesis in zebrafish. *Semin. Cell. Dev. Biol.* **31**, 106–114 (2014).
5. Wacker, A. & Gerhardt, H. Endothelial development taking shape. *Curr. Opin. Cell Biol.* **23**, 676–685 (2011).
6. Christ, B., Poelmann, R. E., Mentink, M. M. & Gittenberger-de Groot, A. C. Vascular endothelial cells migrate centripetally within embryonic arteries. *Anat. Embryol.* **181**, 333–339 (1990).
7. Sato, Y. et al. Dynamic analysis of vascular morphogenesis using transgenic quail embryos. *PLoS ONE* **5**, e12674 (2010).
8. Lamalice, L., Le Boeuf, F. & Huot, J. Endothelial cell migration during angiogenesis. *Circ. Res.* **100**, 782–794 (2007).
9. Michaelis, U. R. Mechanisms of endothelial cell migration. *Cell. Mol. Life Sci.* **71**, 4131–4148 (2014).
10. Jakobsson, L. et al. Endothelial cells dynamically compete for the tip cell position during angiogenic sprouting. *Nature* **12**, 943–953 (2010).
11. Bentley, K. et al. The role of differential VE-cadherin dynamics in cell rearrangement during angiogenesis. *Nature* **16**, 309–321 (2014).
12. Perryn, E. D., Czirók, A. & Little, C. D. Vascular sprout formation entails tissue deformations and VE-cadherin-dependent cell-autonomous motility. *Dev. Biol.* **313**, 545–555 (2008).
13. Sauteur, L. et al. Cdh5/VE-cadherin promotes endothelial cell interface elongation via cortical actin polymerization during angiogenic sprouting. *Cell Rep.* **9**, 504–513 (2014).
14. Xu, C. et al. Arteries are formed by vein-derived endothelial tip cells. *Nat. Commun.* **5**, 5758 (2014).
15. Franco, C. A. et al. Dynamic endothelial cell rearrangements drive developmental vessel regression. *PLoS Biol.* **13**, e1002125 (2015).
16. Dejana, E., Tournier-Lasserve, E. & Weinstein, B. M. The control of vascular integrity by endothelial cell junctions: molecular basis and pathological implications. *Dev. Cell* **16**, 209–221 (2009).
17. Harris, T. J. C. & Tepass, U. Adherens junctions: from molecules to morphogenesis. *Nat. Rev. Mol. Cell Biol.* **11**, 502–514 (2010).
18. Lagendijk, A. K. & Hogan, B. M. VE-cadherin in vascular development: a coordinator of cell signaling and tissue morphogenesis. *Curr. Top. Dev. Biol.* **112**, 325–352 (2015).
19. Herwig, L. et al. Distinct cellular mechanisms of blood vessel fusion in the zebrafish embryo. *Curr. Biol.* **21**, 1942–1948 (2011).
20. Lenard, A. et al. In vivo analysis reveals a highly stereotypic morphogenetic pathway of vascular anastomosis. *Dev. Cell* **25**, 492–506 (2013).
21. Lagendijk, A. K. et al. Live imaging molecular changes in junctional tension upon VE-cadherin in zebrafish. *Nat. Commun.* **8**, 1402 (2017).
22. Coué, M., Brenner, S. L., Spector, I. & Korn, E. D. Inhibition of actin polymerization by latrunculin A. *FEBS Lett.* **213**, 316–318 (1987).
23. Gao, Y., Dickerson, J. B., Guo, F., Zheng, J. & Zheng, Y. Rational design and characterization of a Rac GTPase-specific small molecule inhibitor. *Proc. Natl Acad. Sci. USA* **101**, 7618–7623 (2004).
24. Sauteur, L., Affolter, M. & Belting, H.-G. Distinct and redundant functions of Esama and VE-cadherin during vascular morphogenesis. *Development* **144**, 1554–1565 (2017).
25. Ridley, A. J., Paterson, H. F., Johnston, C. L., Diekmann, D. & Hall, A. The small GTP-binding protein rac regulates growth factor-induced membrane ruffling. *Cell* **70**, 401–410 (1992).
26. Friedl, P. & Mayor, R. Tuning collective cell migration by cell–cell junction regulation. *Cold Spring Harb. Perspect. Biol.* **9**, a029199 (2017).
27. Mayor, R. & Etienne-Manneville, S. The front and rear of collective cell migration. *Nat. Rev. Mol. Cell Biol.* **17**, 97–109 (2016).
28. Cai, D. et al. Mechanical feedback through E-cadherin promotes direction sensing during collective cell migration. *Cell* **157**, 1146–1159 (2014).
29. Abu Taha, A., Taha, M., Seebach, J. & Schnittler, H.-J. ARP2/3-mediated junction-associated lamellipodia control VE-cadherin-based cell junction dynamics and maintain monolayer integrity. *Mol. Biol. Cell.* **25**, 245–256 (2014).
30. Cao, J. et al. Polarized actin and VE-cadherin dynamics regulate junctional remodelling and cell migration during sprouting angiogenesis. *Nat. Commun.* **8**, 2210 (2017).
31. Burnette, D. T. et al. A role for actin arcs in the leading-edge advance of migrating cells. *Nature* **13**, 371–381 (2011).
32. Nishimura, T. & Takeichi, M. Remodeling of the adherens junctions during morphogenesis. *Curr. Top. Dev. Biol.* **89**, 33–54 (2009).
33. Takeichi, M. Dynamic contacts: rearranging adherens junctions to drive epithelial remodelling. *Nat. Rev. Mol. Cell Biol.* **15**, 397–410 (2014).
34. Jin, S.-W., Beis, D., Mitchell, T., Chen, J.-N. & Stainier, D. Y. R. Cellular and molecular analyses of vascular tube and lumen formation in zebrafish. *Development* **132**, 5199–5209 (2005).
35. Asakawa, K. et al. Genetic dissection of neural circuits by Tol2 transposon-mediated Gal4 gene and enhancer trapping in zebrafish. *Proc. Natl Acad. Sci. USA* **105**, 1255–1260 (2008).
36. Blum, Y. et al. Complex cell rearrangements during intersegmental vessel sprouting and vessel fusion in the zebrafish embryo. *Dev. Biol.* **316**, 312–322 (2008).
37. Westerfield, M. *The Zebrafish Book: A Guide for the Laboratory Use of Zebrafish Danio rerio* (University of Oregon Press, Eugene, 2000).
38. Lam, A. J. et al. Improving FRET dynamic range with bright green and red fluorescent proteins. *Nat. Methods* **9**, 1005–1012 (2012).
39. Phng, L.-K., Stanchi, F. & Gerhardt, H. Filopodia are dispensable for endothelial tip cell guidance. *Development* **140**, 4031–4040 (2013).
40. Gagnon, J. A. et al. Efficient mutagenesis by Cas9 protein-mediated oligonucleotide insertion and large-scale assessment of single-guide RNAs. *PLoS ONE* **9**, e98186 (2014).
41. Ponti, A., Schwarb, P., Gulati, A. & Bäcker, V. Huygens remote manager: a web interface for high-volume batch deconvolution. *Imaging Microsc.* **9**, 57–58 (2007).
42. Weissgerber, T. L., Milic, N. M., Winham, S. J. & Garovic, V. D. Beyond bar and line graphs: time for a new data presentation paradigm. *PLoS Biol.* **13**, e1002128 (2015).

Acknowledgements

We thank Kumuthini Kulendra for fish care and the Imaging Core Facility of the Biozentrum (University of Basel) for microscopy support. We thank Johanna Ivaska for support and acknowledge Zebrafish Core Facility (Turku Centre for Biotechnology, University of Turku and Åbo Akademi University). This work has been supported by the Kantons Basel-Stadt and Basel-Land and by a grant from the Swiss National Science Foundation to M.A. I.P. was supported by a post-doctoral fellowship from the Finnish Cultural Foundation and Foundations' Post-Doc Pool. M.L., C.W., and L.S. were supported by a Fellowship of Excellence, Biozentrum, University of Basel.

Author contributions

H.G.B., I.P., and M.A. conceived the idea and directed the work. I.P. and H.G.B. designed the experiments. I.P., L.S., M.L., C.W., and D.H. performed experiments. D.B., A.K.L., and B.M.H. provided unpublished reagents. C.G. helped with data analysis. I.P. and H.G.B. wrote the manuscript. All authors reviewed the manuscript.

Additional information

Supplementary Information accompanies this paper at https://doi.org/10.1038/s41467-018-05851-9.

Competing interests: The authors declare no competing interests.

Reprints and permission information is available online at http://npg.nature.com/reprintsandpermissions/

Publisher's note: Springer Nature remains neutral with regard to jurisdictional claims in published maps and institutional affiliations.

Supplementary Information

Paatero et al. “Junction-based lamellipodia drive endothelial cell rearrangements in vivo via a VE-cadherin-F-actin based oscillatory cell-cell interactions”

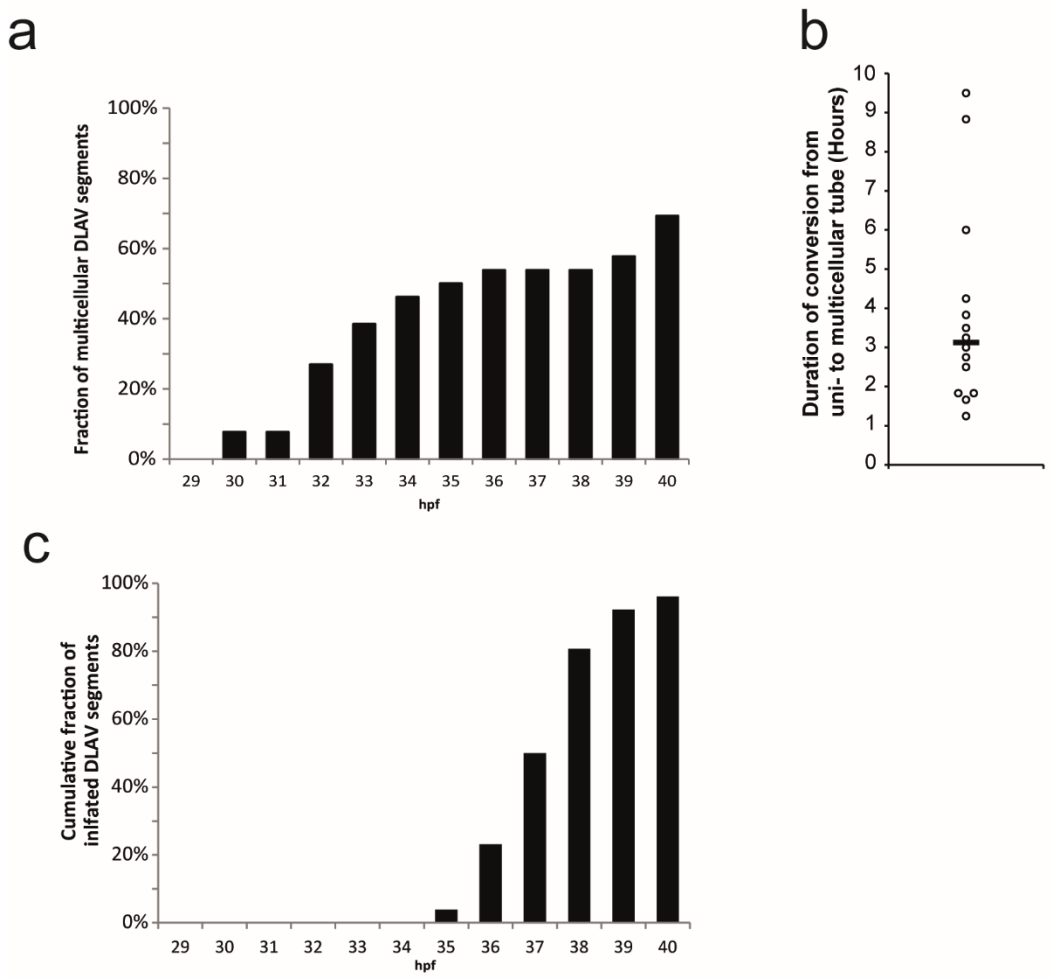

Supplementary Figure 1. *Description of the transition of dorsal longitudinal anastomosing vessel (DLAV) from unicellular to multicellular architecture.*

a) Quantification of the fraction of multicellular DLAV segments using Tg(BAC(*cdh5:cdh5-ts*)) embryos during development. n=26 DLAV segments (8 embryos). b) Quantification of the duration from anastomosis until final conversion into a multicellular tube. Black line is median. n=14 segments (8 embryos). c) Quantification of DLAV segments carrying blood flow during development. n=26 segments (8 embryos). hpf, hours post-fertilization.

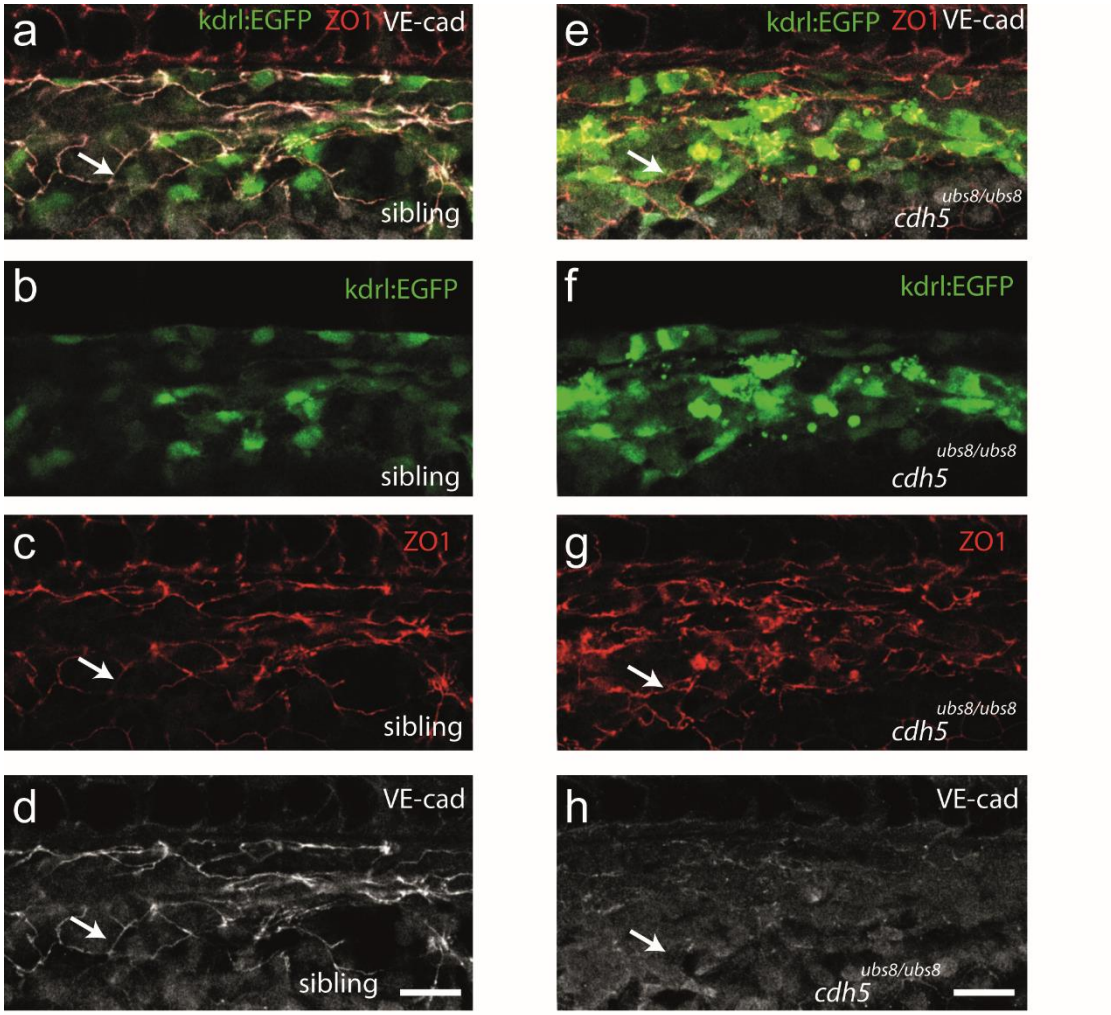

Supplementary Figure 2. *Validation of the rat Ve-cadherin antibody in zebrafish embryo whole-mount immunofluorescence analysis.*

a-h) Confocal images of a Tg(*kdrl:EGFP*^{s843}) wild-type sibling (a-d) or a VE-cad null mutant embryo (Tg(*kdrl:EGFP*^{s843});*cdh5*$^{ubs8/ubs8}$) (e-h), stained for VE-cadherin (rat anti-Cdh5) and ZO1. a and e shows the merged channels, b-d and e-h the individual channels. Arrow points to an endothelial cell-cell junction. Scale bar 20 µm.

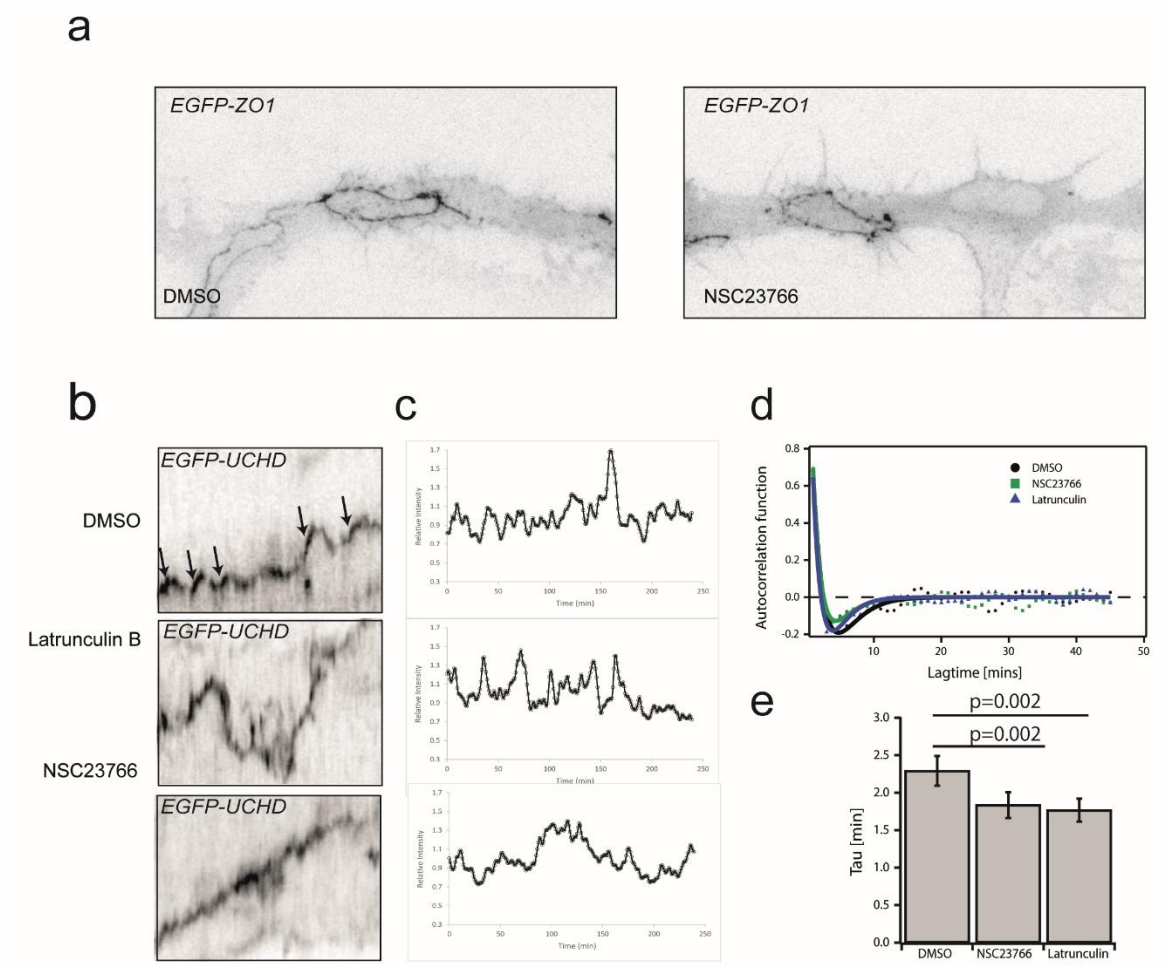

Supplementary Figure 3. *Analysis of F-actin oscillations of the remodeling junctions.*

a) Kymograph across the junction in dorsal aorta in EGFP-UCHD fish (data generated as in Fig. 3). Solid arrow denotes forward movement. b) Intensity plotting of EGFP-UCHD kymographs. c) Averaged autocorrelation functions of EGFP-UCHD intensity. DMSO, n=14 kymographs; Latrunculin B, n=16 kymographs; NSC23766, n=16 kymographs. d) Comparison of autocorrelation lifetime (tau parameter). Means and standard deviations are plotted. ANOVA and Dunnet´s post-hoc test was used.

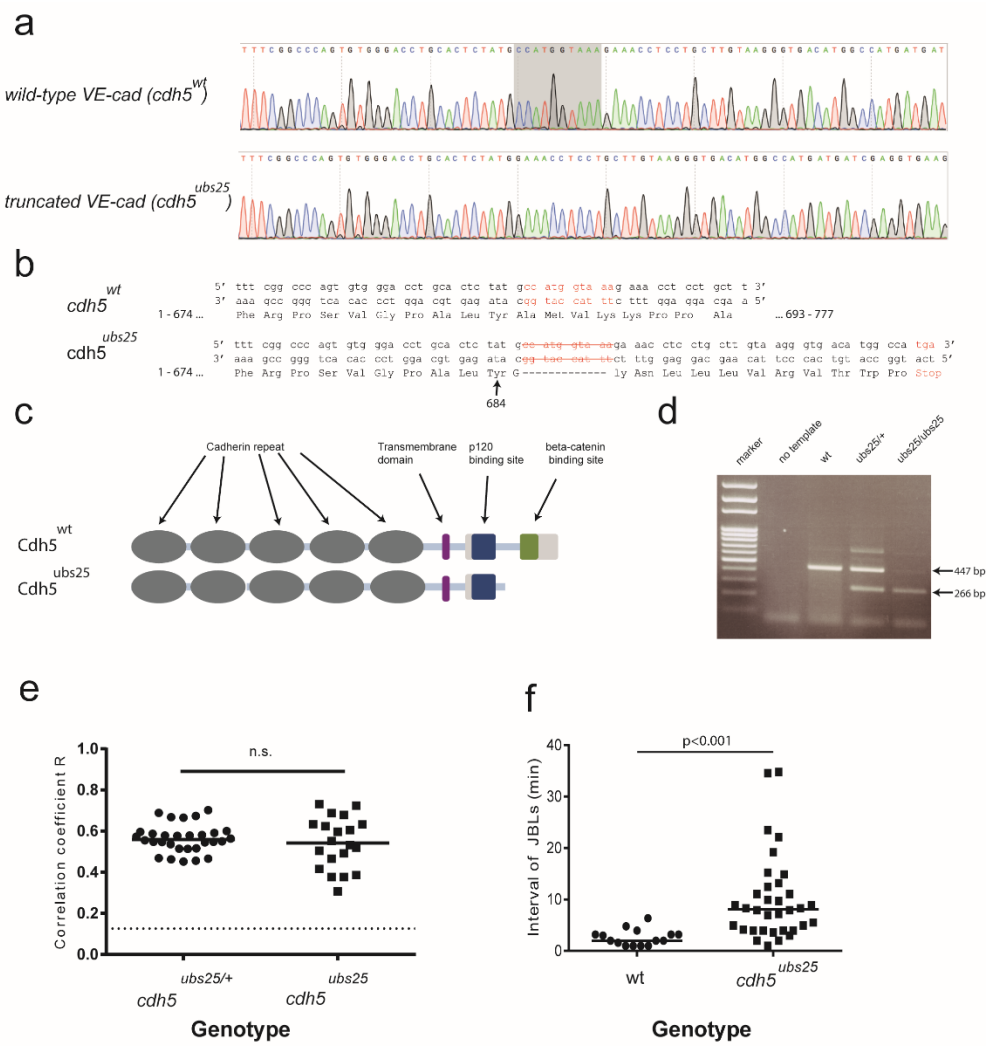

Supplementary Figure 4. *Generation and validation of VE-cad truncation mutant allele.*

a) Sequencing chromatogram of wild-type *ve-cadherin* (encoded by *cdh5* gene*)* sequence (exon 12) and respective truncation mutant *cdh5*^{ubs25} sequence. b) The wild-type and mutant DNA sequences and their respective translations. The *cdh5*^{ubs25} mutation leads to a premature stop. c) Schematic illustration of the domains in both full-length wild-type VE-cad and in truncated VE-cad (Cdh5^{ubs25}). d) Example of genotyping PCR and different *cdh5*^{ubs25} allelic combinations. e) Plot showing colocalization of ZO1 and truncated Cdh5 at endothelial cell junctions. Pearson correlation coefficients of colocalization analysis of anti-VEC and anti-ZO1 in heterozygote (*cdh5*$^{ubs25+/-}$) and homozygote (*cdh5*$^{ubs25/ubs25}$) VE-cad mutants. *cdh5*$^{ubs25/+}$, n=30 cell-cell junctions (2 embryos) ; *cdh5*$^{ubs25/ubs25}$, n=20 cell-cell junctions (1 embryo).n.s., non-significant (p=0.75, non-parametric Mann-Whitney test). f) Quantitation of the interval of subsequently occuring JBLs based on EGFP-UCHD signal. Time from end of the first JBL to emergence of new JBL in the same spot was measured ; wild-type n=15 (2 embryos) and *cdh5*$^{ubs25/ubs25}$ n=36 (4 embryos). All embryos carried EGFP-UCHD transgene Tg*(fli:GFF ; UAS:EGFP-UCHD).* Non-parametric Mann-Whitney statistical test was used.

a

56 hpf	no blood flow	blood flow only in DA and PCV/CV	normal blood flow
WT (n=32)	0%	0%	100% (32/32)
ubs25-het (n=37)	0%	0%	100% (37/37)
ubs25-mut (n=18)	61% (11/18)	39% (7/18)	0%
ubs8-het (n=39)	0%	0%	100% (39/39)
ubs8-mut (n=18)	100% (18/18)	0%	0%

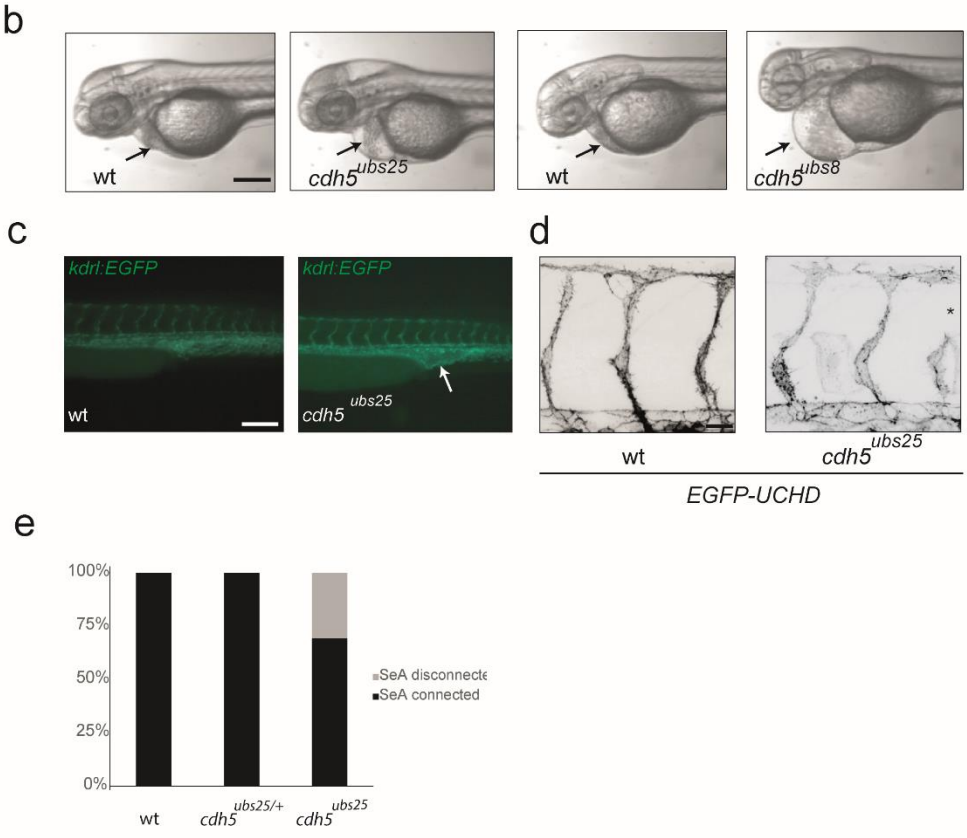

Supplementary Figure 5. *Phenotypic analysis of the ve-cad truncation mutant zebrafish.*

a) Table of blood flow phenotype of 56hpf VE-cadherin null mutant (*cdh5*$^{ubs8/ubs8}$) and the truncation mutant (*cdh5*$^{ubs8/ubs8}$) embryos. b) Stereomicroscope images of the embryos. Arrows point to pericardiac area, pronounced oedema is observed in mutant embryos. Scale bar, 400µm. c) Fluorescence images of Tg(*kdrl:EGFP*^{s843}) embryos at 48hpf. Arrow points of enlarged cardinal vein in *cdh5*^{ubs25} homozygote embryo. Scale bar, 200 µm. d) Confocal images illustrating the tip cell /stalk cell disconnection (arrow) in the *cdh5*^{ubs25} homozygote embryo. In normal SeA the connection between tip cell and stalk cell is intact. Scale bar, 20 µm. e) Quantification of tip cell stalk cell disconnection; *cdh5*$^{ubs25/+}$, n=7 SeA; *cdh5*$^{ubs25/ubs25}$, n=36 SeA; wild-type n=22 SeA.

References

Abu Taha, A., Taha, M., Seebach, J., Schnittler, H.-J., 2014. ARP2/3-mediated junction-associated lamellipodia control VE-cadherin-based cell junction dynamics and maintain monolayer integrity. Mol. Biol. Cell 25, 245–256. https://doi.org/10.1091/mbc.E13-07-0404

Adams, R.H., Alitalo, K., 2007. Molecular regulation of angiogenesis and lymphangiogenesis. Nat. Rev. Mol. Cell Biol. 8, 464–478. https://doi.org/10.1038/nrm2183

Alberts, B., Johnson, A., Lewis, J., Raff, M., Roberts, K., Walter, P., 2002. Cell Junctions. Mol. Biol. Cell 4th Ed.

Andrew, D.J., Ewald, A.J., 2010. Morphogenesis of epithelial tubes: Insights into tube formation, elongation, and elaboration. Dev. Biol. 341, 34–55. https://doi.org/10.1016/j.ydbio.2009.09.024

Baer, M.M., Chanut-Delalande, H., Affolter, M., 2009. Cellular and molecular mechanisms underlying the formation of biological tubes. Curr. Top. Dev. Biol. 89, 137–162. https://doi.org/10.1016/S0070-2153(09)89006-6

Barry, A.K., Wang, N., Leckband, D.E., 2015. Local VE-cadherin mechanotransduction triggers long-ranged remodeling of endothelial monolayers. J. Cell Sci. 128, 1341–1351. https://doi.org/10.1242/jcs.159954

Bazzoni, G., Dejana, E., 2004. Endothelial cell-to-cell junctions: molecular organization and role in vascular homeostasis. Physiol. Rev. 84, 869–901. https://doi.org/10.1152/physrev.00035.2003

Bear, J.E., Gertler, F.B., 2009. Ena/VASP: towards resolving a pointed controversy at the barbed end. J. Cell Sci. 122, 1947–1953. https://doi.org/10.1242/jcs.038125

Beckers, C.M.L., van Hinsbergh, V.W.M., van Nieuw Amerongen, G.P., 2010. Driving Rho GTPase activity in endothelial cells regulates barrier integrity. Thromb. Haemost. 103, 40–55. https://doi.org/10.1160/TH09-06-0403

Bershadsky, A., 2004. Magic touch: how does cell-cell adhesion trigger actin assembly? Trends Cell Biol. 14, 589–593. https://doi.org/10.1016/j.tcb.2004.09.009

Blum, Y., Belting, H.-G., Ellertsdottir, E., Herwig, L., Lüders, F., Affolter, M., 2008. Complex cell rearrangements during intersegmental vessel sprouting and vessel fusion in the zebrafish embryo. Dev. Biol. 316, 312–322. https://doi.org/10.1016/j.ydbio.2008.01.038

Borghi, N., Sorokina, M., Shcherbakova, O.G., Weis, W.I., Pruitt, B.L., Nelson, W.J., Dunn, A.R., 2012. E-cadherin is under constitutive actomyosin-generated tension that is increased at cell-cell contacts upon externally applied stretch. Proc. Natl. Acad. Sci. U. S. A. 109, 12568–12573. https://doi.org/10.1073/pnas.1204390109

Breslin, J.W., Zhang, X.E., Worthylake, R.A., Souza-Smith, F.M., 2015. Involvement of local lamellipodia in endothelial barrier function. PloS One 10, e0117970. https://doi.org/10.1371/journal.pone.0117970

Broman, M.T., Kouklis, P., Gao, X., Ramchandran, R., Neamu, R.F., Minshall, R.D., Malik, A.B., 2006. Cdc42 regulates adherens junction stability and endothelial permeability by inducing alpha-catenin interaction with the vascular endothelial cadherin

complex. Circ. Res. 98, 73–80. https://doi.org/10.1161/01.RES.0000198387.44395.e9

Cai, D., Chen, S.-C., Prasad, M., He, L., Wang, X., Choesmel-Cadamuro, V., Sawyer, J.K., Danuser, G., Montell, D.J., 2014. Mechanical Feedback through E-Cadherin Promotes Direction Sensing during Collective Cell Migration. Cell 157, 1146–1159. https://doi.org/10.1016/j.cell.2014.03.045

Carmeliet, P., 2000. Mechanisms of angiogenesis and arteriogenesis. Nat. Med. 6, 389–395. https://doi.org/10.1038/74651

Carmeliet, P., Lampugnani, M.G., Moons, L., Breviario, F., Compernolle, V., Bono, F., Balconi, G., Spagnuolo, R., Oosthuyse, B., Dewerchin, M., Zanetti, A., Angellilo, A., Mattot, V., Nuyens, D., Lutgens, E., Clotman, F., de Ruiter, M.C., Gittenberger-de Groot, A., Poelmann, R., Lupu, F., Herbert, J.M., Collen, D., Dejana, E., 1999. Targeted deficiency or cytosolic truncation of the VE-cadherin gene in mice impairs VEGF-mediated endothelial survival and angiogenesis. Cell 98, 147–157. https://doi.org/10.1016/s0092-8674(00)81010-7

Carmeliet, P., Tessier-Lavigne, M., 2005. Common mechanisms of nerve and blood vessel wiring. Nature 436, 193–200. https://doi.org/10.1038/nature03875

Chesarone, M.A., Goode, B.L., 2009. Actin nucleation and elongation factors: mechanisms and interplay. Curr. Opin. Cell Biol. 21, 28–37. https://doi.org/10.1016/j.ceb.2008.12.001

Colas, J.F., Schoenwolf, G.C., 2001. Towards a cellular and molecular understanding of neurulation. Dev. Dyn. Off. Publ. Am. Assoc. Anat. 221, 117–145. https://doi.org/10.1002/dvdy.1144

Collins, C., Guilluy, C., Welch, C., O'Brien, E.T., Hahn, K., Superfine, R., Burridge, K., Tzima, E., 2012. Localized tensional forces on PECAM-1 elicit a global mechanotransduction response via the integrin-RhoA pathway. Curr. Biol. CB 22, 2087–2094. https://doi.org/10.1016/j.cub.2012.08.051

Coluccio, L.M., 2008. Myosins: a superfamily of molecular motors. Springer, Dordrecht.

Cong, L., Ran, F.A., Cox, D., Lin, S., Barretto, R., Habib, N., Hsu, P.D., Wu, X., Jiang, W., Marraffini, L.A., Zhang, F., 2013. Multiplex genome engineering using CRISPR/Cas systems. Science 339, 819–823. https://doi.org/10.1126/science.1231143

Conway, D.E., Breckenridge, M.T., Hinde, E., Gratton, E., Chen, C.S., Schwartz, M.A., 2013. Fluid shear stress on endothelial cells modulates mechanical tension across VE-cadherin and PECAM-1. Curr. Biol. CB 23, 1024–1030. https://doi.org/10.1016/j.cub.2013.04.049

Conway, D.E., Schwartz, M.A., 2015. Mechanotransduction of shear stress occurs through changes in VE-cadherin and PECAM-1 tension: implications for cell migration. Cell Adhes. Migr. 9, 335–339. https://doi.org/10.4161/19336918.2014.968498

Coon, B.G., Baeyens, N., Han, J., Budatha, M., Ross, T.D., Fang, J.S., Yun, S., Thomas, J.-L., Schwartz, M.A., 2015. Intramembrane binding of VE-cadherin to VEGFR2 and VEGFR3 assembles the endothelial mechanosensory complex. J. Cell Biol. 208, 975–986. https://doi.org/10.1083/jcb.201408103

Cost, A.-L., Ringer, P., Chrostek-Grashoff, A., Grashoff, C., 2015. How to Measure Molecular Forces in Cells: A Guide to Evaluating Genetically-Encoded FRET-Based Tension Sensors. Cell. Mol. Bioeng. 8, 96–105. https://doi.org/10.1007/s12195-014-0368-1

Costa, G., Harrington, K.I., Lovegrove, H.E., Page, D.J., Chakravartula, S., Bentley, K., Herbert, S.P., 2016. Asymmetric division coordinates collective cell migration in angiogenesis. Nat. Cell Biol. 18, 1292–1301. https://doi.org/10.1038/ncb3443

Coucouvanis, E., Martin, G.R., 1995. Signals for death and survival: a two-step mechanism for cavitation in the vertebrate embryo. Cell 83, 279–287. https://doi.org/10.1016/0092-8674(95)90169-8

Daneshjou, N., Sieracki, N., van Nieuw Amerongen, G.P., Conway, D.E., Schwartz, M.A., Komarova, Y.A., Malik, A.B., 2015. Rac1 functions as a reversible tension modulator to stabilize VE-cadherin trans-interaction. J. Cell Biol. 208, 23–32. https://doi.org/10.1083/jcb.201409108

Dejana, E., Tournier-Lasserve, E., Weinstein, B.M., 2009. The control of vascular integrity by endothelial cell junctions: molecular basis and pathological implications. Dev. Cell 16, 209–221. https://doi.org/10.1016/j.devcel.2009.01.004

Dejana, E., Vestweber, D., 2013. The role of VE-cadherin in vascular morphogenesis and permeability control. Prog. Mol. Biol. Transl. Sci. 116, 119–144. https://doi.org/10.1016/B978-0-12-394311-8.00006-6

DeLisser, H.M., Newman, P.J., Albelda, S.M., 1994. Molecular and functional aspects of PECAM-1/CD31. Immunol. Today 15, 490–495. https://doi.org/10.1016/0167-5699(94)90195-3

Dooley, K., Zon, L.I., 2000. Zebrafish: a model system for the study of human disease. Curr. Opin. Genet. Dev. 10, 252–256. https://doi.org/10.1016/s0959-437x(00)00074-5

Ebnet, K., 2008. Organization of multiprotein complexes at cell-cell junctions. Histochem. Cell Biol. 130, 1–20. https://doi.org/10.1007/s00418-008-0418-7

Eden, S., Rohatgi, R., Podtelejnikov, A.V., Mann, M., Kirschner, M.W., 2002. Mechanism of regulation of WAVE1-induced actin nucleation by Rac1 and Nck. Nature 418, 790–793. https://doi.org/10.1038/nature00859

Eder, D., Basler, K., Aegerter, C.M., 2017. Challenging FRET-based E-Cadherin force measurements in Drosophila. Sci. Rep. 7, 1–12. https://doi.org/10.1038/s41598-017-14136-y

Ellertsdóttir, E., Lenard, A., Blum, Y., Krudewig, A., Herwig, L., Affolter, M., Belting, H.-G., 2010. Vascular morphogenesis in the zebrafish embryo. Dev. Biol. 341, 56–65. https://doi.org/10.1016/j.ydbio.2009.10.035

Gavard, J., Gutkind, J.S., 2006. VEGF controls endothelial-cell permeability by promoting the beta-arrestin-dependent endocytosis of VE-cadherin. Nat. Cell Biol. 8, 1223–1234. https://doi.org/10.1038/ncb1486

Gebala, V., Collins, R., Geudens, I., Phng, L.-K., Gerhardt, H., 2016. Blood flow drives lumen formation by inverse membrane blebbing during angiogenesis in vivo. Nat. Cell Biol. 18, 443–450. https://doi.org/10.1038/ncb3320

Georgiou, M., Marinari, E., Burden, J., Baum, B., 2008. Cdc42, Par6, and aPKC regulate Arp2/3-mediated endocytosis to control local adherens junction stability. Curr. Biol. CB 18, 1631–1638. https://doi.org/10.1016/j.cub.2008.09.029

Glickman, N.S., Yelon, D., 2002. Cardiac development in zebrafish: coordination of form and function. Semin. Cell Dev. Biol. 13, 507–513. https://doi.org/10.1016/s1084952102001040

Goley, E.D., Ohkawa, T., Mancuso, J., Woodruff, J.B., D'Alessio, J.A., Cande, W.Z., Volkman, L.E., Welch, M.D., 2006. Dynamic nuclear actin assembly by Arp2/3 complex and a

baculovirus WASP-like protein. Science 314, 464–467. https://doi.org/10.1126/science.1133348

Gory-Fauré, S., Prandini, M.H., Pointu, H., Roullot, V., Pignot-Paintrand, I., Vernet, M., Huber, P., 1999. Role of vascular endothelial-cadherin in vascular morphogenesis. Dev. Camb. Engl. 126, 2093–2102.

Grashoff, C., Hoffman, B.D., Brenner, M.D., Zhou, R., Parsons, M., Yang, M.T., McLean, M.A., Sligar, S.G., Chen, C.S., Ha, T., Schwartz, M.A., 2010. Measuring mechanical tension across vinculin reveals regulation of focal adhesion dynamics. Nature 466, 263–266. https://doi.org/10.1038/nature09198

Habeck, H., Odenthal, J., Walderich, B., Maischein, H.-M., Schulte-Merker, S., 2002. Analysis of a Zebrafish VEGF Receptor Mutant Reveals Specific Disruption of Angiogenesis. Curr. Biol. 12, 1405–1412. https://doi.org/10.1016/S0960-9822(02)01044-8

Haffter, P., Granato, M., Brand, M., Mullins, M.C., Hammerschmidt, M., Kane, D.A., Odenthal, J., Eeden, F.J. van, Jiang, Y.J., Heisenberg, C.P., Kelsh, R.N., Furutani-Seiki, M., Vogelsang, E., Beuchle, D., Schach, U., Fabian, C., Nusslein-Volhard, C., 1996. The identification of genes with unique and essential functions in the development of the zebrafish, Danio rerio. Development 123, 1–36.

Hall, A., 1998. Rho GTPases and the actin cytoskeleton. Science 279, 509–514. https://doi.org/10.1126/science.279.5350.509

Han, S.P., Gambin, Y., Gomez, G.A., Verma, S., Giles, N., Michael, M., Wu, S.K., Guo, Z., Johnston, W., Sierecki, E., Parton, R.G., Alexandrov, K., Yap, A.S., 2014. Cortactin scaffolds Arp2/3 and WAVE2 at the epithelial zonula adherens. J. Biol. Chem. 289, 7764–7775. https://doi.org/10.1074/jbc.M113.544478

Hansen, S.D., Mullins, R.D., 2010. VASP is a processive actin polymerase that requires monomeric actin for barbed end association. J. Cell Biol. 191, 571–584. https://doi.org/10.1083/jcb.201003014

Harper, S.M., Christie, J.M., Gardner, K.H., 2004. Disruption of the LOV-Jalpha helix interaction activates phototropin kinase activity. Biochemistry 43, 16184–16192. https://doi.org/10.1021/bi048092i

Harper, S.M., Neil, L.C., Gardner, K.H., 2003. Structural basis of a phototropin light switch. Science 301, 1541–1544. https://doi.org/10.1126/science.1086810

Harris, T.J.C., Tepass, U., 2010. Adherens junctions: from molecules to morphogenesis. Nat. Rev. Mol. Cell Biol. 11, 502–514. https://doi.org/10.1038/nrm2927

Heisenberg, C.-P., Bellaïche, Y., 2013. Forces in Tissue Morphogenesis and Patterning. Cell 153, 948–962. https://doi.org/10.1016/j.cell.2013.05.008

Heissler, S.M., Manstein, D.J., 2013. Nonmuscle myosin-2: mix and match. Cell. Mol. Life Sci. CMLS 70, 1–21. https://doi.org/10.1007/s00018-012-1002-9

Helker, C.S.M., Schuermann, A., Karpanen, T., Zeuschner, D., Belting, H.-G., Affolter, M., Schulte-Merker, S., Herzog, W., 2013. The zebrafish common cardinal veins develop by a novel mechanism: lumen ensheathment. Dev. Camb. Engl. 140, 2776–2786. https://doi.org/10.1242/dev.091876

Herwig, L., Blum, Y., Krudewig, A., Ellertsdottir, E., Lenard, A., Belting, H.-G., Affolter, M., 2011. Distinct cellular mechanisms of blood vessel fusion in the zebrafish embryo. Curr. Biol. CB 21, 1942–1948. https://doi.org/10.1016/j.cub.2011.10.016

Hill, A.J., Teraoka, H., Heideman, W., Peterson, R.E., 2005. Zebrafish as a model vertebrate for investigating chemical toxicity. Toxicol. Sci. Off. J. Soc. Toxicol. 86, 6–19. https://doi.org/10.1093/toxsci/kfi110

Howe, K., Clark, M.D., Torroja, C.F., Torrance, J., Berthelot, C., Muffato, M., Collins, J.E., Humphray, S., McLaren, K., Matthews, L., McLaren, S., Sealy, I., Caccamo, M., Churcher, C., Scott, C., Barrett, J.C., Koch, R., Rauch, G.-J., White, S., Chow, W., Kilian, B., Quintais, L.T., Guerra-Assunção, J.A., Zhou, Y., Gu, Y., Yen, J., Vogel, J.-H., Eyre, T., Redmond, S., Banerjee, R., Chi, J., Fu, B., Langley, E., Maguire, S.F., Laird, G.K., Lloyd, D., Kenyon, E., Donaldson, S., Sehra, H., Almeida-King, J., Loveland, J., Trevanion, S., Jones, M., Quail, M., Willey, D., Hunt, A., Burton, J., Sims, S., McLay, K., Plumb, B., Davis, J., Clee, C., Oliver, K., Clark, R., Riddle, C., Elliot, D., Eliott, D., Threadgold, G., Harden, G., Ware, D., Begum, S., Mortimore, B., Mortimer, B., Kerry, G., Heath, P., Phillimore, B., Tracey, A., Corby, N., Dunn, M., Johnson, C., Wood, J., Clark, S., Pelan, S., Griffiths, G., Smith, M., Glithero, R., Howden, P., Barker, N., Lloyd, C., Stevens, C., Harley, J., Holt, K., Panagiotidis, G., Lovell, J., Beasley, H., Henderson, C., Gordon, D., Auger, K., Wright, D., Collins, J., Raisen, C., Dyer, L., Leung, K., Robertson, L., Ambridge, K., Leongamornlert, D., McGuire, S., Gilderthorp, R., Griffiths, C., Manthravadi, D., Nichol, S., Barker, G., Whitehead, S., Kay, M., Brown, J., Murnane, C., Gray, E., Humphries, M., Sycamore, N., Barker, D., Saunders, D., Wallis, J., Babbage, A., Hammond, S., Mashreghi-Mohammadi, M., Barr, L., Martin, S., Wray, P., Ellington, A., Matthews, N., Ellwood, M., Woodmansey, R., Clark, G., Cooper, J.D., Cooper, J., Tromans, A., Grafham, D., Skuce, C., Pandian, R., Andrews, R., Harrison, E., Kimberley, A., Garnett, J., Fosker, N., Hall, R., Garner, P., Kelly, D., Bird, C., Palmer, S., Gehring, I., Berger, A., Dooley, C.M., Ersan-Ürün, Z., Eser, C., Geiger, H., Geisler, M., Karotki, L., Kirn, A., Konantz, J., Konantz, M., Oberländer, M., Rudolph-Geiger, S., Teucke, M., Lanz, C., Raddatz, G., Osoegawa, K., Zhu, B., Rapp, A., Widaa, S., Langford, C., Yang, F., Schuster, S.C., Carter, N.P., Harrow, J., Ning, Z., Herrero, J., Searle, S.M.J., Enright, A., Geisler, R., Plasterk, R.H.A., Lee, C., Westerfield, M., de Jong, P.J., Zon, L.I., Postlethwait, J.H., Nüsslein-Volhard, C., Hubbard, T.J.P., Roest Crollius, H., Rogers, J., Stemple, D.L., 2013. The zebrafish reference genome sequence and its relationship to the human genome. Nature 496, 498–503. https://doi.org/10.1038/nature12111

Huisken, J., Stainier, D.Y.R., 2009. Selective plane illumination microscopy techniques in developmental biology. Dev. Camb. Engl. 136, 1963–1975. https://doi.org/10.1242/dev.022426

Huveneers, S., Oldenburg, J., Spanjaard, E., van der Krogt, G., Grigoriev, I., Akhmanova, A., Rehmann, H., de Rooij, J., 2012. Vinculin associates with endothelial VE-cadherin junctions to control force-dependent remodeling. J. Cell Biol. 196, 641–652. https://doi.org/10.1083/jcb.201108120

Hwang, W.Y., Fu, Y., Reyon, D., Maeder, M.L., Kaini, P., Sander, J.D., Joung, J.K., Peterson, R.T., Yeh, J.-R.J., 2013. Heritable and precise zebrafish genome editing using a CRISPR-Cas system. PloS One 8, e68708. https://doi.org/10.1371/journal.pone.0068708

Insall, R.H., Machesky, L.M., 2009. Actin dynamics at the leading edge: from simple machinery to complex networks. Dev. Cell 17, 310–322. https://doi.org/10.1016/j.devcel.2009.08.012

Ishiyama, N., Tanaka, N., Abe, K., Yang, Y.J., Abbas, Y.M., Umitsu, M., Nagar, B., Bueler, S.A., Rubinstein, J.L., Takeichi, M., Ikura, M., 2013. An autoinhibited structure of α-catenin and its implications for vinculin recruitment to adherens junctions. J. Biol. Chem. 288, 15913–15925. https://doi.org/10.1074/jbc.M113.453928

Isogai, S., Horiguchi, M., Weinstein, B.M., 2001. The vascular anatomy of the developing zebrafish: an atlas of embryonic and early larval development. Dev. Biol. 230, 278–301. https://doi.org/10.1006/dbio.2000.9995

Isogai, S., Lawson, N.D., Torrealday, S., Horiguchi, M., Weinstein, B.M., 2003. Angiogenic network formation in the developing vertebrate trunk. Dev. Camb. Engl. 130, 5281–5290. https://doi.org/10.1242/dev.00733

Itoh, M., Nagafuchi, A., Moroi, S., Tsukita, S., 1997. Involvement of ZO-1 in cadherin-based cell adhesion through its direct binding to alpha catenin and actin filaments. J. Cell Biol. 138, 181–192. https://doi.org/10.1083/jcb.138.1.181

Ivanov, A.I., Hunt, D., Utech, M., Nusrat, A., Parkos, C.A., 2005. Differential Roles for Actin Polymerization and a Myosin II Motor in Assembly of the Epithelial Apical Junctional Complex. Mol. Biol. Cell 16, 2636–2650. https://doi.org/10.1091/mbc.E05-01-0043

Jakobsson, L., Franco, C.A., Bentley, K., Collins, R.T., Ponsioen, B., Aspalter, I.M., Rosewell, I., Busse, M., Thurston, G., Medvinsky, A., Schulte-Merker, S., Gerhardt, H., 2010. Endothelial cells dynamically compete for the tip cell position during angiogenic sprouting. Nat. Cell Biol. 12, 943–953. https://doi.org/10.1038/ncb2103

Ji, L., Lim, J., Danuser, G., 2008. Fluctuations of intracellular forces during cell protrusion. Nat. Cell Biol. 10, 1393–1400. https://doi.org/10.1038/ncb1797

Jin, S.-W., Beis, D., Mitchell, T., Chen, J.-N., Stainier, D.Y.R., 2005. Cellular and molecular analyses of vascular tube and lumen formation in zebrafish. Dev. Camb. Engl. 132, 5199–5209. https://doi.org/10.1242/dev.02087

Kamei, M., Saunders, W.B., Bayless, K.J., Dye, L., Davis, G.E., Weinstein, B.M., 2006. Endothelial tubes assemble from intracellular vacuoles in vivo. Nature 442, 453–456. https://doi.org/10.1038/nature04923

Kimmel, C.B., Ballard, W.W., Kimmel, S.R., Ullmann, B., Schilling, T.F., 1995. Stages of embryonic development of the zebrafish. Dev. Dyn. Off. Publ. Am. Assoc. Anat. 203, 253–310. https://doi.org/10.1002/aja.1002030302

Knezevic, I.I., Predescu, S.A., Neamu, R.F., Gorovoy, M.S., Knezevic, N.M., Easington, C., Malik, A.B., Predescu, D.N., 2009. Tiam1 and Rac1 are required for platelet-activating factor-induced endothelial junctional disassembly and increase in vascular permeability. J. Biol. Chem. 284, 5381–5394. https://doi.org/10.1074/jbc.M808958200

Kobielak, A., Pasolli, H.A., Fuchs, E., 2004. Mammalian formin-1 participates in adherens junctions and polymerization of linear actin cables. Nat. Cell Biol. 6, 21–30. https://doi.org/10.1038/ncb1075

Kotini, M.P., Mäe, M.A., Belting, H.-G., Betsholtz, C., Affolter, M., 2019. Sprouting and anastomosis in the Drosophila trachea and the vertebrate vasculature: Similarities and differences in cell behaviour. Vascul. Pharmacol. 112, 8–16. https://doi.org/10.1016/j.vph.2018.11.002

Kovacs, E.M., Goodwin, M., Ali, R.G., Paterson, A.D., Yap, A.S., 2002. Cadherin-directed actin assembly: E-cadherin physically associates with the Arp2/3 complex to direct actin assembly in nascent adhesive contacts. Curr. Biol. CB 12, 379–382. https://doi.org/10.1016/s0960-9822(02)00661-9

Kovacs, E.M., Verma, S., Ali, R.G., Ratheesh, A., Hamilton, N.A., Akhmanova, A., Yap, A.S., 2011. N-WASP regulates the epithelial junctional actin cytoskeleton through a non-canonical post-nucleation pathway. Nat. Cell Biol. 13, 934–943. https://doi.org/10.1038/ncb2290

Krause, M., Dent, E.W., Bear, J.E., Loureiro, J.J., Gertler, F.B., 2003. Ena/VASP proteins: regulators of the actin cytoskeleton and cell migration. Annu. Rev. Cell Dev. Biol. 19, 541–564. https://doi.org/10.1146/annurev.cellbio.19.050103.103356

Lagendijk, A.K., Gomez, G.A., Baek, S., Hesselson, D., Hughes, W.E., Paterson, S., Conway, D.E., Belting, H.-G., Affolter, M., Smith, K.A., Schwartz, M.A., Yap, A.S., Hogan, B.M., 2017. Live imaging molecular changes in junctional tension upon VE-cadherin in zebrafish. Nat. Commun. 8, 1402. https://doi.org/10.1038/s41467-017-01325-6

Lagendijk, A.K., Hogan, B.M., 2015. VE-cadherin in vascular development: a coordinator of cell signaling and tissue morphogenesis. Curr. Top. Dev. Biol. 112, 325–352. https://doi.org/10.1016/bs.ctdb.2014.11.024

Lampugnani, M.G., Zanetti, A., Breviario, F., Balconi, G., Orsenigo, F., Corada, M., Spagnuolo, R., Betson, M., Braga, V., Dejana, E., 2002. VE-cadherin regulates endothelial actin activating Rac and increasing membrane association of Tiam. Mol. Biol. Cell 13, 1175–1189. https://doi.org/10.1091/mbc.01-07-0368

Lancino, M., Majello, S., Herbert, S., De Chaumont, F., Tinevez, J.-Y., Olivo-Marin, J.-C., Herbomel, P., Schmidt, A., 2018. Anisotropic organization of circumferential actomyosin characterizes hematopoietic stem cells emergence in the zebrafish. eLife 7, e37355. https://doi.org/10.7554/eLife.37355

Lecuit, T., Lenne, P.-F., Munro, E., 2011. Force generation, transmission, and integration during cell and tissue morphogenesis. Annu. Rev. Cell Dev. Biol. 27, 157–184. https://doi.org/10.1146/annurev-cellbio-100109-104027

Leerberg, J.M., Gomez, G.A., Verma, S., Moussa, E.J., Wu, S.K., Priya, R., Hoffman, B.D., Grashoff, C., Schwartz, M.A., Yap, A.S., 2014. Tension-sensitive actin assembly supports contractility at the epithelial zonula adherens. Curr. Biol. CB 24, 1689–1699. https://doi.org/10.1016/j.cub.2014.06.028

Lenard, A., Ellertsdottir, E., Herwig, L., Krudewig, A., Sauteur, L., Belting, H.-G., Affolter, M., 2013. In Vivo Analysis Reveals a Highly Stereotypic Morphogenetic Pathway of Vascular Anastomosis. Dev. Cell 25, 492–506. https://doi.org/10.1016/j.devcel.2013.05.010

Lessman, C.A., 2011. The developing zebrafish (Danio rerio): a vertebrate model for high-throughput screening of chemical libraries. Birth Defects Res. Part C Embryo Today Rev. 93, 268–280. https://doi.org/10.1002/bdrc.20212

Liang, X., Gomez, G.A., Yap, A.S., 2015. Current perspectives on cadherin-cytoskeleton interactions and dynamics [WWW Document]. Cell Health Cytoskelet. https://doi.org/10.2147/CHC.S76107

Liu, Y., Collins, C., Kiosses, W.B., Murray, A.M., Joshi, M., Shepherd, T.R., Fuentes, E.J., Tzima, E., 2013. A novel pathway spatiotemporally activates Rac1 and redox signaling in response to fluid shear stress. J. Cell Biol. 201, 863–873. https://doi.org/10.1083/jcb.201207115

Liu, Z., Tan, J.L., Cohen, D.M., Yang, M.T., Sniadecki, N.J., Ruiz, S.A., Nelson, C.M., Chen, C.S., 2010. Mechanical tugging force regulates the size of cell-cell junctions. Proc. Natl. Acad. Sci. U. S. A. 107, 9944–9949. https://doi.org/10.1073/pnas.0914547107

Lubarsky, B., Krasnow, M.A., 2003. Tube morphogenesis: making and shaping biological tubes. Cell 112, 19–28. https://doi.org/10.1016/s0092-8674(02)01283-7

Makanya, A.N., Hlushchuk, R., Djonov, V.G., 2009. Intussusceptive angiogenesis and its role in vascular morphogenesis, patterning, and remodeling. Angiogenesis 12, 113–123. https://doi.org/10.1007/s10456-009-9129-5

Martin, A.C., Gelbart, M., Fernandez-Gonzalez, R., Kaschube, M., Wieschaus, E.F., 2010. Integration of contractile forces during tissue invagination. J. Cell Biol. 188, 735–749. https://doi.org/10.1083/jcb.200910099

Mattila, P.K., Lappalainen, P., 2008. Filopodia: molecular architecture and cellular functions. Nat. Rev. Mol. Cell Biol. 9, 446–454. https://doi.org/10.1038/nrm2406

Mehta, D., Konstantoulaki, M., Ahmmed, G.U., Malik, A.B., 2005. Sphingosine 1-Phosphate-induced Mobilization of Intracellular Ca2+ Mediates Rac Activation and Adherens Junction Assembly in Endothelial Cells. J. Biol. Chem. 280, 17320–17328. https://doi.org/10.1074/jbc.M411674200

Melnick, M., Jaskoll, T., 2000. Mouse submandibular gland morphogenesis: a paradigm for embryonic signal processing. Crit. Rev. Oral Biol. Med. Off. Publ. Am. Assoc. Oral Biol. 11, 199–215. https://doi.org/10.1177/10454411000110020401

Mertz, A.F., Che, Y., Banerjee, S., Goldstein, J.M., Rosowski, K.A., Revilla, S.F., Niessen, C.M., Marchetti, M.C., Dufresne, E.R., Horsley, V., 2013. Cadherin-based intercellular adhesions organize epithelial cell–matrix traction forces. Proc. Natl. Acad. Sci. 110, 842–847. https://doi.org/10.1073/pnas.1217279110

Monaghan-Benson, E., Burridge, K., 2009. The regulation of vascular endothelial growth factor-induced microvascular permeability requires Rac and reactive oxygen species. J. Biol. Chem. 284, 25602–25611. https://doi.org/10.1074/jbc.M109.009894

Montero-Balaguer, M., Swirsding, K., Orsenigo, F., Cotelli, F., Mione, M., Dejana, E., 2009. Stable vascular connections and remodeling require full expression of VE-cadherin in zebrafish embryos. PloS One 4, e5772. https://doi.org/10.1371/journal.pone.0005772

Nagafuchi, A., Takeichi, M., 1988. Cell binding function of E-cadherin is regulated by the cytoplasmic domain. EMBO J. 7, 3679–3684.

Nakagawa, M., Fukata, M., Yamaga, M., Itoh, N., Kaibuchi, K., 2001. Recruitment and activation of Rac1 by the formation of E-cadherin-mediated cell-cell adhesion sites. J. Cell Sci. 114, 1829–1838.

Navarro, P., Ruco, L., Dejana, E., 1998. Differential localization of VE- and N-cadherins in human endothelial cells: VE-cadherin competes with N-cadherin for junctional localization. J. Cell Biol. 140, 1475–1484. https://doi.org/10.1083/jcb.140.6.1475

Noren, N.K., Niessen, C.M., Gumbiner, B.M., Burridge, K., 2001. Cadherin engagement regulates Rho family GTPases. J. Biol. Chem. 276, 33305–33308. https://doi.org/10.1074/jbc.C100306200

Osawa, M., Masuda, M., Kusano, K., Fujiwara, K., 2002. Evidence for a role of platelet endothelial cell adhesion molecule-1 in endothelial cell mechanosignal transduction. J. Cell Biol. 158, 773–785. https://doi.org/10.1083/jcb.200205049

Paatero, I., Sauteur, L., Lee, M., Lagendijk, A.K., Heutschi, D., Wiesner, C., Guzmán, C., Bieli, D., Hogan, B.M., Affolter, M., Belting, H.-G., 2018. Junction-based lamellipodia drive endothelial cell rearrangements in vivo via a VE-cadherin-F-actin based oscillatory cell-cell interaction. Nat. Commun. 9, 1–13. https://doi.org/10.1038/s41467-018-05851-9

Parng, C., Seng, W.L., Semino, C., McGrath, P., 2002. Zebrafish: a preclinical model for drug screening. Assay Drug Dev. Technol. 1, 41–48. https://doi.org/10.1089/154065802761001293

Parsons, J.T., Horwitz, A.R., Schwartz, M.A., 2010. Cell adhesion: integrating cytoskeletal dynamics and cellular tension. Nat. Rev. Mol. Cell Biol. 11, 633–643. https://doi.org/10.1038/nrm2957

Pasic, L., Kotova, T., Schafer, D.A., 2008. Ena/VASP proteins capture actin filament barbed ends. J. Biol. Chem. 283, 9814–9819. https://doi.org/10.1074/jbc.M710475200

Patan, S., 2000. Vasculogenesis and angiogenesis as mechanisms of vascular network formation, growth and remodeling. J. Neurooncol. 50, 1–15. https://doi.org/10.1023/a:1006493130855

Perryn, E.D., Czirók, A., Little, C.D., 2008. Vascular sprout formation entails tissue deformations and VE-cadherin-dependent cell-autonomous motility. Dev. Biol. 313, 545–555. https://doi.org/10.1016/j.ydbio.2007.10.036

Phng, L.-K., Stanchi, F., Gerhardt, H., 2013. Filopodia are dispensable for endothelial tip cell guidance. Dev. Camb. Engl. 140, 4031–4040. https://doi.org/10.1242/dev.097352

Pollard, T.D., 2016. Actin and Actin-Binding Proteins. Cold Spring Harb. Perspect. Biol. 8, a018226. https://doi.org/10.1101/cshperspect.a018226

Pollard, T.D., Blanchoin, L., Mullins, R.D., 2000. Molecular mechanisms controlling actin filament dynamics in nonmuscle cells. Annu. Rev. Biophys. Biomol. Struct. 29, 545–576. https://doi.org/10.1146/annurev.biophys.29.1.545

Poole, T.J., Coffin, J.D., 1989. Vasculogenesis and angiogenesis: two distinct morphogenetic mechanisms establish embryonic vascular pattern. J. Exp. Zool. 251, 224–231. https://doi.org/10.1002/jez.1402510210

Potente, M., Mäkinen, T., 2017. Vascular heterogeneity and specialization in development and disease. Nat. Rev. Mol. Cell Biol. 18, 477–494. https://doi.org/10.1038/nrm.2017.36

Priya, R., Yap, A.S., 2015. Active tension: the role of cadherin adhesion and signaling in generating junctional contractility. Curr. Top. Dev. Biol. 112, 65–102. https://doi.org/10.1016/bs.ctdb.2014.11.016

Ridley, A.J., 2001. Rho GTPases and cell migration. J. Cell Sci. 114, 2713–2722.

Ridley, A.J., Paterson, H.F., Johnston, C.L., Diekmann, D., Hall, A., 1992. The small GTP-binding protein rac regulates growth factor-induced membrane ruffling. Cell 70, 401–410. https://doi.org/10.1016/0092-8674(92)90164-8

Rossman, K.L., Der, C.J., Sondek, J., 2005. GEF means go: turning on RHO GTPases with guanine nucleotide-exchange factors. Nat. Rev. Mol. Cell Biol. 6, 167–180. https://doi.org/10.1038/nrm1587

Rottner, K., Faix, J., Bogdan, S., Linder, S., Kerkhoff, E., 2017. Actin assembly mechanisms at a glance. J. Cell Sci. 130, 3427–3435. https://doi.org/10.1242/jcs.206433

Sauteur, L., Affolter, M., Belting, H.-G., 2017. Distinct and redundant functions of Esama and VE-cadherin during vascular morphogenesis. Development 144, 1554–1565. https://doi.org/10.1242/dev.140038

Sauteur, L., Krudewig, A., Herwig, L., Ehrenfeuchter, N., Lenard, A., Affolter, M., Belting, H.-G., 2014. Cdh5/VE-cadherin promotes endothelial cell interface elongation via cortical actin polymerization during angiogenic sprouting. Cell Rep. 9, 504–513. https://doi.org/10.1016/j.celrep.2014.09.024

Schnittler, H., Taha, M., Schnittler, M.O., Taha, A.A., Lindemann, N., Seebach, J., 2014. Actin filament dynamics and endothelial cell junctions: the Ying and Yang between stabilization and motion. Cell Tissue Res. 355, 529–543. https://doi.org/10.1007/s00441-014-1856-2

Seebach, J., Donnert, G., Kronstein, R., Werth, S., Wojciak-Stothard, B., Falzarano, D., Mrowietz, C., Hell, S.W., Schnittler, H.-J., 2007. Regulation of endothelial barrier function during flow-induced conversion to an arterial phenotype. Cardiovasc. Res. 75, 596–607. https://doi.org/10.1016/j.cardiores.2007.04.017

Shen, L., Turner, J.R., 2008. Intercellular junctions: actin the PARt. Curr. Biol. CB 18, R1014-1017. https://doi.org/10.1016/j.cub.2008.10.010

Shewan, A.M., Maddugoda, M., Kraemer, A., Stehbens, S.J., Verma, S., Kovacs, E.M., Yap, A.S., 2005. Myosin 2 is a key Rho kinase target necessary for the local concentration of E-cadherin at cell-cell contacts. Mol. Biol. Cell 16, 4531–4542. https://doi.org/10.1091/mbc.e05-04-0330

Siekmann, A.F., Covassin, L., Lawson, N.D., 2008. Modulation of VEGF signalling output by the Notch pathway. BioEssays News Rev. Mol. Cell. Dev. Biol. 30, 303–313. https://doi.org/10.1002/bies.20736

Siekmann, A.F., Lawson, N.D., 2007. Notch signalling limits angiogenic cell behaviour in developing zebrafish arteries. Nature 445, 781–784. https://doi.org/10.1038/nature05577

Smutny, M., Cox, H.L., Leerberg, J.M., Kovacs, E.M., Conti, M.A., Ferguson, C., Hamilton, N.A., Parton, R.G., Adelstein, R.S., Yap, A.S., 2010. Myosin II isoforms identify distinct functional modules that support integrity of the epithelial zonula adherens. Nat. Cell Biol. 12, 696–702. https://doi.org/10.1038/ncb2072

Spindler, V., Schlegel, N., Waschke, J., 2010. Role of GTPases in control of microvascular permeability. Cardiovasc. Res. 87, 243–253. https://doi.org/10.1093/cvr/cvq086

Strilić, B., Eglinger, J., Krieg, M., Zeeb, M., Axnick, J., Babál, P., Müller, D.J., Lammert, E., 2010. Electrostatic cell-surface repulsion initiates lumen formation in developing blood vessels. Curr. Biol. CB 20, 2003–2009. https://doi.org/10.1016/j.cub.2010.09.061

Strilić, B., Kucera, T., Eglinger, J., Hughes, M.R., McNagny, K.M., Tsukita, S., Dejana, E., Ferrara, N., Lammert, E., 2009. The molecular basis of vascular lumen formation in the developing mouse aorta. Dev. Cell 17, 505–515. https://doi.org/10.1016/j.devcel.2009.08.011

Sugden, W.W., Meissner, R., Aegerter-Wilmsen, T., Tsaryk, R., Leonard, E.V., Bussmann, J., Hamm, M.J., Herzog, W., Jin, Y., Jakobsson, L., Denz, C., Siekmann, A.F., 2017. Endoglin controls blood vessel diameter through endothelial cell shape changes in response to haemodynamic cues. Nat. Cell Biol. 19, 653–665. https://doi.org/10.1038/ncb3528

Tambe, D.T., Hardin, C.C., Angelini, T.E., Rajendran, K., Park, C.Y., Serra-Picamal, X., Zhou, E.H., Zaman, M.H., Butler, J.P., Weitz, D.A., Fredberg, J.J., Trepat, X., 2011. Collective cell guidance by cooperative intercellular forces. Nat. Mater. 10, 469–475. https://doi.org/10.1038/nmat3025

Tang, V.W., Brieher, W.M., 2012. α-Actinin-4/FSGS1 is required for Arp2/3-dependent actin assembly at the adherens junction. J. Cell Biol. 196, 115–130. https://doi.org/10.1083/jcb.201103116

Tilney, L.G., Bonder, E.M., DeRosier, D.J., 1981. Actin filaments elongate from their membrane-associated ends. J. Cell Biol. 90, 485–494. https://doi.org/10.1083/jcb.90.2.485

Timmerman, I., Heemskerk, N., Kroon, J., Schaefer, A., van Rijssel, J., Hoogenboezem, M., van Unen, J., Goedhart, J., Gadella, T.W.J., Yin, T., Wu, Y., Huveneers, S., van Buul,

J.D., 2015. A local VE-cadherin and Trio-based signaling complex stabilizes endothelial junctions through Rac1. J. Cell Sci. 128, 3041–3054. https://doi.org/10.1242/jcs.168674

Tornavaca, O., Chia, M., Dufton, N., Almagro, L.O., Conway, D.E., Randi, A.M., Schwartz, M.A., Matter, K., Balda, M.S., 2015. ZO-1 controls endothelial adherens junctions, cell–cell tension, angiogenesis, and barrier formation. J. Cell Biol. 208, 821–838. https://doi.org/10.1083/jcb.201404140

Tzima, E., Irani-Tehrani, M., Kiosses, W.B., Dejana, E., Schultz, D.A., Engelhardt, B., Cao, G., DeLisser, H., Schwartz, M.A., 2005. A mechanosensory complex that mediates the endothelial cell response to fluid shear stress. Nature 437, 426–431. https://doi.org/10.1038/nature03952

van Hinsbergh, V.W.M., van Nieuw Amerongen, G.P., 2002. Intracellular signalling involved in modulating human endothelial barrier function. J. Anat. 200, 549–560. https://doi.org/10.1046/j.1469-7580.2002.00060.x

van Wetering, S., van den Berk, N., van Buul, J.D., Mul, F.P.J., Lommerse, I., Mous, R., ten Klooster, J.-P., Zwaginga, J.-J., Hordijk, P.L., 2003. VCAM-1-mediated Rac signaling controls endothelial cell-cell contacts and leukocyte transmigration. Am. J. Physiol. Cell Physiol. 285, C343-352. https://doi.org/10.1152/ajpcell.00048.2003

Verma, S., Han, S.P., Michael, M., Gomez, G.A., Yang, Z., Teasdale, R.D., Ratheesh, A., Kovacs, E.M., Ali, R.G., Yap, A.S., 2012. A WAVE2-Arp2/3 actin nucleator apparatus supports junctional tension at the epithelial zonula adherens. Mol. Biol. Cell 23, 4601–4610. https://doi.org/10.1091/mbc.E12-08-0574

Verma, S., Shewan, A.M., Scott, J.A., Helwani, F.M., Elzen, N.R. den, Miki, H., Takenawa, T., Yap, A.S., 2004. Arp2/3 Activity Is Necessary for Efficient Formation of E-cadherin Adhesive Contacts. J. Biol. Chem. 279, 34062–34070. https://doi.org/10.1074/jbc.M404814200

Vestweber, D., Winderlich, M., Cagna, G., Nottebaum, A.F., 2009. Cell adhesion dynamics at endothelial junctions: VE-cadherin as a major player. Trends Cell Biol. 19, 8–15. https://doi.org/10.1016/j.tcb.2008.10.001

Vicente-Manzanares, M., Ma, X., Adelstein, R.S., Horwitz, A.R., 2009. Non-muscle myosin II takes centre stage in cell adhesion and migration. Nat. Rev. Mol. Cell Biol. 10, 778–790. https://doi.org/10.1038/nrm2786

Vincent, P.A., Xiao, K., Buckley, K.M., Kowalczyk, A.P., 2004. VE-cadherin: adhesion at arm's length. Am. J. Physiol. Cell Physiol. 286, C987-997. https://doi.org/10.1152/ajpcell.00522.2003

Wallrabe, H., Periasamy, A., 2005. Imaging protein molecules using FRET and FLIM microscopy. Curr. Opin. Biotechnol., Analytical biotechnology 16, 19–27. https://doi.org/10.1016/j.copbio.2004.12.002

Walsh, S.V., Hopkins, A.M., Chen, J., Narumiya, S., Parkos, C.A., Nusrat, A., 2001. Rho kinase regulates tight junction function and is necessary for tight junction assembly in polarized intestinal epithelia. Gastroenterology 121, 566–579. https://doi.org/10.1053/gast.2001.27060

Watanabe, T., Hosoya, H., Yonemura, S., 2007. Regulation of myosin II dynamics by phosphorylation and dephosphorylation of its light chain in epithelial cells. Mol. Biol. Cell 18, 605–616. https://doi.org/10.1091/mbc.e06-07-0590

Weis, W.I., Nelson, W.J., 2006. Re-solving the Cadherin-Catenin-Actin Conundrum. J. Biol. Chem. 281, 35593–35597. https://doi.org/10.1074/jbc.R600027200

Westerfield, M., 2000. The Zebrafish Book: A Guide for the Laboratory Use of Zebrafish (Danio Rerio). University of Oregon Press.

Wild, R., Klems, A., Takamiya, M., Hayashi, Y., Strähle, U., Ando, K., Mochizuki, N., Impel, A. van, Schulte-Merker, S., Krueger, J., Preau, L., Noble, F. le, 2017. Neuronal sFlt1 and Vegfaa determine venous sprouting and spinal cord vascularization. Nat. Commun. 8, 1–17. https://doi.org/10.1038/ncomms13991

Winkelman, J.D., Bilancia, C.G., Peifer, M., Kovar, D.R., 2014. Ena/VASP Enabled is a highly processive actin polymerase tailored to self-assemble parallel-bundled F-actin networks with Fascin. Proc. Natl. Acad. Sci. U. S. A. 111, 4121–4126. https://doi.org/10.1073/pnas.1322093111

Wolff, J.R., Bär, T., 1972. "Seamless" endothelia in brain capillaries during development of the rat's cerebral cortex. Brain Res. 41, 17–24. https://doi.org/10.1016/0006-8993(72)90613-0

Wu, Y.I., Frey, D., Lungu, O.I., Jaehrig, A., Schlichting, I., Kuhlman, B., Hahn, K.M., 2009. A genetically encoded photoactivatable Rac controls the motility of living cells. Nature 461, 104–108. https://doi.org/10.1038/nature08241

Yamada, S., Nelson, W.J., 2007. Localized zones of Rho and Rac activities drive initiation and expansion of epithelial cell-cell adhesion. J. Cell Biol. 178, 517–527. https://doi.org/10.1083/jcb.200701058

Yonemura, S., Wada, Y., Watanabe, T., Nagafuchi, A., Shibata, M., 2010. alpha-Catenin as a tension transducer that induces adherens junction development. Nat. Cell Biol. 12, 533–542. https://doi.org/10.1038/ncb2055

Yoo, S.K., Deng, Q., Cavnar, P.J., Wu, Y.I., Hahn, K.M., Huttenlocher, A., 2010. Differential regulation of protrusion and polarity by PI(3)K during neutrophil motility in live zebrafish. Dev. Cell 18, 226–236. https://doi.org/10.1016/j.devcel.2009.11.015

Zygmunt, T., Gay, C.M., Blondelle, J., Singh, M.K., Flaherty, K.M., Means, P.C., Herwig, L., Krudewig, A., Belting, H.-G., Affolter, M., Epstein, J.A., Torres-Vázquez, J., 2011. Semaphorin-PlexinD1 Signaling Limits Angiogenic Potential via the VEGF Decoy Receptor sFlt1. Dev. Cell 21, 301–314. https://doi.org/10.1016/j.devcel.2011.06.033